

Anaysis of Nano-Sized Irradiation-Induced Defects in Fe-base Materials by Means of Small Angle Neutron Scattering and Molecular Dynamics Simulations

THÈSE N° 4279 (2008)

PRÉSENTÉE LE 18 DÉCEMBRE 2008

À LA FACULTE SCIENCES DE BASE

CRPP GROUPE MATÉRIAUX

PROGRAMME DOCTORAL EN SCIENCE ET GÉNIE DES MATÉRIAUX

ÉCOLE POLYTECHNIQUE FÉDÉRALE DE LAUSANNE

POUR L'OBTENTION DU GRADE DE DOCTEUR ÈS SCIENCES

PAR

Gang YU

acceptée sur proposition du jury:

Prof. L. Zuppiroli, président du jury

Prof. N. Baluc, directrice de thèse

Prof. J. Bonneville, rapporteur

Dr Y. Dai, rapporteur

Prof. M. Q. Tran, rapporteur



ÉCOLE POLYTECHNIQUE
FÉDÉRALE DE LAUSANNE

Suisse
2008

ABSTRACT

Thermonuclear fusion of light atoms is considered since decades as an unlimited, safe and reliable source of energy that could eventually replace classical sources based on fossile fuel or nuclear fuel. Fusion reactor technology and materials studies are important parts of the fusion energy development program. For the time being, the most promising materials for structural applications in the future fusion power reactors are the Reduced Activation Ferritic/Martensitic (RAFM) steels for which the greatest technology maturity has been achieved, i.e., qualified fabrication routes, welding technology and a general industrial experience are almost available. The most important issues concerning the future use of RAFM steels in fusion power reactors are derived from their irradiation by 14 MeV neutrons that are the product, together with 3.5 MeV helium ions, of the envisaged fusion reactions between deuterium and tritium nuclei. Indeed, exposure of metallic materials to intense fluxes of 14 MeV neutrons will result in the formation of severe displacement damage (about 20-30 dpa per year) and high amounts of helium, which are at the origin of significant changes in the physical and mechanical of materials, such as hardening and embrittlement effects, for instance.

This PhD Thesis work was aimed at investigating how far the Small Angle Neutron Scattering (SANS) technique could be used for detecting and characterizing nano-sized irradiation-induced defects in RAFM steels. Indeed, the resolution limit of Transmission Electron Microscopy (TEM) is about 1 nm in weak beam TEM imaging, and it is usually thought that a large number of irradiation-induced effects have a size below 1 nm in RAFM steels and that these very small defects actually contribute to the irradiation-induced hardening and embrittlement of RAFM steels occurring at irradiation temperatures below about 400°C.

The aim of this work was achieved by combing SANS experiments on unirradiated and irradiated specimens of RAFM steels with Molecular Dynamics (MD) simulations of main expected nano-sized defects in irradiated pure Fe and Fe-He alloys, as model materials for RAFM steels, and simulations of their corresponding TEM images and SANS signals. In particular, the SANS signal of various types of defects was simulated *for the first time*.

The methodology used in this work was the following:

- SANS experiments were performed by applying a strong saturating magnetic field to unirradiated and irradiated specimens of three types of RAFM steels, namely the European EUROFER 97, the Japanese F82H and the Swiss OPTIMAX A steels. The available irradiated specimens included specimens which had been irradiated with 590 MeV protons in the Proton IRradiation EXperiment (PIREX) facility at the Paul Scherrer Institute (PSI) at temperatures in the range of 50-350°C to doses in the range of 0.3-2.0 dpa. SANS spectra as well as values of the so-called A ratio, which represents the ratio of the total scattered intensity to the nuclear scattered intensity, were obtained for the various irradiation doses and temperatures investigated.

- MD simulations of atomic displacement cascades in pure Fe and in Fe-He alloys were performed using Embedded Atom Method (EAM) many-body interatomic potentials. The main nano-sized defects that should be produced in RAFM steels under irradiation were created by means of MD in pure Fe. These included dislocation loops of various types, voids, helium bubbles with various He concentration and Cr precipitates.
- TEM images of cascade damage and all the defects created by MD were simulated in the dark field/weak beam imaging modes by using the Electron Microscopy Software (EMS) developed by P.A. Stadelmann (EPFL) and analyzed in terms of variations of contrast intensities versus depth inside the specimen.
- The SANS signal provided by cascade damage and all the defects created by MD was simulated by using a slightly modified version of EMS, accounting for neutrons instead of electrons.

The SANS technique has been proven in this work to be a very powerful tool for detecting nano-sized irradiation-induced defects and a tool well complementary to TEM for characterizing such very small irradiation-induced defects. Indeed, TEM appears most adapted to investigate structural defects, such as dislocation loops and helium bubbles with high helium concentration, which yield significant lattice deformation of the surrounding matrix, while SANS is most adapted to investigate phase defects, such as voids, helium bubbles with low helium concentration and Cr precipitates. By combining the results of SANS experiments with those of MD simulations, TEM image simulations and SANS signal simulations, the nano-sized irradiation-induced defects were tentatively identified as small helium bubbles. While the radiation hardening measured for RAFM steels cannot be explained by accounting only for the defects observed in TEM, it could be successfully modeled by accounting also for a reasonable number density of the nano-sized defects evidenced using the SANS technique.

Keywords: RAFM steels, radiation damage, small angle neutron scattering, molecular dynamics simulations, transmission electron microscopy image simulations.

RÉSUMÉ

La fusion thermonucléaire d'atomes légers est considérée depuis plusieurs décennies comme une source d'énergie sûre et illimitée, qui pourrait éventuellement remplacer le combustible fossile ou nucléaire. La technologie et les matériaux pour les futurs réacteurs de fusion thermonucléaire constituent des points importants du programme de développement de l'énergie de fusion. A l'heure actuelle, les aciers ferritiques/martensitiques à activation réduite (aciers RAFM) sont les principaux matériaux candidats à des applications structurales dans les futurs réacteurs de fusion, leur méthode de fabrication et technologie de soudage au niveau industriel étant relativement bien avancées. Les incertitudes les plus importantes relatives à la future utilisation des aciers RAFM dans les réacteurs de fusion est reliée à leur irradiation par les neutrons de 14 MeV, qui seront le produit des réactions de fusion entre un ion de deutérium et un ion de tritium, en plus d'un ion d'hélium de 3.5 MeV. En effet, l'exposition de matériaux métalliques à un flux élevé de neutrons de 14 MeV résultera en la formation d'un endommagement microstructural important (de l'ordre de 20 à 30 dpa par année) ainsi que d'une concentration élevée d'hélium, qui sont à l'origine de modifications significatives des propriétés physiques et mécaniques des matériaux concernés, comme par exemple des effets de durcissement et de fragilisation.

Le but de cette thèse de doctorat était d'étudier s'il est possible, et jusqu'à quel point il est possible, d'utiliser la technique de diffusion neutronique à petits angles (SANS) afin de détecter et de caractériser les défauts de taille nanométrique produits sous irradiation par les neutrons de 14 MeV dans les aciers RAFM. En effet, la résolution de la technique de microscopie électronique en transmission (MET) est limitée à environ 1 nm en utilisant la technique dite des 'faisceaux faibles'. Néanmoins, il est généralement estimé que, en réalité, il existe de nombreux petits défauts produits par irradiation qui présentent une taille inférieure au nanomètre et qui sont donc invisibles en MET, mais qui contribuent malgré tout de façon importante aux phénomènes de durcissement et de fragilisation observés pour des températures d'irradiation inférieures à environ 400°C.

Le but de cette thèse a été atteint en effectuant des expériences de SANS sur des échantillons non irradiés et irradiés d'aciers RAFM, combinées à des simulations en dynamique moléculaire de défauts de taille nanométrique dans le Fer pur et des alliages Fe-He, comme matériaux modèles pour les aciers RAFM, ainsi qu'à des simulations de leurs images en MET et de leurs signaux correspondant en SANS. En particulier, la simulation du signal SANS émis par les différents défauts créés en dynamique moléculaire fut réalisée *pour la toute première fois*. La méthodologie qui fut utilisée dans le cadre de ce travail est la suivante:

- Les expériences de SANS furent effectuées en appliquant un champ magnétique intense à des échantillons non irradiés et irradiés de trois types d'aciers RAFM: l'acier européen EUROFER 97, l'acier japonais F82H et l'acier suisse OPTIMAX A. Les échantillons irradiés disponibles comprenaient des échantillons qui furent irradiés par des protons de 590 MeV au moyen de l'installation PIREX (Proton IRradiation EXperiment) située à l'Institut Paul Scherrer (PSI) à des températures comprises entre 50 et 350°C et des doses comprises entre 0.3 et 2.0 dpa. Des spectres SANS furent ainsi obtenus, de même que des

valeurs du fameux coefficient A , qui représente le rapport de l'intensité diffusée totale à l'intensité diffusée de type purement nucléaire, pour les différentes conditions de dose et de température étudiées.

- Des simulations en dynamique moléculaire de cascades de déplacements atomiques dans le Fer pur et différents alliages Fe-He ont été réalisées au moyen de potentiels interatomiques à plusieurs corps basés sur la méthode de l'atome encastré. Les principaux défauts de taille nanométrique qui devraient être produits sous irradiation dans les aciers RAFM ont été créés par dynamique moléculaire dans le Fer pur. Les défauts créés comprenaient des boucles de dislocation de différents types, des vides, des bulles d'hélium à différentes concentrations d'hélium et des précipités de chrome.
- Des simulations d'images en MET des résidus de cascades de déplacements atomiques et de tous les défauts créés par dynamique moléculaire ont été réalisées en conditions de diffraction du type champ sombre ou faisceaux faibles au moyen du programme EMS développé par P.A. Stadelmann (EPFL) et analysées en termes de variations d'intensité du contraste en fonction de la profondeur.
- Des simulations du signal SANS émis par les résidus de cascades de déplacements atomiques et de tous les défauts créés par MD ont été réalisées en utilisant une version légèrement modifiés du programme EMS, tenant compte des neutrons en lieu et place des électrons.

Il a été démontré dans cette étude que la technique de diffusion neutronique à petits angles est un outil très utile à la détection de tout petits défauts produits sous irradiations ainsi qu'un outil complémentaire à la microscopie électronique en transmission en ce qui concerne la caractérisation de ces tout petits défauts. En effet, la microscopie électronique en transmission semble bien adaptée à l'étude de défauts structuraux du type boucles de dislocation et bulles d'hélium à forte concentration d'hélium, qui induisent une déformation de réseau de la matrice environnante, alors que la technique de diffusion neutronique à petits angles semble mieux adaptée à l'étude de défauts de phase, tels les vides, les bulles d'hélium à faible concentration d'hélium et les précipités de chrome. En combinant les résultats des expériences de diffusion neutronique à petits angles et des simulations en dynamique moléculaire, ainsi que des simulations d'images de microscopie électronique en transmission et du signal de diffusion neutronique à petits angles, les petits défauts de taille nanométrique ont été identifiés comme devant être des petites bulles d'hélium. Bien que le durcissement des aciers RAFM sous irradiation ne puisse être expliqué en ne tenant compte que des défauts visibles en microscopie électronique en transmission, il a été modélisé avec succès en tenant compte également d'une densité raisonnable des tout petits défauts de taille nanométrique détectés en utilisant la technique de diffusion neutronique à petits angles.

Mots clés: Aciers ferritiques/martensitiques à activation réduite, dégâts d'irradiation, diffusion neutronique à petits angles, simulations en dynamique moléculaire, simulations d'images en microscopie électronique en transmission.

TABLE OF CONTENTS

ABSTRACT	I
RÉSUMÉ	III
INTRODUCTION	1
CHAPTER 1: LITERATURE SURVEY.....	3
1.1 Introduction to reduced activation ferritic/martensitic steels	3
1.2 Fundamentals of radiation damage and effects	4
1.2.1 Introduction to the interaction between particles and atoms.....	4
1.2.2 Introduction to radiation damage	8
1.2.3 Introduction to radiation effects	10
1.3 Fundamentals of Small Angle Neutron Scattering (SANS).....	11
1.3.1 Small angle scattering methods.....	11
1.3.2 Small angle neutron scattering	13
1.3.3 Cross section of neutron scattering by one atom.....	14
1.3.4 Theory of small angle neutron scattering.....	17
1.3.5 Scattered intensity for a mixing of $(p+1)$ (≥ 3) species	20
1.3.6 Intra- and inter-species interferences.....	21
1.3.7 Asymptotic behavior of scattering.....	25
1.3.8 Fractal objects	26
1.4 Practical use of the SANS technique	29
1.5 Examples of applications of the SANS technique	33
1.5.1 As-annealed steels	33
1.5.2 Irradiated steels.....	33
1.6 Introduction to simulation methods	35
1.6.1 Molecular Dynamics (MD) simulations	35
1.6.2 Transmission Electron Microscopy (TEM) image simulations	40
1.6.3 SANS signal simulations	41
1.7 Motivation of the thesis	41
CHAPTER 2: EXPERIMENTAL AND SIMULATION TOOLS	43
2.1 Materials	43
2.2 Irradiation experiments.....	44
2.2.1 Specimens	44
2.2.2 Irradiation facility.....	45
2.2.3 Irradiation conditions.....	47
2.2.4 Dosimetry.....	47
2.3 SANS experiments	48
2.3.1 Specimens	48
2.3.2 Specimen holders.....	49
2.3.3 SANS facility	51
2.3.4 Measurement procedure.....	54

2.3.5	Measurement conditions	56
2.3.6	Reduction of the raw data	57
2.4	Simulation tools	59
2.4.1	MD simulations	59
2.4.2	TEM image simulations.....	65
2.4.3	SANS signal simulations	67
CHAPTER 3: RESULTS.....		69
3.1	SANS experiments	69
3.1.1	Examples of SANS spectra.....	69
3.1.2	Effects of irradiation dose.....	70
3.1.3	Effects of irradiation temperature.....	72
3.1.4	Analysis model for the SANS spectra	73
3.1.5	Size distribution of irradiation-induced defects	73
3.1.6	Magnetic versus nuclear scattering.....	78
3.2	Simulations	82
3.2.1	MD simulations	82
3.2.2	TEM image simulations.....	99
3.2.3	SANS signal simulations	119
CHAPTER 4: DISCUSSION.....		125
4.1	SANS experiments	125
4.1.1	Size of irradiation-induced defects.....	125
4.1.2	Number density of irradiation-induced defects.....	126
4.1.3	Geometry of irradiation-induced defects	127
4.1.4	Type of irradiation-induced defects.....	129
4.2	Simulations	133
4.2.1	MD simulations	133
4.2.2	TEM image simulations.....	133
4.2.3	SANS signal simulations	135
4.3	General discussion	138
4.3.1	TEM/SANS comparison.....	138
4.3.2	Summary of main results available for RAFM steels.....	139
4.3.3	Radiation hardening of the EUROFER 97 RAFM steel.....	142
CHAPTER 5: CONCLUSIONS AND PERSPECTIVES		147
APPENDIX		149
REFERENCES		151

INTRODUCTION

This PhD Thesis work was aimed at investigating how far the Small Angle Neutron Scattering (SANS) technique can be used for detecting and characterizing nano-sized irradiation-induced defects in Reduced Activation Ferritic/Martensitic (RAFM) steels for structural application in the future fusion reactors. Indeed, the resolution limit of Transmission Electron Microscopy (TEM) is about 1 nm in weak beam TEM imaging, and it is usually thought that a large number of irradiation-induced effects in RAFM steels have a size below 1 nm and that these very small defects actually contribute to the irradiation-induced hardening and embrittlement of RAFM steels occurring at irradiation temperatures below about 400°C.

The aim of this work was achieved by combining SANS experiments on unirradiated and irradiated specimens of RAFM steels with Molecular Dynamics (MD) simulations of main expected nano-sized defects in irradiated pure Fe and Fe-He alloys, as model materials for RAFM steels, and simulations of their corresponding TEM images and SANS signals.

This manuscript is divided into five chapters.

- Chapter 1 contains an introduction to RAFM steels for fusion power reactors, to the theory of neutron scattering and to the bases of the simulation tools that were used in this work. It also presents the motivation of this work.
- Chapter 2 contains a description of the RAFM steels investigated, the irradiation facility and conditions, the SANS facility and conditions, and the simulation tools and conditions, with an emphasis on the description of the main defects expected to be produced by irradiation in pure Fe and Fe-He materials.
- Chapter 3 presents the results obtained by means of SANS experiments on unirradiated and irradiated specimens of RAFM steels, and MD simulations, TEM image simulations and SANS signal simulations of all the defects described under chapter 2.
- Chapter 4 discusses the main results obtained under chapter 3, with an emphasis on the identification of nano-sized irradiation-induced defects and their impact on the radiation hardening of RAFM steels.
- Chapter 5 presents the main conclusion of this work and a few perspectives for further possible activities.

CHAPTER 1: LITERATURE SURVEY

1.1 Introduction to reduced activation ferritic/martensitic steels

Fusion reactor technology and materials studies are important parts of the fusion energy development program. Austenitic stainless steels have been selected as first wall and breeding blanket structural materials for the International Thermonuclear Experimental Reactor (ITER) that should become operational around 2018. The development of ferritic/martensitic steels for structural application in the future fusion power reactors emanates from the limitations of the austenitic stainless steels and the promising high dose experience with ferritic/martensitic steel fuel cladding in liquid metal cooled fast reactors.

The austenitic steels suffer from severe helium embrittlement at elevated temperatures and swell to a degree not acceptable for fusion reactor components. The ferritic/martensitic steels exhibit superior performance to austenitic steels in both swelling and helium embrittlement resistance. At a temperature of about 300°C the swelling rate of ferritic/martensitic steels is about 1 vol.% after 100 dpa, while it is about 1 vol.% after 10 dpa for typical austenitic steels. Ferritic/martensitic steels also exhibit a better surface heat capability than austenitic steels (5.4 kW/m at 400°C, i.e., about three times that of austenitic steels) [1], favorable cost, availability and service experience, and their good compatibility with aqueous, gaseous, and liquid metal coolants permits a range of design options. At the same time ferritic/martensitic steels with alloying elements such as chromium, some tungsten, vanadium and tantalum activate little compared to conventional austenitic stainless steels with nickel and molybdenum. In addition, manganese-stabilized austenitic stainless steels are not attractive due to high decay heat (safety) concerns. In Europe, Japan and Russia it has been demonstrated that it is now feasible to produce Reduced Activation Ferritic/Martensitic (RAFM) steels on an industrial scale with sufficiently low impurity levels, e.g. [2-8]. Industry has also shown to be able to reproduce the required quality. The promise remains to produce low activation varieties that allow recycling within a century [9, 10]. The production of RAFM steels with even stricter impurity control is technically feasible, but requires fabrication equipment used for *clean* steels only [11]. Main RAFM steels that are being investigated include the Chinese Low Activation Martensitic (CLAM) steel, the European EUROFER 97 alloy, the Japanese F82H and JLF-1 alloys, and the Russian RUSFER-EK-181 alloy. Their composition lies in the following range: Fe-(7.5-12)Cr-(1.1-2)W-(0.15-0.25)V, in weight percent.

The most important issues concerning the future use of RAFM steels in fusion power reactors are derived from their irradiation by 14 MeV neutrons that are the product, together with energy and helium ions, of the envisaged fusion reactions between deuterium and tritium nuclei. Indeed, exposure of metallic materials to intense neutron fluxes results in the formation of severe displacement damage (about 20-30 dpa per year) and significant amounts of helium, which are at the origin of significant changes in the physical and mechanical of materials, such as hardening and embrittlement effects, for instance. To date, many research

activities, scientific papers and international workshops have been devoted to these steels regarding their development and characterization of their microstructure and mechanical/physical properties before and after irradiation, e.g. [12-18].

1.2 Fundamentals of radiation damage and effects

1.2.1 Introduction to the interaction between particles and atoms

Radiation damage relates to the initial disturbance of a material under irradiation and arises from the interaction of incident beam particles with the atoms (electrons and nuclei) of a target material. The interaction depends on the mass, electrical charge and energy of the incident particles, as well as on the features of the target material. In general, three types of interaction between the incident beam particles and the target material atoms may take place [19]:

- 1) Elastic interaction between the particles and the target material atoms;
- 2) Inelastic interaction between the particles and the target material electrons;
- 3) Inelastic interaction between the particles and the target material nuclei.

As a result of these interactions, the following phenomena may take place [19, 20]:

- i) Atomic displacements or atomic displacement cascades;
- ii) Excitation of electrons;
- iii) Introduction of foreign atoms, either by nuclear transmutation reactions or by the impinging particles stopping in the solid.

These three phenomena are described in detail just below.

i) During the elastic collision between a particle and an atom, the transferred energy can be sufficient, i.e., above a certain threshold energy T_d that is dependent on the material and the temperature, to move the atom out of its lattice site, creating a Frenkel pair (vacancy-interstitial pair). The initial collision is called the primary collision and the first displaced atom is called the Primary Knock-on Atom (PKA).

The sequence of basic events resulting from the interaction of an incident high-energy particle with lattice atoms and leading to the formation of defects and defect clusters is illustrated in Figure 1.2.1.1 and can be described as follows [21-23]. Within less than 1 fs, the primary knock-on event takes place, and a PKA with a recoil energy T is created. At the same time, transmutation of the knocked-on atom can occur and result in the formation of an impurity, such as a He or a H gas atom or a heavier element. Here, we are interested in lattice defect production. If its energy is high enough, the PKA can engender other atomic displacements via collision cascades [24]. A collision cascade takes place after a very short period of time, about 0.2 ps, and results in a large number of displaced atoms. Then, in about 3 ps, the energy inside the cascade is released to the surroundings and yields the so-called thermal spike, which refers to the volume inside the cascade that has a very high temperature, usually much higher than the melting point. In another 7 ps, the cascade cools down to form a

vacancy-rich zone, while an interstitial shell appears around this depleted zone. Afterwards, a fraction of the interstitials and vacancies, which is temperature dependent and of about 70-90%, annihilates by thermal intra-cascade recombination. The surviving vacancies and interstitials agglomerate to form small clusters, or annihilate at sinks (e.g. dislocations, grain boundaries, interfaces), or move as free point defects. Table 1.2.1.1 gives a summary of the time evolution of a displacement cascade. The size and lifetime of the cascade increase with the PKA energy. If it is above about 20 keV in copper, for instance, the cascade subdivides into sub-cascades.

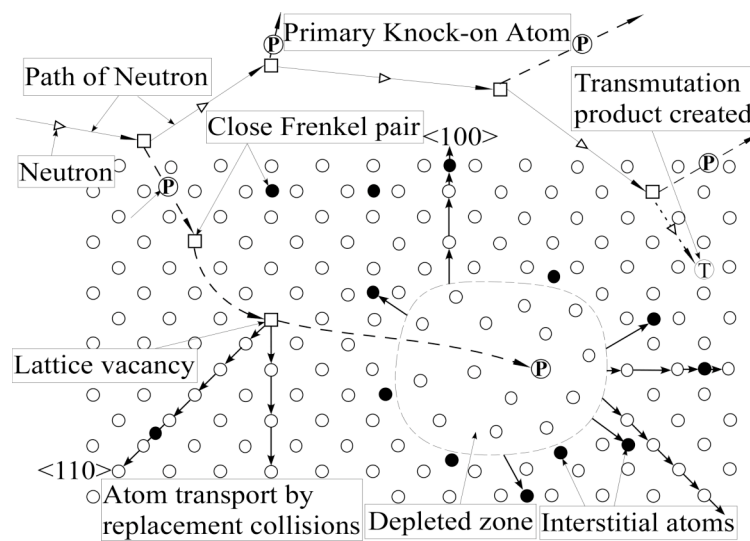


Figure 1.2.1.1: Conceptual representation of events occurring during collision of a neutron with metal lattice atoms [20].

Duration (ps)	Event	Result
10^{-3}	Transfer of recoil energy from the impinging particle	PKA
$10^{-3} \sim 0.2$	Slowing down of the PKA by the generation of a collision cascade: binary collisional phase	Vacancies and low-energy recoil collisions, sub-cascades
$0.2 \sim 0.3$	Thermal spike: equipartition of the energy in the cascade volume	Low energy density, hot molten droplet, propagation of a shock wave front in the matrix
0.33	Interstitial ejection, transition from heated to undercooled liquid core	Stable interstitials, atomic mixing
$3 \sim 10$	Cascade core solidification and cooling to ambient temperature	Depleted zone, disordered zone, amorphous zone, vacancy collapse
10 or more	Thermal intra-cascade recombination, thermal escape of self-interstitial atoms (SIAs)	Surviving defects (SD), escaping interstitials (EI), escaping vacancies (EV), stationary fluxes of EI and EV, growth/shrinkage of SIA or vacancy clusters, solute segregation

Table 1.2.1.1: Time evolution of atomic displacement cascades in metals [19].

During the collision between a particle with a mass m and an energy E and a PKA with a mass M , the maximum recoil energy T_{\max} that can be transferred is given by [25, 26]:

$$T_{\max} = \frac{4(mM)}{(m+M)^2} E \quad (1.2.1.1).$$

Therefore, the energy of the PKA lies in the range $0 \leq T \leq T_{\max}$ and can be described by a recoil energy spectrum. A number of codes, e.g. HETC [27] and SPECTER [28], which were developed on the basis of the nuclear reaction theory, can be used to calculate recoil energy spectra and other parameters such as the displacement damage cross section and the production of transmutation elements.

Kinchin and Pease (1955) [29] were the first ones to affirm that when a lattice atom receives a recoil energy larger than a threshold displacement energy, T_d , it will be displaced from its lattice position. However, if $T < T_d$, the atom will return rapidly to its initial position after a short displacement. T_d is therefore the energy above which a *stable* Frenkel pair is created. Table 1.2.1.2 gives examples of T_d values for different metals.

Metal	Al	Fe	Ni	Cu	Ag	Nb	Ta
T_d (eV)	22	24	24	22	28	36	32

Table 1.2.1.2: Examples of T_d values for different metals, as measured at 20 K [30, 31].

Kinchin and Pease gave the number of displaced atoms produced by a PKA of energy T as:

$$N_d(T) = T/2T_d \quad (1.2.1.2).$$

In order to account for the electronic stopping power, Lindhard et al (1963) [32] studied the process of slowing down of an energetic PKA by using the Thomas-Fermi atomic theory and proposed the well-known Lindhard-Scharff-SchiØtt (LSS) theory, which demonstrates that the damage energy (T_d) for displacing lattice atoms is a function of the PKA energy (T), the mass and atomic number of the PKA ($m_1; Z_1$) and of the lattice atoms ($m_2; Z_2$):

$$T_d = f(T; m_1; Z_1; m_2; Z_2) \quad (1.2.1.3).$$

Norgett, Robinson and Torrens (NRT) (1974) [33] then modified the Kinchin-Pease model by taking the electronic stopping power into account and obtained the following equations:

$$N_d = \begin{cases} 0, & \text{for } T < T_d \\ 1, & \text{for } T_d < T < 2.5T_d \\ 0.8T_d/2T_d, & \text{for } T > 2.5T_d \end{cases} \quad (1.2.1.4).$$

This is the widely used NRT approximation for the calculation of displacement damage, quoted in dpa (number of displacements per atom), which is currently used as the irradiation dose unit. The NRT value refers to the number of displacements produced in the collisional

phase. Experimental results [34, 35] as well as Molecular Dynamics (MD) simulations [36, 37] have shown that the number of defects surviving at the end of the cascade evolution is only a small fraction (about 10-30%, temperature dependent) of the number of atomic displacements given by the NRT approximation.

By considering the number of Frenkel pairs generated in several metals, Bacon et al. (1995) [38] have shown that a new empirical relationship between N_d and T fits well the MD simulation results for PKA energies between 5 and 10 keV:

$$N_d = A(T)^m \quad (1.2.1.5),$$

where A and m are constants that depend on the material and the irradiation temperature. For the aluminum at 10 K, Almazouzi (1999) [39] has found $A = 7.85$ and $m = 0.733$. The obtained data indicate that the differences in N_d values for different metals are due mainly to their atomic mass, N_d decreasing with the increasing mass of the target atoms. As one cascade produces fewer defects in average than those produced by two separate cascades of the same total energy, sub-cascade formation leads to an increase in the number of the Frenkel pairs produced.

Fundamental findings of MD simulations of atomic displacement cascades are that the core region undergoes a local melting that has a strong influence on the number of displaced atoms in the cascade and on the primary state of damage. The observation of local melting, with its attendant features of high pressure, liquid-like diffusion, and re-solidification, provides the basis for understanding many aspects of cascade damage. In most materials the high pressure developed in cascades does not cause plastic deformation. This is largely because the spherical stress state created by a cascade is nearly hydrostatic.

ii) Inelastic interaction between the particles and the electrons of the solid leads to excitation of electrons. In metallic materials under consideration here, all electronic excitations are quickly thermalized and do not, in general, lead to radiation damage.

iii) Inelastic interaction between the particles and the nuclei of the target leads to the production of transmutation products. Nuclear reactions where gaseous elements are generated are very important because gases, particularly helium, are known to affect materials properties already at very low concentrations. Transmutation helium can affect the behavior of irradiated metallic materials (e.g. steels) in three ways. First, helium stabilizes vacancy clusters, which, in turn, cause an increase in the number of interstitial clusters (i.e., helium ties up vacancies and reduces interstitial-vacancy recombination). Interstitial clusters can then grow into dislocation loops and increase the strength of materials. Secondly, helium stabilizes the clusters up to higher temperatures than in the absence of helium. The third effect involves the migration of helium to grain boundaries during irradiation, causing intergranular brittle failure under load, a phenomenon referred to as helium embrittlement.

1.2.2 Introduction to radiation damage

It is well known that changes in mechanical, physical and dimensional properties of irradiated materials, such as steels, result directly from the production and evolution of the damage microstructure. Although the features of the damage microstructure depend on the type of steel investigated, the kinds of defects that evolve and the processes involved are common to a wide range of steels. These defects and processes include:

- Perfect dislocation loops and network dislocations: perfect dislocation loops can move on their glide cylinders and continue to expand by net self-interstitial absorption. These large, perfect loops ultimately become indistinguishable from the network dislocations originally present in the materials. Network dislocations and large loops can climb and glide into lower energy configurations or annihilate with neighboring dislocation segments of opposite type (recovery) [40, 41].
- Frank loops: self-interstitial clustering leads initially to the formation of what is referred to as ‘black dot’ damage in conventional transmission electron microscopy (TEM). However, high resolution TEM techniques allow identifying these small defect clusters as faulted, interstitial-type dislocation loops [42]. Once nucleated, they continue to grow by net self-interstitial absorption and are clearly distinguishable at larger sizes as Frank loops. Their growth continues until they become unstable and unfault into perfect loops or until they interact with network dislocations to be directly incorporated [43].
- Bubbles: bubbles are primarily helium-gas filled cavities in irradiated materials. Helium is produced by endothermic (n, α) reactions in virtually all of the major constituents of steels by neutrons with energies in the MeV range and, hence, will be produced in large quantities in the fusion reactor environment. As an insoluble species, helium combines with vacancies to form bubbles. Once nucleated, the bubbles grow by a combination of helium and net vacancy absorption to maintain a mechanical equilibrium between their internal pressure and the sintering stress given by $2\gamma/r$, where γ is the surface energy and r is the bubble radius [40].
- Voids: it is believed that beyond a certain critical radius, helium bubbles become unstable and grow as voids by net vacancy absorption without the need to maintain mechanical equilibrium, because of the lowest free energy of cleavage system [44]. Hence, a cavity population with a bimodal size distribution develops, which includes small sub-critical sized helium bubbles and large voids.
- Stacking fault tetrahedra (SFTs): they are the most stable defect clusters of vacancy type observed in low stacking fault energy fcc metals and alloys like Cu, Au, austenitic stainless steels, etc. A commonly accepted mechanism for SFT formation considers the expansion of partial dislocations from a faulted Frank vacancy loop. SFTs can also form directly from cascade collapse. Some works showed that voids nucleate preferentially at SFTs and that bubbles could also grow at the expense of SFTs [45].
- Precipitates: a variety of second phases form as a result of thermally induced precipitation and irradiation-induced segregation. These include M_6C and $M_{23}C_6$ carbides, Ni_3Si (γ), Fe_2Mo (*Laves*) and $Ti_6Ni_{16}Si_7$ (*G*) phases. The propensity to form these phases depends strongly on the material composition and environment [46].

Irradiation-induced dislocation loops in Fe-base materials with a bcc crystalline structure have at small sizes a Burgers vector of $1/2 a_0 \langle 111 \rangle$ [47-50] and occasionally $a_0 \langle 100 \rangle$, as reported in [48]. At larger sizes, beyond about 5 nm, they may present both $1/2 a_0 \langle 111 \rangle$ and $a_0 \langle 100 \rangle$ Burgers vectors [49, 50]. It should be noted that $a_0 \langle 100 \rangle$ loops are more frequently observed in Fe as compared to other bcc metals. Using e.g. the inside-outside contrast technique in TEM the $a_0 \langle 100 \rangle$ loops reveal an interstitial nature [49]. At high doses the ferritic/martensitic steels develop a network of dislocations with both $1/2 a_0 \langle 111 \rangle$, which is favored in the bcc structure [51], and $a_0 \langle 100 \rangle$ Burgers vectors, the latter being predominant when the Cr content is below 6 wt.% [52]. Irradiation-induced $a_0 \langle 100 \rangle$ dislocations arise from the growth of $1/2 a_0 \langle 111 \rangle$ interstitial loops [50, 52, 53]. The Burgers vector of irradiation-induced dislocation loops depends also on irradiation temperature; in Fe at 60°C it is $1/2 a_0 \langle 111 \rangle$, while at 550°C it is $a_0 \langle 100 \rangle$ [54]. With increasing the irradiation temperature, but below 300°C, the dislocation loop structure slightly coarsens; in e.g. the F82H RAFM steel the loop number density decreases and the loop size increases [55]. From about 300°C [50] to 350°C [55-57] this coarsening becomes more significant.

In ferritic/martensitic steels, irradiation-induced precipitation of secondary phase precipitates is often observed [58]. One of the most detrimental precipitation expected in steels containing more than about 10 wt.% Cr, the composition beyond which the enthalpy of mixing of Fe and Cr becomes positive [59], is the formation of α' precipitates (Cr-rich). This was observed in TEM a long time ago following thermal ageing [60] and leads to the so-called 475°C embrittlement [61]. There have been several studies of Cr-Mo steels irradiated in fast reactors or mixed-spectrum reactors in the temperature range from 300 to 650°C up to 70 dpa. These studies revealed the formation of irradiation-induced precipitates already below about 450°C. The identified precipitates include M_6C carbides, G -phase, α' -phase and Chi -phase (compound with a complex cubic structure, like $Fe_{36}Cr_{12}Mo_{10}$) precipitates. This kind of precipitation superimposes on the as-tempered precipitates and the tempered martensite microstructure, which generally remains stable, although the 9Cr-1MoVNb steel substructure was observed to coarsen as a result from irradiation at 300 to 500°C to 37-39 dpa. Laves phases may also form during thermal aging at 400 to 600°C [62-65].

Amorphization of $M_{23}C_6$ precipitates was first observed [66] in the ferritic/martensitic steel DIN 1.4926 irradiated with 800 MeV protons at temperatures up to 230°C. Amorphization was initially observed at a dose of 0.39 dpa, the amorphous structure coexisting with a crystalline structure in the same precipitate, and appeared to be complete at 3.4 dpa, as a result from segregation processes enhanced by irradiation.

The presence of solute gas atoms, such as O and He [67-69], plays an important role in the nucleation of voids, as they stabilize the 3-dimensional geometry for a small vacancy cluster, which is actually less stable than the platelet geometry [70]. There have been a number of studies regarding helium effects on the microstructural evolution of ferritic/martensitic steels using 'single beam' He implantation experiments or the so-called 'dual-beam' experiments, whereby He is injected while the specimen is being simultaneously irradiated with Fe ions, for instance, in order to create displacement damage. The latter experiments allow adjusting the He/dpa ratio to a chosen value [71-74]. For example, ion implantation of He to 5000 appm into the EM10 and 9Cr-1Mo ferritic/martensitic steels at 250 and 550°C [75] produces cavities that are visible only at 550°C using TEM [76]. Note that this implantation

corresponds to an irradiation dose and a dose rate of 0.8 dpa and 2.5×10^{-6} dpa·s⁻¹, respectively [75]. In this case there is clear evidence of cavities at the grain boundaries [76]. Increasing the He injection rate at a given temperature and total He content, or decreasing the implantation temperature with the implantation rate and the accumulated He amount kept constant, results in a decrease of the mean He bubble size and in an increase in the bubble number density. At higher He implantation temperatures, typically above $0.4 T_m$, where T_m is the melting temperature, bubble nucleation in ferritic/martensitic steels occurs preferentially at dislocations, martensitic laths, grain boundaries and precipitates. Bubbles tend to be elongated and strongly faceted [71, 76, 77], with facets parallel to {100} planes. At lower temperatures and/or high implantation rates the tiny nanometric bubbles that are created appear spherical when characterized by means of conventional TEM techniques. However, a recent study revealed, using holography in a TEM, that these small bubbles may be actually faceted, as well [78]. Some attempts have also been made to evaluate the He content inside bubbles using techniques such as SANS [76, 79] and electron energy loss spectroscopy (EELS) [80]. However, they simultaneously sample a number of bubbles that may exhibit various sizes, He contents and pressures. Furthermore, following dual-beam irradiation, a bimodal cavity size distribution can be seen in a given temperature range that depends on the irradiation conditions (see for instance [73, 74]). The larger cavities contain a He pressure below the equilibrium pressure. Such voids appear when a helium bubble reaches a critical size/gas content beyond which the cavity begins to grow more quickly as a result of an excess flux of vacancies over interstitials, due to a bias in the point defect elimination at sinks [81].

1.2.3 Introduction to radiation effects

The irradiation-induced microstructure may strongly affect the materials properties. Changes of the physical properties may include a decrease of electrical conductivity (especially at low temperatures) and/or of thermal conductivity (especially for ceramic materials). Changes of the mechanical properties may include hardening (referred to as ‘radiation hardening’), embrittlement effects and/or a loss of creep strength. Embrittlement effects include a loss of ductility in tensile tests, a loss of fracture toughness, and an increase in the ductile-to-brittle transition temperature associated with a decrease in the upper shelf energy. Void formation may engender a macroscopic increase in the volume of the irradiated material, a phenomenon referred to as ‘void swelling’, favored by the presence of He, leading to a loss of dimensional stability. Irradiation creep and irradiation growth may also occur, as well as irradiation-assisted stress corrosion cracking. In addition, irradiated materials may become radioactive, due to the formation of radioactive impurities by nuclear transmutation reactions.

1.3 Fundamentals of Small Angle Neutron Scattering (SANS)

1.3.1 Small angle scattering methods

Scattering methods are commonly used for the analysis of nano-sized objects such as clusters and precipitates. They relate to the analysis of the pattern generated when a planar wave hits a scattering system composed of any number of scattering centers or objects.

Due to the reverse relationship between the real and reciprocal lattices, information on large distances in the real space is confined to small scattering vectors (q) in the reciprocal space, i.e., to small scattering angles. For larger q values, one distinguishes three regimes of small angle scattering: the Guinier regime, the fractal regime and the Porod regime. The Guinier regime provides information about the average size of isolated diffracting objects, when these objects are small in comparison to the size of the incident beam. The fractal regime provides information about the fractal dimension (d) of these objects. In this regime, the scattered intensity varies as q^{-d} . The Porod regime provides information about the shape of the smaller entities composing the investigated objects. For still larger q values, one has access to the Bragg regime and therefore to the interatomic distances.

Small angle scattering (SAS) is the collective name given to the techniques of Small Angle Neutron Scattering (SANS), Small Angle X-ray Scattering (SAXS) and (Small Angle) Light Scattering (LS or SALS). In each of these techniques a radiation is elastically scattered by a sample, and the resulting scattering pattern may provide information about the nature, size, shape, orientation and number density of certain components of the sample.

LS cannot be used to study optically opaque samples and SAXS cannot be employed to study thick samples or samples requiring complex containers, while SANS (and SAXS) probe different length scales than LS. Thus, these techniques are complementary to a large extent. They do, however, also share several similarities. The most important of these is the fact that, with minor adjustments to account for the different types of radiation, the same basic equations and laws (for example, those proposed by Guinier, Zimm, Kratky or Porod) may be used to analyze data obtained by means of any of these three techniques.

Figure 1.3.1.1 illustrates the various interaction mechanisms occurring between a beam of neutrons, X-rays or electrons and a material. X-rays (red) and electron beams (green) both interact with electrons in the material; with X-rays the interaction is electromagnetic, whereas with electrons it is electrostatic. Both of these interactions are strong, and none of these two beams penetrates the matter very deeply. Neutrons (blue) interact with atomic nuclei via the very short-range strong nuclear force and thus penetrate the matter much more deeply than X-rays or electrons. If there are unpaired electrons in the material, neutrons may also interact with them by a second mechanism: a dipole-dipole interaction between the magnetic moment of the neutron and the magnetic moment of the unpaired electron [82].

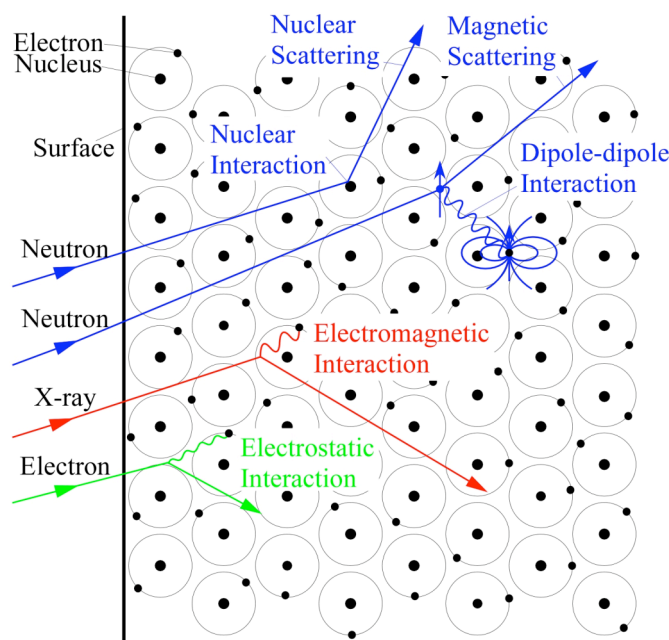


Figure 1.3.1.1: Beams of neutrons, X-rays and electrons interacting with a material by different mechanisms [82].

Neutrons have particular advantages over X-rays [12]:

- 1) The energy of a neutron with a short wavelength is six orders less than that of X-rays. The energy of a 0.15 nm X-ray photon is about 8.2 keV. Deposition of such an amount of energy in a sample can yield serious molecular degradation in biological materials and polymers, for instance;
- 2) In the case of X-rays, the scattering cross-section increases with Z , while the magnitude of the neutron-nucleus interaction varies non-monotonously with Z . As the nuclei of all atoms are compact and of comparable size, neutrons are capable of interacting strongly with all atoms, including very light ones. Neutrons cannot only 'see' hydrogen, but they can differentiate between hydrogen isotopes, as well as between other chemical elements;
- 3) Atomic nuclei being some 104 to 106 times smaller than typical neutron wavelengths, the nuclei act as point scatterers and neutron scattering is spherically symmetric. Atomic diameters being 0.1 to 10 times typical X-ray wavelengths, the use of X-rays results in a decrease of the scattering intensity with increasing scattering angle;
- 4) The interaction of neutrons with matter is weak, and the absorption of neutrons by most materials is correspondingly small. Therefore, neutrons are very penetrating;
- 5) Neutrons have a small magnetic moment that can interact with the spin and orbital magnetic moments present in a sample containing atoms with unpaired electrons, giving rise to an additional scattering mechanism;
- 6) The neutron refractive indices of materials being slightly less than unity, this allows neutrons to be totally externally reflected from surfaces (provided the angle of incidence is less than some critical angle), a property that has spawned an entire field of research: neutron reflectometry (NR). This technique has been proven to be a powerful means of investigating surfaces and interfaces.

1.3.2 Small angle neutron scattering

In this technique a neutron radiation is scattered by a sample (an aqueous solution, a solid, a powder or a crystal) and the resulting scattering pattern is analyzed to provide information about the nature, size, shape, orientation and number density of certain components of the sample (e.g. cavities, precipitates). This technique allows the resolution of objects between 0.5 and 200 nm in diameter, and the scattering signal increases with the sample thickness. Typical samples for SANS measurements have a surface of about 1 cm² and a thickness of about 1 mm.

Neutron scattering is classified into elastic and inelastic scattering. In the case of inelastic scattering, the wavelength of the scattered neutrons is different from that of the incident neutrons. In the case of elastic scattering, the neutrons transfer a small part of their kinetic energy T to the atoms as the following [83]:

$$T = \frac{4M_n M}{(M_n + M)^2} E \sin^2 \frac{\theta}{2} \quad (1.3.2.1),$$

where M_n and M are the neutron mass and the atom mass, respectively, θ is the scattering angle, as shown in Fig.1.3.2.1, and E is the incident neutron energy. When $\sin(\theta/2)$ is equal to 0.1, the neutron energy loss is less than 1%. The wavelength of the scattered neutrons is approximately unchanged.

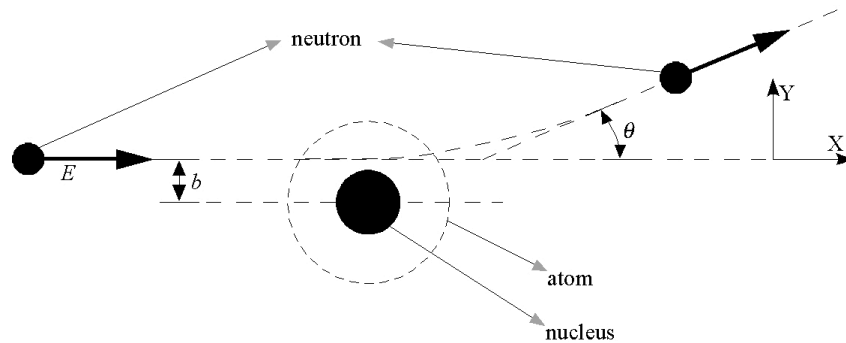


Figure 1.3.2.1: Schematics of neutron elastic scattering [83].

There exist four different neutron scattering modes, i.e., elastic coherent scattering, elastic incoherent scattering, inelastic coherent scattering and inelastic incoherent scattering. The elastic coherent scattering at small angles is the most useful mode for the microstructural investigation of materials. Since the other three kinds of scattering reduce the coherence of the scattered neutron beam, it is very important to design a SANS experiment to reduce the contributions of the elastic incoherent scattering and the inelastic scattering and to subtract these interferences at the time of data analysis.

Thus, SANS is ascribed to small angle elastic coherent neutron scattering, which is an isotropic scattering mode, and the behavior of the SANS intensity versus the employed diffraction vectors can be analyzed using the relevant coherent scattering law, such as the Guinier law, the Porod law, etc.

1.3.3 Cross section of neutron scattering by one atom

Neutrons are scattered by the nuclei because of the nuclear force. As the range of the nuclear force is very short (10^{-13} - 10^{-12} cm) and the size of the nuclei is much smaller than that of an atom ($\sim 10^{-8}$ cm), most of the materials appear very 'dilute' for the 'eye' of a neutron, as schematically illustrated in Figure 1.3.3.1 [84].

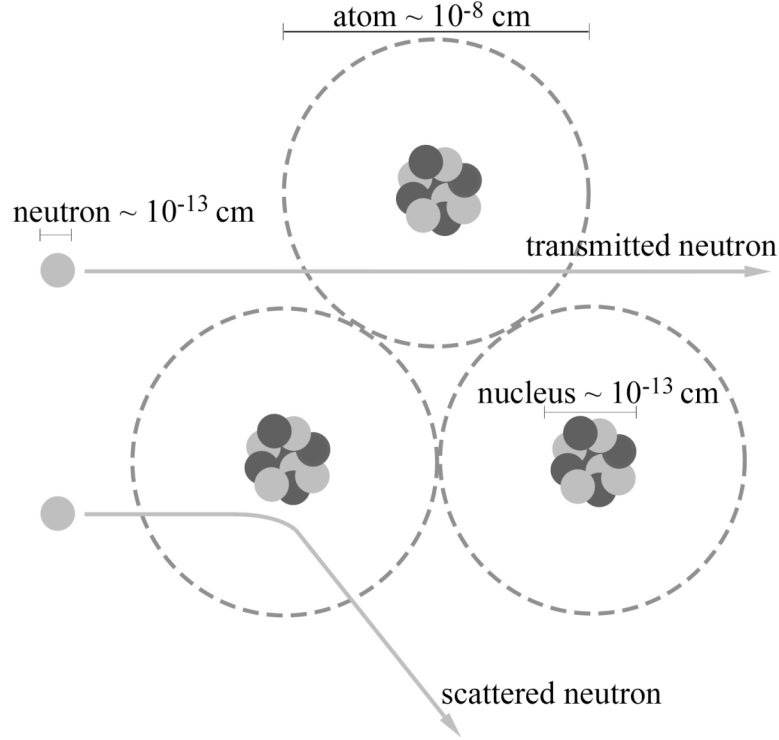


Figure 1.3.3.1: Schematics of neutron scattering [84].

When a monochromatic, collimated and uniform neutron beam with an intensity I_0 and an energy E_0 bombards a homogeneous sample, as illustrated in Figure 1.3.3.2, the beam intensity is attenuated at dx as [85, 86]:

$$dI = I \cdot (N/V) \cdot \sigma \cdot dx \quad (1.3.3.1),$$

where dI is the attenuated intensity after having passed through dx , I is the incident intensity at x , N is the number of atoms in the sample volume V , and σ is the interaction cross section.

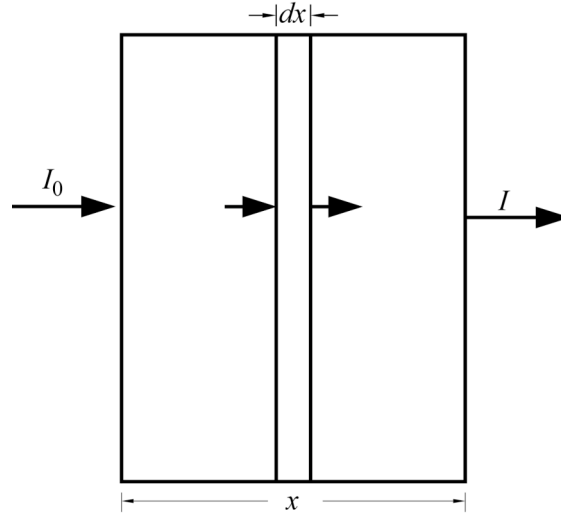


Figure 1.3.3.2: Schematics of attenuation of a neutron flux [85, 86].

The macro-cross section is defined as $\Sigma = (N/V)\sigma$ [85, 86]. The total cross section, σ_T , includes the coherent scattering cross section, σ_{coh} , the incoherent scattering cross section, σ_{inc} , and the absorption cross section, σ_{abs} . Correspondingly, they have a macro-cross section equal to $\Sigma_{total} = (N/V)\sigma_T$, $\Sigma_{coh} = (N/V)\sigma_{coh}$, $\Sigma_{inc} = (N/V)\sigma_{inc}$ and $\Sigma_{abs} = (N/V)\sigma_{abs}$ [85, 86]:

$$\Sigma_{total} = \Sigma_{coh} + \Sigma_{inc} + \Sigma_{abs} \quad (1.3.3.2).$$

By integrating over the sample thickness d , the transmission T is equal to:

$$T = \frac{I_{(\theta=0)}}{I_0} = \exp(-\Sigma_{total} \cdot d) \quad (1.3.3.3).$$

The scattered intensity I_s is equal to:

$$I_s = I_0 \exp(-\Sigma_{coh} + \Sigma_{inc}) \cdot d \quad (1.3.3.4).$$

If the scattering is isotropic, the scattering cross section ($\sigma_s = \sigma_{coh} + \sigma_{inc}$) is given by:

$$\sigma_s = 4\pi b^2 \quad (1.3.3.5),$$

where b is the scattering length.

The scattered intensity for an assembly of N atoms can be calculated by accounting for the phase of scattered waves in the context of the Born approximation [87]:

$$\left(\frac{d\sigma}{d\Omega} \right) = \frac{1}{V} \left\langle \sum_{i,j} b_i b_j \exp[-i\vec{q} \cdot (\vec{r}_i - \vec{r}_j)] \right\rangle \quad (1.3.3.6),$$

where Ω is the solid angle of the detector element, and b_i and \vec{r}_i are the scattering length and position vector of the atom i , respectively. $\langle \dots \rangle$ denotes the average. $(d\sigma/d\Omega)$ is called the

differential cross section, and q is the magnitude of the momentum transfer (or scattering vector) given by:

$$q = |\vec{q}| = \frac{4\pi}{\lambda} \sin\left(\frac{\theta}{2}\right) \quad (1.3.3.7),$$

where θ is the scattering angle. q is the most important variable describing the structure of the matter. The differential cross section may be divided into two terms [85, 86]:

$$\begin{aligned} \left(\frac{d\sigma}{d\Omega}\right) &= \frac{1}{V} \sum_i \langle b_i^2 \rangle + \frac{1}{V} \sum_{i \neq j} \langle b_i b_j \exp[-i\vec{q} \cdot (\vec{r}_i - \vec{r}_j)] \rangle \\ &= \frac{N}{V} \langle b^2 \rangle + \frac{\langle b \rangle^2}{V} \sum_{i \neq j} \langle \exp[-i\vec{q} \cdot (\vec{r}_i - \vec{r}_j)] \rangle \end{aligned} \quad (1.3.3.8),$$

where the relation $\langle b_i b_j \rangle = \langle b_i \rangle \langle b_j \rangle \equiv \langle b \rangle^2$ was assumed for $j \neq i$.

This means that there is no correlation between b_i and b_j . By defining the dispersion of the scattering length as [85, 88]:

$$\langle (\Delta b)^2 \rangle \equiv \langle (b - \langle b \rangle)^2 \rangle = \langle b^2 \rangle - \langle b \rangle^2 \quad (1.3.3.9),$$

one may rewrite the equation (1.3.3.8) as [85]:

$$\begin{aligned} \left(\frac{d\sigma}{d\Omega}\right) &= \frac{N}{V} \langle b \rangle^2 + \frac{\langle b \rangle^2}{V} \sum_{i \neq j} \langle \exp[-i\vec{q} \cdot (\vec{r}_i - \vec{r}_j)] \rangle + \frac{N}{V} \langle b^2 \rangle - \frac{N}{V} \langle b \rangle^2 \\ &= \frac{\langle b \rangle^2}{V} \sum_{i,j} \langle \exp[-i\vec{q} \cdot (\vec{r}_i - \vec{r}_j)] \rangle + \frac{N}{V} \langle (\Delta b)^2 \rangle \end{aligned} \quad (1.3.3.10).$$

The first term of the equation (1.3.3.10), which is relative to the structure of the matter, is called coherent scattering. The second term is the incoherent scattering, which is constant and independent of the structure of the matter. Thus [85]:

$$\left(\frac{d\sigma}{d\Omega}\right) = \left(\frac{d\sigma}{d\Omega}\right)_{coh} + \left(\frac{d\sigma}{d\Omega}\right)_{inc} \quad (1.3.3.11),$$

where

$$\left(\frac{d\sigma}{d\Omega}\right)_{coh} = \frac{\langle b \rangle^2}{V} \sum_{i,j} \langle \exp[-i\vec{q} \cdot (\vec{r}_i - \vec{r}_j)] \rangle \quad (1.3.3.12),$$

and

$$\left(\frac{d\sigma}{d\Omega}\right)_{inc} = \frac{N}{V} \langle (\Delta b)^2 \rangle \quad (1.3.3.13).$$

Thus, the coherent and incoherent scattering cross sections, σ_{coh} and σ_{inc} , for an atom are respectively given by [88, 89]:

$$\sigma_{coh} = \int \left(\frac{d\sigma}{d\Omega} \right)_{coh} d\Omega = 4\pi \langle b \rangle^2 \quad (1.3.3.14),$$

and

$$\sigma_{inc} = \int \left(\frac{d\sigma}{d\Omega} \right)_{inc} d\Omega = 4\pi \langle \Delta b \rangle^2 \quad (1.3.3.15).$$

The incoherent scattering is ascribed to the different isotopes or species of the nuclei. It does not depend on \mathbf{q} and is considered as an internal background originating from the sample. The magnitude of the incoherent scattering must be measured and subtracted before the coherent differential scattering cross-section (microstructure-relevant term) is further analyzed. No incoherent scattering is expected from isotropically pure samples. However, hydrogen (^1H) has an extraordinarily large incoherent scattering cross section. This is due to the nuclear spin incoherence. A neutron has two quantum spin states, $+1/2$ and $-1/2$, each of which having a scattering length of b^+ and b^- , respectively. The neutron interacts with the nuclear spin of the atom. If the nucleus has a spin number of I , one obtains [89, 90]:

$$\langle b \rangle = \left(\frac{I+1}{2I+1} \right) b^+ + \left(\frac{I}{2I+1} \right) b^- \quad (1.3.3.16),$$

and

$$\langle b^2 \rangle = \left(\frac{I+1}{2I+1} \right) (b^+)^2 + \left(\frac{I}{2I+1} \right) (b^-)^2 \quad (1.3.3.17).$$

Substituting $b^+ = 1 \times 10^{-12}$ cm, $b^- = -4.7 \times 10^{-12}$ cm, and $I = 1/2$, one obtains $\sigma_{inc} = 4\pi \langle \Delta b \rangle^2 = 78 \times 10^{-24}$ cm² for hydrogen, which is larger than $\sigma_{coh} = 2 \times 10^{-24}$ cm².

1.3.4 Theory of small angle neutron scattering

The coherent cross section is obtained by accounting for the scattering length of nuclei and the phase difference. The intensity scattered by a one-component system may be then written as [85, 91]:

$$\begin{aligned} I(\vec{q}) &\equiv \left(\frac{d\sigma}{d\Omega} \right)_{coh} = \frac{b^2}{V} \sum_{i,j}^N \langle \exp[-i\vec{q} \cdot \vec{r}_{ij}] \rangle \\ &= \frac{b^2}{V} \sum_i^N \sum_j^N \langle \exp[-i\vec{q} \cdot \vec{r}_{ij}] \rangle \end{aligned} \quad (1.3.4.1),$$

where $I(\mathbf{q})$ is the absolute scattered intensity with the unit of the inverse of length. $I(\mathbf{q})$ is also called the differential cross section. The vector quantity \mathbf{r}_{ij} is given by $\mathbf{r}_{ij} = \mathbf{r}_i - \mathbf{r}_j$. Here, we treat the diffracting objects as point scatters. As only the coherent scattering is considered, $\langle b \rangle^2$ may be written as b^2 and the relation $\langle b_i b_j \rangle = \langle b_i \rangle \langle b_j \rangle \equiv \langle b \rangle^2$ is assumed for $j \neq i$. Therefore, a structure factor $S(\mathbf{q})$ may be defined as [85, 91]:

$$S(\vec{q}) = \frac{1}{N} \sum_i^N \sum_j^N \langle \exp[-i\vec{q} \cdot \vec{r}_{ij}] \rangle \quad (1.3.4.2).$$

The quantity $S(\mathbf{q})$ does not depend on the scattering method, e.g. X-rays, neutrons, or light, but on the structure of the system itself. The SANS intensity $I(\mathbf{q})$ is then given by [85, 91]:

$$I(\bar{\mathbf{q}}) = \frac{b^2}{v_0} S(\bar{\mathbf{q}}) \quad (1.3.4.3),$$

where v_0 is the volume of a scattering object, defined by:

$$V = v_0 N \quad (1.3.4.4).$$

In most cases, the scattering objects are regarded as very dilute objects in a system consisting of N scattering objects in a volume V , each scattering element having a scattering length b . Therefore, the scattered intensity is given by [85, 91]:

$$I(\bar{\mathbf{q}}) = \frac{b^2}{v_0} \iint \langle \Delta n(\bar{\mathbf{r}}) \Delta n(\bar{\mathbf{r}}' - \bar{\mathbf{r}}) \rangle \exp[-i\bar{\mathbf{q}} \cdot (\bar{\mathbf{r}}' - \bar{\mathbf{r}})] d\bar{\mathbf{r}} d\bar{\mathbf{r}}' \quad (1.3.4.5),$$

where $\Delta n(\mathbf{r})$ is the fluctuation in the number density of scattering objects from the mean value at a position \mathbf{r} . Thus,

$$\Delta n(\bar{\mathbf{r}}) = n(\bar{\mathbf{r}}) - \frac{N}{V} \quad (1.3.4.6),$$

and

$$\int \Delta n(\bar{\mathbf{r}}) d\bar{\mathbf{r}} = 0 \quad (1.3.4.7).$$

$\langle \Delta n(\mathbf{r}) \Delta n(\mathbf{r}' - \mathbf{r}) \rangle$ refers to the density correlation of the objects, where $\langle \dots \rangle$ denotes the average over the space. A correlation function, $G(\mathbf{r})$, can be then introduced [85, 91]:

$$G(\bar{\mathbf{r}}) \equiv \langle \Delta n(\bar{\mathbf{r}}) \Delta n(\bar{\mathbf{r}}' - \bar{\mathbf{r}}) \rangle = \frac{1}{V} \int \Delta n(\bar{\mathbf{r}}) \Delta(\bar{\mathbf{r}}' - \bar{\mathbf{r}}) d\bar{\mathbf{r}}' \quad (1.3.4.8).$$

In comparing equations (1.3.4.7) and (1.3.4.8), it can be seen that the equation (1.3.4.7) is a Fourier transform of $G(\mathbf{r})$. A Fourier transform of $\Delta n(\mathbf{r})$ gives the scattering amplitude, $f(\mathbf{q})$:

$$f(\bar{\mathbf{q}}) = \int \Delta n(\bar{\mathbf{r}}) \exp[-i\bar{\mathbf{q}} \cdot \bar{\mathbf{r}}] d\bar{\mathbf{r}} \quad (1.3.4.9).$$

By multiplying $f(\mathbf{q})$ with its Fourier conjugate, $f^*(\mathbf{q})$, the scattering intensity can be obtained:

$$\begin{aligned} I(\bar{\mathbf{q}}) &\equiv \frac{b^2}{v_0} S(\bar{\mathbf{q}}) = \frac{b^2}{v_0} f(\bar{\mathbf{q}}) f^*(\bar{\mathbf{q}}) \\ &= \frac{b^2}{v_0} |f(\bar{\mathbf{q}})|^2 = \frac{b^2}{v_0} \left| \int \Delta n(\bar{\mathbf{r}}) \exp[-i\bar{\mathbf{q}} \cdot \bar{\mathbf{r}}] d\bar{\mathbf{r}} \right|^2 \end{aligned} \quad (1.3.4.10).$$

By using equations (1.3.4.4), (1.3.4.6) and (1.3.4.8), $S(\mathbf{q})$ can be written as [85, 91]:

$$S(\bar{\mathbf{q}}) = \int G(\bar{\mathbf{r}}) \exp[-i\bar{\mathbf{q}} \cdot \bar{\mathbf{r}}] d\bar{\mathbf{r}} \quad (1.3.4.11).$$

Figure 1.3.4.1 shows the relationship between the density fluctuation function, $\Delta n(\mathbf{r})$, the correlation function, $G(\mathbf{r})$, the scattering amplitude, $f(\mathbf{q})$, and the structure factor, $S(\mathbf{q})$ [85]. When a monochromatic neutron beam of wavelength λ bombards a sample, the incident

neutrons are transmitted, scattered or absorbed by the sample. Scattered neutrons at positions P and Q interfere with each other because of the phase difference related to $\mathbf{q} \cdot \mathbf{r}$, where \mathbf{q} is the scattering vector as already defined in the equation (1.3.4.7). The space described by \mathbf{q} is called the Fourier space or reciprocal space (\mathbf{q} -space). The term ‘reciprocal’ originates from the fact that \mathbf{q} has the unit of a reciprocal length, i.e., $1/\lambda$. On the other hand, the space defined by \mathbf{r} vectors is called the real space. The structure in the real space, as observed through $G(\mathbf{r})$, is related to the structure factor $S(\mathbf{q})$ in the \mathbf{q} -space by the Fourier transform given by the equation (1.3.4.11). Therefore, the information on large objects appears in the region of low \mathbf{q} values and that on small objects appears in the region of large \mathbf{q} values.

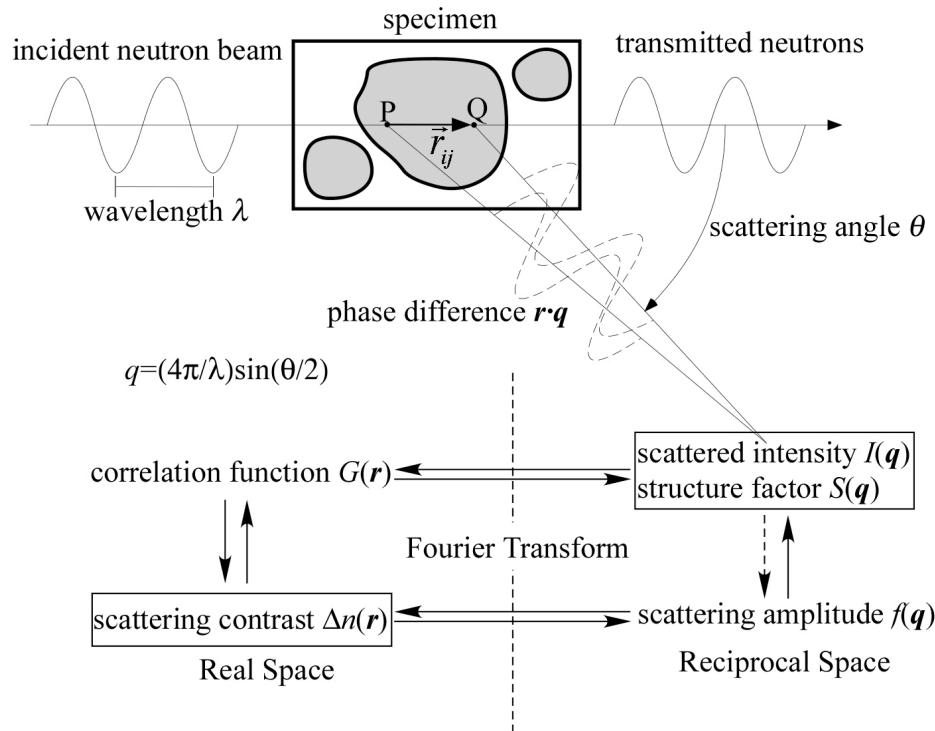


Figure 1.3.4.1: Schematic representation of the scattering principle and the relationship between the density fluctuation function, $\Delta n(\mathbf{r})$, the correlation function, $G(\mathbf{r})$, the scattering amplitude, $f(\mathbf{q})$, and the structure factor, $S(\mathbf{q})$ [85].

The goal of an elastic coherent scattering experiment is to get knowledge about the static structures existing in a sample, $\Delta n(\mathbf{r})$, by analyzing the scattered intensity, $I(\mathbf{q})$, from the sample. $G(\mathbf{r})$ can be obtained by calculating the inverse Fourier transform of $I(\mathbf{q})$ or $S(\mathbf{q})$ [85, 91]:

$$G(\vec{r}) = \frac{1}{(2\pi)^3} \int S(\vec{q}) \exp[i\vec{q} \cdot \vec{r}] d\vec{q} \quad (1.3.4.12).$$

It is not possible, however, to evaluate $f(\mathbf{q})$ from $I(\mathbf{q})$ because information on the phase in $f(\mathbf{q})$ is missing. Therefore, in many cases, a model describing $\Delta n(\mathbf{r})$ is first constructed. Then, comparison of the experiment with theory (model) is made in terms of $G(\mathbf{r})$ or $I(\mathbf{q})$.

1.3.5 Scattered intensity for a mixing of $(p+1) (\geq 3)$ species

Equation (1.3.4.1) can be easily extended to the case of a two-components mixture with N_α objects of scattering length b_α ($\alpha = 1$ or 2). The scattered intensity in the unit solid angle is then given by [85]:

$$I(\vec{q}) = \frac{b_1^2}{V} \sum_i^{N_1} \sum_j^{N_2} \langle \exp[-i\vec{q} \cdot \vec{r}_{ij}] \rangle + \frac{2b_1b_2}{V} \sum_i^{N_1} \sum_j^{N_2} \langle \exp[-i\vec{q} \cdot \vec{r}_{ij}] \rangle + \frac{b_2^2}{V} \sum_i^{N_1} \sum_j^{N_2} \langle \exp[-i\vec{q} \cdot \vec{r}_{ij}] \rangle \quad (1.3.5.1),$$

or

$$I(\vec{q}) = \frac{b_1^2}{v_0} S_{11}(\vec{q}) + \frac{2b_1b_2}{v_0} S_{12}(\vec{q}) + \frac{b_2^2}{v_0} S_{22}(\vec{q}) \\ = \frac{1}{v_0} \begin{pmatrix} b_1 & b_2 \end{pmatrix} \begin{pmatrix} S_{11} & S_{12} \\ S_{21} & S_{22} \end{pmatrix} \begin{pmatrix} b_1 \\ b_2 \end{pmatrix} \quad (1.3.5.2),$$

where $S_{12} = S_{21}$. $S_{\alpha\beta}$ is the partial structure factor defined by:

$$S_{\alpha\beta}(\vec{q}) = \frac{1}{N_\alpha + N_\beta} \sum_i^{N_\alpha} \sum_j^{N_\beta} \langle \exp[-i\vec{q} \cdot \vec{r}_{ij}] \rangle \\ = \int \int_V \exp[-i\vec{q} \cdot (\vec{r}' - \vec{r})] \langle \Delta n_\alpha(\vec{r}) \Delta n_\beta(\vec{r}') \rangle d\vec{r} d\vec{r}' \quad (1.3.5.3).$$

In order to examine the inter-relationships between $S_{\alpha\beta}(\vec{q})$ values, the following identity has to be considered [85]:

$$\int \int_V \exp[-i\vec{q} \cdot (\vec{r}' - \vec{r})] \langle [\Delta n_1(\vec{r}) + \Delta n_2(\vec{r})] \Delta n_1(\vec{r}') \rangle d\vec{r} d\vec{r}' \\ = S_{11}(\vec{q}) + S_{12}(\vec{q}) \quad (1.3.5.4).$$

In the case of an incompressible system, which states that the density of the whole system is constant, the left-hand side of the above equation becomes zero because:

$$\Delta n_1(\vec{r}) + \Delta n_2(\vec{r}) = 0 \quad (1.3.5.5).$$

Thus,

$$S_{11}(\vec{q}) = -S_{12}(\vec{q}) \quad (1.3.5.6).$$

A similar argument leads to:

$$S_{11}(\vec{q}) = S_{22}(\vec{q}) = -S_{12}(\vec{q}) = -S_{21}(\vec{q}) \equiv S(\vec{q}) \quad (1.3.5.7).$$

Therefore, the scattered intensity function, $I(\vec{q})$, for an incompressible binary system having two different scattering lengths, b_1 and b_2 , is given by [85]:

$$I(\bar{q}) = \frac{1}{v_0} \begin{pmatrix} b_1 & b_2 \end{pmatrix} \begin{pmatrix} S_{11} & S_{12} \\ S_{21} & S_{22} \end{pmatrix} \begin{pmatrix} b_1 \\ b_2 \end{pmatrix} = \frac{1}{v_0} (b_1 - b_2)^2 S(\bar{q}) \quad (1.3.5.8).$$

The scattered intensity function for a mixture of $(p+1) (\geq 3)$ species can be obtained by generalizing the argument of equation (1.3.5.1):

$$I(\bar{q}) = \frac{1}{v_0} \begin{pmatrix} \dots & b_\alpha & \dots \end{pmatrix} \begin{pmatrix} S_{\alpha\beta}(\bar{q}) \end{pmatrix} \begin{pmatrix} \dots \\ b_\beta \\ \dots \end{pmatrix} = \frac{1}{v_0} \sum_{\alpha=0}^p \sum_{\beta=0}^p (b_\alpha - b_\beta)^2 S_{\alpha\beta}(\bar{q}) \quad (1.3.5.9),$$

where $0 \leq \alpha \leq p$ and $0 \leq \beta \leq p$. Equation (1.3.5.9) can be rewritten with respect to a reference component. For example, in the case of an alloy containing more than two kinds of defect clusters, i.e., $(p+1) (\geq 3)$, the alloy matrix is denoted as $\alpha = 0$, and one may rearrange the equation (1.3.5.9) as:

$$I(\bar{q}) = \frac{1}{v_0} \sum_{\alpha=1}^p (b_\alpha - b_0)^2 S_{\alpha\alpha}(\bar{q}) + \frac{2}{v_0} \sum_{\alpha=1}^p \sum_{\beta(>\alpha)}^p (b_\alpha - b_0)(b_\beta - b_0) S_{\alpha\beta}(\bar{q}) \quad (1.3.5.10),$$

where $\alpha = 1$ to p represent the different types of defect clusters, such as precipitates, voids, bubbles, and dislocation loops.

1.3.6 Intra- and inter-species interferences

In the preceding sections the diffracting objects or species were treated as point scatters. Species, however, cannot be treated as point scatters. The typical size of a nano-species is of the order of a few nanometres or a few tens of nanometers, which is much larger than the wavelength of neutrons. It is essential, therefore, to decompose the structure factor into intra-species and inter-species interference functions [85, 91]. Let us start with a one-component macro-species system of N species in a volume V . Each species consists of z segments with a scattering length b . A segment can be the statistical unit of a macro-species. In that case, the structure factor is given by [85]:

$$S(\bar{q}) = \frac{1}{Nz} \sum_{\alpha}^N \sum_{\beta}^N \sum_{i=1}^z \sum_{j=1}^z \left\langle \exp \left[-i\bar{q} \cdot (\bar{r}_{\alpha,i} - \bar{r}_{\beta,j}) \right] \right\rangle \quad (1.3.6.1),$$

where $\bar{r}_{\alpha,i}$ refers to the position of the segment i of species α . Equation (1.3.6.1) can be decomposed into two functions [85]:

$$\begin{aligned} S(\bar{q}) &= \frac{1}{Nz} \sum_{\alpha}^N \sum_{i=1}^z \sum_{j=1}^z \left\langle \exp \left[-i\bar{q} \cdot (\bar{r}_{\alpha,i} - \bar{r}_{\alpha,j}) \right] \right\rangle + \\ &\quad \frac{1}{Nz} \sum_{\alpha}^N \sum_{\beta \neq \alpha}^N \sum_{i=1}^z \sum_{j=1}^z \left\langle \exp \left[-i\bar{q} \cdot (\bar{r}_{\alpha,i} - \bar{r}_{\beta,j}) \right] \right\rangle = zP(\bar{q}) + NzQ(\bar{q}) \end{aligned} \quad (1.3.6.2),$$

where $P(\bar{q})$ and $Q(\bar{q})$ are the normalized intra-species and inter-species interference functions, respectively, given by:

$$\begin{aligned}
 P(\bar{q}) &= \frac{1}{Nz^2} \sum_{\alpha}^N \sum_i^z \sum_j^z \left\langle \exp \left[-i\bar{q} \cdot (\bar{r}_{\alpha,i} - \bar{r}_{\alpha,j}) \right] \right\rangle \\
 &= \frac{1}{z^2} \sum_i^z \sum_j^z \left\langle \exp \left[-i\bar{q} \cdot \bar{r}_{ij} \right] \right\rangle
 \end{aligned} \tag{1.3.6.3}$$

and

$$Q(\bar{q}) = \frac{1}{z^2} \sum_i^z \sum_j^z \left\langle \exp \left[-i\bar{q} \cdot (\bar{r}_{\alpha,i} - \bar{r}_{\beta,j}) \right] \right\rangle \tag{1.3.6.4}.$$

The average $\langle \dots \rangle$ has to be made over all orientations and configurations. Figure 1.3.6.1 shows the relationship between the \mathbf{q} and \mathbf{r} vectors, where α is the polar angle between the two vectors.

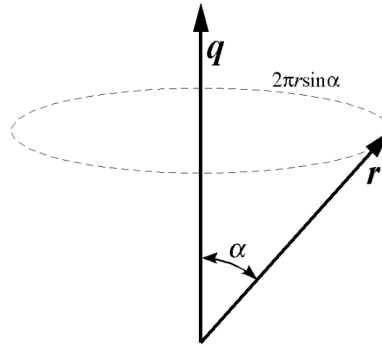


Figure 1.3.6.1: Relationship between the \mathbf{q} and \mathbf{r} vectors, α being the polar angle between the two vectors.

For an isotropic system, the average over all orientations can be achieved by doing [85]:

$$\begin{aligned}
 \left\langle \exp \left[-i\bar{q} \cdot \bar{r} \right] \right\rangle_{orient} &= \int_{\alpha=0}^{\pi} \exp \left[-i\bar{q} \cdot \bar{r} \right] d\bar{r} \bigg/ \int_{\alpha=0}^{\pi} d\bar{r} \\
 &= \int_{\alpha=0}^{\pi} \exp \left[-iqr \cos \alpha \right] 2\pi r \sin \alpha dr d\alpha \bigg/ \int_{\alpha=0}^{\pi} 2\pi r dr = \sin qr / qr
 \end{aligned} \tag{1.3.6.5}$$

Thus,

$$P(\bar{q}) = \frac{1}{z^2} \sum_{i=1}^z \sum_{j=1}^z \left\langle \sin(qr_{ij}) / qr_{ij} \right\rangle \tag{1.3.6.6}.$$

Here, the average is made only on the distances r_{ij} . Recalling the Taylor expression for $\sin x/x$:

$$\frac{\sin x}{x} = \sum_{k=1}^{\infty} \frac{(-1)^{k-1} x^{2(k-1)}}{(2k-1)!} = 1 - \frac{x^2}{3!} + \frac{x^4}{5!} - \frac{x^6}{7!} + \dots \tag{1.3.6.7},$$

one obtains [85]:

$$P(\bar{q}) = 1 - \frac{q^2}{6z^2} \sum_{i=1}^z \sum_{j=1}^z \langle r_{ij}^2 \rangle + \frac{q^4}{5!z^2} \sum_{i=1}^z \sum_{j=1}^z \langle r_{ij}^4 \rangle - \dots \quad (1.3.6.8).$$

The average over r_{ij}^2 is related to the radius of gyration, R_g , one of the most important parameters describing the size of a diffracting object. The square of the radius of gyration is given by [85]:

$$\langle R_g^2 \rangle = \frac{1}{z} \sum_{i=1}^z \left\langle (r_i - r_G)^2 \right\rangle \equiv R_g^2 \quad (1.3.6.9),$$

where r_G refers to the position of the center of the gravity of the object. We simply write the ‘average over R_g^2 ’ as R_g^2 hereafter unless the kind of average has to be specified. R_g^2 can be also written as [85]:

$$R_g^2 = \frac{1}{2z^2} \sum_{i=1}^z \sum_{j=1}^z \langle r_{ij}^2 \rangle \quad (1.3.6.10),$$

where the following identity was used:

$$r_{ij}^2 = (r_i - r_j)^2 = r_i^2 + r_j^2 - 2r_i r_j \quad (1.3.6.11),$$

By substituting equation (1.3.6.10) to equation (1.3.6.8), one obtains [85]:

$$P(\bar{q}) = 1 - \frac{q^2}{3} R_g^2 + \dots \quad (1.3.6.12),$$

or for $qR_g \ll 1$:

$$P(q) \equiv \exp \left[-\frac{R_g^2 q^2}{3} \right] \quad (1.3.6.13).$$

Equation (1.3.6.13) is called the Law of Guinier [92].

The square of the radius of gyration, R_g^2 , for a given shape of diffracting objects can be easily obtained by using the following equation [85]:

$$R_g^2 = \int_V (r - r_G)^2 dr / \int_V dr \quad (1.3.6.14).$$

For example, for a rod of length L :

$$R_g^2 = 2 \int_0^{\frac{L}{2}} r^2 dr / 2 \int_0^{\frac{L}{2}} dr = \frac{L^2}{12} \quad (1.3.6.15).$$

For a sphere of radius R :

$$R_g^2 = \int_0^R 4\pi r^2 r^2 dr \bigg/ \int_0^R 4\pi r^2 dr = \frac{3R^2}{5} \quad (1.3.6.16).$$

For a disk of radius R :

$$R_g^2 = \frac{R^2}{2} \quad (1.3.6.17).$$

For a disk of radius R and length L :

$$R_g^2 = \frac{R^2}{2} + \frac{L^2}{12} \quad (1.3.6.18).$$

For an ellipsoid of half-axes a , b and c :

$$R_g^2 = \frac{a^2 + b^2 + c^2}{5} \quad (1.3.6.19).$$

When the shape of the scattering objects is known and the objects are dispersed in a medium with a low concentration, R_g^2 can be evaluated by using the Law of Guinier [93].

For a dilute and dispersed system, the inter-objects interference term, $Q(\mathbf{q})$, can be neglected and the scattered intensity is simply given by [85]:

$$I(\bar{q}) \equiv \frac{b^2}{v_0} \phi z P(\bar{q}) \equiv \frac{b^2}{v_0} \phi z \exp \left[-\frac{R_g^2 q^2}{3} \right] \quad (1.3.6.20),$$

where ϕ is the volume fraction of the scattering objects. Therefore, by plotting the logarithm of $I(\mathbf{q})$ as a function of q^2 , R_g^2 is easily evaluated from the slope of the curve in the region of low q values. This plot is called a Guinier plot. The intercept with $\log I$ is proportional to the product of the number of segments for all species, z , with the volume fraction, ϕ , of the scattering objects.

The intra-species interference function, $P(\mathbf{q})$, can be calculated for some limited cases. For objects with a well-defined shape $P(\mathbf{q})$ can be calculated analytically to some extent. Since $P(\mathbf{q})$ represents the shape of the objects, it is also referred to as a ‘form factor’. We list here the exact expression of the form factor of various objects, which may take all orientations with the same probability [92]:

For a sphere of radius R , where $J_{3/2}(x)$ is the Bessel function of order $3/2$:

$$P(\bar{q}) \equiv \Phi^2(\bar{q}) = 3 \left[\frac{\sin qR - qR \cos qR}{q^3 R^3} \right]^2 = \frac{9\pi}{2} \left[\frac{J_{3/2}(qR)}{(qR)^{3/2}} \right]^2 \quad (1.3.6.21).$$

For an ellipsoid with axes of $2a$, $2a$, and $2\mu a$ [94], where ψ is the angle between the main axis of the ellipsoid and the scattering vector:

$$P(\bar{q}) = \int_{\psi=0}^{\frac{\pi}{2}} \Phi^2 \left(qa \sqrt{\cos^2 \psi + \mu^2 \sin^2 \psi} \right) \cos \psi d\psi \quad (1.3.6.22).$$

For a cylinder of diameter $2R$ and height $2H$ [95], where $J_1(x)$ is the Bessel function of order 1, and ψ is the angle between the main axis of the cylinder and the scattering vector:

$$P(\bar{q}) = \int_{\psi=0}^{\frac{\pi}{2}} \frac{\sin^2(qH \cos \psi)}{(qH \cos \psi)^2} \frac{4 \left[J_1(qR \sin \psi) \right]^2}{(qR \sin \psi)^2} \sin \psi d\psi \quad (1.3.6.23).$$

For a rod of infinitesimal transverse dimensions and length $2H$ [96], where $Si(x)$ is the sine integral:

$$P(\bar{q}) = \frac{Si(qH)}{qH} - \frac{\sin^2(qH)}{(qH)^2} \quad \text{with} \quad Si(x) = \int_0^x \frac{\sin t}{t} dt \quad (1.3.6.24).$$

For a disk of infinitesimal thickness and diameter $2R$ [97]:

$$P(\bar{q}) = \frac{2}{q^2 R^2} \left[1 - \frac{1}{qR} J_1(2qR) \right] \quad (1.3.6.25).$$

1.3.7 Asymptotic behavior of scattering

In small angle neutron scattering, the asymptotic behavior of the scattered intensity function provides useful information about the geometry of the scattering objects. As for a dilute and dispersed system the inter-object interference can be neglected, i.e., $Q(\mathbf{q}) \approx 0$, the structure factor of the system, $S(\mathbf{q})$, is given by [85]:

$$S(\bar{q}) = Nz^2 P(\bar{q}) \sim NM^2 P(\bar{q}) \sim V \phi M P(\bar{q}) \equiv V \phi M P(x) \quad (1.3.7.1),$$

where ϕ and M are the volume fraction ($\phi \sim NM/V$) and the mass ($M \sim z$) of the scattering objects, respectively, and $x (\equiv qR_g)$ is a dimensionless variable. $P(x)$ is quite general and represents an object structure factor. Since the characteristic size of the system, i.e., the gyration radius of species, is given by R_g , $P(x)$ can be written as [85]:

$$P(x) = P(qR_g) \rightarrow x^{-\gamma} \quad (1.3.7.2)$$

for large qR_g or x values, where γ is the scattering exponent. The gyration radius can be written as $R_g \sim M^\alpha$. In two-phases systems in which each phase is homogeneous, the scattering function becomes sensitive to the interface structure at large \mathbf{q} values ($q \gg 1/R_g$).

For an assembly of two-dimensional objects, the structure factor is proportional to the total area of two-dimensional objects, $A_T = NA$. Since the molar mass M is proportional to A for two-dimensional objects, the structure factor can be written as [85]:

$$S(\bar{q}) \approx NM^2 P\left(qA^{\frac{1}{2}}\right) \sim A_T A \left(qA^{\frac{1}{2}}\right)^{-\gamma} = A_T q^{-\gamma} A^{1-\frac{\gamma}{2}} \sim A^0 A_T q^{-\gamma} \quad (1.3.7.3).$$

Here, $S(q)$ is assumed to become independent of A at large q values. Hence, one obtains $\gamma = 2$ and $S(q) \sim A_T q^{-2}$ (surface scattering from an assembly of two-dimensional objects).

For three-dimensional objects, where the mass M is proportional to $A^{3/2}$ and the total area of the objects $A_T = NA$, the structure factor has the following form [85]:

$$S(\bar{q}) \sim A_T A^2 P\left(qA^{\frac{1}{2}}\right) = A_T A^2 \left(qA^{\frac{1}{2}}\right)^{-\gamma} = A_T q^{-\gamma} A^{2-\frac{\gamma}{2}} = A^0 A_T q^{-\gamma} \quad (1.3.7.4).$$

If $S(q)$ becomes independent of A at large q values, one obtains $\gamma = 4$ and $S(q) \sim A_T q^{-4}$ (surface scattering from an assembly of three-dimensional objects). This relation, i.e., the q^{-4} power dependence of the structure factor (or of the scattered intensity), is called the Porod law [98, 99]. The exact form of the Porod equation is given by:

$$I(\bar{q}) = \frac{L}{v_0} (b_1 - b_2)^2 \frac{2\pi A_T}{q^4} \quad (1.3.7.5),$$

where L is a proportional constant having the unit of length. A modification regarding the contrast factor had to be made here to suit SANS, because the original equation was derived for small-angle X-ray scattering. The asymptotic behavior for objects having a large aspect ratio and a preferential orientation is highly dependent on their orientation distribution, as discussed by Shibayama et al. [92].

Deviations from the Porod law when a finite interface thickness is accounted for were investigated by Ruland [100] and Vonk [101]. The interface curvature was investigated by Tomita [102, 103]. The principles derived have been applied to determine the interface thickness and the interface curvature (area-averaged scattering mean curvature) [104, 105].

1.3.8 Fractal objects

Small angle neutron scattering is a powerful technique to study materials with a random structure, such as fractal objects [106]. A pioneering work describing 'fractals' or 'fractal geometry' has been reported by Mandelbrot [107]. Hereafter, we present the scattering law for fractal objects. Fractal objects exhibit dilution symmetry (or self similarity). In other words, they look similar in spite of zooming-out or zooming-in the view. There are two types of fractals: mass fractals and surface fractals [107].

We introduce the fractal dimension for mass fractals, D_m , and for surface fractals, D_s . These dimensions are different from the space dimension, d .

The fractal dimension of a topologically $(d-1)$ -dimensional surface is given by [85]:

$$A \sim R^{D_s} \quad (1.3.8.1),$$

where A is the $(d-1)$ -dimensional Euclidean measure of the surface area. The lower limit of D_s is $(d-1)$. This is the case of a perfectly smooth minimal surface like the one of a soap bubble. The upper limit of D_s is d . This value can be achieved by a highly convoluted surface that fills the d -dimensional space. Therefore,

$$d-1 < D_s < d \quad (1.3.8.2).$$

Percolation, gels and porous media can be described by mass fractals, for which the following relation holds [85, 91]:

$$M \sim R^D \quad (1.3.8.3).$$

The scattering intensity (or structure factor) becomes extensive depending on the total surface area A_T for surface fractals and on the total mass M for mass fractals. Hence, for surface fractals:

$$I(\bar{q}) \sim R^{D_s} \quad (1.3.8.4),$$

and for mass fractals:

$$I(\bar{q}) \sim R^D \quad (1.3.8.5).$$

On the other hand, the asymptotic behavior of the scattered intensity has the following scaling form [85, 91]:

$$I(\bar{q}) \sim M^2 P(qR) \sim M^2 (qR)^{-\gamma} \quad (1.3.8.6).$$

Thus, by substituting equation (1.3.8.5) into equation (1.3.8.6) and by rearranging, one obtains:

$$I(\bar{q}) \sim M^2 (qR)^{-\gamma} \sim R^{2D} (qR)^{-\gamma} = q^{-\gamma} R^{2D-\gamma} \sim R^D \quad (1.3.8.7).$$

This gives $\gamma = D$. Hence, for mass fractals:

$$I(\bar{q}) \sim \frac{R^D}{q^D} \sim q^{-D} \quad (1.3.8.8).$$

Similarly, for surface fractals:

$$I(\bar{q}) \sim M^2 (qR)^{-\gamma} \sim R^{2d} (qR)^{-\gamma} = q^{-\gamma} R^{2d-\gamma} \sim R^{D_s} \quad (1.3.8.9).$$

As $\gamma = 2d - D_s$ for surface fractals, one may write:

$$I(\bar{q}) \sim \frac{R^{D_s}}{q^{2d-D_s}} \sim q^{-(2d-D_s)} \quad (1.3.8.10).$$

Note that equation (1.3.8.10) can be reduced to the Porod equation by introducing $d = 3$ (three dimensions) and $D_s = 2$ (smooth surface), i.e.,

$$I(\bar{q}) \sim q^{-(6-2)} = q^{-4} \quad (1.3.8.11).$$

In the above discussion, it was assumed that the masses are uniform in the system. However, in many cases, the masses of the objects are not uniform but are distributed in size. If the distribution is narrow (weak polydispersity), it does not change the asymptotic behavior, i.e., $I(q) \sim q^{-D}$. On the contrary, objects having a polydispersity of power law type (strong polydispersity) are often found in random structures, e.g. in percolation models and in sols near the gelation threshold. In that case, the number distribution of objects of mass M is given by [85, 91]:

$$N(M) = M^{-\tau} h\left(\frac{M}{M_z}\right) \quad (1.3.8.12),$$

where τ is the polydispersity exponent, $h(M/M_z)$ is a scaling function for the polydispersity, which decays rapidly for $M > M_z$ [108], and M_z is the z -averaged mass that is given by [85, 91]:

$$M_z \equiv \frac{\sum M^3 N(M)}{\sum M^2 N(M)} \quad (1.3.8.13).$$

Note that $\tau = 2.2$ for three-dimensional percolation model and $\tau = 2.5$ for Bethe lattice. The polydispersity averaged scattered intensity $I(q)$ is given by [85]:

$$I(\bar{q}) = \frac{\int N(M) I_M(\bar{q}) dM}{\int N(M) dM} \quad (1.3.8.14).$$

The asymptotic behavior of $I(q)$ for polydispersed mass and surface fractals is then given by [85, 91]:

$$I(\bar{q}) \sim \begin{cases} q^{-D(3-\tau)} & (\tau > 2) \\ q^{-D} & (\tau < 2) \end{cases} \quad (1.3.8.15),$$

for mass fractals, and by:

$$I(\bar{q}) \sim \begin{cases} q^{-d(3-\tau)} & (\tau > 2) \\ q^{-(2d-D_s)} & (\tau < 2) \end{cases} \quad (1.3.8.16),$$

for surface fractals.

The relation between the scattering exponent $\gamma = -[\log I(q)/\log q]$ and τ is shown in Figure 1.3.8.1 [85].

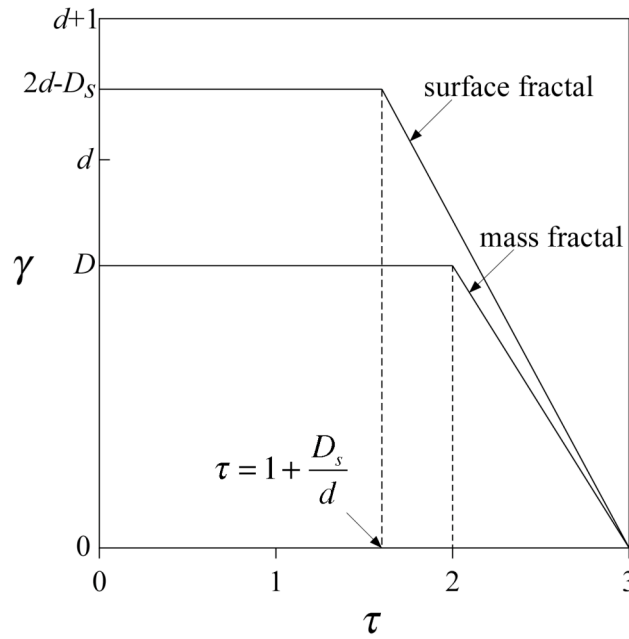


Figure 1.3.8.1: Relation between the scattering exponent $\gamma = -[\log I(q)/\log q]$ and τ [85, 106].

To summarize, SANS allows obtaining quantitative information from a specimen such as the nature, size distribution, number density, geometry and orientation of scattering objects, even if these objects are of fractal nature.

1.4 Practical use of the SANS technique

Scattering of a neutron beam by a sample is illustrated in Figure 1.4.1 [85]. \mathbf{k}_i and \mathbf{k}_f are the wave vectors of the transmitted beam and the diffracted beam, respectively. Their magnitudes are equal to $2\pi/\lambda_i$ and $2\pi/\lambda_f$, respectively, where λ_i and λ_f are the wavelengths of the transmitted beam and the diffracted beam, respectively. Small angle approximation yields $\lambda_i \approx \lambda_f \approx \lambda$. θ is the scattering angle and \mathbf{q} is the diffraction vector. Small angle approximation also yields $\sin\theta \approx \theta$. Therefore, the Bragg's law $2d \sin(\theta/2) = n\lambda$ may be written as $d \propto \lambda/\theta$, where d is the diffraction length scale in the real space of the scattering objects of interest. On the other hand, as $|\mathbf{q}| = \sin\theta |\mathbf{k}_f| \approx \sin\theta 2\pi/\lambda \approx \theta 2\pi/\lambda$ one obtains:

$$d \propto \frac{2\pi}{q} \quad (1.4.1)$$

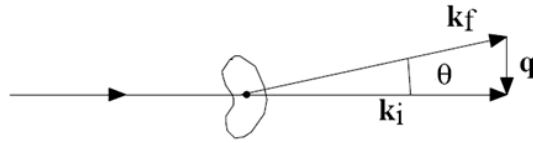


Figure 1.4.1: Scattering of a neutron beam by a sample [85].

In SANS the magnitude of scattering is described by a cross section σ . The differential cross section of scattering of a macroscopic sample is $(d\sigma/d\Omega)(q)$, where Ω is the scattering solid angle, which describes quantitatively the interaction between the neutrons and the sample and contains complete information on the microstructure of the sample. When the differential cross section can be normalized by a scattering volume the scattering intensity per unit volume may be written as [85]:

$$\frac{d\Sigma}{d\Omega}(\bar{q}) = \frac{N}{V} \frac{d\sigma}{d\Omega}(\bar{q}) \quad (1.4.2),$$

where N and V are the number and volume of the diffracting objects, respectively. A typical SANS experiment is illustrated in Figure 1.4.2, and the various interaction modes between the neutrons and the sample are represented in Figure 1.4.3.

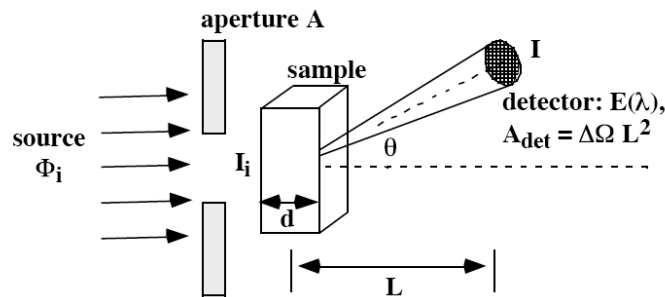


Figure 1.4.2: Schematics of a SANS experiment.

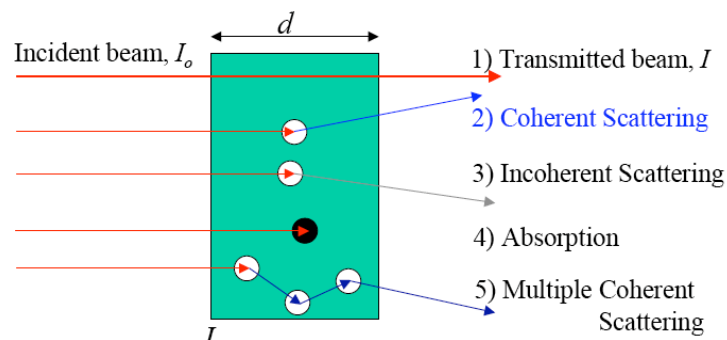


Figure 1.4.3: Schematics of the interaction modes between the neutrons and the sample.

Most of the incident neutrons are transmitted, some are absorbed and some are scattered ($\theta > 0$). In general, there are some energy transfer ($\Delta E \neq 0$), but in the case of elastic small angle scattering it is very small, i.e., $\Delta E \approx 0$ and $\theta \leq 10^\circ$. The scattered intensity, I , is a function of θ and ε (detector efficiency, < 1) [85]:

$$I = f(\bar{q}, \varepsilon) \quad (1.4.3),$$

where

$$q = |\bar{q}| = \frac{4\pi}{\lambda} \sin\left(\frac{\theta}{2}\right) \quad (1.4.4).$$

A SANS experiment allows measuring the scattered intensity, I , at a distance L and an angle θ , in comparison to the incident intensity, I_0 , to get the differential scattering cross section per unit solid angle [85]:

$$\frac{d\sigma}{d\Omega} = \frac{I}{I_0} \cdot L^2 \quad (1.4.5).$$

The incident intensity, I_0 , is equal to $\phi_0 \cdot A \cdot \varepsilon$, where ϕ_0 is the incident flux, A is the sample aperture size and ε is the detector efficiency that depends on the neutron wavelength λ . The wavelengths of interest are in the range of 10-5000 Å. The diffraction length scale, d' , is proportional to $2\pi/q$ or to λ/θ (see Figure 1.4.1.).

SANS can handle various forms of material (liquids, gels and solids). Typical SANS samples have an area of about 1 cm², but their optimal thickness, d , is actually determined by the features of the material to be measured. As shown in Figure 1.4.3, the incident beam, I_0 , entering the sample may be subject to coherent scattering, incoherent scattering, absorption and/or multiple coherent scattering. As previously mentioned, the elastic coherent scattering at small angle is the most useful interaction mode for microstructural investigation of the materials. Since the other three kinds of interaction reduce the coherence of the scattered neutron beam, it is very important to optimize the thickness of sample, in order to obtain sufficient signal and to minimize the contributions of the incoherent scattering, absorption and multiple coherent scattering, and to make a series of measurements on reference materials and samples to be able to subtract these interferences at the time of data analysis.

As previously mentioned, if the number density of scattering objects is N/V , the scattering per unit volume, $d\Sigma/d\Omega$, is equal to $(N/V)d\sigma/d\Omega$. When a scattering event occurs at $0 \leq x \leq d$ with a probability $d\sigma/d\Omega$, the attenuation of the incident neutron beam before the collision is $\exp(-\Sigma_T x)$ and the attenuation after the event is $\exp(-\Sigma_T(d-x))/\cos\theta$, where Σ_T is the total scattering cross section given by [85]:

$$\Sigma_{total} = \Sigma_{coh} + \Sigma_{inc} + \Sigma_{abs} \quad (1.4.6).$$

Integration of the scattered intensity, $I(\theta)$, along x , i.e. through the sample, with $\cos\theta \approx 1$ (small angle approximation), yields [85]:

$$\begin{aligned} I(\theta) &= \Phi_i \varepsilon \Delta\Omega A d \left[\exp(-\Sigma_T d) \right] (N/V) \frac{d\sigma}{d\Omega} \\ &= \Phi_i \varepsilon \Delta\Omega A d \left[\exp(-\Sigma_T d) \right] \frac{d\Sigma}{d\Omega} \end{aligned} \quad (1.4.7).$$

Transmission is defined as the attenuation of the incident beam intensity due to scattering and absorption. The attenuation of the beam intensity, $-dI$, through dx is equal to [85]:

$$-dI = I \cdot \Sigma_T \cdot dx \quad (1.4.8).$$

By integrating over the sample thickness, one obtains [85]:

$$\int_{I_0}^I \frac{dI}{I} = -\Sigma_T \int_0^t dx \quad (1.4.9),$$

and

$$\ln \frac{I}{I_0} = -\Sigma_T \cdot t \quad (1.4.10).$$

The transmission, T , is given by [85]:

$$\frac{I}{I_0} = \text{transmission} = e^{-\Sigma_T \cdot t} \quad (1.4.11),$$

or

$$T = \frac{I_{(\theta=0)}}{I_0} = \exp(-\Sigma_T d) \quad (1.4.12).$$

The scattered intensity, I_s , is given by [85]:

$$I_s \propto dT \frac{d\Sigma_{coh}}{d\Omega} \propto d e^{-\Sigma_T \cdot t} \quad (1.4.13).$$

The relation between I_s and d is shown in Figure 1.4.4. It can be seen that I_s reaches a maximum for $d = 1/\Sigma_T$. At this point the transmission is equal to 37%. However, this thickness value is optimal only when $\Sigma_{coh} \ll \Sigma_T \approx \Sigma_{inc} + \Sigma_{abs}$. When $\Sigma_{coh} \approx \Sigma_T$, the thickness value $d = 1/\Sigma_T$ is too large, as in that case the specimen undergoes severe multiple scattering problems. Therefore, it is necessary to reduce the specimen thickness in order to increase the transmission value so that $T \geq 90\%$.

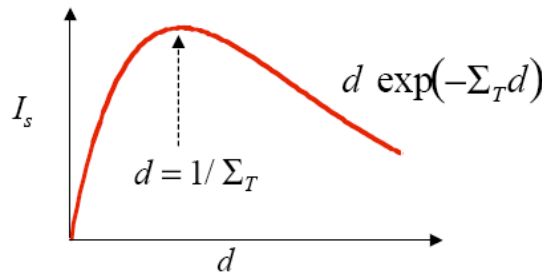


Figure 1.4.4: Relation between the scattered intensity and the specimen thickness.

1.5 Examples of applications of the SANS technique

A number of SANS investigations of the microstructure of ferritic/martensitic steels, in the as-annealed or irradiated condition, have been reported.

1.5.1 As-annealed steels

The microstructure of a modified version of the ferritic/martensitic steel referred to as MANET has been investigated using small- and wide-angle polarized neutron scattering [109]. The specimens were measured in the ferromagnetic state at room temperature, magnetized to saturation in a vertical magnetic field of 1 T. With respect to the conventional SANS technique, the use of polarized neutron beams provides additional microstructural information through the analysis of the interference term. Furthermore, it has the advantage of eliminating spurious background contributions to SANS. Finally, the availability of SANS data for a Q -range extended over three orders of magnitude, as it was the case in this study, is extremely useful to properly characterize complex steels such as ferritic/martensitic steels. SANS measurements were performed on two specimens that were heat-treated at two different austenization temperatures, namely 1075°C and 1200°C, for 0.5 h followed by rapid air quenching (3600°C/min). The nuclear-magnetic interference term and the comparison of the size distribution functions obtained from the nuclear and magnetic scattering components allowed identification of three kinds of microstructural inhomogeneities for an austenization temperature below 1200°C: (1) tiny C-Cr elementary aggregates (1 nm or less in size), (2) larger (1-25 nm) Fe-carbides, and (3) much larger inhomogeneities arising either from $M_{23}C_6$ carbides or from fluctuations in the Cr distribution.

1.5.2 Irradiated steels

It was already demonstrated, in the case of stainless steels, that the irradiation-induced defects can be clearly distinguished in SANS, and that SANS results well correlate to TEM results in the case of defects larger than about 1 nm [110].

On the other hand, a series of RAFM steels with a Cr content ranging between 7 and 12 wt.% were investigated by SANS following neutron irradiation between 250 and 400°C to doses between 0.7 and 2.9 dpa [111]. SANS measurements were performed at room temperature in a saturating magnetic field of 2 T perpendicular to the incident neutron beam direction, in order to separate the magnetic and nuclear scattering cross-sections. It is difficult by using TEM to detect and study the α - α' phase separation, because of the very weak difference in electron scattering contrasts of Fe and Cr. Furthermore, in ferritic/martensitic steels, the ferromagnetic character of the matrix and the high density of interfaces limit the possibilities of fine structure analysis by TEM. SANS is much more powerful to characterize the mean size, shape and number density of precipitates, because of the large difference between the neutron coherent scattering lengths of Fe and Cr. In addition, since the ferrite is ferromagnetic, the ratio of the magnetic and nuclear SANS contrasts is different for the matrix and the precipitates and can provide information on their chemical composition. This study showed that when the Cr content of the bcc ferritic matrix is larger than a critical threshold

value (about 7.2 at% at 325°C), the ferrite separates under neutron irradiation into two isomorphous phases, Fe-rich (α) and Cr-rich (α'). The kinetics of phase separation was found much faster than under thermal aging. The quantity of α' -phase precipitates, which contribute significantly to the irradiation-induced hardening of the 9-12 wt.% Cr steels, was observed to increase with the Cr content, the irradiation dose and when the irradiation temperature is reduced. The influence of Ta and W added to the RAFM steels was found negligible. In the case of the low Cr content F82H RAFM steel irradiated at 325°C to 2.9 dpa, where α' phase does not form, a small SANS intensity was detected, which was attributed to irradiation-induced point defect clusters of vacancy-type.

The α - α' phase separation has been also studied in detail by SANS in thermally aged [112] and, to a lesser extent, in irradiated binary [113] Fe-Cr model alloys. SANS has also revealed the precipitation of nano-sized M_2C carbides, responsible for the first stages of secondary hardening in a Fe-9Cr-1Mo alloy, particles which were too small to be detected using TEM [114]. The SANS technique was also used to determine the composition and structure of nano-sized precipitates in irradiated reactor pressure vessel steels [115]. A careful analysis of an extensive SANS database showed clearly that the precipitates that form in aged and irradiated Fe-Cu alloys are essentially pure Cu. These precipitates are believed to be the dominant hardening feature resulting in severe embrittlement of irradiated reactor pressure vessel steels.

SANS has been also used to study the growth of helium bubbles in the F82H RAFM steel [115]. Specimens have been homogeneously implanted at 250°C with 400 appm He and then annealed at temperatures up to 975°C. SANS measurements were performed at room temperature in an horizontal magnetic field applied perpendicular to the incoming neutron beam in order to fully align the magnetic moments in the specimens. Thus, only nuclear scattering occurs in the horizontal plane, while nuclear and magnetic scattering occur in the vertical one. In that case the purely magnetic scattering is given by the difference between the vertical and horizontal macroscopic differential SANS cross-sections. The helium bubble volume distribution functions obtained showed that a dense population of small bubbles, 1 nm or less in size, is accompanied by a secondary distribution of bubbles, one order of magnitude larger, as expected from results of TEM observations performed after post-implantation annealing. The microstructure evolution was found to be temperature dependent. The uniform bubble distribution produced by low temperature implantation evolves into a bimodal one when the post-implantation annealing temperature is increased. In a more recent investigation, Henry et al. [76] have studied with both TEM and SANS the microstructure resulting from implantation of helium (as 23 MeV α particles) at 250°C and 550°C into two 9%Cr ferritic/martensitic steels (T91 and EM10). Of particular interest are the results of the implantation at 250°C. By applying a magnetic field during the SANS measurements, helium bubbles were evidenced, their mean size was determined (1.15-1.2 nm) as well as their volume fraction (0.95-0.79%), which corresponds to a very high number density of helium bubbles ($1.17 \times 10^{24} \text{ m}^{-3}$ in T91 and $8.5 \times 10^{23} \text{ m}^{-3}$ in EM10), while only a high density of small dislocation loops was observed in TEM.

1.6 Introduction to simulation methods

Multiscale simulations constitute nowadays a major tool in the investigation of radiation damage and effects, as it allows establishing solid foundations for understanding the relationship between radiation damage and the induced mechanical response of the target material, starting at the atomic scale. Molecular dynamics simulations is one of the techniques that is largely used in this field as it allows an atomistic description of the generation of the damage by irradiation and of the interaction of mobile dislocations with irradiation-induced defects.

1.6.1 Molecular Dynamics (MD) simulations

Molecular dynamics is a method that allows simulation of the dynamics of an N -body system, that is to say its evolution in time. It is a mean to probe the dynamic properties but also the static properties of a system. It is based on a deterministic interpretation of nature where the behavior of a system can be computed if we know the initial conditions and forces of interaction between the atoms in the system. The methodology consists in identifying or constructing a model describing the interaction forces between the atoms, computing the trajectories of the atoms using the discretized laws of classical Newton mechanics, and finally analyzing those trajectories to obtain observables. The method used to describe the interaction forces characterizes the simulation. Chemists usually use the idea of ‘force field’, whereas physicists prefer to use the idea of ‘interaction potential’ from which the forces are derived. In the case of classical MD, the electronic information on the binding between atoms is implicitly included in an analytic function through empirical parameters fitted on known physical properties of the material of interest. *ab-initio* methods can be also used to calculate the potential energy of the system. In that case, one speaks of *ab-initio* or quantum MD.

Atomic displacement cascades take place in length and time scales of the order of the nanometer and the picosecond [116], respectively, and can be ideally studied by MD simulations [117]. It should be noted that there is at present no direct experimental information on the structure and dynamic energetics of atomic displacement cascades that last less than 25 ps in volumes smaller than thousands cubic nanometers. The development of computer technology allows using sufficiently large simulation box sizes and time scales to simulate the time evolution of a cascade to its complete cool down and to avoid self-annealing effects due to periodic boundary conditions. Furthermore, due to their highly inhomogeneous and non-equilibrium nature, binary-collision approaches such as the linear transport theory [118] and Monte-Carlo simulations do not provide information regarding the cooling stage of the cascade during which many-body effects are important.

In principle, a very simple method to implement foundations of MD simulations relies on classical mechanics, classical non-linear dynamics, kinetic rate theory, statistical mechanics, sampling theory, conservation principles and solid-state physics, as summarized below.

Newton’s second law of motion relates the acceleration of an atom to the force acting on it:

$$\vec{F}_i = m\ddot{\vec{r}}_i \quad (1.6.1),$$

where m is the mass of the atom. The acceleration of the atom is given by:

$$\ddot{\vec{r}}_i = \frac{d^2 \vec{r}_i}{dt^2} \quad (1.6.2),$$

where \vec{r}_i is the position vector of the atom i . For an N -body system, $3N$ second-order, ordinary differential equations of motion may be derived from the Newton's second law of motion. If the system of N atoms is an isolated system, the total energy of the system is conserved, i.e., the sum of the potential energy and kinetic energy is kept constant. In that case, the Hamiltonian of the system may be written as [119]:

$$H = \sum_{i=1}^N \frac{P_i^2}{2m_i} + U(\vec{r}_i) \quad (1.6.3),$$

where P_i is the momentum of the atom i . The potential energy U arises from interactions between atoms. By deriving the equation 1.6.3, one obtains [119]:

$$\begin{aligned} \dot{p}_k &= \frac{\partial H}{\partial r_k} \\ \dot{r}_k &= \frac{\partial H}{\partial p_k} \end{aligned} \quad (1.6.4).$$

The Hamilton's equations of motion are equivalent to the Newton's second law of motion [119]:

$$\vec{F}_i = m\ddot{\vec{r}}_i = \frac{-\partial H}{\partial \vec{r}_i} = \frac{-\partial U}{\partial \vec{r}_i} \quad (1.6.5).$$

The Hamiltonian above is only valid for an isolated system. If the system is not isolated additional terms appear and the value of the Hamiltonian is no more equivalent to the total energy of the system. In a non-isolated system the Hamiltonian is conserved but not the total energy of the system.

As previously mentioned, the goal of MD simulations is to obtain the trajectories of a set of N atoms interacting with each other through a potential function U by solving the above equations of motion. In an isolated system the derivative of the potential with respect to the atom positions gives the forces acting on these atoms. Given the force values, the new positions of the atoms can be calculated using the Newton's second law of motion. Therefore, the key component of MD simulations is the interatomic potential, since it characterizes the properties of the system.

An interatomic potential $U(\vec{r}^N)$ can be approximated as the sum of two-body to N -body contributions of the form [120]:

$$U(\vec{r}^N) = \sum_i U_1(\vec{r}_i) + \sum_{i \langle j} U_2(\vec{r}_i, \vec{r}_j) + \sum_{i \langle j \langle k} U_3(\vec{r}_i, \vec{r}_j, \vec{r}_k) + \dots \quad (1.6.6),$$

where the first term represents external forces and the other ones refer to interactions between atoms. The most important term is the second one: the pair potential. This pair potential depends only on the separation between two atoms, r_{ij} .

Lennard-Jones [121] introduced a soft-sphere pair potential of the form:

$$U_2(\vec{r}_{ij}) = k\epsilon \left[\left(\frac{\sigma}{\vec{r}_{ij}} \right)^n - \left(\frac{\sigma}{\vec{r}_{ij}} \right)^m \right] \quad (1.6.7),$$

which includes both a short-range, repulsive force and a longer-range attractive force. The short-range force prevents the system from collapsing and the long-range attractive interaction maintains the structure bonded. The range and strength of the forces depend on the values of n and m . The usual choice is $m = 6$ and $n = 12$. The value of $m = 6$ comes from the London's theory for dispersion [121-125], but there is no justification for the value of $n = 12$. The Lennard-Jones potential (also known as the 6-12 potential) may be then written as [125]:

$$U_2(r_{ij}) = 4\epsilon \left[\left(\frac{\sigma}{r_{ij}} \right)^{12} - \left(\frac{\sigma}{r_{ij}} \right)^6 \right] \quad (1.6.8).$$

This potential is well adequate for noble gases, and it has been used also for metals. For example, in the case of Fe-Fe the parameters to be used are $\sigma = 2.209 \text{ \AA}$ and $\epsilon = 40.00 \times 10^{-21} \text{ J}$ [126]. Figure 1.6.1 shows the potential energy in reduced unit ($u^* = u/\epsilon$ and $r^* = r/\sigma$) versus the distance between two atoms for the Lennard-Jones potential.

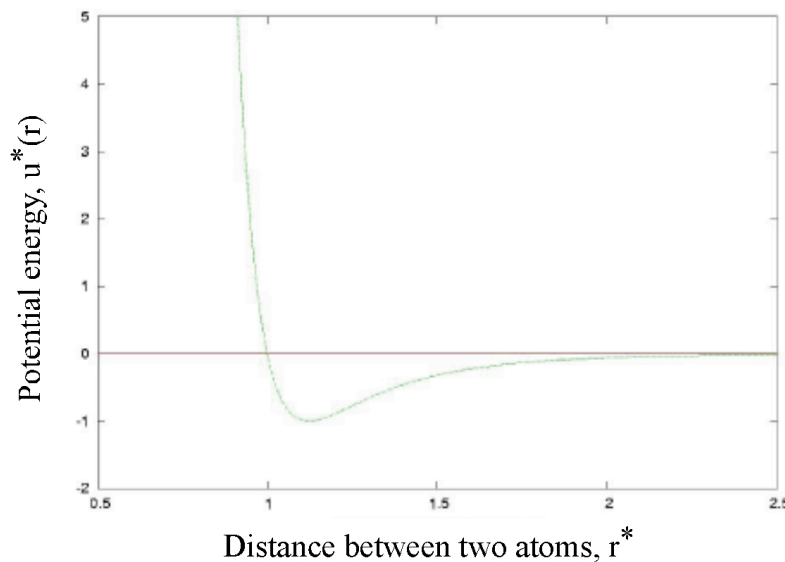


Figure 1.6.1: Lennard-Jones pair potential in reduced unit [127].

In the case of metals, an interatomic potential developed by Daw and Baskes in 1984 [128] is probably the most widely used and successful. This potential considers that a metallic bond occurs due to the immersion of an ion into a free electron gas. Under this assumption, the energy of N atoms is given by:

$$U(\vec{r}^N) = \frac{1}{2} \sum_{i,j} \Phi_{ij}(R_{ij}) + \sum_i F_i(\rho_{h,i}) \quad (1.6.9).$$

This so-called ‘embedded atom potential’ (EAM) consists of two terms. The first term is a two-body potential that represents the repulsion between the ion of interest and the rest of the ions in the system. The second term is a multi-body function that represents the energy to embed an atom i with an electron density $\rho_{h,i}$ that arises from the linear superposition of spherically averaged atomic electron densities. One of the main advantages of this potential is environmental dependent, since a change in the coordination number of an atom results in a different electron density, which changes the bond energy. The embedding function, electron density and pair potentials can be obtained either from *ab-initio* calculations or from fitting to experimental properties, such as the atomic volume, the elastic constants or the ground state structure.

When angular-dependent interactions contribute significantly to the bonding, pair potentials like those described above are not sufficient and three-body or higher-order terms must be included in the potential energy. This was done in the case of covalently bonded systems like silicon [129, 130], carbon [131, 132] and transition metals [133].

MD simulations of radiation damage and effects on ferritic/martensitic steels are presently limited by the availability and accuracy of empirical interatomic potentials capable to describe the alloying elements present in such materials. Radiation damage and effects on bcc Fe (α -Fe) and Fe-base model steels (e.g. Fe-C, Fe-Cr, Fe-Cr-C) were recently addressed in a comprehensive manner from a computational perspective, using large-scale MD simulations, with an emphasis on both the qualitative and quantitative aspects of the processes under study by identifying the operating mechanisms and extracting numerical information that allowed the quantification of the relevant parameters [134]. All the MD simulations were performed following a logical sequence of events, encompassing the pertinent time and space scales from the formation of small interstitial clusters in atomic displacement cascades to the determination of the irradiation-induced yield stress increase (radiation hardening), useful for micromechanical estimations. Examples of recent results are reported just below.

Dislocation loops in ferritic/martensitic steels exhibit both $1/2 a_0 \langle 111 \rangle$ and $a_0 \langle 100 \rangle$ Burgers vectors in TEM, with a predominance of $a_0 \langle 100 \rangle$ loops. It is believed, but not confirmed, that these loops are interstitial in nature [47, 135-137]. Both experimental observations [47, 135-137] and atomistic simulations [117, 138] have confirmed the stability of $1/2 a_0 \langle 111 \rangle$ and $a_0 \langle 100 \rangle$ loops in ferritic/martensitic steels. Molecular dynamics simulations of high-energy atomic displacement cascades in Fe have revealed the formation of small, one-dimensionally mobile $1/2 a_0 \langle 111 \rangle$ self-interstitial atom clusters following the thermal stage of high-energy displacement cascades collapse, within a few picoseconds after the initiation of the event, as a consequence of cooperative phenomena without long-range diffusion [117, 139]. The $a_0 \langle 100 \rangle$ loops have been recently proposed to form from the direct interaction of these small, cascade-produced, $1/2 a_0 \langle 111 \rangle$ clusters [136, 140] and grow by

the biased absorption of $1/2 a_0 \langle 111 \rangle$ loops to sizes visible in TEM, i.e., ≥ 1 nm [140]. Therefore, the population of $a_0 \langle 100 \rangle$ loops is directly related to the fate of $1/2 a_0 \langle 111 \rangle$ clusters produced in atomic displacement cascades and, in this sense, the effect of impurities and solute atoms, or other foreign inclusions, on the formation, evolution and migration of these clusters may provide critical insight into the understanding of how the population of $a_0 \langle 100 \rangle$ loops evolves as a function of the specific irradiation parameters. However, the $1/2 a_0 \langle 111 \rangle$ clusters are sub-nanometer in size and their detection by experimental means is limited by the time and spatial scales involved. In addition, the kinetics governing the nucleation and growth of $a_0 \langle 100 \rangle$ loops occur over time scales that cannot be easily captured experimentally.

Fe-Cr potentials are needed to model radiation damage in ferritic/martensitic steels. Recently, two different interatomic potentials for Fe-Cr were developed [141, 142], which reproduce the change in sign of the heat of mixing of the Fe-Cr system occurring at 10% Cr [59]. One of these potentials [141] was used to simulate the damage production in Fe-Cr alloys [143]. It was found that the content in Cr does not cause drastic changes in the cascade efficiency relatively to pure Fe. No clustering of Cr was observed. A fraction of Cr atoms remains in interstitial position after the cool down of the cascade, an effect that could influence the long-term evolution of the microstructure.

Molecular dynamics simulations of the primary state of damage in Fe-He showed that the presence of He in interstitial sites promotes the formation of self-interstitial atom clusters [144]. Their size and number density are drastically increased as compared to the case of pure Fe or Fe with He in substitutional sites [144, 145]. When He is in interstitial sites, it tends to combine with self-interstitial atom clusters [144]. This feature may drastically reduce the mobility of interstitial clusters relatively to pure Fe, with a significant impact on the subsequent evolution of irradiation-induced defects in the alloy, as vacancy clusters may grow more easily due to the reduced annihilation rate, and then on its mechanical properties.

In bcc metals, the propagation mechanism of screw dislocations dictates the plastic response at low temperatures and their behavior in the presence of irradiation-induced defects (e.g. small dislocation loops) and the dynamics of their interaction are the key for understanding radiation hardening in conditions relevant to fusion power reactors. For instance, a high number density of irradiation-induced defects in the appropriate temperature range can result in radiation hardening by dislocation pinning, leading to a characteristic yield stress increase that can be measured experimentally using standard methods (e.g. tensile tests). However, the atomistic nature of the interaction makes these processes very difficult to study using conventional experimental techniques, whereas MD has been successfully applied to a number of scenarios involving mobile dislocations and various types of lattice defects [146-153]. Note that, akin to atomic displacement cascade simulations, such MD simulations are dependent on the used interatomic potential [154, 155]. A major issue in simulating by MD the dislocation glide in bcc structures is the mobility of the screw dislocation with its three-fold symmetry core [155, 156]. Voids appear to be strong obstacles to moving dislocations [151, 153, 157]. A 2 nm void presents an obstacle strength of 590 MPa to the passage of an edge dislocation [157]. He in solid solution doesn't have a significant effect on the yield stress before it reaches 1.0 at.% He [157]. A 2 nm He bubble is a weaker obstacle than a 2 nm void when the He content is low, at 1 to 2 He atoms per vacancy [157]. Beyond 2 He atoms

per vacancy, a content at which the bubble is the weakest, the resistance of the He bubble increases with He content. At 5 He atoms per vacancy, the He bubble becomes a much stronger obstacle than the void, which is due to significant loop punching [157], whose stochastic nature induces scatter in the resulting obstacle strength [158]. With increasing the temperature the cavity obstacle strength decreases [159]. In the literature there is experimental evidence of gas bubble induced loop punching, such as for H bubbles in Cu [160] and He bubbles in Al-0.4Li [161]. *ab-initio* calculations suggest that such an effect might be also effective in Fe [162], which would lead to pressurized He bubbles that could release their pressure by emitting self interstitial atoms. This so-called self-trapping of He [163] was however to our knowledge never observed experimentally in ferritic/martensitic steels.

1.6.2 Transmission Electron Microscopy (TEM) image simulations

From the atomistic perspective, the difficulty associated with results of MD studies is their lack of experimental confirmation, resulting from the sample sizes that can be treated with the current computing capabilities and the non-trivial relation between the defects generated with MD and their equivalent TEM images. This has led to the development of special tools to investigate the correlation between defect structures produced by atomistic simulations and their observation in TEM [164]. These tools partially bridge the gap existing between simulations and experimental observations and help in assessing experimental limitations in the observation of small defect clusters. The weak beam TEM imaging technique [165] is the most appropriate technique for observing and analyzing irradiation-induced defect clusters with a size ≥ 1 nm, as it provides an improved spatial resolution and signal-to-background ratio over the usual bright/dark field TEM imaging mode. However, as there exists a non-trivial relation between the actual configuration of defect clusters (size and geometry) and their TEM image, whatever the imaging technique being used, TEM image simulations of all possible types of irradiation-induced defect clusters created by MD simulations are indispensable to interpret results of experimental TEM observations and to close the gap between experimental TEM images and MD simulations [166-168].

Such a procedure has been already extensively applied to irradiated fcc metals. In such materials, beside SFTs and voids originating from vacancy clusters, small defect clusters are in the form of faulted dislocation loops (Frank loops) that have a Burger's vector equal to $\mathbf{b} = a_0/3 \langle 111 \rangle$, where a_0 is the lattice parameter, and can be either vacancy or interstitial in nature [169-172]. The correlation between the features of defect clusters created by MD and their corresponding TEM image was investigated by simulating conventional TEM images of pre-defined defect clusters, using a novel technique [164], in terms of: (1) the visibility or image contrast of the defect clusters, (2) the limits to which they can be identified on the basis of their TEM image features, and (3) the correlation between their real size and their TEM image size. The study focused on interstitial Frank loops in Al and SFTs in Cu, which are smaller than about 3 nm. It was shown that this virtual microscopy allows not only addressing the above-mentioned points, but also assessing experimental TEM limitations for observing small defect clusters. It appeared that a defect cluster of Frank loop-type in Al would in principle be visible experimentally down to surprisingly small sizes (from two interstitials upwards), provided that the specimen preparation is optimized, while SFTs in Cu

would be difficult to identify below a size of 19 vacancies. The defect clusters obtained by MD simulations of high-energy displacement cascades in Al and Ni were also studied by means of TEM image simulations via the multislice method [166].

1.6.3 SANS signal simulations

Analysis of the SANS signal provided by irradiation-induced defect clusters, in terms of type, size and number density of the defects, is a non-trivial task. Therefore, simulations of the SANS signal of all possible types of irradiation-induced defect clusters created by MD simulations would be needed for interpreting the results of SANS experiments. However, to my knowledge, only analytical solutions have been published, but no such simulations. Therefore, within the framework of this thesis I have developed a new method for simulating the SANS signal of defects created by MD. The method developed is described in Chapter 2.

1.7 Motivation of the thesis

The importance of obtaining detailed information about the irradiation-induced microstructure has been recently demonstrated by the fact that the resistance to radiation damage of a material can be modeled and quantified from a set of parameters that include the structure of the material, the type and size distribution of the irradiation-induced defects and their accumulation rate as a function of the irradiation dose [173]. In recent investigations using TEM [174], a certain number of characteristics of the defect accumulation in the primary damage state have been established:

- (i) a linear increase in the defect number density with dose in body centered cubic metals, up to a saturation value which corresponds to the onset of the cascade overlap process;
- (ii) a difference of three orders of magnitude in the accumulation rate of defect clusters between face centered cubic and body centered cubic metals.

However, the irradiation-induced microstructure is very difficult to assess by means of TEM, as this method samples a very small volume of material. Moreover, the annealing of the defect microstructure, which provides important information on its kinetic behavior, can hardly be studied with TEM, where due to the small thickness of the specimen the surface controls the annealing behavior. In addition, the attempts to quantify such a microstructure with TEM are limited by the spatial resolution of the method, which only allows the direct observation of defects whose size is larger than about 1 nm in weak beam TEM imaging. However, it is thought that a number of irradiation-induced defects have a size below 1 nm, which actually contribute to the hardening and/or embrittlement behavior of materials under irradiation.

The SANS technique under applied magnetic field appears to be a very powerful technique, complementary to TEM, for studying irradiation-induced defects at the nanometer scale in ferromagnetic RAFM steels, either when the irradiation-induced defects are very small (< 1 nm), or because of a more favorable difference in the contrasts provided by the defects

and the matrix [175]. Indeed, it was clearly demonstrated that, in addition to the basic parameters (size, number density, geometry), SANS can provide information on the composition of the scattering objects on the basis of the magnetic to nuclear scattering ratio, and then it allows distinguishing metallic precipitates from voids or helium bubbles, for instance [76]. For a magnetically saturated Fe matrix, this ratio is governed by the square of the difference between the average scattering length of the scattering objects and that of the surrounding Fe matrix [176]. Therefore, the use of polarized neutron beams provides additional and unique microstructural information through analysis of the nuclear-magnetic interference term. It has also the advantage of eliminating spurious background contributions to SANS [109]. In addition, the possibility of obtaining SANS data over an extended Q -range (Q being the magnitude of the diffraction vector) is extremely useful to properly characterize complex steels, where various inhomogeneities of quite different sizes are present [109, 177]. Finally, SANS examines a much larger volume of material than TEM.

On the other hand, MD simulations have proven to be very useful in understanding the production and evolution of defects during irradiation [117]. Since the great advantage of the MD treatment is that unequivocal determination of irradiation-induced defects is possible, due to its fully atomic resolution [178], MD simulations may be used to create a number of microstructural features typical of the irradiation-induced damage in pure metals.

Therefore, the aim of this Thesis was to investigate very small irradiation-induced defects in RAFM steels for fusion reactor application by combining SANS experiments on RAFM steels with MD simulations of a number of possible irradiation-induced defects in pure Fe, as a model materials for RAFM steels and simulations of their corresponding SANS signal. TEM image simulations of the defects created by MD were also performed in order to help closing the gap between TEM experimental images [166, 167] and MD simulations [168] of irradiation-induced defects.

CHAPTER 2: EXPERIMENTAL AND SIMULATION TOOLS

2.1 Materials

The main material investigated in this Thesis work is the EUROFER 97 RAFM steel, heat E83697, produced by Böhler AG. Its composition is given in Table 2.1.1 [179]. This material was normalized at 1253 K for 0.5 hour and tempered at 1033 K for 1.5 hour. Therefore, it exhibits a tempered martensitic microstructure, as illustrated in Figure 2.1.1 [180]. In addition to the EUROFER 97 RAFM steel, a few specimens from the F82H (a Japanese material) and OPTIMAX A (a Swiss material) alloys have been also investigated, for comparison purposes. The chemical composition of the F82Hmod RAFM steel is also reported in Table 2.1.1. The chemical composition of the OPTIMAX A RAFM steel is reported in Table 2.1.2.

		Radiologically desired (mass%)	EUROFER-97 specified (mass%)	EUROFER-97 achieved (mass%)	F82Hmod.Heat 9741 (mass%)
(a)	C		0.09–0.12 [0.11]	0.11–0.12	0.09
	Cr		8.5–9.5 [9.0]	8.82–8.96	7.7
	W		1.0–1.2 [1.1]	1.07–1.15	1.94
	Mn		0.20–0.60 [0.40]	0.38–0.49	0.16
	V		0.15–0.25	0.18–0.20	0.16
	Ta		0.10–0.14 [0.12]	0.13–0.15	0.02
	N ₂		0.015–0.045 [0.030]	0.018–0.034	0.006
	P		<0.005	0.004–0.005	0.002
	S		<0.005	0.003–0.004	0.002
	B		<0.001	0.0005–0.0009	0.0002
	O ₂		<0.01	0.0013–0.0018	(0.01)
(b)	Nb	<0.000001	<0.001	0.0002–0.0007	0.0001
	Mo	<0.0001	<0.005	0.001–0.0032	0.003
	Ni	<0.001	<0.005	0.007–0.028	0.02
	Cu	<0.001	<0.005	0.0015–0.022	0.01
	Al	<0.0001	<0.01	0.006–0.009	0.003
	Ti	<0.02	<0.01	0.005–0.009	0.01
	Si	<0.04	<0.05	0.04–0.07	0.11
	Co	<0.001	<0.005	0.003–0.007	0.05

Table 2.1.1: Chemical composition of the EUROFER 97 and F82Hmod RAFM steels [179]. Target values are given in parentheses. (a) Main alloying elements, (b) radiologically undesired elements in wt.% and ppm.

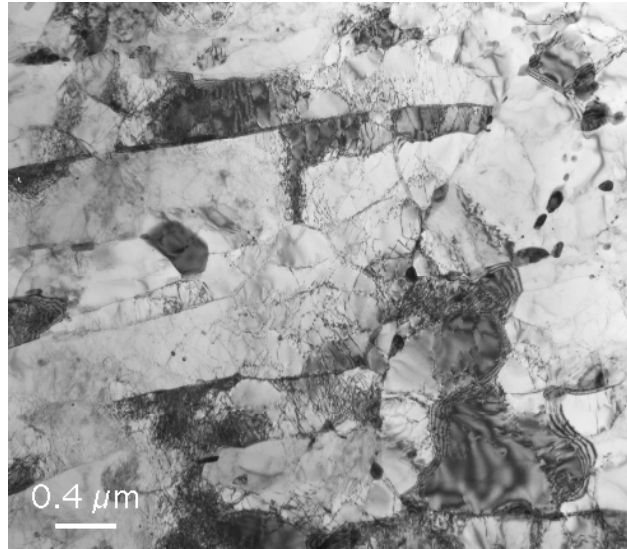


Figure 2.1.1: TEM image of the microstructure of the EUROFER 97 RAFM steel showing martensite laths joining one pre-austenite grain (PAG) boundary running across the image from the top right of the image to the bottom right [2]. Carbides (dark regions) decorate PAG boundaries and martensite lath boundaries. A few carbides are visible inside the laths.

Element	Fe	Cr	W	Mn	V	C	Mo	Ta
Content [wt.%]	balance	9.24	0.96	0.56	0.24	0.094	0.093	0.08
Element	Ce	Ni	P	B	Nb	O2	S	N2
Content [wt.%]	0.036	0.01	0.007	0.0061	0.005	0.00105	0.0002	0.00035

Table 2.1.2: Main chemical elements contained in the OPTIMAX A RAFM steel.

2.2 Irradiation experiments

2.2.1 Specimens

Series of small flat tensile specimens, 5.5 mm in gauge length, 20 mm in total length, 5 mm in width all along the gauge length and 0.3 mm in thickness, were cut out by spark erosion from the RAFM steels. Their geometry is illustrated in Figure 2.2.1.1. The two main surfaces of specimens were polished with papers of successively finer grades up to grade 1000. Some of these specimens have been kept apart for SANS measurements on reference specimens.

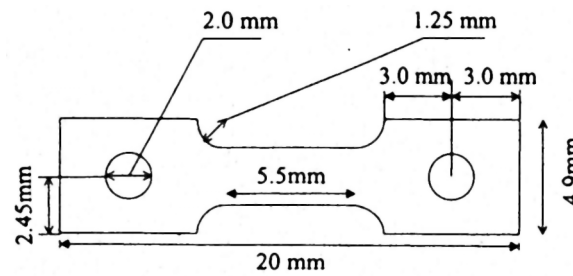


Figure 2.2.1.1: Geometry of small flat tensile specimens.

2.2.2 Irradiation facility

As no intense source of 14 MeV neutrons is presently available on earth, it is necessary to simulate irradiation by 14 MeV neutrons, by using for instance fission neutrons or high-energy protons or heavy ions. The present Thesis work is based on the investigation of flat tensile specimens that were irradiated with 590 MeV protons in the PIREX (Proton Irradiation Experiment) facility, at the Paul Scherrer Institute (Switzerland), in various irradiation campaigns that took place between 2000 and 2003, i.e., before the start of this work. The PIREX facility was decommissioned at the end of 2003.

As 14 MeV neutrons, 590 MeV protons produce atomic displacement cascades and transmutation nuclear reactions within the irradiated materials. However, it should be noted that while fission neutrons produce not enough helium and hydrogen, with respect to the amounts of gas atoms that will be produced in a fusion power reactor, 590 MeV protons produce too large amounts of impurities, including metallic impurities (Table 2.2.2.1). In particular, 590 MeV protons produce about 130 appm He/dpa and 800 appm H/dpa (in steels). The damage rate (in dpa/year) produced by 590 MeV protons is also slightly different from the one expected to occur in a fusion power reactor. Only the future International Fusion Materials Irradiation Facility (IFMIF) will actually provide irradiation conditions close to the ones expected to occur in a fusion power reactor at the level of the first wall.

Defect production (in steels)	Fusion neutrons (3-4 GW reactor, first wall conditions)	Fission neutrons (BOR 60 reactor)	High energy protons (PIREX)	IFMIF (high-flux test module)
Damage rate [dpa/year]	20-30	~ 20	~ 10	20-55
Helium [appm/dpa]	10-15	≤ 1	~ 130	10-12
Hydrogen [appm/dpa]	40-50	≤ 10	~ 800	40-50

Table 2.2.2.1: Defect production in steels for various irradiation facilities [181].

In the PIREX facility, six flat tensile specimens could be irradiated simultaneously in similar conditions of dose and temperature. The six specimens were mounted two by two, face to face, in three specimen holders (Figure 2.2.2.1). The three specimen holders were then inserted into three irradiation tubes. The three tubes were then fixed to the bottom extremity of the irradiation head (Figure 2.2.2.2).

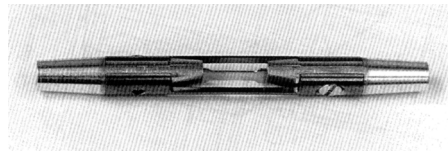


Figure 2.2.2.1: PIREX specimen holder for two flat tensile specimens.

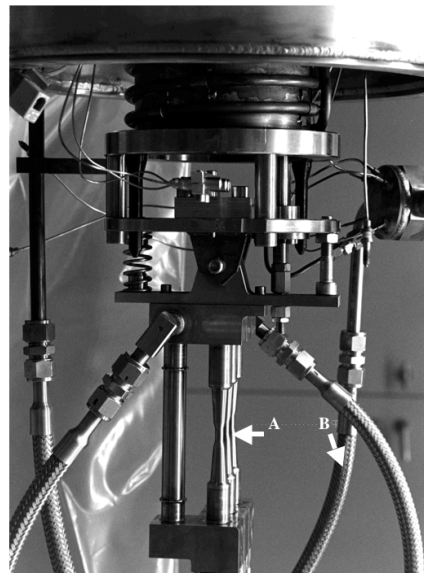
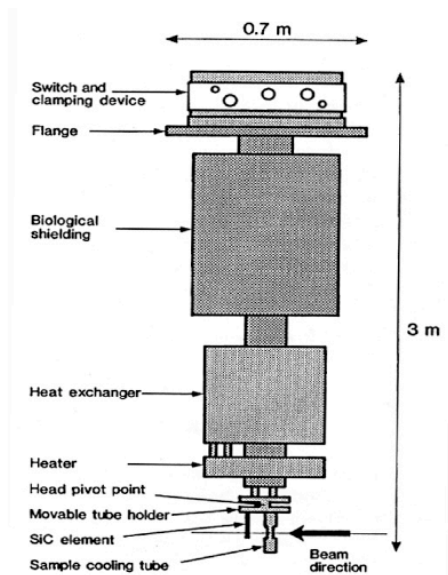


Figure 2.2.2.2: Left: Schematics of the PIREX irradiation head (only one irradiation tube is drawn instead of three). Right: Picture of the bottom part of the irradiation head: (A) shows the three tubes containing the six specimens, (B) shows a pipe belonging to the helium loop. The proton beam direction is perpendicular to the picture.

A large amount of heat, between $2'000$ and $11'000 \text{ W.cm}^{-3}$, depending on the type of irradiated material, was deposited in the volume of the specimens by the proton beam. One of the main problems encountered in this type of irradiation is the cooling of the specimens. In the PIREX installation, a helium gas flowing through the system and the irradiation tubes was used as coolant. The helium gas circulated at a pressure of up to 50 bars and its temperature was regulated by a heat exchanger, cooled with liquid nitrogen, which cooled the gas at the exit of the specimen region, and a 9 kW electrical heater that preheated the input gas. Depending on the helium gas pressure being used and the helium gas temperature, the specimens could be more or less strongly cooled. As a consequence, the temperature of the specimens could be controlled to any desired value between 50°C and 350°C with a fluctuation of $\pm 20^{\circ}\text{C}$. The temperature of the specimens was measured by means of a

thermocouple welded on either of the two central specimens. In the PIREX facility the beam intensity was around 15 μA and the damage rate was approximately 10^{-7} dpa/s. By assuming a practical irradiation time of about 60 hours per week, about 1 and 10 dpa (in steels) could be reached in one month and one year, respectively, accounting for the winter shutdown of the proton accelerator.

The 590 MeV proton beam had a two-dimensional Gaussian-distribution profile. The beam size was set to $3 \times 4 \text{ mm}^2$, using small magnets, for most of the irradiation experiments. Then, using a wobbling device, the beam was made to move continuously along the gauge length of the specimens in order to achieve homogeneous irradiation conditions.

2.2.3 Irradiation conditions

Specimens of RAFM steels have been irradiated at various temperatures to various doses. The irradiation matrix of the specimens investigated in this work is reported in Table 2.2.3.1.

Material	EUROFER 97	F82H	OPTIMAX A
Temperature [°C]	50, 250, 350	50	50
Dose [dpa]	0.3, 1.0, 2.0	0.3, 1.47	0.3

Table 2.2.3.1: Irradiation conditions of specimens of RAFM steels.

2.2.4 Dosimetry

The dose achieved by the irradiated specimens was calculated using a method developed by D. Gavillet [182], which is based on the measurement of the activity (or amount of gamma ray emission) stemming from the radioisotopes formed in the irradiated specimens by nuclear transmutations. In the case of RAFM steels the main radioisotopes produced and measured are ^{54}Mn , ^{51}Cr , ^{57}Co , ^{56}Co and ^{46}Sc . In this method, the dose is calculated by using a modified NRT formula (see § 1.2.1):

$$D = \frac{0.8 \delta_{ED} \rho_m}{2 T_d \rho_a \sigma_i \lambda_i} \frac{A_{im}}{P_i} \quad [\text{dpa}] \quad (2.2.4.1),$$

where

- D : Displacement damage or irradiation dose [dpa]
- δ_{ED} : Damage energy cross section [$\text{eV} \cdot \text{cm}^2$]
- E_d : Threshold energy for displacement damage [eV]
- σ_i : Production cross section of the isotope i [cm^2]
- λ_i : Decay constant of the isotope i [s^{-1}]
- Δt : Decay time (time between the end of irradiation and the γ -counting) [s]
- ρ_m : Specimen mass density [$\text{g} \cdot \text{cm}^{-3}$]
- ρ_a : Specimen atomic density [cm^{-3}]
- A_{im} : Measured activity of the isotope i after a cooling time Δt [Bq]

A_i : Activity of the isotope i after the end of irradiation [Bq]

P_i : Weight of the specimen [g]

The variation of dose value all along the gauge of a tensile specimen lies within 20%.

2.3 SANS experiments

2.3.1 Specimens

As mentioned under § 1.3.2, the usual size of a SANS specimen is about 1 cm^2 by about 1 mm in thickness. However, as mentioned under § 1.4, the thickness has actually to be optimized for each kind of material, in order to obtain a sufficient SANS signal and to minimize the contributions of the incoherent scattering and the absorption and multiple coherent scattering. In order to achieve this compromise it is necessary to calculate Σ_{coh} and Σ_T . In the case of the EUROFER 97 RAFM steel, the macroscopic cross-sections are given by:

$$\Sigma_{coh} = \sum_{i=1}^k n_i \sigma_{coh}^i, \quad \Sigma_{inc} = \sum_{i=1}^k n_i \sigma_{inc}^i, \quad \Sigma_{abs} = \sum_{i=1}^k n_i \sigma_{abs}^i \quad (2.3.1.1),$$

where n_i is the number density of the element i , which is equal to $f_i \cdot \rho_i \cdot N_A / A_i$, where f_i , ρ_i and A_i are the weight concentration, the density and the atom mass per mole of the element i , respectively. N_A is the Avogadro number, and k refers to the number of chemical elements contained in the material. The values of these parameters are reported in Table 2.3.1.1 for the main chemical elements contained in the EUROFER 97 RAFM steel.

It was found that $\Sigma_{coh} = 0.8618 \text{ cm}^{-1}$ and $\Sigma_T = 1.1377 \text{ cm}^{-1}$ for the EUROFER 97 RAFM steel. Therefore, $\Sigma_{coh} \approx \Sigma_T$. This indicates that the thickness has to satisfy $T \geq 90\%$. The corresponding thickness value is $d \leq 0.9 \text{ mm}$. The flat tensile specimens that were irradiated in the PIREX facility well satisfy this condition and were directly used as specimens for the SANS measurements.

Element	Fe	Cr	W	Mn	V	Ta	C	He
f_i (wt.%)	89.1	8.9	1.07	0.46	0.2	0.15	0.12	
ρ_i (g/cm ³)	6.98	6.3	17.6	5.95	5.5	15.0	2.1	
A_i (g)	55.847	51.996	183.85	54.938	50.996	180.948	12.011	4.003
n_i ($\times 10^{23}$)	0.7520	0.0807	0.0027	0.0039	0.0018	0.0004	0.0047	
b_c (fm)	9.452	3.6357	4.7552	3.7502	0.4413	6.917	6.6484	3.263
σ_{coh} (barn)	11.225	1.6606	2.972	1.752	0.0184	6.0012	5.5512	
σ_{inc} (barn)	0.4011	1.832	1.636	0.402	5.086	0.0117	0.0014	
σ_{abs} (barn)	2.563	3.056	18.32	13.32	5.084	20.65	0.0035	
Σ_{coh} (cm ⁻¹)	0.8441	0.0134	0.0008	0.0007	0.000034	0.0002	0.0026	
Σ_{inc} (cm ⁻¹)	0.0302	0.0148	0.0004	0.0002	0.0009	4.57×10^{-7}	6.59×10^{-7}	
Σ_{abs} (cm ⁻¹)	0.1927	0.0247	0.0050	0.0053	0.0009	0.0008	1.65×10^{-6}	

Table 2.3.1.1: Typical values for the main chemical elements contained in the EUROFER 97 RAFM steel.

2.3.2 Specimen holders

Two specimen holders were designed and constructed for the SANS experiments that were performed in this work. One was dedicated to reference (unirradiated) specimens and the other one to irradiated specimens. A picture of such a specimen holder is shown in Figure 2.3.2.1(left). It can be seen that a single specimen holder may contain up to eight specimens. In such a specimen holder each tensile specimen is actually located in between a series of plates including metallic fixing/alignment plates, a Cd plate that allows selecting precisely the specimen area to be measured, Cd being a neutron blocker element, and Al foils aimed at avoiding radioactive contamination of the other pieces by the irradiated specimens, as illustrated in Figure 2.3.2.1(right).

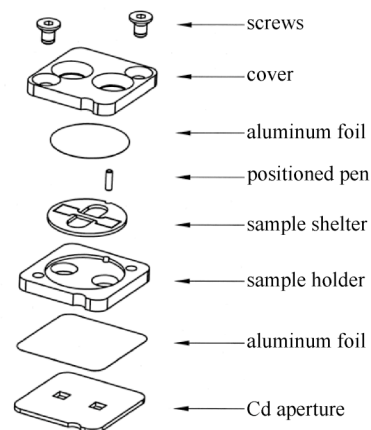
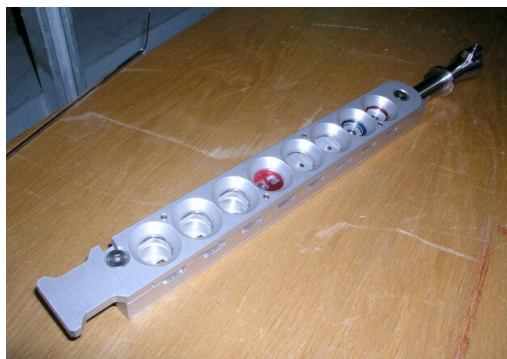


Figure 2.3.2.1: Left: picture of a specimen holder. Right: example of the fixation system of a single tensile specimen.

In addition to unirradiated tensile specimens of the three RAFM steels investigated in this work, the specimen holder for reference specimens contained an empty place and a place with a Cd plate, for background measurements, as well as a standard specimen having a well-known differential cross section, namely a water specimen, for calibration of the SANS intensity provided by the specimens of RAFM steels. Indeed, water provides isotropic neutron scattering, and furthermore coherent scattering can be neglected in the case of water. The differential cross section of a specimen of RAFM steel could be then calibrated by using the following equation:

$$\left(\frac{d\sigma}{d\Omega} \right)_{S,i,j} = \frac{I_{S,i,j}}{I_{W,i,j}} \times \left(\frac{d\sigma}{d\Omega} \right)_{W,i,j} \quad (2.3.2.1),$$

where S and W stand for the specimen of RAFM steel and the water specimen, respectively, and I is the intensity measured at the pixel (i,j) of the detector.

In what concerns the irradiated specimens, they were inserted into the series of plates and the eight assemblies were mounted into the specimen holder dedicated to irradiated specimens. This procedure was conducted in a hot cell at the hot laboratory of the Paul Scherrer Institute, using a remote handling system, due to the relatively important residual radioactivity provided by the irradiated specimens. This procedure is illustrated in Figure 2.3.2.2(left). In a further step, the specimen holder was inserted into a Pb bottle, as shown in Figure 2.3.2.2(right), which was transported to the SANS-I line of the SINQ facility. Once the SANS measurements on irradiated specimens were achieved, the specimen holder was transported back to the hot cell for dismantling of the irradiated, i.e., radioactive specimens.

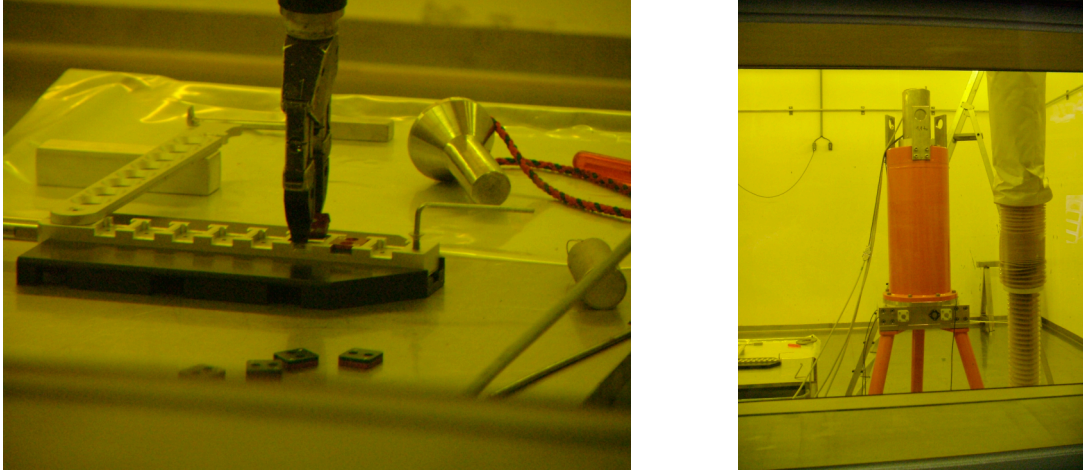


Figure 2.3.2.2: Left: mounting of the irradiated specimens into the series of plates and the specimen holder. Right: Pb transport bottle.

2.3.3 SANS facility

All SANS experiments have been performed in the SANS-I facility at the Paul Scherrer Institute (PSI). The SANS-I facility uses neutrons that are being produced by the Swiss Spallation Neutron Source (SINQ), as shown in Figure 2.3.3.1(left). The SINQ target is made of lead. Under irradiation by 570 MeV protons, which are produced by the PSI proton accelerator, the lead atoms emit neutrons via spallation nuclear reactions.

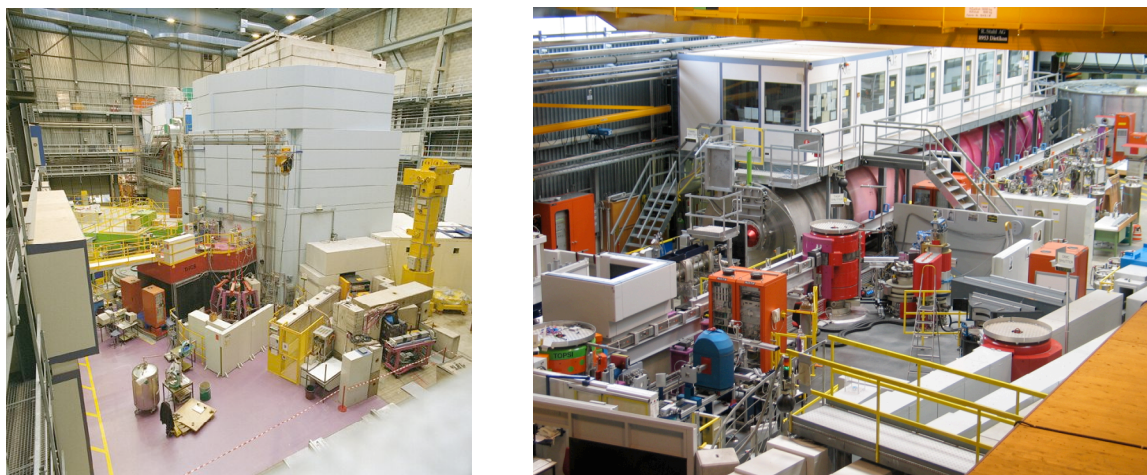


Figure 2.3.3.1: Left: picture of the SINQ facility at the PSI. Right: picture of the SANS-I facility at the PSI.

The design of the SANS-I instrument follows the classical concept of the D11-instrument at the Institut Laue-Langevin (ILL) in Grenoble (France). Installed at a cold neutron guide of the SINQ facility, it uses in its basic configuration a mechanical velocity selector for monochromatization and a straight pin-hole collimation system for the primary beam tailoring. Behind the specimen, in the secondary flight path, a two-dimensional position sensitive detector is used to register the neutrons scattered around the primary beam. Apart the velocity selector, the instrument is located in the guide hall of the SINQ facility, as shown in Figure 2.3.3.1(right), stretching to a total length of about 40 m with a secondary flight path of up to 20 m. The main components of the SANS-I facility are illustrated in Figure 2.3.3.2 and described more in detail just below [183].

Neutron beam and wavelength selection: The neutron guide, facing the cold D₂-moderator of the SINQ facility at its entrance, is curved to filter epithermal and higher energy neutrons. Coated with isotopically enriched ⁵⁸Ni in the curved section, its lower cut-off wavelength (characteristic wavelength) is 0.42 nm. The cross section is a square of 50 × 50 mm². Inside the bunker, the guide has a gap of 43 cm in which the beam shutter, a primary beam monitor, and the mechanical velocity selector are placed. A Dornier velocity selector [184] is used, rotating at a maximum speed of 28300 rpm for neutrons with a wavelength of 0.45 nm. The standard wavelength spread is 10%.

Collimation: The collimator allows for the adjustment of the collimation length, i.e., the distance between the two pinholes at the guide exit and at the specimen position, in discrete steps between 1 and 18 m, which then matches the Q -range chosen by selecting a certain specimen-to-detector distance. Mechanically, this flexibility is achieved by a system of eight collimator segments between 1 and 4 m long, mounted in sequence with vacuum-tight connections. Each section is a revolving device with three tubes. The aperture sizes at the beginning and at the end of the collimation system can be freely chosen up to the cross section of the neutron guide of $50 \times 50 \text{ mm}^2$.

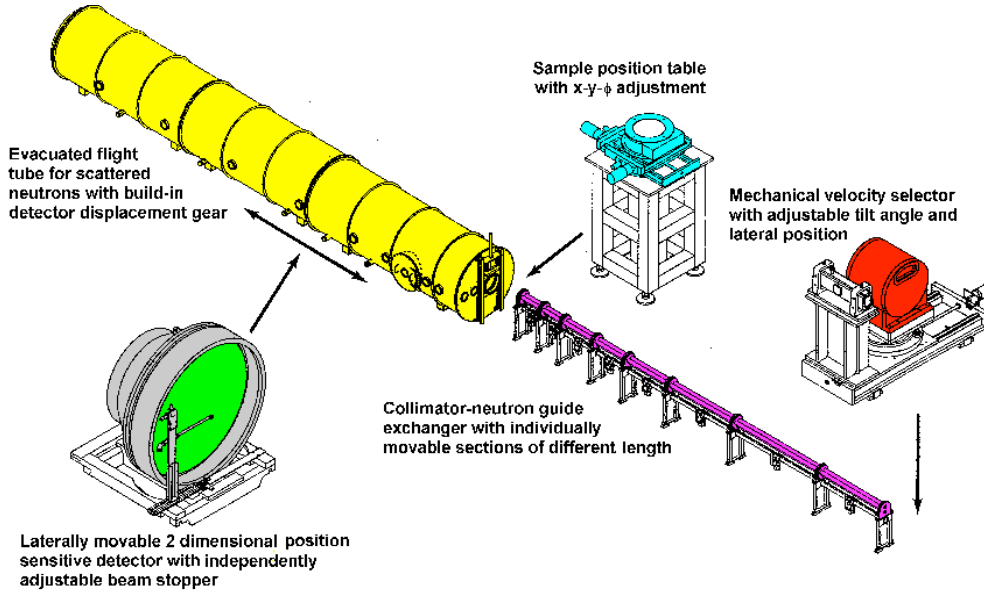


Figure 2.3.3.2: Main components of the SANS-I facility at the PSI.

Detection: The secondary flight path is enclosed by a steel vacuum tube with a diameter of 2.7 m. It houses a two-dimensional ^3He multi-wire proportional counter with a sensitive area of $96 \times 96 \text{ cm}^2$ and 128×128 detection elements of $7.5 \times 7.5 \text{ mm}^2$ each. The detector is mounted on a rail-guided trolley such that it may be positioned with its detection plane at any distance between 1.50 m and 20 m from the specimen. Further, an increase in the Q -range at any detector distance can be achieved by an optional lateral displacement of the detector of up to 50 cm, combined with a rotation around the central vertical axis to minimize parallax effects. Immediately in front of the detector, a beamstop of B_4C -plates is mounted on a thin-walled Al tube, moveable in vertical and horizontal directions.

Performance: The momentum transfer, Q , which corresponds to a given spot on the detector, is given by:

$$Q = \frac{4\pi}{\lambda} \sin \left(\frac{\tan^{-1} \left(\frac{r}{D} \right)}{2} \right) \quad (2.3.3.1),$$

where λ is the neutron wavelength, r is the radial distance of the spot from the beam center, and D is the specimen-to-detector distance. If it is assumed that the closest distance to the beam center at which reliable data may be recorded is $r_{min} = 5$ cm, which is half the size of the largest beam stop, then the minimum Q value at $D = 20$ m and $\lambda = 2$ nm is $Q_{min} = 8 \times 10^{-3} \text{ nm}^{-1}$. The maximal Q value at $D = 1.5$ m and $\lambda = 0.45$ nm with the detector centered to the beam axis ($r_{max} = 48$ cm) is $Q_{max} = 4.3 \text{ nm}^{-1}$ or, for a 50 cm lateral detector displacement ($r_{max} = 96$ cm), $Q_{max} = 8 \text{ nm}^{-1}$. The neutron flux data measured for various collimation distances, D , and wavelengths, λ , are shown in Figure 2.3.3.3.

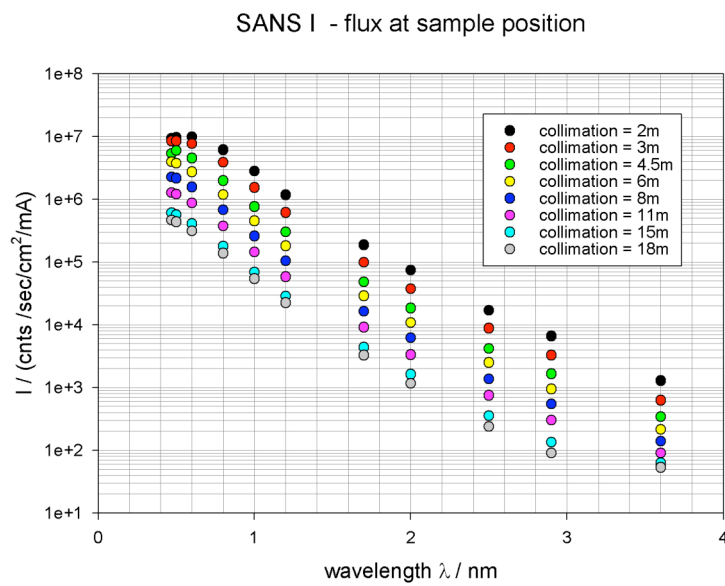


Figure 2.3.3.3: Neutron intensity at specimen position versus neutron wavelength for a 1 mA proton current entering the SINQ facility [183].

The main features of the SANS-I facility are summarized in Table 2.3.3.1 [183].

Neutron wavelength	0.45-4 nm
Beam collimation	1-20 m
Specimen-to-detector distance	1-20 m
2D ^3He detector	$7.5 \times 7.5 \text{ mm}^2$, 128×128 pixels
Accessible Q -range	6×10^{-3} - 10.5 nm^{-1}
Spatial resolution	0.5-400 nm
Neutron flux in the specimen position for 4 m collimation and $\lambda = 0.45$ nm	$30'000 \text{ n/cm}^2 \cdot \text{s} \cdot \text{mrad}^2 \cdot \text{mA}$

Table 2.3.3.1: Main features of the SANS-I facility at the PSI [183].

2.3.4 Measurement procedure

In order to obtain the SANS intensity provided by a given specimen of a given material, the following procedure was applied [185]:

1. Beam alignment: The center of the specimen is aligned with the incident neutron beam using a laser beam and a neutron camera.
2. Transmission factor measurements: The scattered intensities arising from a specimen, I , and from an empty place, I_0 , are measured at $\theta = 0$, where θ is the scattering angle, in exactly the same conditions, and circularly averaged. The transmission factor of the specimen is then given by $T_S = I/I_0$ at $\theta = 0$. In the case of a specimen located in a container, the transmission factor of the specimen is given by $T_S = T_{S+SB}/T_{SB} = I_{S+SB}/I_{SB}$ at $\theta = 0$, where S refers to the specimen and $S+SB$ refers to the specimen plus its container. The incident beam intensity has eventually to be attenuated to avoid saturation of the detector. This procedure was applied to all kinds of specimens, including irradiated and reference (unirradiated) specimens of RAFM steels, specimen holders, empty place, water specimen and water specimen holder.
3. Background measurements:
 - a. *Measurements from an empty place*: The scattered signal I_{EMP} arises from scattering by the container, the windows and the collimation slits, and from air scattering:

$$I_{EMP} = C_0 T_{SB} \left(\frac{d\Sigma(Q)}{d\Omega} \right)_{EMP} + I_{Blocked-beam} \quad (2.3.4.1),$$

where $C_0 = \Phi_i A d \Delta\Omega \varepsilon t$, Φ_i is the incident neutron flux, A is the illuminated specimen area, d is the specimen thickness, $\Delta\Omega$ is the solid angle of each pixel, ε is the detector efficiency, and t is the counting time.

- b. *Blocked beam measurements*: A Cd specimen that absorbs all neutrons is used. The measured intensity, I_{BDG} , arises from the detector dark current, stray neutrons and cosmic radiation:

$$I_{BDG} = I_{Blocked-beam} \quad (2.3.4.2).$$

4. Measurements of the intensity scattered by a given specimen:

The raw scattered intensity is given by:

$$I_S = C_0 T_{S+SB} \left(\left(\frac{d\Sigma(Q)}{d\Omega} \right)_{sample} + \left(\frac{d\Sigma(Q)}{d\Omega} \right)_{EMP} \right) + I_{Blocked-beam} \quad (2.3.4.3).$$

The corrected scattered intensity is given by:

$$I_{cor} = (I_S - I_{BDG}) - (T_{S+SB}/T_{SB})(I_{EMP} - I_{BDG}) \quad (2.3.4.4).$$

The corrected scattered intensity is then calibrated with the detector sensitivity:

$$I_{cal} = I_{cor} / (\text{Normalized Detector Sensitivity}) \quad (2.3.4.5).$$

Therefore:

$$I(q)_{cal} = \Phi_i AdT_{S+SB} \left(\frac{d\Sigma(Q)}{d\Omega} \right)_S \Delta\Omega\epsilon t \quad (2.3.4.6).$$

There exist several methods for obtaining $(d\Sigma(Q)/d\Omega)_S$ [85]. We used the direct beam flux method to obtain $(d\Sigma(Q)/d\Omega)_W$ for the water specimen. Then, we applied the standard sample calibration method to obtain $(d\Sigma(Q)/d\Omega)_S$ for the specimens of RAFM steels by using $(d\Sigma(Q)/d\Omega)_W$ as a reference.

- a. *Direct beam flux method:* One measures the intensity from a direct beam with nothing along the beam, to the exception of an attenuator, in order to get I_{Direct} :

$$I_{Direct} = \Phi_i AT_{atten} \Delta\Omega\epsilon t \quad (2.3.4.7).$$

$$\left(\frac{d\Sigma(Q)}{d\Omega} \right)_S = \left(\frac{I(Q)_{cal}}{I_{Direct}} \right) \frac{1}{d} \left(\frac{T_{atten.}}{T_{S+SB}} \right) \quad (2.3.4.8).$$

- b. *Standard sample calibration method:* One measures the intensity scattered by a specimen with a known absolute scattering cross-section (standard specimen), i.e., a water specimen in our case, at $\theta = 0$ and in exactly the same conditions than in the case of other specimens, in order to get I_{STD} at $\theta = 0$:

$$I_{STD} = \Phi_i Ad_{STD} T_{STD+SB} \left(\frac{d\Sigma(Q)}{d\Omega} \right)_{STD} \Delta\Omega\epsilon t \quad \text{at } \theta = 0 \quad (2.3.4.9),$$

where d_{STD} is the thickness of the standard specimen and T_{STD+SB} is the transmission factor of the standard specimen plus its container. The scattering differential cross section of the specimen to be measured, $(d\Sigma(Q)/d\Omega)_S$, is then given by:

$$\left(\frac{d\Sigma(Q)}{d\Omega} \right)_S = \left(\frac{I(Q)_{cal}}{I(Q=0)_{STD}} \right) \left(\frac{d_{STD}}{d} \right) \left(\frac{T_{STD+SB}}{T_{S+SB}} \right) \left(\frac{d\Sigma(Q=0)}{d\Omega} \right)_{STD} \quad (2.3.4.10).$$

Examples of a SANS intensity pattern and corresponding $(d\Sigma(Q)/d\Omega)_S$ values versus Q values are shown in Figure 2.3.4.1 [186]. The Q -resolution function is given by:

$$Q = \frac{4\pi}{\lambda} \sin\left(\frac{\theta}{2}\right) \approx \frac{2\pi}{\lambda} \theta \quad \text{and} \quad \left(\frac{\delta Q}{Q} \right) = \left(\frac{\delta\theta}{\theta} \right) + \left(\frac{\delta\lambda}{\lambda} \right) \quad (2.3.4.10).$$

In the above equation $\delta\theta/\theta$ refers to the accuracy of collimation, which depends on the parameters reported in Table 2.3.3.1, and on the detector resolution. The term $\delta\lambda/\lambda$ refers to the wavelength spread.

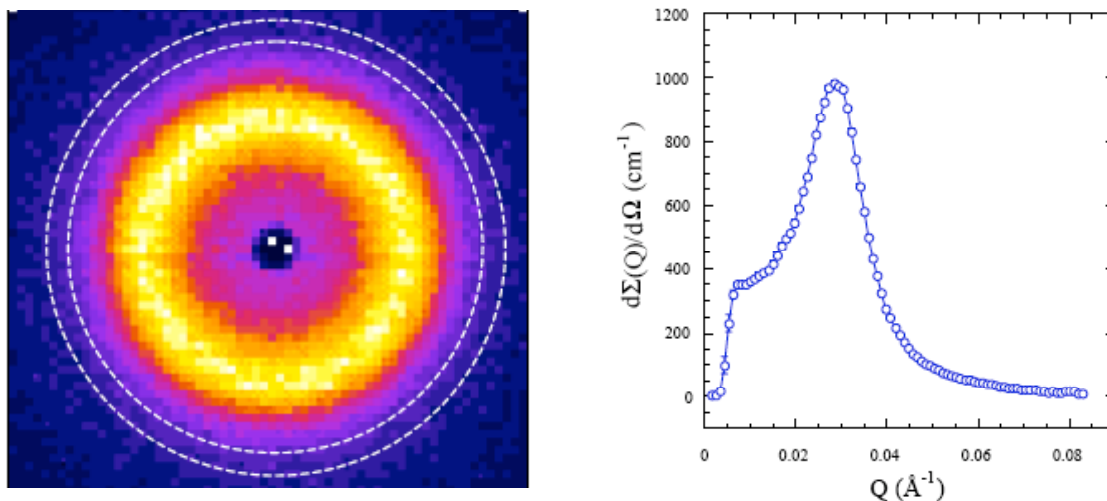


Figure 2.3.4.1: Left: intensity scattered by a specimen, as recorded by the 2D detector. Right: circularly averaged $d\Sigma(Q)/d\Omega$ values versus Q values, Q being the magnitude of the scattering vector. Each annulus on the left corresponds to a single data point on the right [186].

2.3.5 Measurement conditions

The SANS instrument is computer controlled by the SINQ instrument control software SICS [185] developed at the PSI. In practice, at the beginning of a campaign of SANS measurements on a series of specimens being part of a given specific holder, the beam was made to stay at each specimen position for about 1 minute, using a beam collimation distance of 3 m and a specimen-to-detector distance of 2 m, in order to measure the beam center position for all the specimens. Then, the transmission factor for all the specimens was measured during 5 minutes using a beam collimation distance of 18 m and a specimen-to-detector distance of 18 m. Finally, the main measurement procedure was launched to get the SANS signal from all the specimens, including all kinds of reference specimens. During this procedure, each specimen was measured three times, for 30 to 100 minutes each time, depending on the intensity of the SANS signal obtained at the occasion of the first measurement.

SANS measurements on the various specimens were performed with a neutron wavelength of $\lambda = 0.47$ nm and using a beam collimation distance of 3 m and a specimen-to-detector distance of 2 m, which allowed measurements over the Q -range $0.35 < Q < 4.7$ nm⁻¹, where Q is the scattering vector magnitude. The measurements were performed at room temperature with a horizontal, saturating magnetic field ($H = 0.6$ Tesla) applied to the specimen to be measured, using the device shown in Figure 2.3.5.1, perpendicularly to the incident neutron beam, in order to fully align the magnetic moments in the specimen. Thus, only nuclear scattering occurs in the horizontal plane, while nuclear and magnetic scattering occur in the vertical one. The purely magnetic scattering can be then obtained by calculating the difference between the vertical and horizontal macroscopic differential SANS cross sections.

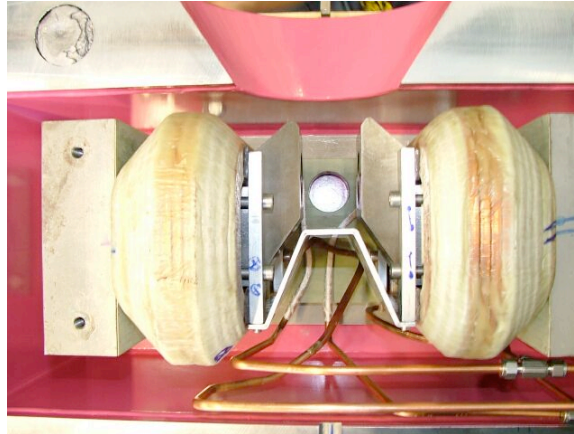


Figure 2.3.5.1: Device generating a horizontal, saturating magnetic field ($H = 0.6$ Tesla) perpendicular to the neutron beam.

2.3.6 Reduction of the raw data

The BerSANS software package from Hans-Meier Institute (HMI) in Berlin (Germany) has been used for performing raw data reduction. This software is composed of a series of programs whose functions are listed in Table 2.3.6.1.

Program	Function
SANSInit	Initialization of the BerSANS programs
SANSTrans	Calculation of the transmission factors
SANSArea	Determination of the beam center
SANSAni	Background correction and data normalization
SANSIso	Reduction to 1D spectrum
SANSIsoPlot	Plotting of 1D spectrum
corr,corr2	Projection of water file to another distance/collimation

Table 2.3.6.1: Description of BerSANS software package functions.

As described under § 2.3.4, the transmission factors for all the specimens were calculated by using the SANSTrans program of Table 2.3.6.1, and then the raw data have been corrected by first subtracting off the background and parasitic scattering and second accounting for the anisotropy of the detector by normalizing the scattered signal from a specimen of RAFM steel with the SANS signal from a water reference specimen with a known isotropic cross section, by using the SANSAni programs of Table 2.3.6.1.

In a further step, SANSAni has been also used to treat the data in order to calculate the absolute scattering cross section $d\sigma/d\Omega$. In this program the data treatment is done for each detector cell (i,j) individually. The raw intensities $I_{ij-Measured}$ were first corrected to account for the detector dead time τ by using the following formula:

$$I_{ij-Corrected} = I_{ij-Measured} \left/ 1 - \frac{\tau}{t} \sum_{i,j} I_{ij-Measured} \right. \quad (2.3.6.1).$$

In the above equation, I refers to each data type, i.e., cadmium, water, water background, specimen background, and specimen, and t is the total measurement time used for obtaining the corresponding data type. After this treatment, the intensities were normalized to the individual monitor values recorded in the data files.

In the standard case, the program calculates the absolute scattering cross section, $d\sigma/d\Omega$, from the treated and normalized intensities obtained for the data of the types cadmium (Cd), water (W), water background (WB), specimen background (SB), and specimen (S), for each cell (i,j) , according to the formula:

$$\left(\frac{d\sigma}{d\Omega} \right)_{i,j} = \frac{\left(\frac{S_{ij} - Cd_{ij}}{T_s} \right) \cdot A(S) - \left(\frac{SB_{ij} - Cd_{ij}}{T_{SB}} \right) \cdot (1 - p(S))}{\left(\frac{W_{ij} - Cd_{ij}}{T(W)} \right) - \left(\frac{WB_{ij} - Cd_{ij}}{T(WB)} \right)} \cdot \frac{ScalingFactor(W)}{ScalingFactor(S)} \quad (2.3.6.2),$$

where T parameters are the transmission factors associated with the various data types, and A ($A \geq 1$) and p ($0 \leq p \leq 1$) are the attenuation factor and the scattering probability of the specimen data type, respectively. The absolute error $\Delta(d\sigma/d\Omega)$ was calculated from the errors of the various data types, using partial derivatives of equation (2.3.6.2), according to the formula:

$$\Delta \left(\frac{d\sigma}{d\Omega} \right)_{ij} = \sqrt{\left(\frac{\partial \frac{d\sigma}{d\Omega}}{\partial Cd} \Delta Cd_{ij} \right)^2 + \left(\frac{\partial \frac{d\sigma}{d\Omega}}{\partial W} \Delta W_{ij} \right)^2 + \left(\frac{\partial \frac{d\sigma}{d\Omega}}{\partial WB} \Delta WB_{ij} \right)^2 + \left(\frac{\partial \frac{d\sigma}{d\Omega}}{\partial SB} \Delta SB_{ij} \right)^2 + \left(\frac{\partial \frac{d\sigma}{d\Omega}}{\partial S} \Delta S_{ij} \right)^2} \quad (2.3.6.3).$$

When the two-dimensional data were reduced to one-dimensional data (e.g. through spherical averaging), one needed to determine the beam center. Finally the reduced SANS 1D spectra were calculated by using the SANSIs program of Table 2.3.6.1.

2.4 Simulation tools

2.4.1 MD simulations

Interatomic potentials: MD simulations have been performed using the MDCASK code [187] with the Ackland 97 [188] and Ackland 04 [189] versions of the Finnis-Sinclair potential to describe the atomic interactions in Fe. The Ackland 97 and Ackland 04 potentials are embedded atom method (EAM) potentials developed within the Finnis-Sinclair framework. Then, the total energy of the simulation cell may be expressed using the equation (1.6.9). The Wilson-Johnson potential [190] and the Beck potential [191], which were used to describe Fe-He and He-He atomic interactions, respectively, include only pair-wise interactions. The Wilson-Johnson potential is purely repulsive and derived from Hartree-Fock-Slater (HFS) calculations using the modified Wedepohl method [190-193]. The Olsson potential [141], which was used to describe in Fe-Cr and Cr-Cr atomic interactions, is also an EAM potential developed within the Finnis-Sinclair framework. All the potentials were smoothly connected to the short-range, universal Ziegler-Biersack-Littmark (ZBL) potential [194] that is adequate at high energy (short interatomic distances). Note that these potentials were fitted to quantum physics calculation results in order to describe exactly the materials physical properties, like the lattice parameters the elastic constants, etc.

Following a common practice [195], all presented results were obtained by working in the NVT canonical ensemble with periodic boundary conditions. Ensembles refer to thermodynamic systems with certain quantities kept constant and corresponding to different physical situations. Generally, systems can be described by three quantities (a fact arising from thermodynamics). The ensembles the most often used in MD simulations include the NVE (micro-canonical), the NVT (canonical for the common laboratory condition of fixed temperature), the NPT (isothermal-isobaric for the common laboratory conditions of fixed pressure and temperature) and the μ PT (grand-canonical for the common laboratory condition of a fixed source of atoms or chemical potential) ensembles, where N , V , E , μ , P and T are the fixed atom number, volume, energy, chemical potential, pressure and temperature, respectively. Temperature control was made through boundary regions, which mimic a thermal bath. The final atomic configuration was analyzed using the Wigner-Seitz cell method (described later in this chapter) in the aim to detect and count defects. An empty cell corresponds to a vacancy and two atoms in the same cell correspond to an interstitial atom.

Integration algorithms (predictor-corrector algorithms): Predictor-corrector algorithms are commonly used for integrating the equations of motion. The fourth-order Gear predictor-corrector algorithm [196] was used in the present calculations. It includes three steps:

1. *Predictor:* From the atom positions and their time derivatives up to a certain order, q , all known at a time t , one may predict the same quantities at a time $t+\Delta t$ by means of a Taylor expansion.
2. *Force evaluation:* The force is computed using the gradient of the potential at the predicted positions. The resulting acceleration will be in general different from the predicted acceleration. The difference between the two constitutes an error signal.

3. *Corrector*: The error signal is used to correct the positions and their derivatives. All the corrections are proportional to the error signal, the coefficient of proportionality being a ‘magic number’ determined to maximize the stability of the algorithm.

As explained under § 1.6.1, the goal of MD simulations is to compute the phase-space trajectories of a set of atoms. Given the interatomic potential, the force acting on each atom is calculated. From the force value and using the Newton’s second law of motion the acceleration of each atom is determined. By integrating these equations the next atom position due to the applied force is obtained. One of the standard methods to solve these ordinary differential equations is the finite difference approach. It is based on the idea that, given a set of positions, velocities and accelerations of atoms at a time t , the positions, velocities and accelerations of atoms at a time $t+\Delta t$ can be computed, i.e., predicted, with a certain accuracy:

$$\begin{aligned} x(t+\Delta t) &= x(t) + u_1 + u_2 + u_3 \\ u_1(t+\Delta t) &= u_1(t) + 2u_2 + 3u_3 \\ u_2(t+\Delta t) &= u_2(t) + 3u_3 \\ u_3(t+\Delta t) &= u_3(t) \end{aligned} \quad (2.4.1.1),$$

where $x(t)$ = coordinate, $u_1 = x'(t) \Delta t$, $u_2 = (1/2) x''(t) \Delta t^2$, and $u_3 = (1/6) x'''(t) \Delta t^3$, Δt being the time step. The correct atom trajectories cannot be obtained using these predicted values, as the equations of motion were not accounted for. However, using the predicted values of the atom positions at a time $t+\Delta t$ the new values of acceleration can be calculated and compared to the calculated ones just above to estimate the error in the predicted values.

$$\phi = \left(\frac{1}{2} \right) \left(\frac{F}{m} \right) (\Delta t)^2 - u(t+\Delta t) \quad (2.4.1.2).$$

Using the error value the predicted values of positions, etc., can be then corrected:

$$\begin{aligned} x^c(t+\Delta t) &= x(t+\Delta t) + c_0 \phi \\ u_{1c}(t+\Delta t) &= u_1(t+\Delta t) + c_1 \phi \\ u_{2c}(t+\Delta t) &= u_2(t+\Delta t) + c_2 \phi \\ u_{3c}(t+\Delta t) &= u_3(t+\Delta t) \end{aligned} \quad (2.4.1.3).$$

The coefficients c_0 , c_1 , and c_2 were calculated by Gear [196]. The values depend on the number of derivatives included and the order of the differential equation being solved. For example, in the case of the predictor-correction algorithm of 4th order presented just above, the values of the coefficients are: $c_0 = 19/120$, $c_1 = 3/4$, $c_2 = 1$, $c_3 = 1/2$, and $c_4 = 1/12$. This type of algorithm is called a predictor-corrector algorithm. The MD procedure that is based on the use of this algorithm then consists in:

1. Predicting the atom positions, velocities and accelerations at a time $t+\Delta t$,
2. Evaluating the forces required for obtaining the new atom positions,
3. Correcting the predicted atom positions using the new acceleration values.

Boundary conditions: Even with the most powerful computers only a small number of atoms can be followed using MD simulations. In addition, the atoms on the surfaces of the simulation box will experience very different forces than those present inside the bulk. In many situations it is important to avoid surface effects on the variables computed. In order to solve that problem, in the present work it was chosen to immerse the system into an infinite medium. This was achieved using periodic boundary conditions. This method consists in making infinite replicas of the original simulation box. Implementation is very simple: the atoms leaving the simulation box re-enter the box on its opposite side.

As shown in Figure 2.4.1.1, the central box is the original simulation box and the surrounding boxes are replicas of it. When an atom leaves the simulation box on the one side of it, one of its images re-enters the box on the other side, keeping always the total number of atoms constant in the central box. At the same time, when energies or forces acting on each atom are computed, the periodic images must be taken into account.

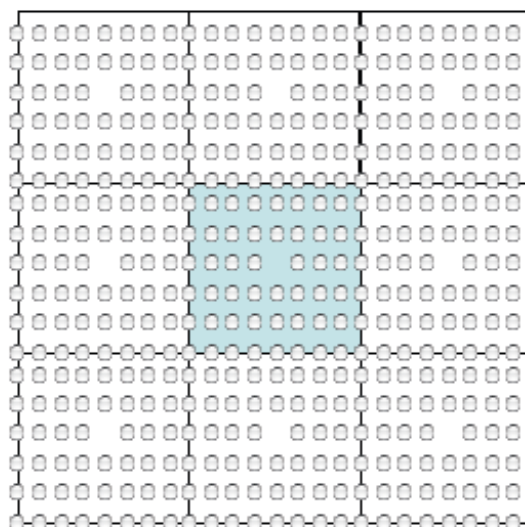


Figure 2.4.1.1: Schematic illustration of periodic boundary conditions for a simulation box.

When a short-range interatomic potential is used, a cut-off radius is defined such that for distances far larger than the cut-off radius the interaction between atoms is zero. Therefore, the idea of periodic boundary conditions can be used to compute the interactions between the atoms in the central simulation box and all the surrounding images. This is done using the minimum image convention: each atom interacts only with atoms in a region equal in size to the main simulation box and centered around that atom. When the interatomic potential is not a short-range one, this approximation cannot be used and the total contribution of all images must be included. This is the case of Coulomb-type interatomic potentials.

It is important to understand the limits of this approximation. When using short-range potentials the dimensions of the simulation box can be set such that a given atom does not feel the presence of its periodic image. However, in the case of long-range interatomic potentials, this is not true. Periodicity can be also a problem for modeling amorphous systems

and inhibits the occurrence of long wavelength fluctuations. If the side length of the simulation box is equal to L , no density waves with a wavelength larger than L will exist. However, periodic boundary conditions are still appropriate for short-range interactions and equilibrium thermodynamic properties. Repeating the simulations for different box sizes may provide an assessment of the validity of periodicity.

Neighbor lists: In order to compute the forces acting over a set of N atoms, one has to account for the j neighbors of each atom i being part of the N atoms. In that case, if the distance between two atoms is smaller than the cut-off radius of the interatomic potential, one has to go to the next atom. This implies a total of N^2 calculations. There are techniques to improve the calculation of the neighbors of each atom in the case of short-range interatomic potentials, where a cut-off radius for the interaction is well defined. One of these algorithms is the ‘link cell list’. This method consists in computing a set of cells on the top of the simulation box, with dimensions such that the side length of these link cells are as close as possible to the cut-off radius of the interatomic potential. Once these cells are defined, the number of neighbors of a given atom is obtained by taking into account only the atoms inside its link cell and those in the nearest neighbor link cells. For example, in Figure 2.4.1.2 a system is divided into 25 cells. In order to find the neighbors of atoms located inside cell **13**, one should look only at those located inside cells **7, 8, 9, 12, 14, 17, 18, and 19** and inside the cell **13**. By using this method in three dimensions $27 \cdot N \cdot N_c$ interactions have to be computed, where N_c is the number of atoms in each cell. The number of calculations is reduced significantly by this way.

21	22	23	24	25
16	17	18	19	20
11	12	13	14	15
6	7	8	9	10
1	2	3	4	5

Figure 2.4.1.2: Example of a link cell map: eight neighbor cells (**7, 8, 9, 12, 14, 17, 18, 19**) have to be accounted for around cell **13**.

Common neighbor analysis method: The method of common neighbor analysis [197] was employed to characterize local atomic environments inside the defect clusters. This code calculates the number of vacancies, interstitial atoms and replacement atoms by using the Wigner-Seitz cell for fcc and bcc lattices. The nearest neighbors of a given atom are those that are closer to it than an appropriately chosen distance, r_c , taken from the Wigner-Seitz cell, midway between the nearest and next-nearest neighbor shells. Results from such an

analysis are insensitive to the precise value of r_c . One speaks of each pair of nearest neighbor atoms as being bonded and being connected by a bond, but this merely denotes a geometrical relationship and not a chemical one. Each of a bond's two atoms has a set of nearest neighbors, the intersection of these two sets including the neighbors that the two atoms have in common. The bond can be characterized by examining this set of common neighbors and specifying three numbers: the total number of atoms inside the set, the total number of bonds between atoms inside the set, and the number of bonds inside the largest continuously bonded subset. While, in general, a given bond type may correspond to more than one possible common-neighbor configuration, this problem was not part of the present work.

Simulation conditions:

(1) MD calculations were performed to investigate the damage produced by atomic displacement cascades in pure Fe and in Fe containing either 0.1 or 1 at.% He uniformly and randomly distributed in either interstitial or substitutional sites. The interatomic potentials employed were the Ackland 97 potential [188], the Wilson-Johnson potential [190] and the Beck potential [191] to describe Fe-Fe, Fe-He and He-He atomic interactions, respectively. Prior to the cascade, a simulation box containing 0, 0.1 or 1.0 at.% interstitial or substitutional He in a uniform random distribution was equilibrated for 0.4-1.3 ps at the chosen temperature. Each cascade was realized in imparting a specified kinetic energy, E_{MD} , to the selected PKA along a high-index crystallographic direction to avoid channeling. Each cascade was followed by a defect and cluster analysis using the tool described just above. Simulation conditions for atomic displacement cascades are summarized in Table 2.4.1.1.

Sample types	He sites	Temperature (K)	E_{MD} (keV)	Time (ps)	Box size (nm ³)
Fe, Fe-0.1He, Fe-1.0He	Substitutional, Interstitial	10, 300, 523	3, 5, 7, 10	25	18×18×18 10×10×80*

Table 2.4.1.1: Summary of MD simulation conditions for atomic displacement cascades in pure Fe, Fe-0.1 at.% He and Fe-1.0 at.% He with He either in interstitial or substitutional positions. * The cell size and orientation were fitted to the TEM image simulation conditions.

(2) The most commonly observed interstitial dislocation loops (I-loops) in α -Fe using TEM were created by means of MD simulations. MD simulations were performed using the moldy code [187] with the Ackland 97 [188] version of the Finnis-Sinclair empirical potential to describe the Fe-Fe atomic interactions. The simulation cell was created with the I-loop located at different depths corresponding respectively to a zone close to the surface, at a quarter of the depth and in the middle of the foil. The procedure to create I-loops was the following: (1) $1/2 a_0 \langle 111 \rangle \{110\}$ and $1/2 a_0 \langle 110 \rangle \{110\}$ loops were generated by inserting one platelet of atoms, with a circular shape and a diameter of 1 or 2 nm, in between two adjacent $\{110\}$ planes. This allowed us obtaining the appropriate Burgers vector of $\mathbf{b} = 1/2 a_0 \langle 110 \rangle$ or $\mathbf{b} = 1/2 a_0 \langle 111 \rangle$; (2) $a_0 \langle 100 \rangle \{100\}$ I-loops were generated by inserting two consecutive platelets of atoms, with a circular shape and a diameter of 2 nm, in between two adjacent $\{100\}$ planes. Since the unit cell of a bcc structure has a stacking sequence of the type 'ABAB' along the $\langle 100 \rangle$ direction, the introduction of two consecutive $\{100\}$ planes ensures that the normal stacking sequence is conserved. After having inserted the

platelets of atoms the simulation cell was equilibrated by performing a conjugate-gradient relaxation. Simulation conditions for I-loops are summarized in Table 2.4.1.2.

Burgers vector b	Habit plane	Loop diameter (nm)	Box size (nm ³)
$a_0 \langle 100 \rangle$	$\{100\}$	2.0	10×10×80, 23×23×23**
$1/2 a_0 \langle 110 \rangle$	$\{110\}$	1.0, 2.0	10×10×80
$1/2 a_0 \langle 111 \rangle$	$\{110\}$	2.0	10×10×80

Table 2.4.1.2: Summary of MD simulation conditions for I-loops in α -Fe. Note that all the cell sizes and orientations were fitted to the TEM image simulation conditions, except ** that was fitted to the SANS signal simulation conditions.

(3) Cavities (voids and helium bubbles) were also created in α -Fe by MD simulations. The interatomic potentials employed were the Ackland 97 potential [188], the Wilson-Johnson potential [190] and the Beck potential [191] to describe Fe-Fe, Fe-He and He-He atomic interactions, respectively. The cavities had a spherical shape and a diameter of 2.0 nm. The procedure to create such nano-sized cavities was the following: (1) the void was created by removing a certain number of atoms in the central part of the simulation cell; (2) the helium bubble was created by replacing a certain number of Fe atoms by helium atoms in the central part of the simulation cell. After having applied such a procedure the simulation cell was equilibrated by performing a conjugate-gradient relaxation. Simulation conditions for cavities are summarized in Table 2.4.1.3.

Cavity type	Ratio of He/vacancy	Cavity diameter (nm)	Box size (nm ³)
Void	0	2.0	10×10×80, 23×23×23**
He bubble	0.5, 1, 2, 3	2.0	10×10×80, 23×23×23**

Table 2.4.1.3: Summary of MD simulation conditions for cavities in α -Fe. Note that all the cell sizes and orientations were fitted to the TEM image simulation conditions, except ** that were fitted to the SANS signal simulation conditions.

(4) Cr precipitates were also created in α -Fe by MD simulations. The interatomic potentials employed were the Ackland 04 potential [189] and the Olsson potential [141] to describe Fe-Fe and Fe-Cr and Cr-Cr atomic interactions, respectively. The Cr precipitates had a spherical shape and a diameter of 2.0 nm. Such nano-sized Cr precipitates were created by replacing a certain number of Fe atoms by Cr atoms in the central part of the simulation cell. After having applied such a procedure the simulation cell was equilibrated by performing a conjugate-gradient relaxation. Simulation conditions for Cr precipitates are summarized in Table 2.4.1.4.

Defect type	Ratio of Cr/vacancy	Precipitate diameter (nm)	Box size (nm ³)
Cr precipitates	1	2.0	10×10×80, 23×23×23 ^{**}

Table 2.4.1.4: Summary of MD simulation conditions for Cr precipitates in α -Fe. Note that all the cell sizes and orientations were fitted to the TEM image simulation conditions, except ** that was fitted to the SANS signal simulation conditions.

2.4.2 TEM image simulations

Simulations of TEM images were achieved by using the Electron Microscopy Software (EMS) developed by P.A. Stadelmann [198]. The scattering wave function Ψ for electrons may be expressed as:

$$\psi = Ae^{i\varphi} \sum_i f_i(\vec{q}) e^{-2\pi i \vec{q} \cdot \vec{R}_i} \quad (2.4.2.1),$$

where f_i is the electron scattering factor of atom i , which depends on \vec{q} , the wave vector transfer (diffraction vector) defined by $\vec{q} = \vec{k} - \vec{k}'$, R_i is the distance from the scattering center (or atom) i , and φ is the phase factor, as illustrated in Figure 2.4.2.1.

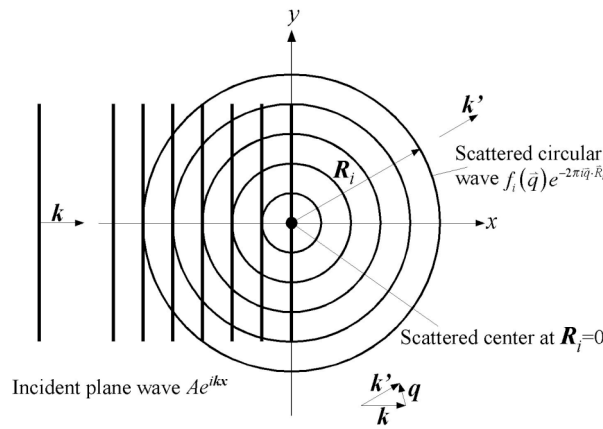


Figure 2.4.2.1: Illustration of electron scattering by a single atom [82].

The multislice method [199] was also used that is illustrated in Figure 2.4.2.2. In this method the sample created by MD simulations is cut into n slices, and the electron wave propagates from one slice to the next one such that:

$$\psi_i(\vec{r}) = [\psi_{i-1}(\vec{r}) \cdot q_i] \times p_{i \rightarrow i+1} \quad (2.4.2.2),$$

where $\Psi_i(\vec{r})$ is the wave function entering the slice $i+1$, q_i is the transmission function of the slice i , and $p_{i \rightarrow i+1}$ is the function of propagation (propagator) from the slice i to the slice $i+1$ [199].

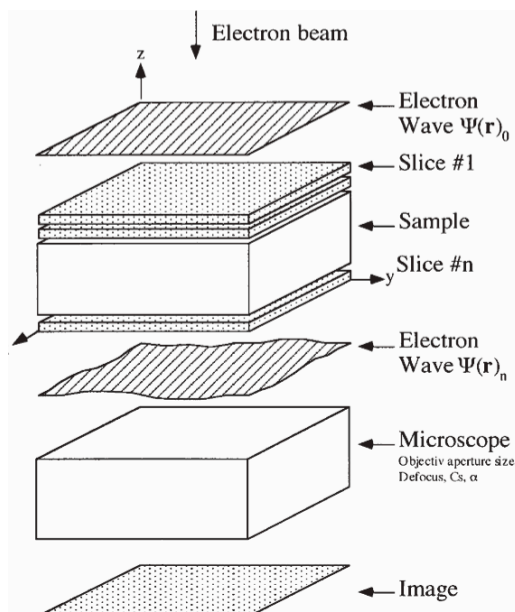


Figure 2.4.2.2: Illustration of the multislice method.

In practice, the sample created by MD simulations was cut perpendicular to the electron beam direction, z , in a certain number of 0.2 nm-thick slices. The sampling for slices was chosen in all cases to be 1024×1024 . As the multislice method is based on Fourier transforms the slices have to be periodic, i.e., of the same thickness, in the cut plane. In order to comply with this rule, the cutting direction was chosen to be a crystallographic direction. The diffraction condition was selected via the choice of the electron beam direction, which is also the cutting direction, in order to isolate the systematic row containing the desired diffraction vector, \mathbf{g} . For optimal TEM imaging using diffraction contrast, a single systematic row of diffraction vectors should be highlighted. The use of a crystallographic direction as cutting direction introduces secondary families of diffracting vectors that may disturb the TEM image contrast. In order to reduce the amount of these secondary systematic rows, relatively high order crystallographic directions are usually selected. It should be noted that one of the advantages of the use of the multislice approach over the classical beam calculation, which uses the defect displacement field described within the framework of the elasticity of the continuum (see for instance [200]), is that it allows one to avoid the deformable ion approximation [201] that may be detrimental for defects as small as the ones that are considered here. In addition, the multislice technique allows avoiding the column approximation that is generally used in classical two- or many-beam calculations. The parameters that were used to simulate TEM images of defects are close to those of modern microscopes, which usually are operated at an acceleration voltage of 200 kV. The beam semi-convergence, the defocus spread and the spherical aberration of the TEM were set to zero in order to avoid extraneous effects from parameters that are generally not controlled in the TEM imaging mode based on diffraction contrast. In addition, absorption (both normal and anomalous) was not considered. For instance, in the case of a MD sample containing a $a_0 \langle 100 \rangle \{100\}$ I-loop, the following TEM image simulation conditions have been used:

- $\mathbf{g} \cdot \mathbf{b} \neq 0$, $\mathbf{g} \cdot \mathbf{z} = 0$, $\theta \cong 90^\circ$ (angle between \mathbf{b} and \mathbf{z}).
- The sample created by MD simulations was cut into 402 slices perpendicular to the \mathbf{z} direction. The slices were roughly square, each one having a side length of 10 nm and a thickness of 0.2 nm and containing approximately 2000 atoms.
- The dislocation loop was imaged edge-on using the $\mathbf{g}(4.1\mathbf{g})$ weak beam TEM diffraction condition, with $\mathbf{g} = (200)$, and assuming 200 keV electrons.

TEM images of all the defects created by MD simulations have been simulated. The defects considered included atomic displacement cascade damage, interstitial dislocation loops, voids, He bubbles and Cr precipitates. An objective aperture size of 2.5 nm^{-1} was used for all TEM image simulations. Other TEM image simulation conditions for the various types of defects are reported in Table 2.4.2.1.

Defect type	I-loop		Others*
Sample thickness (nm)	40, 80	80	80
Electron beam direction \mathbf{z}	[015]	[-115]	[015]
Diffraction conditions	$\mathbf{g}(4.1\mathbf{g})$, $\mathbf{g}(3.1\mathbf{g})$, $\mathbf{g}(2.1\mathbf{g})$, $\mathbf{g}(1.3\mathbf{g})$	$\mathbf{g}(4.1\mathbf{g})$, $\mathbf{g}(3.1\mathbf{g})$, $\mathbf{g}(2.1\mathbf{g})$, $\mathbf{g}(1.3\mathbf{g})$	$\mathbf{g}(4.1\mathbf{g})$, $\mathbf{g}(2.1\mathbf{g})$
Diffraction vector \mathbf{g}	(200)	(110)	(200)
Deviation parameter to the Ewald sphere (nm^{-1})	0.18313, 0.12208, 0.061042, 0.018313	0.091565, 0.061043, 0.030522 0.0091565	0.18313, 0.061042
Effective extinction distance (nm)	5.4323, 8.0962, 15.660, 38.158	10.469, 14.964, 24.462, 34.850	5.4323, 15.660
Number of slices	200, 400	400	400
Slice dimensions (nm^2)	10×10	10×10	10×10

Table 2.4.2.1: TEM image simulation conditions for the simulated defects. Others* refer to displacement cascade damage, voids, He bubbles and Cr precipitates.

2.4.3 SANS signal simulations

The original EMS software, which was developed for electrons, had to be modified to account for neutrons instead of electrons. Then, the modified EMS software was used for simulating the SANS signal of structural defects. The scattering wave function for neutrons is given by:

$$\psi = A e^{i\varphi} \sum_i \frac{b_c^i}{R_i} e^{-2i\pi\vec{q} \cdot \vec{R}_i} \quad (2.4.3.1),$$

where b_c^i is the neutron scattering length of the atom i . Contrary to the case of electrons, the neutron scattering length is constant for a given atomic species, as reported in Table 2.3.1.1.

Neutron diffraction patterns obtained using the modified EMS software appear composed of diffraction spots with different intensities (Figure 2.4.3.1). To identify these diffraction spots, one has to know the neutron beam direction (zone axis) and the direction normal to the simulated cell (foil normal). To obtain the neutron scattering intensity provided by a polycrystalline sample (Figure 2.3.4.1), which depends only on the distance from the centre

of the diffraction pattern, the intensities of the diffraction spots located inside rings were summed, as illustrated in Figure 2.4.3.1. Two methods were used: either the ring area was chosen constant or the circle diameter was increased linearly. In the latter case the summed intensity was then normalized to the area of the ring. Results from the two different ring constructions were found very similar. So, linear increment of the circle diameter was finally used. A Fortran77 program was written for performing such calculations (see APPENDIX).

In fact, this procedure corresponds to the rotation of a singly crystalline sample by an arbitrary angle around the incident neutron beam. In this manner all different grain orientations in a polycrystalline sample are accounted for. However, the incident beam direction is still fixed. To even better simulate a polycrystalline sample, various orientations of the incident neutron beam have to be considered. In the present work, the sample orientations (001), (012), (011) and (043) have been used, and the obtained intensity was averaged. The resulting SANS pattern is then comparable to the experimental one.

In this work, the SANS signal of all the defects created by MD simulations has been simulated. The defects considered included atomic displacement cascade damage, interstitial dislocation loops, voids, helium bubbles and Cr precipitates. The SANS signal simulation conditions that were used for the various types of defects are the following:

- Neutron wavelength = 0.45 nm.
- Diffraction length = 2000 mm, which represent the specimen-to-detector distance as described under § 2.3.3.
- Area to record the diffraction spots = $150 \times 150 \text{ cm}^2$, which represents the sensitive area as described under § 2.3.3.
- Pixel size = $7.5 \times 7.5 \text{ mm}^2$.
- The equation (2.3.3.1) was used to calculate the wave vector transfer, q , which represents the momentum transfer as described under § 2.3.3.

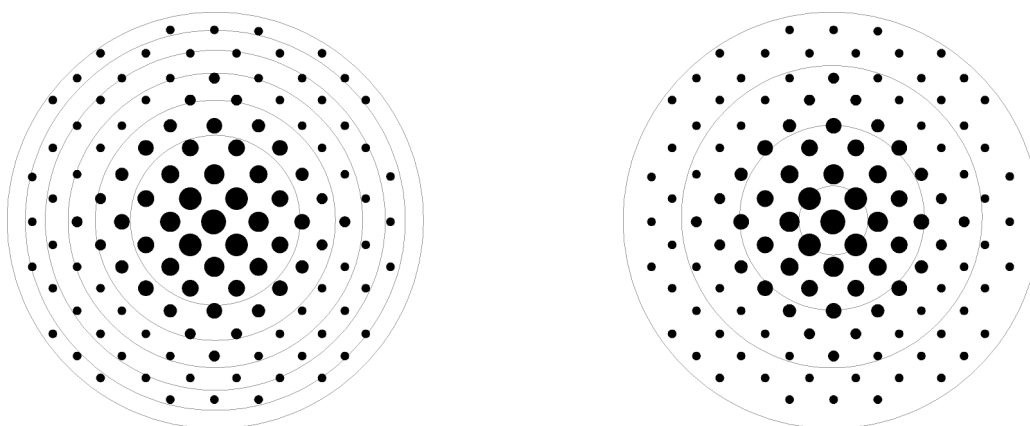


Figure 2.4.3.1: Neutron diffraction patterns of a perfect sample of pure Fe, obtained using the modified EMS program. Left: rings of the same area. Right: rings with linear increment of their diameter. Neutron wavelength = 0.45 nm, diffraction length = 2000 mm, zone axis = [001], foil normal = [001].

CHAPTER 3: RESULTS

3.1 SANS experiments

All SANS spectra presented below refer to *corrected* SANS intensities, in the sense that the raw data counts on the detector were corrected by subtracting off the background and the parasitic scattering and by accounting for the anisotropy of the detector by normalizing the corrected scattered signal with the measurement obtained from a water reference specimen with a known isotropic cross-section. For more details, see § 2.3.4.

3.1.1 Examples of SANS spectra

Typical SANS spectra, i.e., SANS intensities versus scattering vector Q values, which were obtained for an unirradiated specimen of the OPTIMAX A RA FM steel and a specimen of the OPTIMAX A RA FM steel irradiated at 50°C to 0.3 dpa are shown in Figure 3.1.1. It can be seen that the SANS intensity decreases with increasing Q values, Q being the magnitude of the scattering vector, for both types of specimen. In addition, it appears that a significant additional scattered intensity, with respect to the unirradiated specimen, is measured for the irradiated one for Q values larger than about 0.7 nm⁻¹. This additional scattered intensity arises from the irradiation-induced defect microstructure.

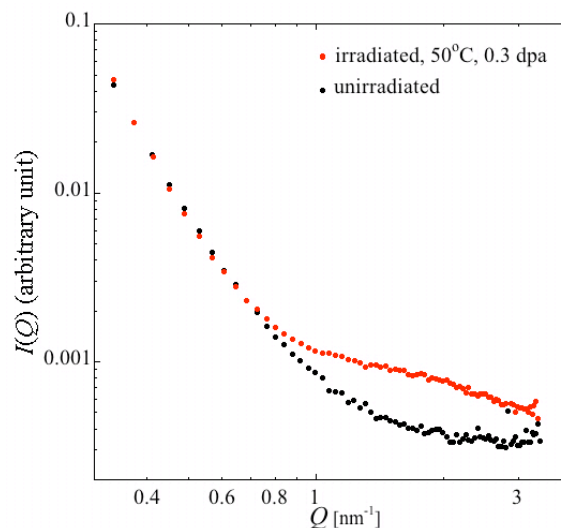


Figure 3.1.1: Examples of SANS spectra for an unirradiated specimen of OPTIMAX A and a specimen of OPTIMAX A irradiated at 50°C to 0.3 dpa

3.1.2 Effects of irradiation dose

F82H RAFM steel

The SANS spectra obtained for an unirradiated specimen of the F82H RAFM steel and two specimens of the F82H RAFM steel irradiated at about 50°C to two different doses of about 0.3 and 1.47 dpa are shown in Figure 3.1.2.1. As in the case of the OPTIMAX A RAFM steel, it can be seen that the SANS intensity decreases with increasing Q values and that a significant additional scattering intensity, with respect to the unirradiated specimen, is measured for the irradiated specimens for Q values larger than about 0.7 nm⁻¹. This additional scattered intensity increases with irradiation dose. However, the amount of increase tends to decrease with increasing irradiation dose.

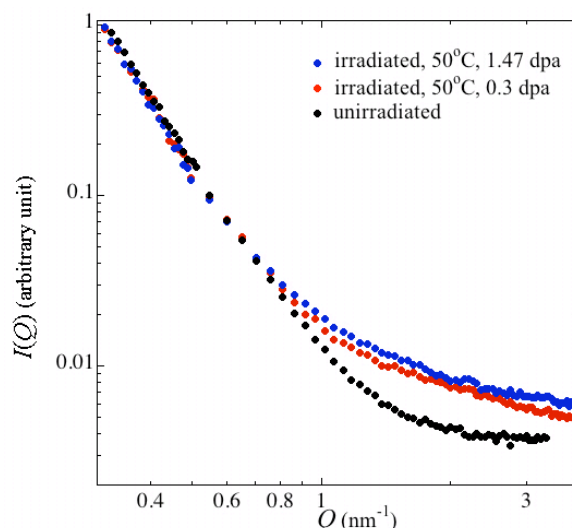


Figure 3.1.2.1: SANS spectra for an unirradiated specimen of F82H and specimens of F82H irradiated at about 50°C to about 0.3 and 1.47 dpa.

EUROFER 97 RAFM steel

The SANS spectra obtained for unirradiated specimens of the EUROFER 97 RAFM steel and three specimens of the EUROFER 97 RAFM steel irradiated at about 50°C, 250°C or 350°C to three different doses of about 0.3, 1.0 or 2.0 dpa are shown in Figure 3.1.2.2. As in the case of the OPTIMAX A and F82H RAFM steels, it can be seen that the SANS intensity decreases with increasing Q values and that a significant additional scattered intensity, with respect to the unirradiated specimen, is measured for the irradiated specimens. The effects of irradiation dose appear strongly dependent on the irradiation temperature.

- At 50°C, the SANS intensity clearly increases with irradiation dose. This phenomenon takes place for Q values above about 0.6 nm⁻¹ in the case of the smallest dose of 0.3 dpa, while it takes place over the whole Q -range investigated in the case of the doses of 1.0 and 2.0 dpa. However, like in the case of the F82H RAFM steel, the amount of increase tends to decrease with increasing irradiation dose, at least at large Q values. The fact that

the additional scattered intensity extends over different Q -ranges, depending on the dose, indicates that larger defects are also present at higher doses, with respect to those present at the smallest one.

- At 250°C, the scattered intensity still clearly increases with irradiation dose. However, this effect is much less marked than at 50°C. The additional scattered intensity takes place for Q values above about 0.6 nm⁻¹, whatever the irradiation dose.
- At 350°C, one observes no significant effects of dose on the scattered intensity, although the scattered intensity of irradiated specimens appears slightly larger than that of the unirradiated specimen at very large Q values.

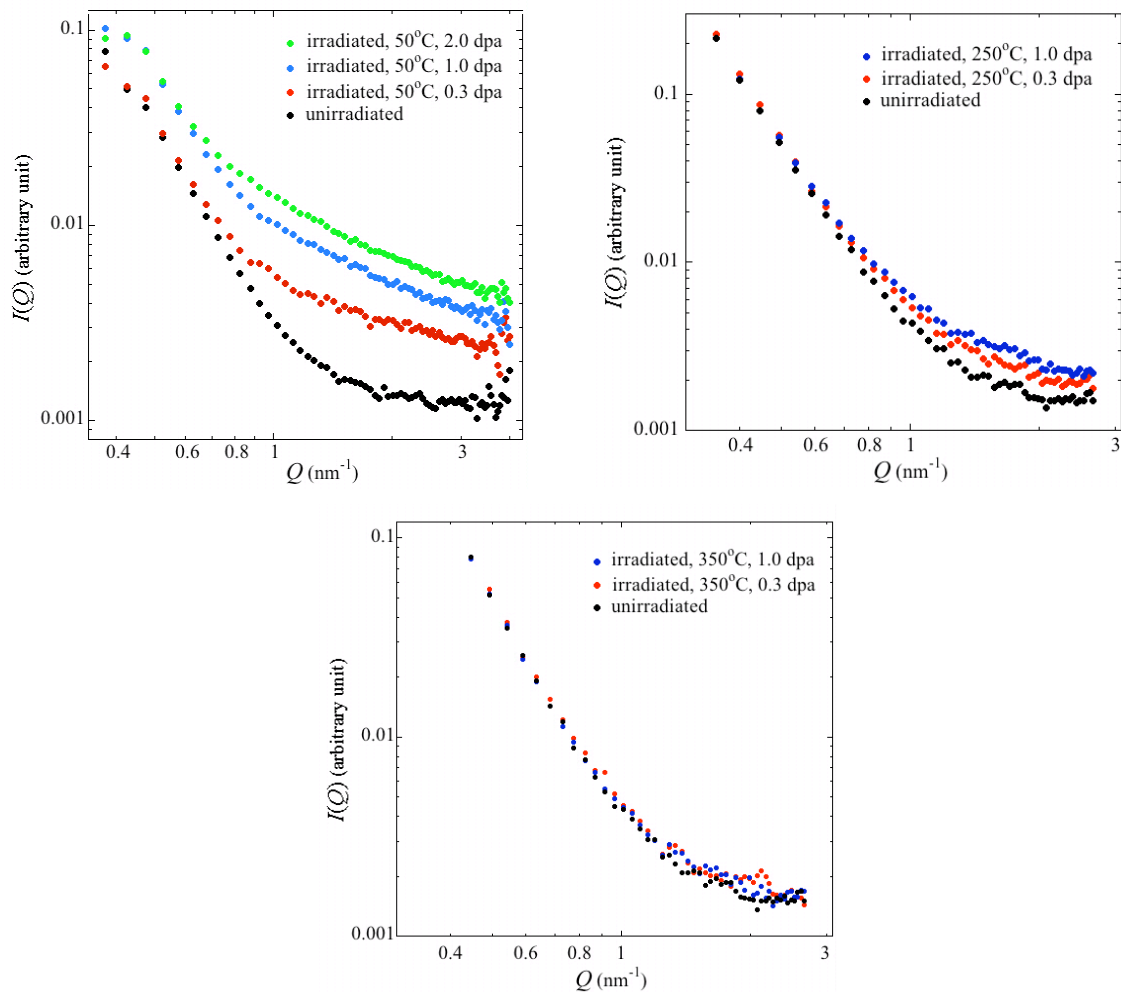


Figure 3.1.2.2: SANS spectra for unirradiated specimens of EUROFER 97 and specimens of EUROFER 97 irradiated at about 50, 250, 350°C to about 0.3, 1.0 and 2.0 dpa.

3.1.3 Effects of irradiation temperature

The SANS spectra obtained for unirradiated specimens of the EUROFER 97 RAFM steel and specimens of the EUROFER 97 RAFM steel irradiated at about 50°C, 250°C or 350°C to 0.3, 1.0 or 2.0 dpa are shown in Figure 3.1.3.1. It can be seen that, while the scattered intensity of irradiated specimens appears always larger than that of unirradiated specimens, this effect increasing with irradiation dose, as previously mentioned, the additional scattered intensity actually decreases with increasing irradiation temperature and tends to reach the intensity scattered by the unirradiated specimen at 350°C, at least for the two smallest doses of 0.3 and 1.0 dpa. The presence of larger irradiation-induced defects at the highest doses, in addition to the small ones evidenced at the lowest dose, is confirmed, at least at low temperatures.

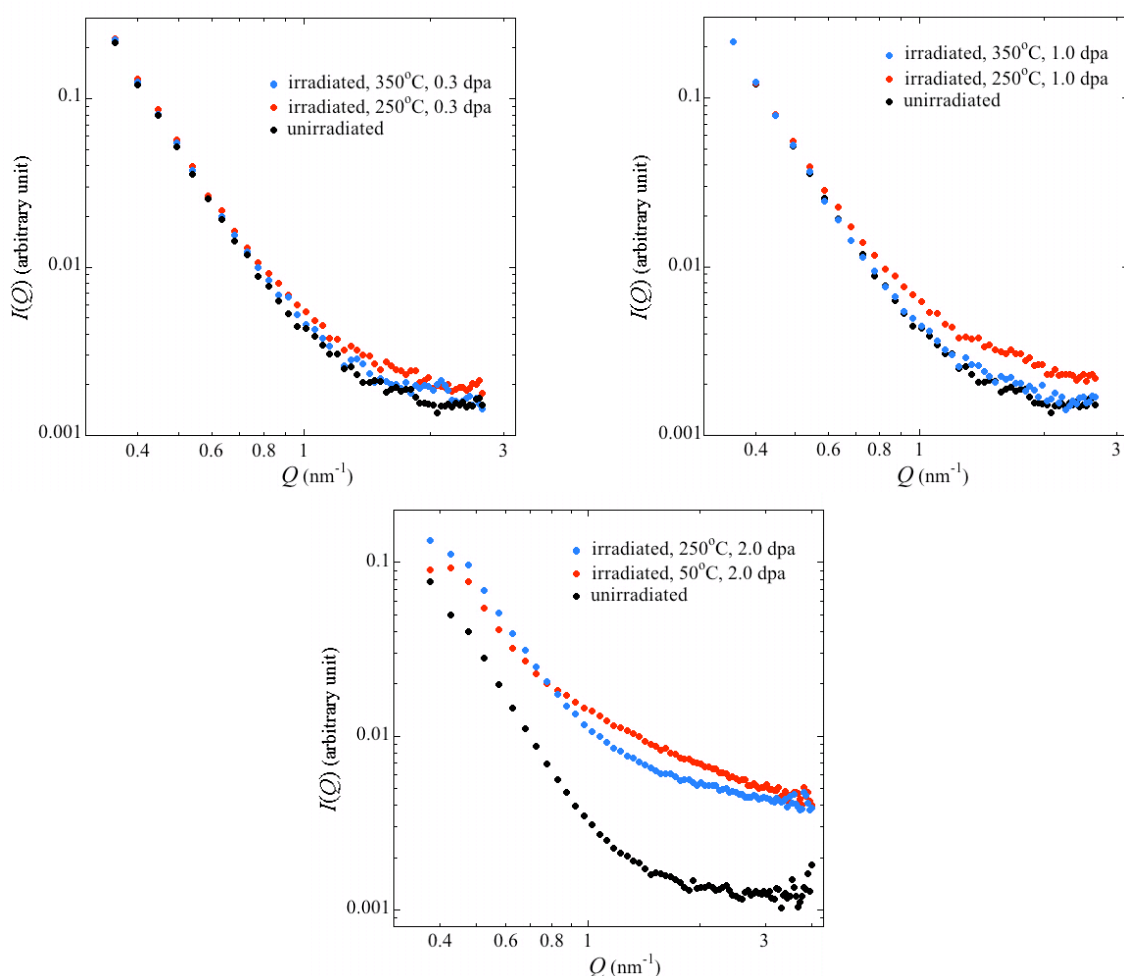


Figure 3.1.3.1: SANS spectra for unirradiated specimens of EUROFER 97 and specimens of EUROFER 97 irradiated at about 50, 250, 350°C to about 0.3, 1.0 and 2.0 dpa.

3.1.4 Analysis model for the SANS spectra

In order to characterize the size distribution of irradiation-induced scattering objects, the equation relating the differential coherent small angle cross-section, $d\Sigma/d\Omega$, which is proportional to the scattered intensity, to a dilute distribution of a single type of spherical scattering objects, was used [202]:

$$\frac{d\Sigma}{d\Omega}(Q) = \Delta\rho^2 \int N(R) V_p^2(R) P(Q, R) dR \quad (3.1.4.1),$$

where $N(R)dR$ is the number of scattering objects per unit volume having a radius between R and $R+dR$, $V_p(R)$ is the volume of a scattering object, and $P(Q, R)$ is the form factor of the scattering objects. $\Delta\rho$ is the difference between the scattering length density of the objects and that of the matrix: $\rho = b/\Omega_a$, with b being the average scattering length and Ω_a being the corresponding average atomic volume. $\Delta\rho$ is the so-called contrast.

In the following and in order to proceed with a qualitative discussion, we assume that we deal with a single distribution of spherical scattering objects. This last assumption constitutes a simplification of the more complex real distribution of different types of nano-sized irradiation-induced defects but allows assessment of the general trend of the evolution of the defect size distribution with irradiation dose and temperature. The distribution function is reflected by $N(R)$ in equation (3.1.4.1). A log-normal function is used for this distribution, which is written as:

$$N(R) = \frac{N}{\sqrt{2\pi}sR} \exp\left(-\frac{(\log(R/R_0))^2}{2s^2}\right) \quad (3.1.4.2),$$

where R_0 and s are the so-called scale and shape parameters and N is the number density. In order to better assess the evolution trend of N and R_0 with irradiation dose and temperature, a value of 0.2 for s was selected.

3.1.5 Size distribution of irradiation-induced defects

The additional scattering intensity evidenced for irradiated specimens was determined by subtracting off the scattering intensity of the unirradiated specimens to that of the irradiated ones. With the previous assumptions, it was possible to satisfactorily fit the scattered intensities of the irradiated specimens by adjusting two parameters of the log-normal distribution function, namely R_0 and N . The size distribution functions, i.e., the density (in arbitrary units) versus the radius of scattering objects, which were obtained for irradiated specimens of the three kinds of RAFM steels are reported below. Due to the non-uniqueness in the fitted parameters, the slight variations in the position of the peak at the different doses and irradiation temperatures are not necessarily representative of a specific physical mechanism of the defect accumulation. For the sake of consistency, each Figure below includes only data arising from the same irradiation campaign.

OPTIMAX A RAFM steel

The size distribution function of irradiation-induced defects in a specimen of the OPTIMAX A RAFM steel irradiated at about 50°C to a dose of about 0.3 dpa is shown in

Figure 3.1.5.1. It can be seen that the size distribution function is of Gaussian type and peaks at about 0.6 nm.

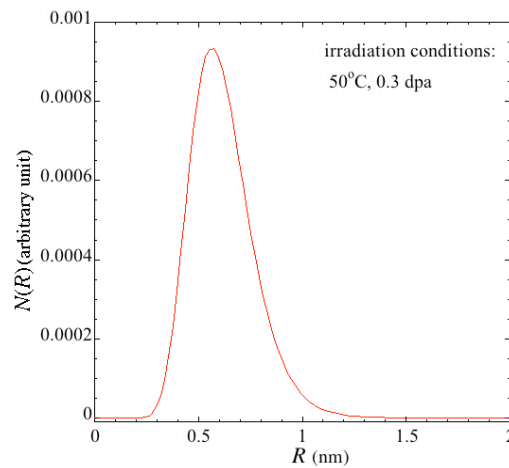


Figure 3.1.5.1: Size distribution function for the irradiation-induced defects in a specimen of the OPTIMAX A RAFM steel irradiated at about 50°C to a dose of about 0.3 dpa.

F82H RAFM steel

The size distribution function of irradiation-induced defects in two specimens of the F82H RAFM steel irradiated at about 50°C to two different doses of about 0.3 dpa and 1.47 dpa are shown in Figure 3.1.5.2. As in the case of the OPTIMAX A RAFM steel, it can be seen that the size distribution function peaks at about 0.6 nm. In addition, it appears that at the irradiation temperature of 50°C the number density of irradiation-induced defects increases strongly with irradiation dose, while the mean size of the defects remains constant.

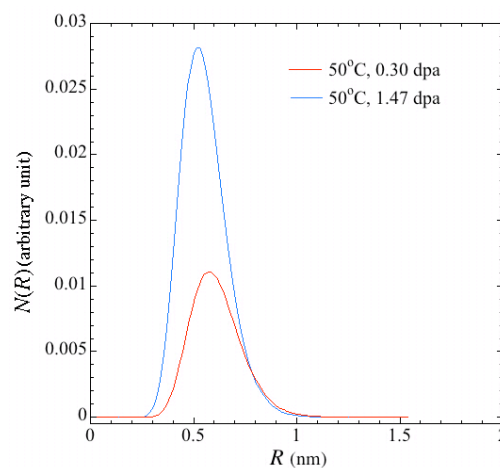


Figure 3.1.5.2: Size distribution function for the irradiation-induced defects in two specimens of the F82H RAFM steel irradiated at about 50°C to two different doses of about 0.3 and 1.47 dpa.

EUROFER 97 RAFM steel

The size distribution function of irradiation-induced defects in specimens of the EUROFER 97 RAFM steel irradiated at about 50°C, 250°C or 350°C to three different doses of about 0.3, 1.0 or 2.0 dpa are shown in Figures 3.1.5.3 and 3.1.5.4. Effects of irradiation dose are emphasized in Figure 3.1.5.3, while effects of irradiation temperature are emphasized in Figure 3.1.5.4. As in the case of the OPTIMAX A and F82H RAFM steels, a family of small irradiation-induced defects was evidenced. They behave as follows:

- The size distribution functions peak at a value below 1 nm.
- At a given irradiation temperature, the number density of irradiation-induced defects increases with the irradiation dose.
- At a given irradiation dose, the number density of irradiation-induced defects decreases with increasing the irradiation temperature, at least for the two lowest investigated dose of 0.3 and 1.0 dpa. The number density doesn't seem to vary between 50°C and 250°C for the irradiation dose of 2.0 dpa.
- The mean size of irradiation-induced defects seems to decrease with increasing the irradiation dose: for instance, for an irradiation temperature of 50°C, it is equal to about 0.4 nm at 0.3 dpa and to about 0.25 nm at 2.0 dpa.
- The mean size of irradiation-induced defects seems to increase with the irradiation temperature, at least for the two lowest investigated dose of 0.3 and 1.0 dpa: for instance, for an irradiation dose of 0.3 dpa, it is equal to about 0.4 nm at 50°C and to about 0.9 nm at 350°C. The mean size doesn't seem to vary between 50°C and 250°C for the irradiation dose of 2.0 dpa.

In addition to this family of small irradiation-induced defects, a second family of larger irradiation-induced defects was evidenced at all irradiation doses and temperatures. For the sake of clarity, the size distribution functions corresponding to this second family of defects are reported only in two plots of the Figures 3.1.5.3 and 3.1.5.4. Their characteristics are as follows:

- The height of the size distribution functions is much lower for the larger irradiation-induced defects than for the smaller ones.
- The width of the size distribution function is much larger for the larger irradiation-induced defects than for the smaller ones.
- As in the case of the smaller irradiation-induced defects, at a given irradiation temperature, the number density of the larger irradiation-induced defects increases with the irradiation dose.
- As in the case of the smaller irradiation-induced defects, at a given irradiation dose, the number density of the larger irradiation-induced defects decreases with increasing the irradiation temperature.
- As in the case of the smaller irradiation-induced defects, the mean size of the larger irradiation-induced defects seems to decrease with increasing the irradiation dose: for instance, for an irradiation temperature of 50°C, it is equal to about 1.8 nm at 1.0 dpa and to about 0.5 nm at 2.0 dpa.

- As in the case of the smaller irradiation-induced defects, the mean size of the larger irradiation-induced defects seems to increase with the irradiation temperature: for instance, for an irradiation dose of 2.0 dpa, it is equal to about 0.5 nm at 50°C and to about 1.4 nm at 250°C.

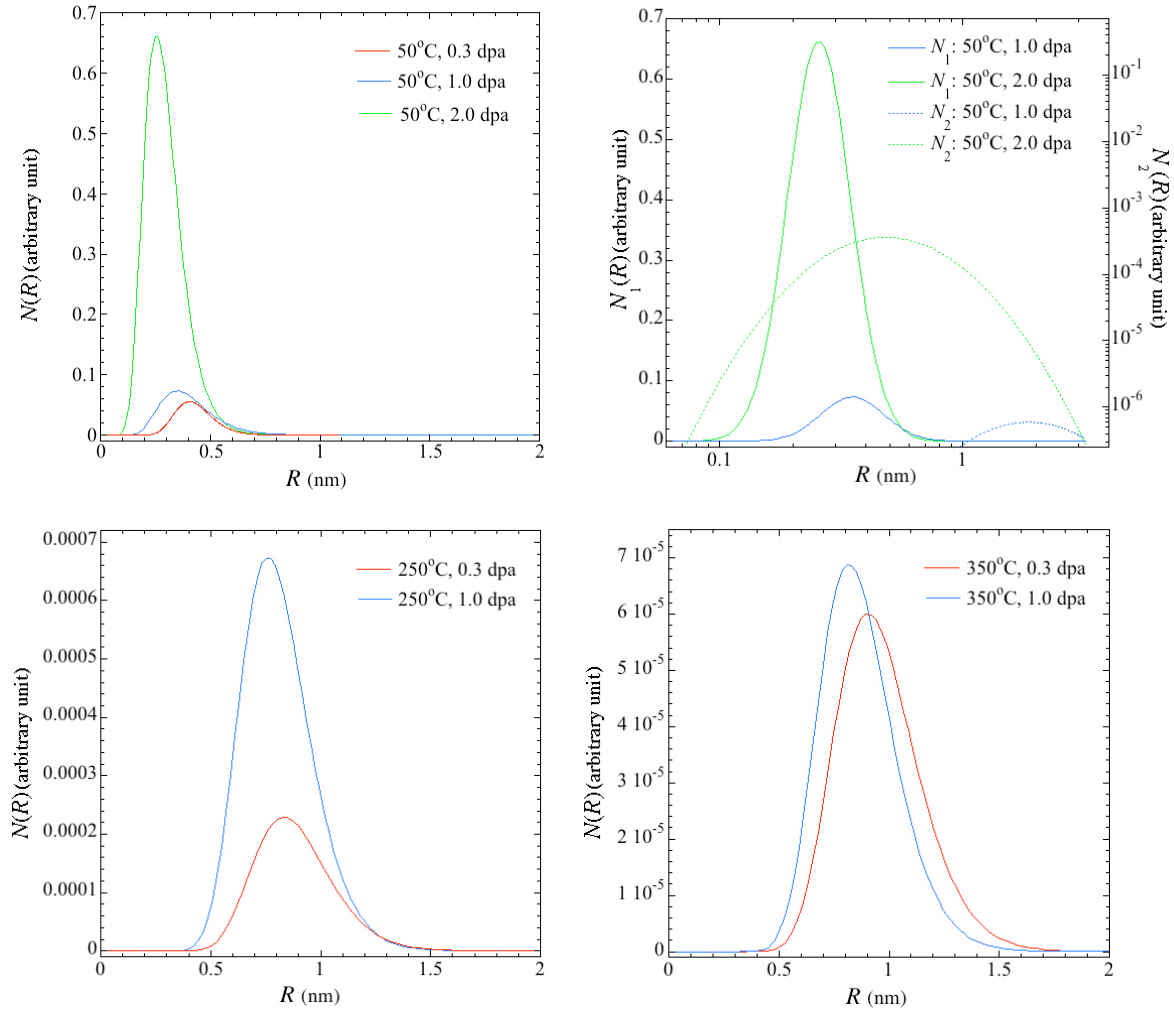


Figure 3.1.5.3: Size distribution function for the irradiation-induced defects in specimens of the EUROFER 97 RAFM steel irradiated at about 50°C, 250°C or 350°C to doses of about 0.3, 1.0 or 2.0 dpa.

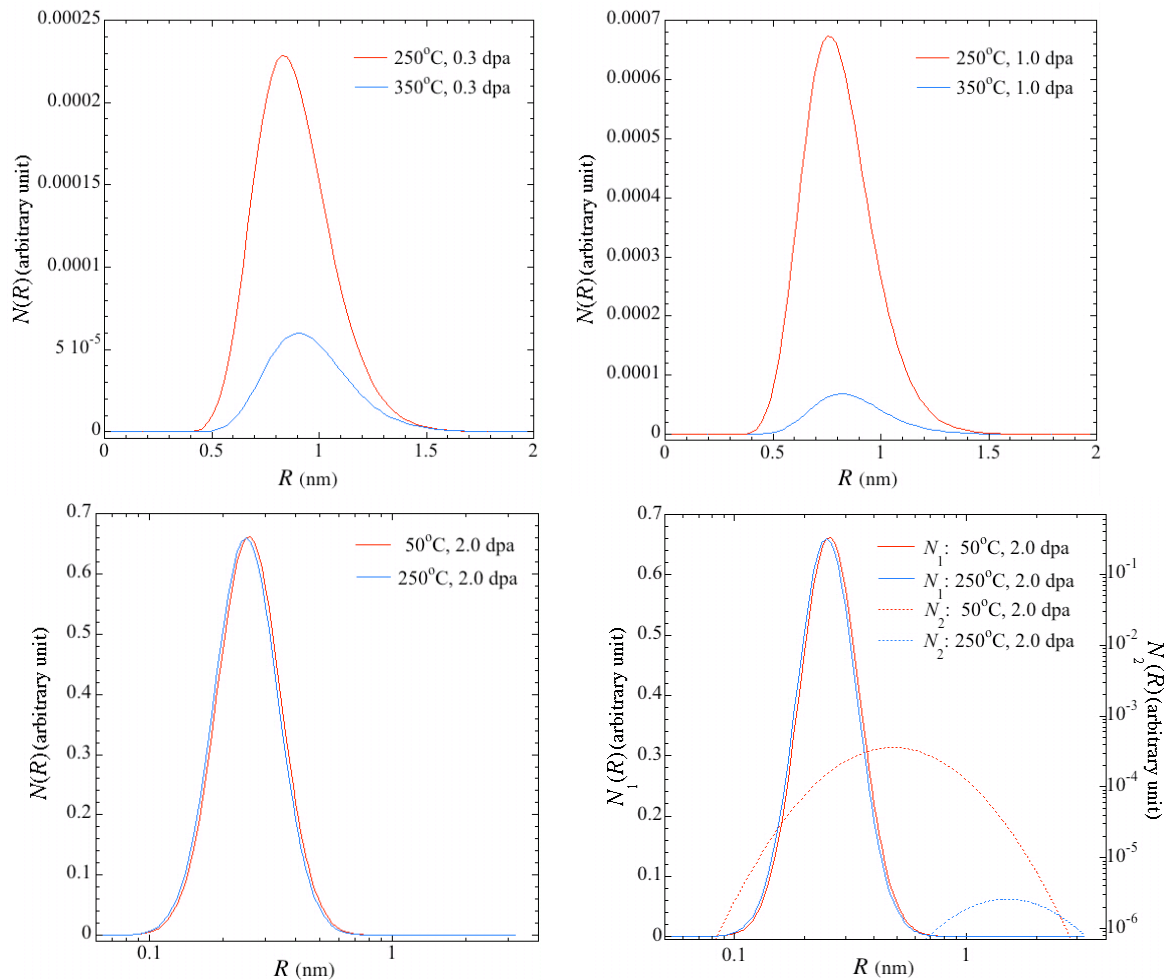


Figure 3.1.5.4: Size distribution function for the irradiation-induced defects in specimens of the EUROFER 97 RAFM steel irradiated to doses of about 0.3, 1.0 or 2.0 dpa at about 50°C, 250°C or 350°C.

The dose and temperature dependence of the number density and mean size (mean radius) of the smaller irradiation-induced defects evidenced in specimens of the EUROFER 97 RAFM steel irradiated at about 50°C, 250°C or 350°C to three different doses of about 0.3, 1.0 or 2.0 dpa are summarized in Figures 3.1.5.5 and 3.1.5.6, respectively. Four main general tendencies can be extracted from these Figures:

1. The number density increases with irradiation dose
2. The number density decreases with increasing irradiation temperature
3. The mean size decreases with increasing irradiation dose
4. The mean size increases with irradiation temperature

However, these tendencies may more or less strongly differ depending on the doses and temperatures investigated and appear no more fully correct for the highest investigated dose of 2.0 dpa.

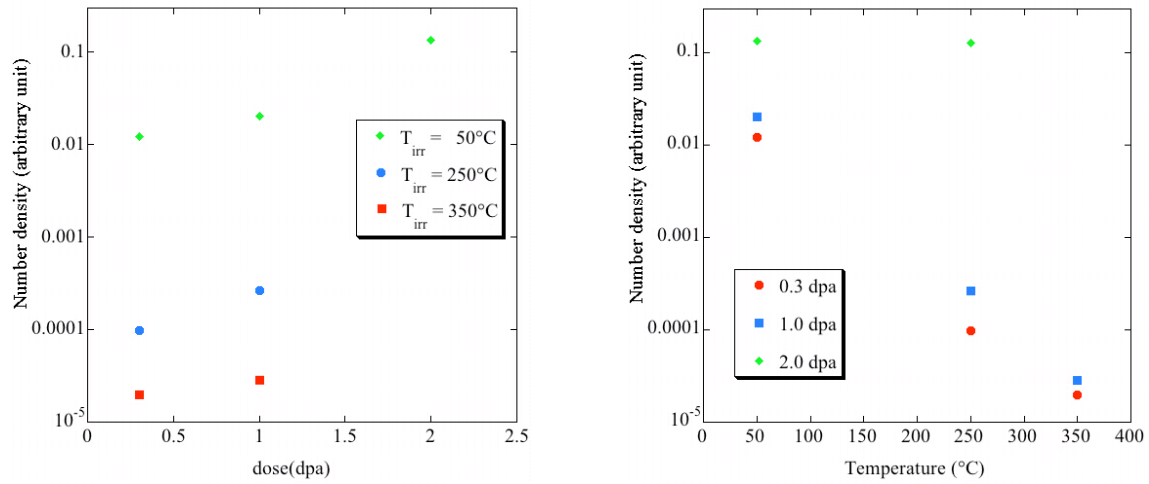


Figure 3.1.5.5: (Left) number density versus dose, and (right) number density versus temperature for the smaller irradiation-induced defects evidenced in specimens of the EUROFER 97 RAFM steel irradiated at about 50°C , 250°C or 350°C to doses of about 0.3, 1.0 or 2.0 dpa.

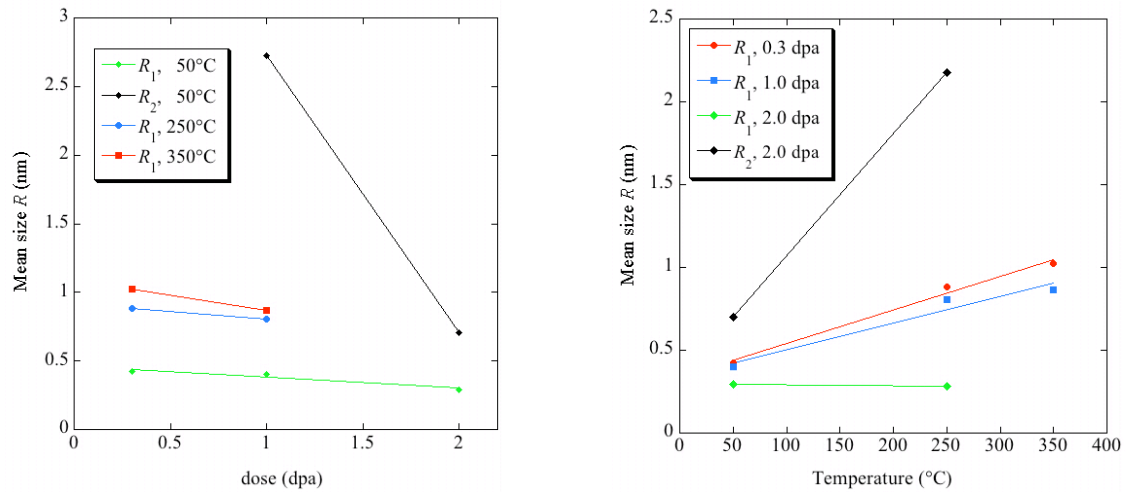


Figure 3.1.5.6: (Left) mean size versus dose, and (right) mean size versus temperature for the smaller irradiation-induced defects evidenced in specimens of the EUROFER 97 RAFM steel irradiated at about 50°C , 250°C or 350°C to doses of about 0.3, 1.0 or 2.0 dpa.

3.1.6 Magnetic versus nuclear scattering

It is possible to get additional information about the nature of the scattering objects by splitting the magnetic and nuclear cross-sections. When a saturating magnetic field (horizontal and perpendicular to the neutron beam) is applied to a specimen, the coherent small angle neutron scattering arises from variations in the scattering length density in nuclear contrast as well as in magnetic contrast so that:

$$\Delta\rho^2 = \Delta\rho_n^2 + \Delta\rho_m^2 \sin^2(\phi) \quad (3.1.6.1),$$

where ϕ is the angle between the applied magnetic field direction and the projected observation direction onto the plane perpendicular to the neutron beam. In the case of voids or helium bubbles, $\Delta\rho_n$ and $\Delta\rho_m$ can be written as:

$$\Delta\rho_n = \frac{b_n^{matrix}}{\Omega^{matrix}} \quad \text{for voids} \quad (3.1.6.2),$$

$$\Delta\rho_n = \frac{b_n^{matrix}}{\Omega^{matrix}} - \frac{b^{He}}{\Omega^{He}} \quad \text{for He bubbles} \quad (3.1.6.3),$$

$$\Delta\rho_m = \frac{b_m^{matrix}}{\Omega^{matrix}} \quad \text{for voids and He bubbles} \quad (3.1.6.4).$$

The general equation for the differential cross section in the case of a magnetic plus nuclear scattering can then be written as:

$$\frac{d\Sigma_{tot}}{d\Omega}(Q, \phi) = \frac{d\Sigma_{Nucl}}{d\Omega}(Q) + \frac{d\Sigma_{Mag}}{d\Omega}(Q) \sin^2(\phi) \quad (3.1.6.5).$$

For a given Q value, the equation 3.1.6.5 can be reduced to an equation of the form $y = b + x m$, where $x = \sin^2(\phi)$. This allows splitting the scattering patterns into nuclear and a magnetic components by choosing $\sin^2(\phi)$ as the independent variable.

Such a splitting may be useful for distinguishing magnetic scattering objects from non-magnetic ones: contrary to Fe-base precipitates, voids and helium bubbles are magnetic holes in the saturated ferromagnetic matrix. In addition, voids and helium bubbles may be a priori distinguished from each other as they exhibit different nuclear contrasts, $\Delta\rho_n^2$.

In order to separate nuclear and magnetic cross sections, a standard least-squares linear regression for successive Q values was performed. When doing such calculations, it is important to check the correlation coefficients of each fit, i.e., to evaluate the quality of the fit for each Q value. If the correlation coefficients are larger than 0.9 over a significant Q -range, it is considered that the data analysis has a physical meaning, and the decomposition into two components can be considered as reliable.

The intensity scattered by a specimen of the EUROFER 97 RAFM steel irradiated at 250°C to 1 dpa is reported in Figure 3.1.6.1 versus Q values. In this Figure the scattered intensity was averaged over angular sectors, 10° wide, and the angle indicated refers to the sector center. A radial and angular average was done in selecting all the cells of the detector that fall into the same radial range and into the same angular sector. For each sector, the scattered intensity was calculated as a function of the radial distance. As expected, it can be seen in Figure 3.1.6.1 that the scattered intensity increases with the angle ϕ , going from pure nuclear scattering at 0° to nuclear plus full magnetic scattering at 90°. Unfortunately, it was possible to separate both contributions only for Q values ranging between 0.3 and 1 nm⁻¹. In this Q -range, the correlation coefficients of the fit provided by the equation (3.1.6.5) were above 0.8, but at larger Q values the correlation coefficients rapidly decreased below 0.5. In addition, the scattered intensity for $\phi = 0^\circ$ was quite noisy above 1 nm⁻¹. Thus, it was not

possible to fully analyze the data in terms of only nuclear or only magnetic scattering, since the additional scattering intensity arising from the irradiation-induced defects appears mainly for Q values larger than about 1 nm^{-1} (see for instance Figure 3.1.1.1). However, the data obtained in the 90° sector were analyzed by considering the sum of the nuclear and magnetic scattering, as described just below. Qualitatively, the same behavior was obtained for the specimens of the EUROFER 97 RAFM steel irradiated in other conditions.

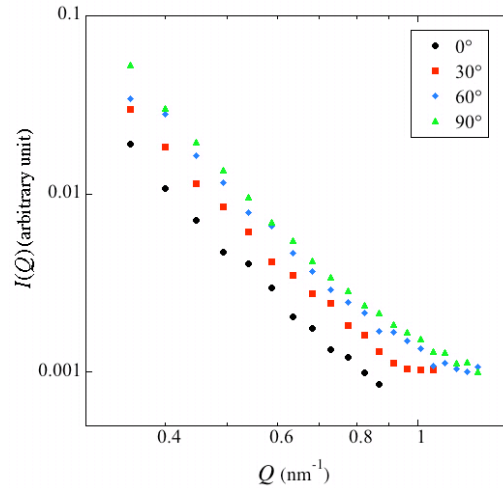


Figure 3.1.6.1: Scattered intensity versus Q values, averaged over different angular sectors of 10° in width, for a specimen of the EUROFER 97 RAFM steel irradiated at 250°C to 1 dpa.

It is possible to get additional information about the nature of scattering objects by splitting the magnetic and nuclear cross sections, in averaging the scattered intensity over angular sectors of 10° in width, and calculating the ratio of the total scattered intensity to the nuclear scattered intensity, namely the so-called A ratio, which was found not to depend on Q for Q values in the range $0.3\text{-}1 \text{ nm}^{-1}$:

$$A = \frac{(d\Sigma_{\text{tot}}/d\Omega)}{(d\Sigma/d\Omega)_n} = \frac{(d\Sigma/d\Omega)_\perp}{(d\Sigma/d\Omega)_\parallel} = \frac{\Delta\rho_{\text{nuc}}^2 + \Delta\rho_{\text{mag}}^2}{\Delta\rho_{\text{nuc}}^2} \quad (3.1.6.6).$$

Values of the A ratio versus $\sin^2\phi$ values were determined in the case of two specimens of the EUROFER 97 RAFM steel irradiated at 250°C to two different doses of 0.3 and 1.0 dpa. Results are reported in Figure 3.1.6.2. It can be seen that, as expected, the A ratio increases with the angle ϕ . More interestingly, a slight increase in the slope of the fit ($A - \sin^2\phi$) takes place with increasing irradiation dose.

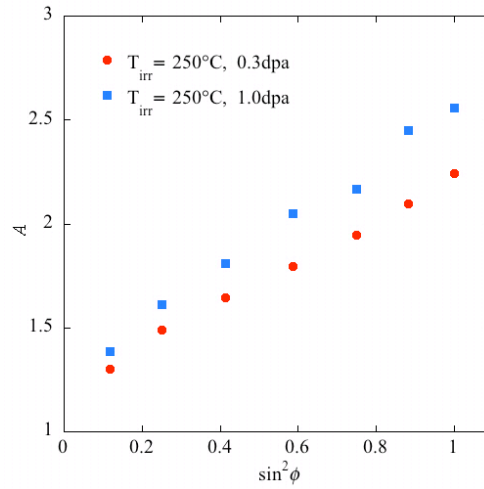


Figure 3.1.6.2: $A = (d\Sigma_{tot}/d\Omega)/(d\Sigma/d\Omega_n)$ ratio versus $\sin^2 \phi$ values for two specimens of the EUROFER 97 RAFM steel irradiated at 250°C to two different doses of 0.3 and 1.0 dpa.

The behavior of the A ratio versus Q values was first determined for an unirradiated specimen of the EUROFER 97 RAFM steel for Q values ranging between 0.426 and 1.914 nm⁻¹. Results are reported in Figure 3.1.6.3. The averaged A value was found to be 1.4549. However, it appears that two regions can be clearly distinguished: one for Q values in the range 0.426-0.70 nm⁻¹, corresponding to an A ratio around 2, and another one for Q values in the range 0.75-1.914 nm⁻¹, corresponding to an A ratio of about 1.4. This indicates that at least two kinds of defects were detected in this range of Q values.

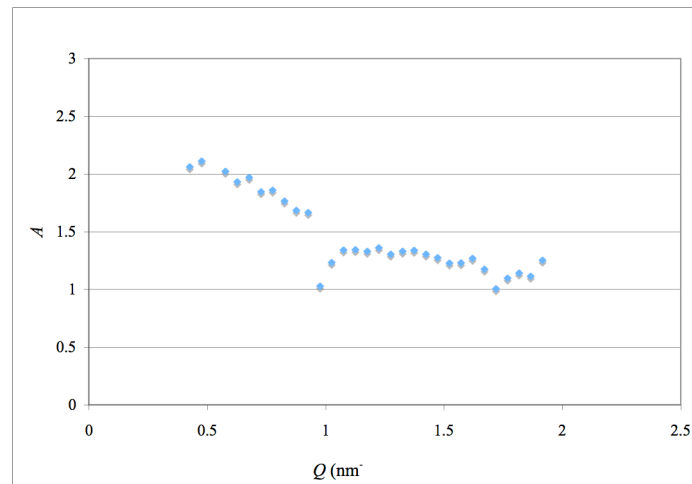


Figure 3.1.6.3: $A = (d\Sigma_{tot}/d\Omega)/(d\Sigma/d\Omega_n)$ ratio versus Q values for an unirradiated specimen of the EUROFER 97 RAFM steel. Analysis was made for the angular sector centered around 90°.

The behavior of the A ratio versus Q values was also determined for specimens of the EUROFER 97 RAFM steel irradiated at 50°C to doses of 0.3, 1.0 or 2.0 dpa or at 250°C to 2.0 dpa. Results are shown in Figure 3.1.6.4. The averaged A values were found to be equal

to 2.198, 2.117, 1.964, 1.901, respectively. It appears that a single type of irradiation-induced defects was detected in each irradiated specimen using Q values ranging between 0.426 and 4.826 nm⁻¹.

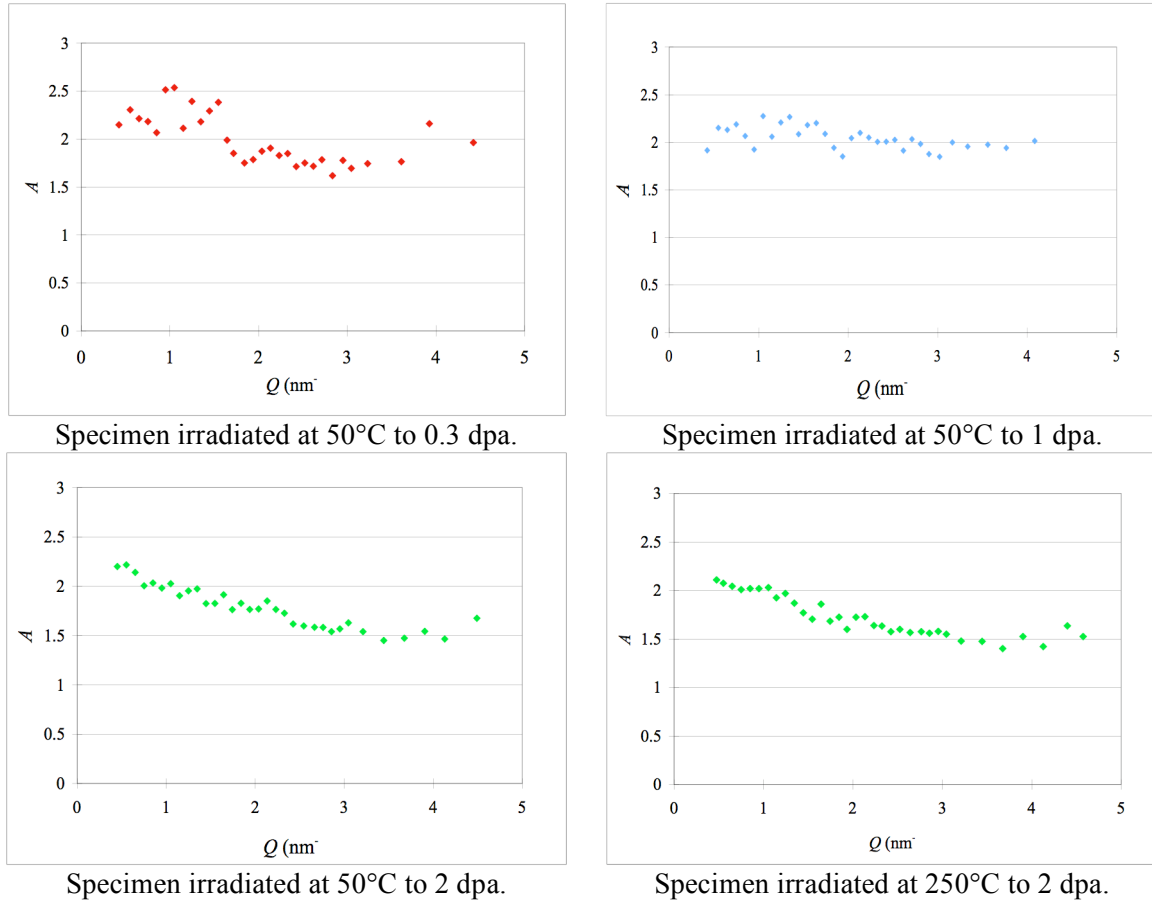


Figure 3.1.6.4: $A = (d\Sigma_{tot}/d\Omega)/(d\Sigma/d\Omega_n)$ ratio versus Q values for specimens of the EUROFER 97 RAJM steel irradiated at about 50°C to about 0.3, 1.0 or 2.0 dpa, or at about 250°C to about 2.0 dpa. Analysis was made for the angular sector centered around 90°.

3.2 Simulations

3.2.1 MD simulations

We present hereafter the results of MD simulations of the effect of He on the damage produced by atomic displacement cascades and MD simulations of the main defects that are expected to be produced by irradiation in RAJM steels, namely interstitial dislocation loops (I-loops), cavities (voids and He bubbles) and Cr precipitates. All MD simulations were performed in bcc Fe, as a model material for RAJM steels, using the method described under § 2.4.1.

Atomic displacement cascades

The properties of the Ackland 97 potential [188], the Wilson-Johnson potential [190] and the Beck potential [191] to describe interactions between Fe-Fe, Fe-He and He-He, respectively, are summarized in Tables 3.2.1.1 and 3.2.1.2. It can be seen that the employed empirical potentials overestimate the formation energy for a He atom in the tetrahedral interstitial position (Figure 3.2.1.1.), which should be the most favorable interstitial site for He according to *ab-initio* calculations. They give instead the octahedral site as the most favorable one (Figure 3.2.1.1). These empirical potentials however do predict the same self-trapping behavior of He as that predicted by *ab-initio* calculations, and do also predict the substitutional site as the most favorable one.

Atom type	Equilibrium lattice parameter (Å)	Cohesive energy per atom (eV)
Perfect bcc Fe	2.8665	− 4.316
Perfect fcc He	3.2523	− 0.00714

Table 3.2.1.1: Equilibrium lattice parameter and corresponding cohesive energy per atom for the employed interatomic potentials [188, 191].

Site position	Formation energy (eV)	
	Combined potentials	<i>ab-initio</i> calculations
Substitutional	3.25	4.22
Tetrahedral	5.34	4.39
Octahedral	5.29	4.58

Table 3.2.1.2: Formation energy for a He atom in a perfect bcc Fe single crystal, determined using either the combined interatomic potentials [203] or *ab-initio* calculations [162].

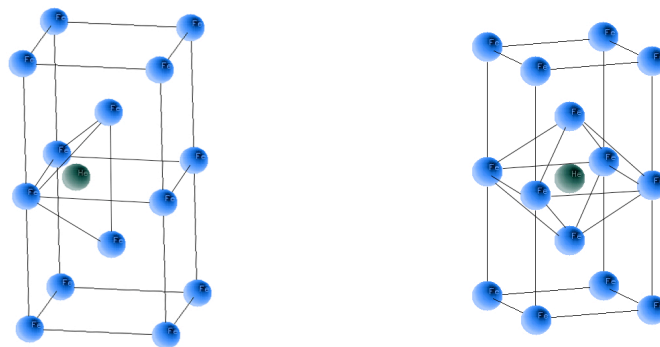


Figure 3.2.1.1: Tetrahedral (left) and octahedral (right) interstitial sites in pure Fe. ●: Fe atoms, ●: He interstitial atoms.

Simulation conditions for atomic displacement cascades are summarized in Table 3.2.1.3. Prior to the cascade, the typical simulation box (side length = 18 nm), containing 0, 0.1 at.% or 1.0 at.% He either in interstitial or in substitutional position, was maintained in equilibrium state for 0.4 to 1.3 ps (picoseconds) at the selected temperature. Each box contained about half million atoms. Each cascade was started in imparting a specified kinetic energy, E_{MD} , to the selected primary knock-on atom (PKA), along a high-index crystallographic direction to avoid channeling. It should be noted that due to this procedure many Fe-He dumbbells aligned along $\langle 100 \rangle$ directions are found. These Fe-He dumbbells are composed of an Fe atom close to its perfect lattice position and an interstitial He atom in octahedral position, as it is the most stable interstitial site predicted by the employed interatomic potentials. In the following, a Fe-He dumbbell will systematically refer to this configuration. Typical results of MD simulations of an atomic displacement cascade in pure Fe and in Fe containing 0.1 at.% He either in interstitial or substitutional position are shown in Figure 3.2.1.2.

T (K)	E_{MD} (keV)	Number of cascades					Other parameters	
		Fe	Fe- 0.1He(I)	Fe- 1.0He(I)	Fe- 0.1He(S)	Fe- 1.0He(S)	Time (ps)	Box size (nm ³)
10	3		10				25	18×18×18
	5		10	2	1		25	18×18×18
	7		10				25	18×18×18
	10	1	10	1	1		25	18×18×18
	10	1			1	1	25	10×10×80*
300	3		10				25	18×18×18
	5		10	2	1		25	18×18×18
	7		10				25	18×18×18
	10		10		1		25	18×18×18
523	3	1	10				25	18×18×18
	5	1	10	2	1		25	18×18×18
	7	1	10				25	18×18×18
	10	2	10	1	1		25	18×18×18

Table 3.2.1.3: Summary of MD simulation conditions of atomic displacement cascades in pure bcc Fe and bcc Fe containing 0.1 at.% or 1.0 at.% He atoms either in interstitial (I) or substitutional (S) position. * The cell size and crystallographic orientation are fitted to the TEM image simulation conditions.

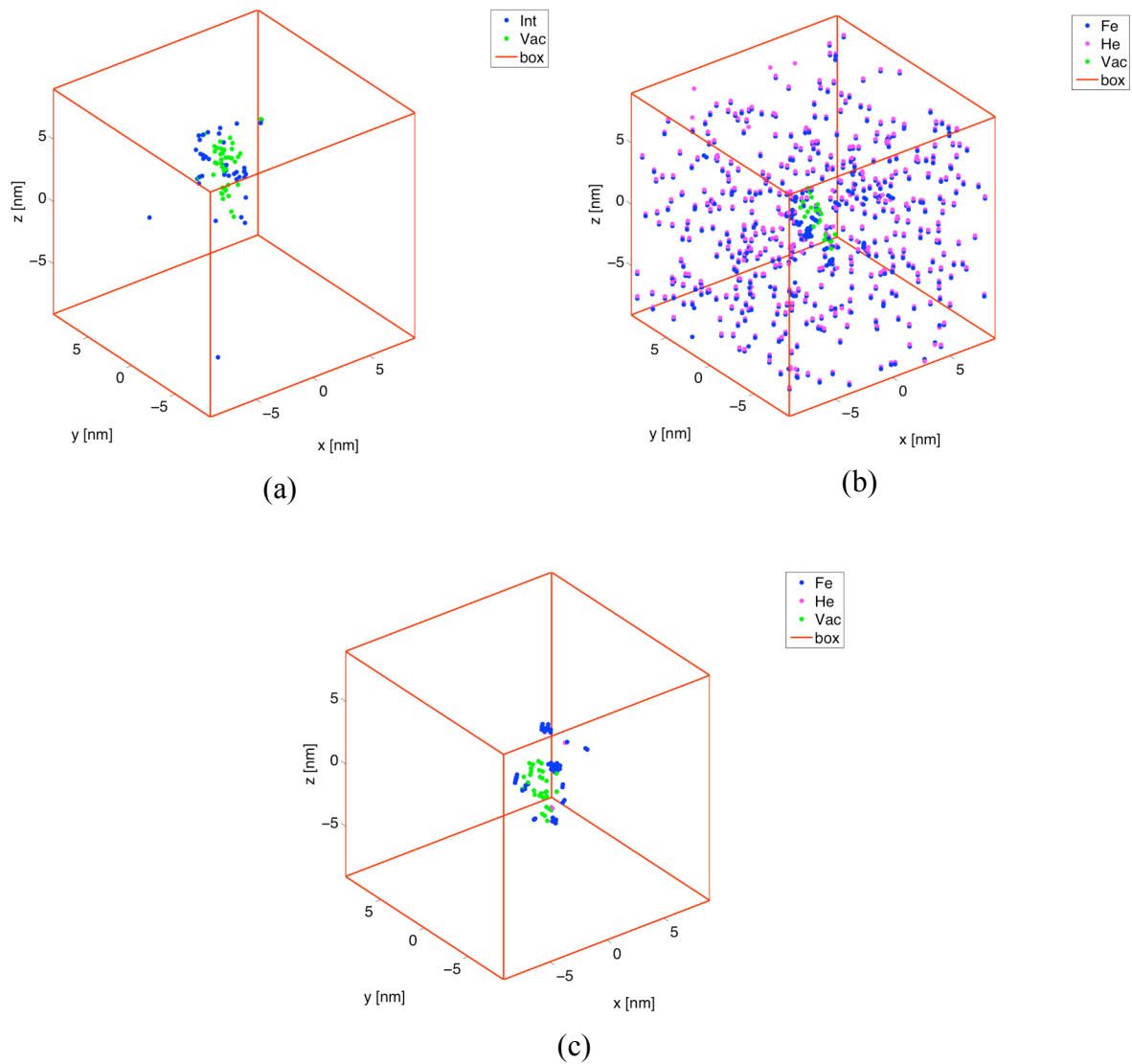


Figure 3.2.1.2: Typical results of a MD simulation of an atomic displacement cascade in pure Fe (a), Fe-0.1 at.% He(I) (b) and Fe-0.1 at.% He(S) (c): number of atoms = 500'094, 500'600 and 500'094, respectively, temperature = 10 K, PKA energy = 10 keV. Only interstitial Fe or He atoms and vacancies are shown.

Analysis of the defects generated by atomic displacement cascades:

Each MD simulation of an atomic displacement cascade was followed by defect and defect cluster analyses, as described under § 2.4.1. The standard statistical errors of the cascade output variables could not be determined, as in most cases only one or two cascades were simulated per condition. In typical cascades the errors lie in the 25 - 35% range. The cluster analysis was based on a simple radius criterion. If two individual defects are closer than a given cutoff radius, they belong to the same defect cluster. Number distributions of defect

clusters, in terms of number of individual defects contained in a given defect cluster, were obtained by considering either the distance to the third nearest neighbor (3-nn) or the sixth nearest neighbor (6-nn). As it was found that the size distribution obtained for the 3-nn criterion is close to the one obtained for the 6-nn criterion, as shown in Figures 3.2.1.3, the later radius criterion was applied in further defect cluster analyses. It allows avoiding defining a cluster made of loose interstitials as several smaller clusters.

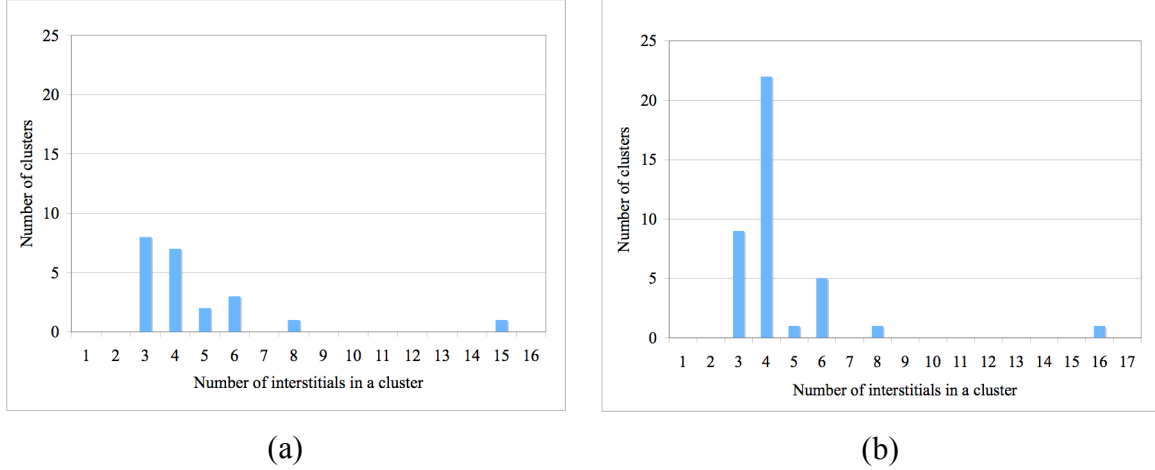


Figure 3.2.1.3: Number distribution of defect clusters, in terms of number of interstitial atoms in a given defect cluster, for the 3-nn (a) and 6-nn (b) criterion, respectively, resulting from a MD simulation of an atomic displacement cascade in Fe-0.1 at.% He(I), number of atoms = 500094, temperature = 10 K, PKA energy = 10 keV.

Traditionally, the number of Frenkel pairs produced by an atomic displacement cascade is estimated using the NRT formula [33], as reported in equation (1.2.1.4) under § 1.2.1, where T_D is the PKA energy and T_d is the threshold energy for atomic displacement damage, averaged over all crystallographic directions. T_D is the fraction of recoil energy that produces displacement damage, after having subtracted the fraction dissipated by electron excitation. Since in the present MD simulations the interaction between ions and electrons was not accounted for, it was assumed that $T_D = E_{MD}$. The production efficiency of Frenkel pairs is defined as the ratio of the surviving Frenkel pairs, resulting from MD simulations, to the number of NRT Frenkel pairs: N_{FP}/N_{NRT} . For the sake of comparison, we selected $T_d = 40$ eV [204] to estimate the number of Frenkel pairs with the NRT formula.

The average number of surviving Frenkel pairs (N_{FP}), resulting from MD simulations of atomic displacement cascades in pure bcc Fe at 523 K, is reported in Figure 3.2.1.4(a) as a function of E_{MD} . The corresponding production efficiency of Frenkel pairs (N_{FP}/N_{NRT}) is reported in Figure 3.2.1.4(b) as a function of E_{MD} . The average number of surviving Frenkel pairs (N_{FP}), resulting from MD simulations of atomic displacement cascades in Fe-0.1 at.% He(I), is reported in Figure 3.2.1.5(a) as a function of E_{MD} and in Figure 3.2.1.5(b) as a function of temperature. The corresponding production efficiency of Frenkel pairs

(N_{FP}/N_{NRT}) is reported in Figure 3.2.1.5(c) as a function of E_{MD} . It can be seen from Figures 3.2.1.4 and 3.2.1.5 that:

- For a given temperature, the number of surviving Frenkel pairs strongly increases with E_{MD} (PKA energy).
- For a given E_{MD} (PKA energy), the number of surviving Frenkel pairs slightly decreases with increasing temperature.
- The production efficiency of Frenkel pairs decreases with increasing E_{MD} and temperature, down to a more or less asymptotic value of about 0.33 at 10 K and 0.26 at 523 K. These values are slightly higher in Fe-0.1 at.% He than in pure Fe. This effect can be explained by the additional stress induced by He interstitials in the lattice, which may help to kick out a lattice atom in self-interstitial position.

The data points in Figures 3.2.1.4(a) and 3.2.1.5(a) have been interpolated using the empirical power law proposed by Bacon et al. [38], as reported in equation (1.2.1.5) under § 1.2.1. The A factor and m exponent values obtained are in agreement with a previous work on Fe [204]. In the case of the Fe-0.1 at.% He(I) material, the A value decreases with increasing temperature, from 6.15 at 10 K down to 3.66 at 525 K, while the m value increases with temperature, from 0.72 at 10 K up to 0.86 at 523 K. This indicates that the number of surviving Frenkel pairs is more sensitive to PKA energy at 523 K than at 10 K.

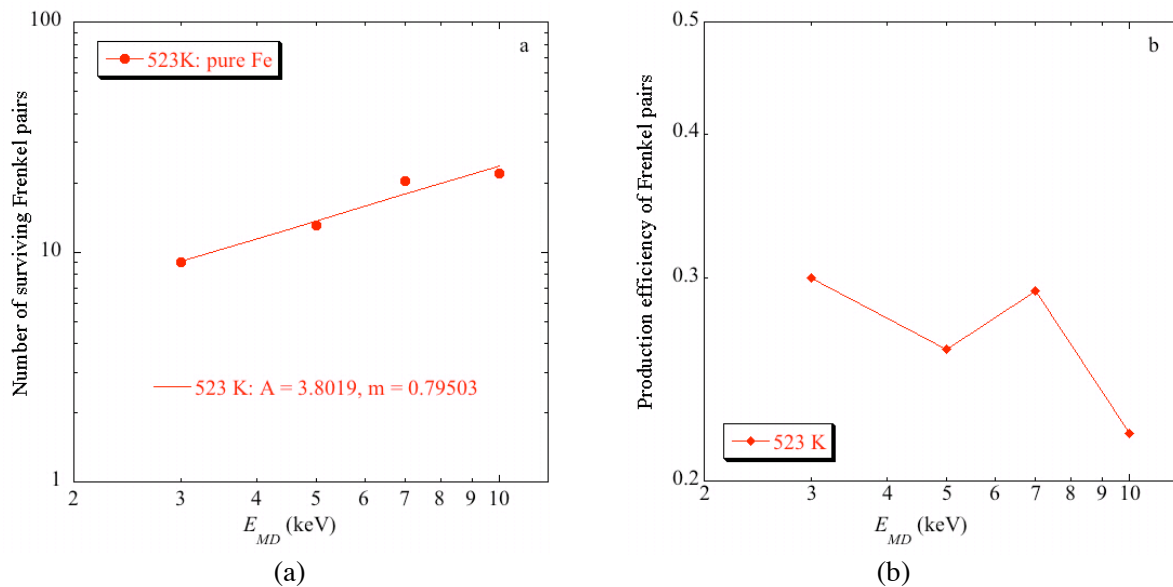


Figure 3.2.1.4: (a) Number of surviving Frenkel pairs versus E_{MD} , and (b) production efficiency of Frenkel pairs versus E_{MD} , resulting from MD simulations of atomic displacement cascades in pure bcc Fe at 523 K. In (a) the data were fitted using the power law reported in equation (1.2.1.5).

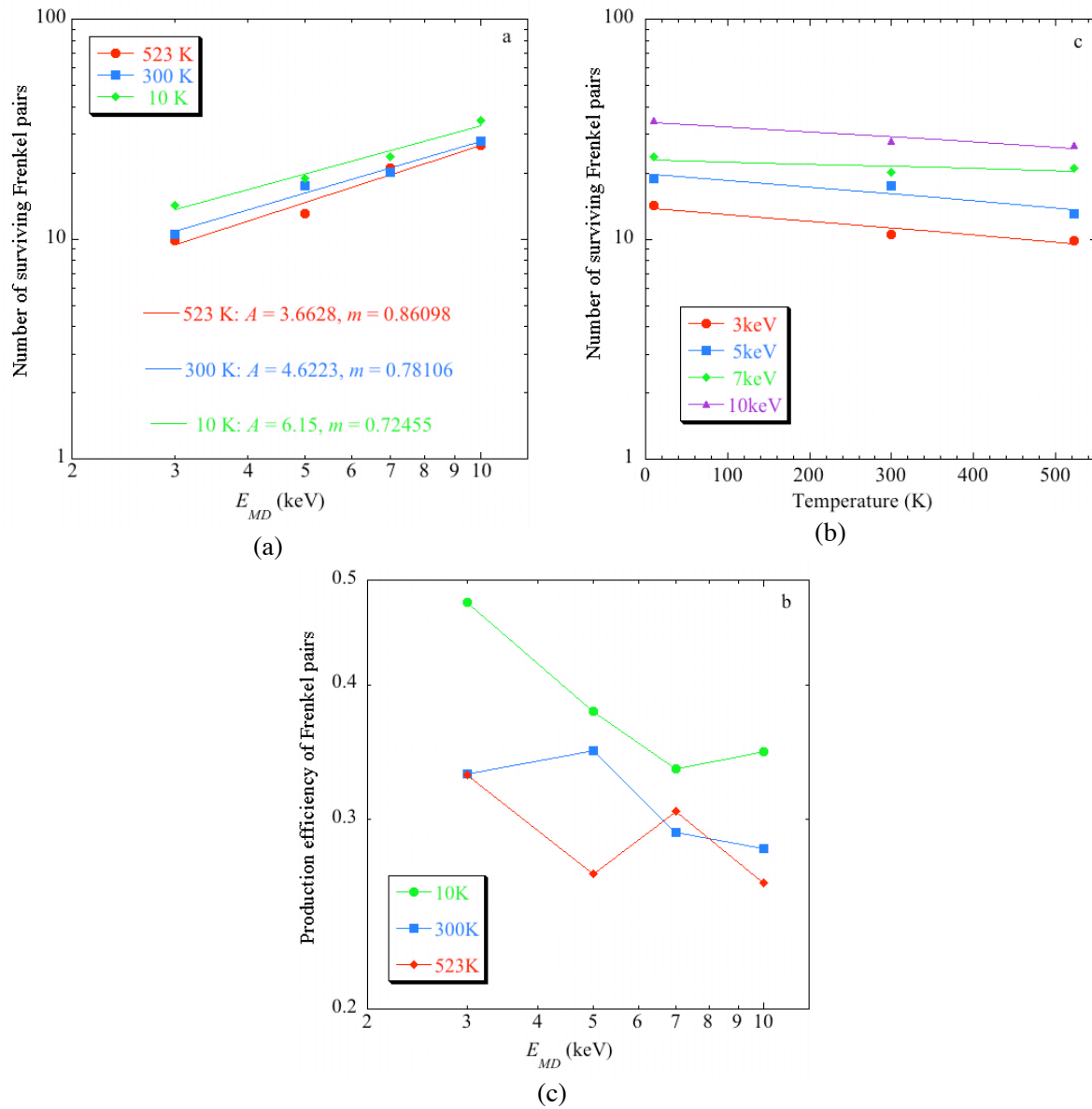


Figure 3.2.1.5: Number of surviving Frenkel pairs versus E_{MD} (a) and temperature (b), respectively, and production efficiency of Frenkel pairs versus E_{MD} (b), resulting from MD simulations of atomic displacement cascades in Fe-0.1 at.% He(I). In (a) the data were fitted using the power law reported in equation (1.2.1.5).

The average number of surviving Frenkel pairs (N_{FP}), resulting from MD simulations of atomic displacement cascades in Fe-0.1 at.% He(S), is reported in Figure 3.2.1.6 as a function of E_{MD} and temperature. Results obtained for the Fe-0.1 at.% He(S) material are approximately the same as in the case of the Fe-0.1 at.% He(I). However, the number of surviving Frenkel pairs after the PKA event appears slightly less than in the case of the Fe-0.1 at.% He(I) material. This means that the presence of substitutional He atoms induces a lower defect production. Indeed, during the first stage of an atomic displacement cascade, a substitutional He atom is easily kicked out from its position to form a vacancy and an

interstitial He atom, as only about 2 eV are needed to free the He atom. Besides that, a self-interstitial atom (SIA) can easily recombine with a substitutional He atom by a kick-out mechanism [205], leading to a significant energy gain and leaving a free interstitial He atom. With the set of potentials we used the energy gain amounts to about 3 eV. Consequently, the number of SIA clusters tends to decrease in presence of substitutional He atoms, as many potential vacancies are made available for recombination.

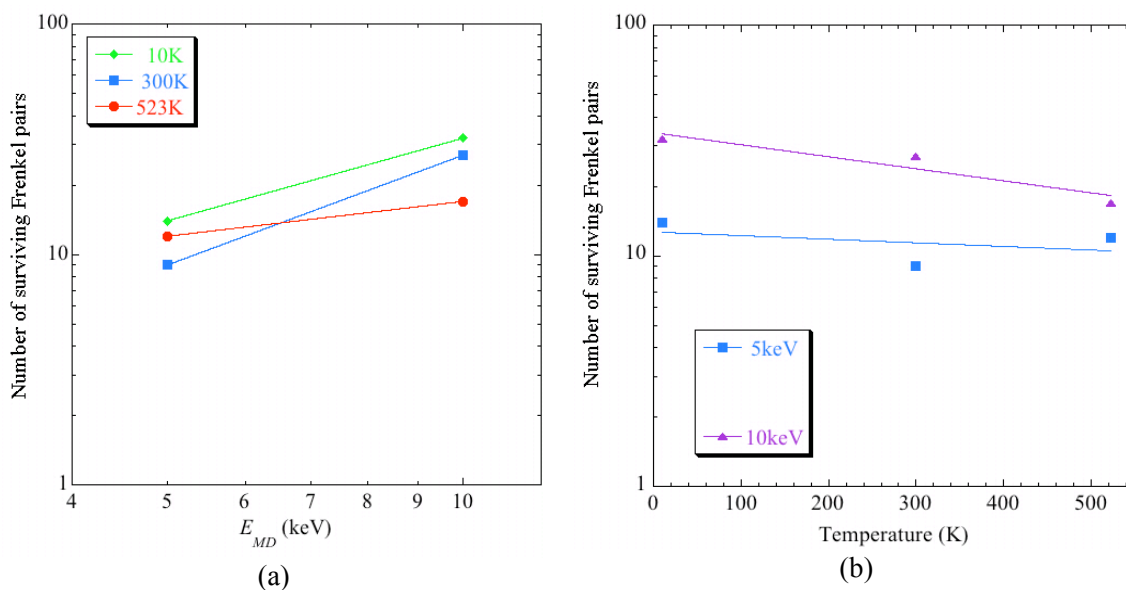


Figure 3.2.1.6: Number of surviving Frenkel pairs versus (a) E_{MD} and (b) temperature, resulting from MD simulation of atomic displacement cascades in Fe-0.1 at.% He(S).

The average number of surviving Frenkel pairs (N_{FP}), resulting from MD simulations of atomic displacement cascades in Fe-1.0 at.% He(I), is reported in Figure 3.2.1.7 as a function of E_{MD} and temperature. Results obtained for the Fe-1.0 at.% He(I) material appear significantly different from those obtained for the other materials. Indeed, the number of surviving defects is significantly less than in the Fe-0.1 at.% He(I) material, for instance, and the behaviors of the number of surviving defects versus E_{MD} and temperature appear also very different from those obtained for the other materials. While the number of surviving Frenkel pairs appears to increase slightly with PKA energy at 10 K, it decreases strongly with increasing PKA energy at 523 K. In addition, for a given PKA energy the number of surviving Frenkel pairs increases slightly with temperature. However, due to the limited number of data, no definitive conclusion can be drawn from these observations.

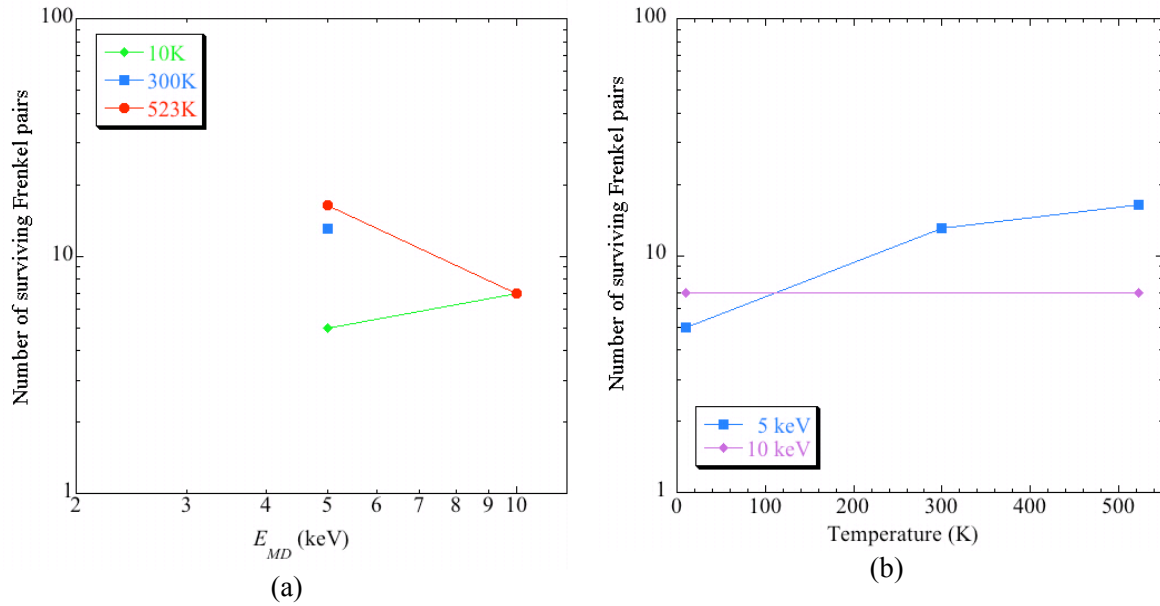


Figure 3.2.1.7: Number of surviving Frenkel pairs versus (a) E_{MD} and (b) temperature, resulting from MD simulation of atomic displacement cascades in Fe-1.0 at.% He(I).

A comparison of the numbers of surviving Frenkel pairs in Fe-0.1 at.% He(I) and Fe-0.1 at.% He(S) is reported in Figure 3.2.1.8 as a function of E_{MD} and temperature values. It can be seen that the number of surviving Frenkel pairs is systematically larger in Fe-0.1 at.% He(I) than in Fe-0.1 at.% He(S), whatever the PKA energy in the range of 3-10 keV and the temperature in the range of 10-523 K.

The orientation of Fe-He dumbbells is mainly along $\langle 100 \rangle$ in Fe-0.1 at.% He(I) and along $\langle 110 \rangle$ in Fe-0.1 at.% He(S), as shown in Figures 3.2.1.9 and 3.2.1.10, respectively. The orientation of Fe-Fe dumbbells is mainly along $\langle 110 \rangle$ in both Fe-0.1 at.% He(I) and Fe-0.1 at.% He(S), as also shown in Figures 3.2.1.9 and 3.2.1.10, which is in agreement with *ab-initio* calculations for SIAs in pure bcc Fe [206].

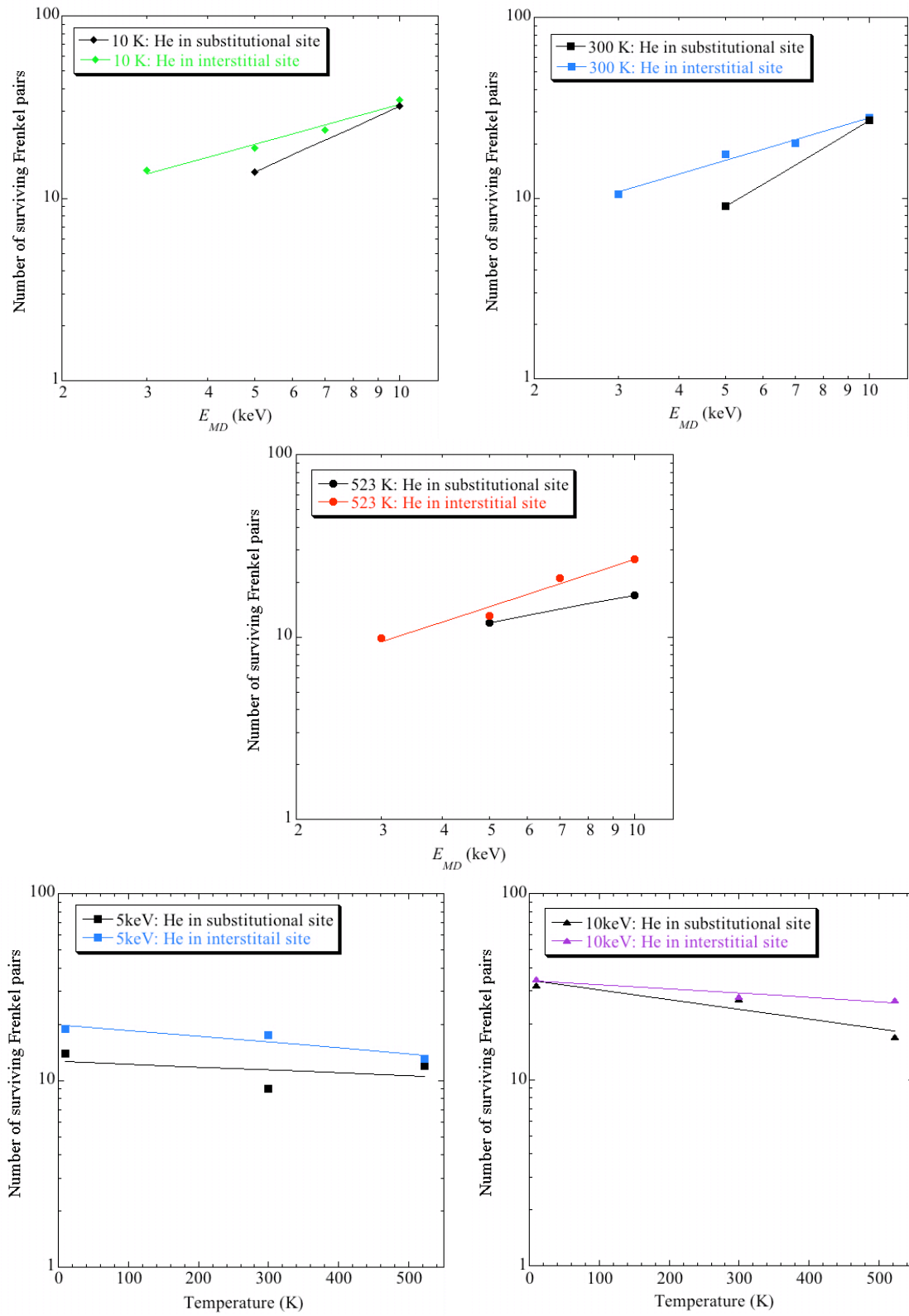


Figure 3.2.1.8: Numbers of surviving Frenkel pairs versus E_{MD} and temperature values, resulting from atomic displacement cascades in Fe-0.1 at.% He(I) and Fe-0.1 at.% He(S).

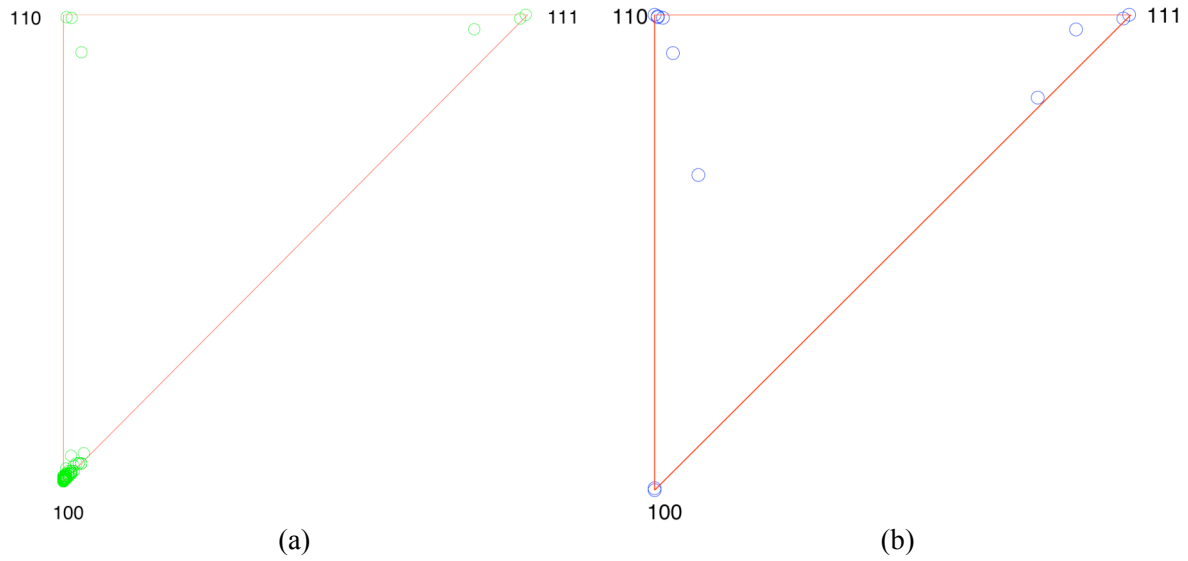


Figure 3.2.1.9: Orientation of (a) Fe-He and (b) Fe-Fe interstitial dumbbells, analyzed using the 3-nn criterion, resulting from atomic displacement cascades in Fe-0.1 at.% He(I): number of atoms = 500094, temperature = 10 K, PKA energy = 10 keV.

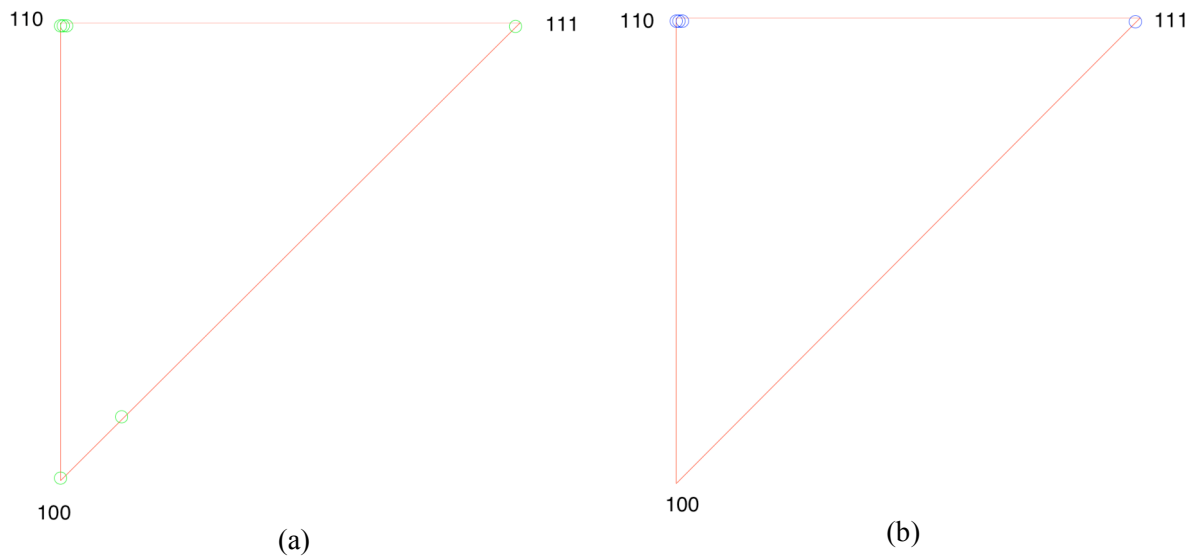


Figure 3.2.1.10: Orientation of (a) Fe-He and (b) Fe-Fe interstitial dumbbells, analyzed using the 3-nn criterion, resulting from atomic displacement cascades in Fe-0.1 at.% He(S): number of atoms = 500094, temperature = 10 K, PKA energy = 10 keV.

Previous studies of atomic displacement cascades in pure bcc Fe showed that very little in-cascade vacancy clustering occurs in this material, while sizeable interstitial clusters are found [38, 195, 204, 206, 207]. Our results agree with these findings.

The total number of interstitials in clusters as a function of E_{MD} and temperature, resulting from MD simulation of atomic displacement cascades in Fe-0.1 at.% He(I), is shown in Figure 3.2.1.11. Results have been obtained for a distance between neighbors of 0.573 nm (6-

nn criterion). 10 atomic displacement cascades per each MD simulation condition have been performed, and results have been summed. Defects containing more than 2 interstitials were considered as defect clusters. It can be seen in Figure 3.2.1.11 that the total number of interstitials in clusters increases significantly with PKA energy and temperature values.

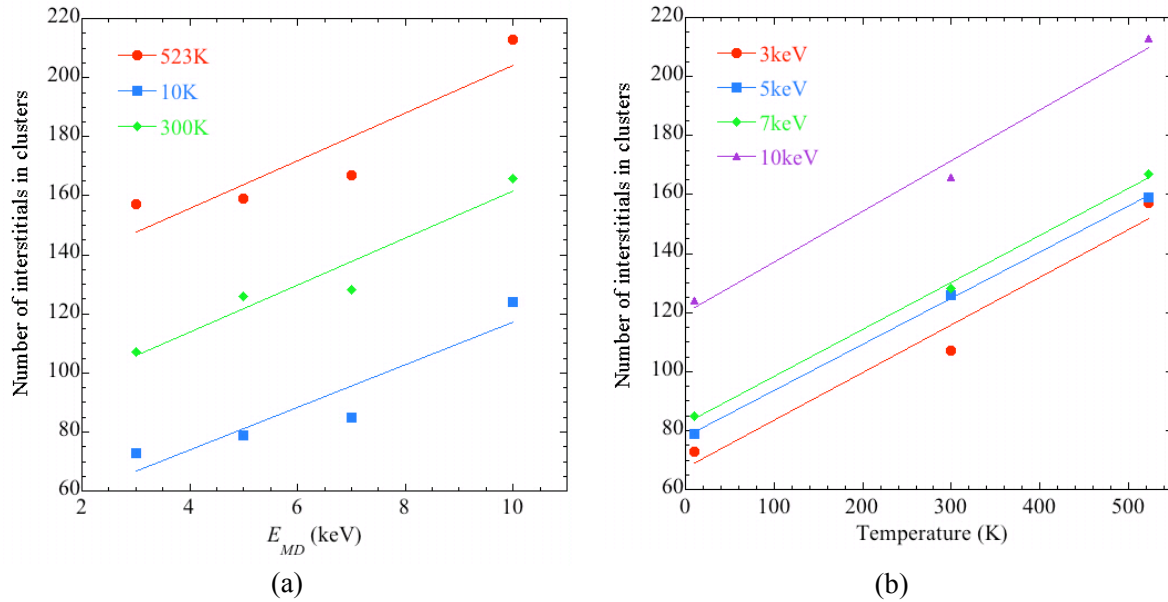


Figure 3.2.1.11: Total number of interstitials in clusters versus (a) E_{MD} and (b) temperature, for the 6-nn criterion, resulting from MD simulations of atomic displacement cascades in Fe-0.1 at.% He(I).

The number distribution of defect clusters, in terms of number of interstitial atoms in a given defect cluster, resulting from MD simulation of atomic displacement cascades in Fe-0.1 at.% He(I), is shown in Figure 3.2.1.12 for various E_{MD} and temperature values. Results have been obtained for a distance between neighbors of 0.573 nm (6-nn criterion). 10 atomic displacement cascades per each MD simulation condition have been performed, and results have been summed. Defects containing more than 4 interstitials were considered as defect clusters. It can be seen in Figure 3.2.1.12 that the number distribution of defect clusters peaks at about 7 interstitials per cluster, whatever the PKA energy and the temperature. The number of interstitial clusters also appears to increase with PKA energy and temperature, although not in a systematic way. In addition, the size of the large clusters is observed to increase with PKA energy and temperature.

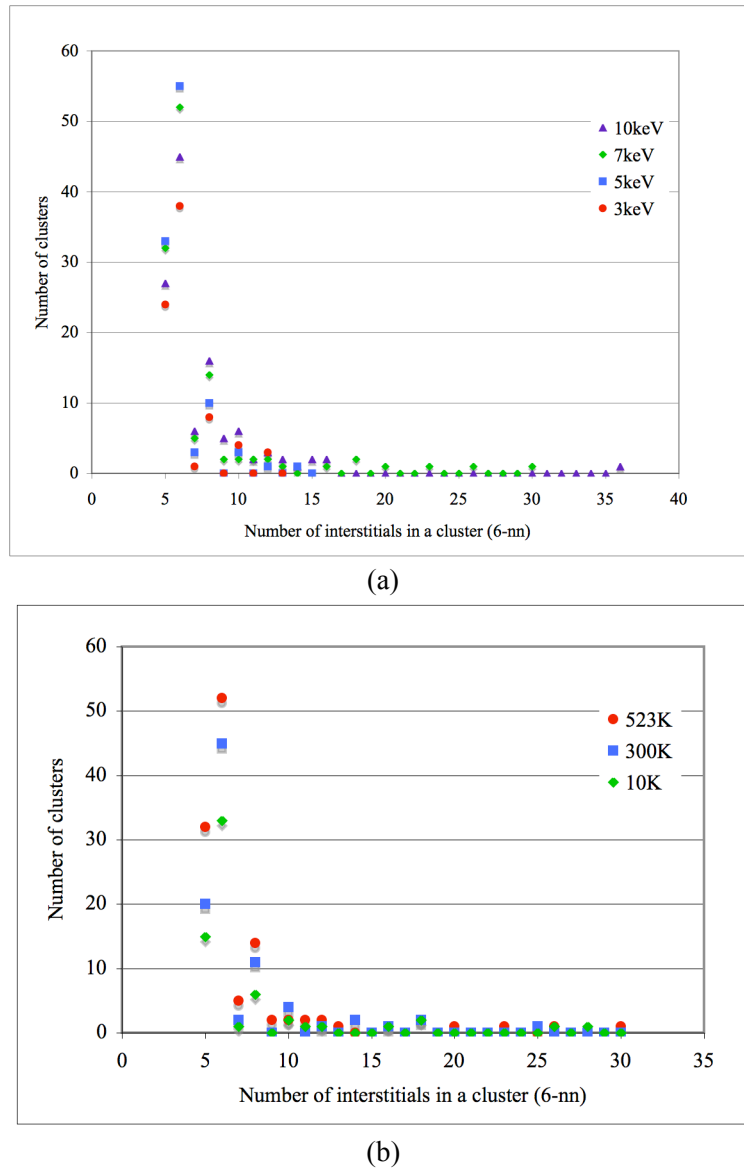


Figure 3.2.1.12: Number distribution of defect clusters, in terms of number of interstitial atoms in a given defect cluster, for the 6-nn criterion, resulting from MD simulation of atomic displacement cascades in Fe-0.1 at.% He(I), (a) at 523 K, and (b) for an E_{MD} value of 7 keV.

The ratio of interstitials in clusters to the total number of interstitials, resulting from atomic displacement cascades in Fe-0.1 at.% He(I), is reported in Figure 3.2.1.13 as a function of E_{MD} and temperature. Results have been obtained for a distance between neighbors of 0.573 nm (6-nn criterion). 10 atomic displacement cascades per each MD simulation condition have been performed, and results have been summed. Defects containing more than 2 interstitials were considered as defect clusters. It can be seen that this ratio increases with PKA energy and temperature values, like the total number of interstitials in clusters (Figure 3.2.1.11) and the number of interstitial clusters (Figure 3.2.1.12).

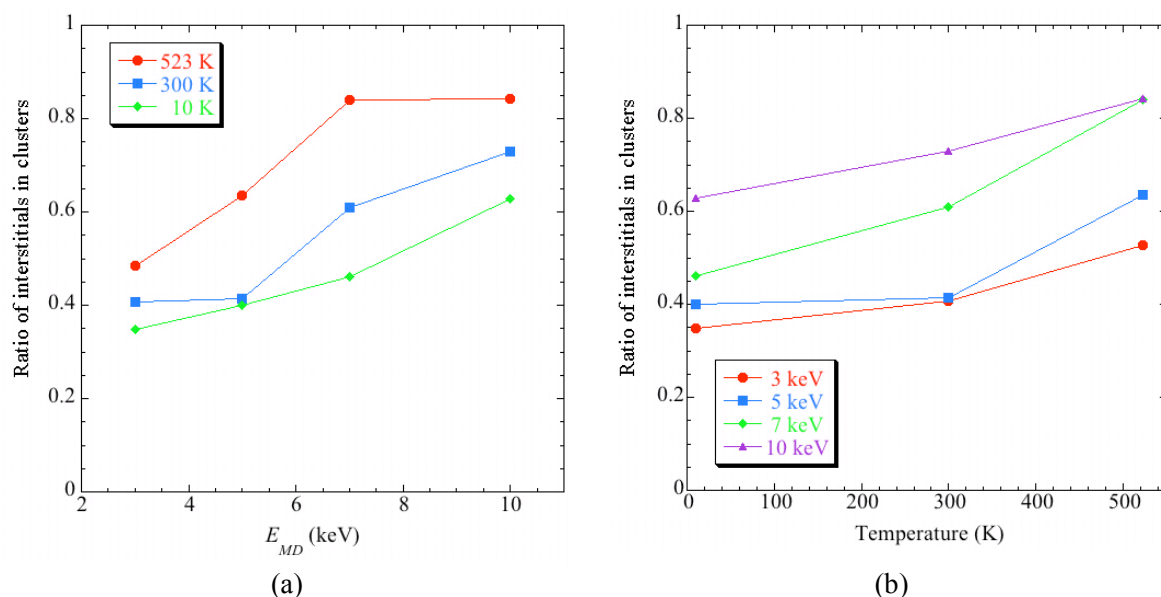


Figure 3.2.1.13: Ratio of interstitials in clusters (minimal size: 2) to the total number of interstitials versus (a) E_{MD} and (b) temperature, resulting from atomic displacement cascades in Fe-0.1 at.% He(I).

As the temperature increases the mobility of point defects also increases, therefore enhancing recombination and reducing the number of surviving Frenkel pairs. At the same time the probability of interstitials meeting with each other increases, thus enhancing the number and size of interstitial clusters. The number and size of interstitial clusters is also much higher in Fe-0.1 at.% He(I) than in Fe-0.1 at.% He(S) and in pure Fe. Indeed, in the former material, when point defects meet with interstitial He atoms, which are already present prior to the cascade, they do not only form interstitial dumbbells, but also bring some kinetic energy to these dumbbells, which prompts their mobility and enhances the probability of He-SIA clustering. Actually, the interstitial He atoms tend to aggregate at the periphery of the self-interstitial clusters and to stabilize them due to a strong binding energy of about 1.2-1.4 eV [208, 209]. As the temperature increases the He-SIA clustering is enhanced. Therefore, the number and size of interstitial clusters increase with temperature and the presence of He in interstitial position does influence the fraction of point defects in interstitial clusters.

It is expected that the formation of Fe-He interstitial clusters, which are stabilized by He, will have a large impact on the subsequent evolution of radiation damage. These Fe-He interstitial clusters may act as obstacles to dislocation motion, leading to hardening associated with embrittlement effects (loss of fracture toughness, decrease in DBTT and upper shelf energy) for irradiation temperatures below than about 400°C [210]. At higher irradiation temperatures (> 450°C) the Fe-He interstitial clusters may become unstable, evolving to bubbles or voids by release of some He atoms [211].

The number of interstitial clusters versus the fraction of the total number of interstitial He atoms to the total number of interstitial atoms in clusters, resulting from atomic displacement cascades in Fe-0.1 at.% He(I) at 523 K, is reported in Figure 3.2.1.14. It can be seen that the number of interstitial clusters increases with PKA energy, but not in a systematic way, and peaks for a fraction of about 0.5. This indicates that most of the interstitial clusters contain

one He atom per Fe atom. However, in large-sized clusters the number of He atoms is much smaller than the number of Fe atoms. For example, by using a 10 keV PKA at 523 K, one obtains a cluster containing 36 self-interstitials and a cluster consisting of 9 self-interstitials and 3 He atoms. By using a 10 keV PKA at 300 K, one obtains a cluster containing 10 self-interstitials and 1 He atom. There are no vacancies near the clusters, neither substitutional He atoms. No detailed analysis was conducted to detect a possible preferential association of vacancies and vacancy clusters with He atoms and self-interstitials. However, according to the conventional cascade picture, vacancies and self-interstitials tend to be physically separated with vacancies dominating in the core of the cascade and interstitials at its periphery [212], making the formation of small SIA-He-vacancy complexes rather unlikely.

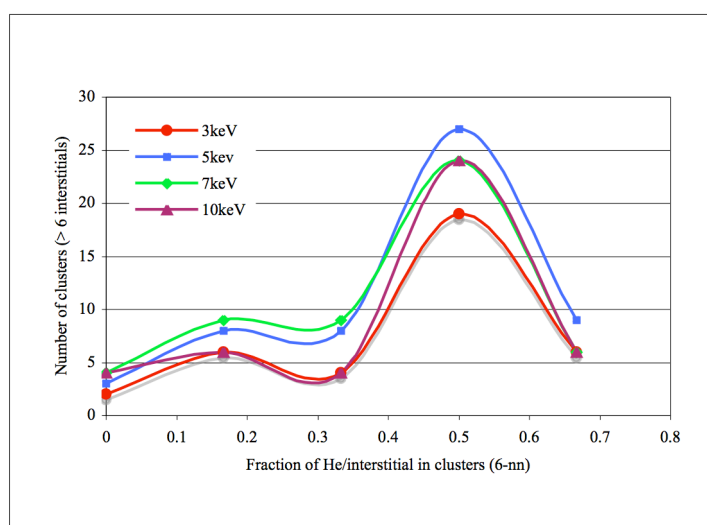


Figure 3.2.1.14: Number of interstitial clusters versus the fraction of the total number of interstitial He atoms to the total number of interstitial atoms in clusters, resulting from atomic displacement cascades in Fe-0.1 at.% He(I) at 523 K.

Creation of interstitial dislocation loops (I-loops)

All possible types of interstitial dislocation loops (I-loops) in bcc Fe have been created by MD simulations, namely $a_0\langle 100 \rangle \{100\}$, $1/2a_0\langle 110 \rangle \{110\}$ and $1/2a_0\langle 111 \rangle \{110\}$ I-loops.

Figure 3.2.1.15 shows three MD samples, each containing one of the three types of I-loops having a diameter of 2 nm, as defined by results of TEM observations. The axes of the sample correspond to a typical experimental observation in TEM using a diffraction vector $\mathbf{g}=(110)$ in a TEM operated at 200 kV. The axes x , y and z are along $[5-52]$, $[110]$ and $[-115]$, respectively. The y -axis corresponds to the operating diffraction vector orientation. The z -axis is actually about 10° away from the $[001]$ direction, as observation along a zone axis is detrimental for proper TEM imaging. The sample thickness was 80 nm and the defect depth was 40 nm, which corresponds to the centre of the thin foil.

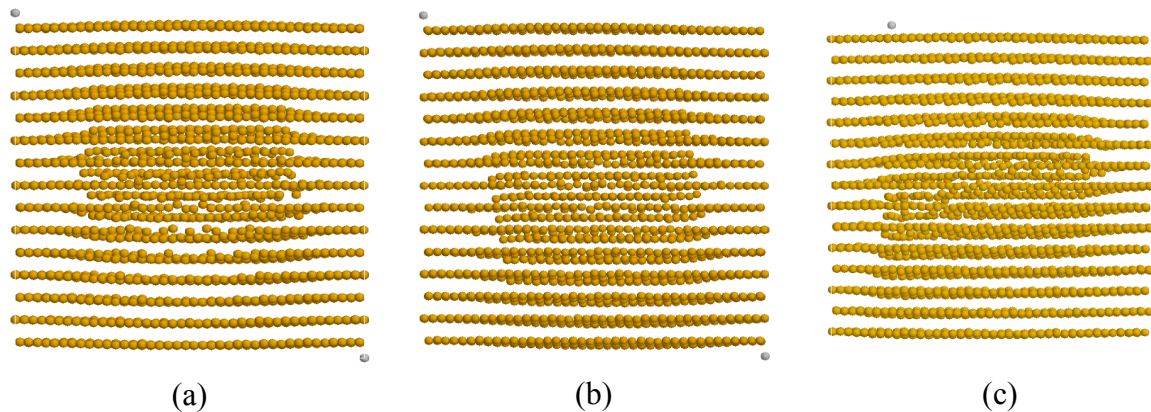


Figure 3.2.1.15: 2 nm-thick cut along $[-115]$ of a 0.8 million atoms MD sample containing (a) a $1/2a_0[110]$ I-loop in a (110) plane, (b) a $1/2a_0[111]$ I-loop in a (110) plane, and (c) a $a_0[100]$ I-loop in a (100) plane. All loops have a diameter of 2 nm.

Voids

A sample containing a spherical void in its centre, 2 nm in diameter, has been created by MD simulation, as shown in Figure 3.2.1.16. The sample contained about 1 million atoms.

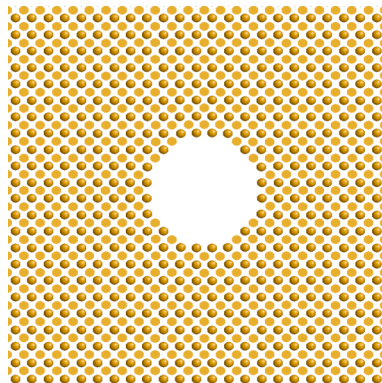


Figure 3.2.1.16: 1 nm-thick cut of a 1 million atoms MD sample containing a spherical void, 2 nm in diameter, in its centre. ● : atoms in the front, ● : atoms in the back.

Helium bubbles

Samples containing a spherical He bubble in their centre, 2 nm in diameter, and different He concentrations have been created by MD simulations, as shown in Figure 3.2.1.17. He concentrations investigated were 50% (1:2), 100% (1:1), 200% (2:1) and 300% (3:1). These values refer to the ratio of the number of He atoms relative to the number of vacancies in the cavity before filling it with He. The samples contained about 1 million atoms.

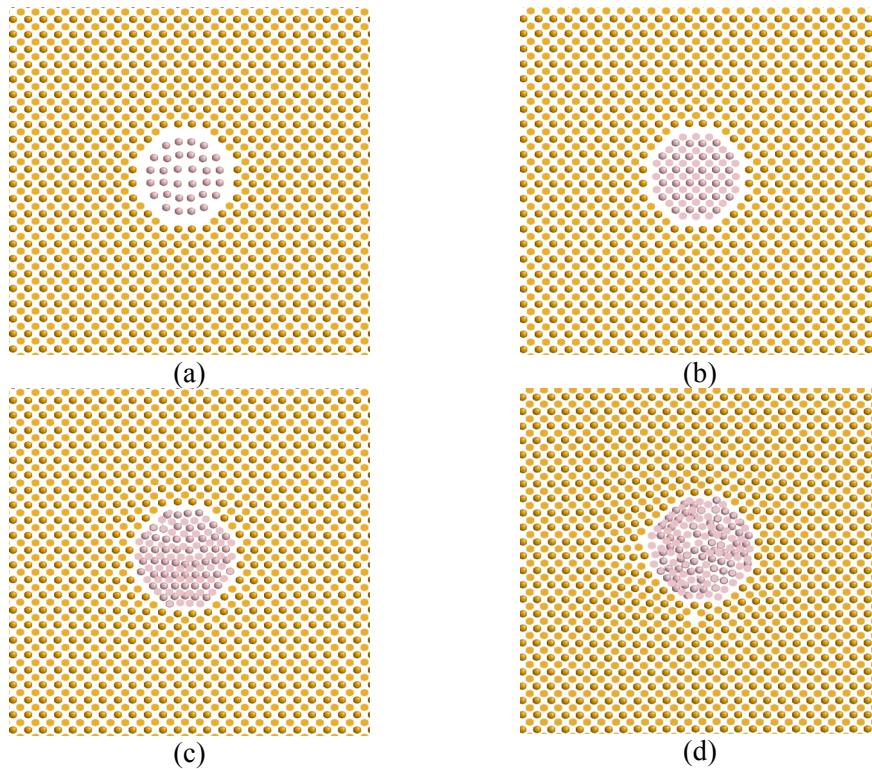


Figure 3.2.1.17: 1.0 nm-thick cuts of MD samples containing a spherical He bubble, 2 nm in diameter, in their centre, and a He concentration of (a) 50%, (b) 100%, (c) 200%, and (d) 300% inside the bubble. ●: Fe atoms in the front, ●: Fe atoms in the back. ●: He atoms in the front, ●: He atoms in the back.

Chromium precipitates

A sample containing a spherical Cr precipitate in its centre, 2 nm in diameter, has been created by MD simulations, as shown in Figure 3.2.1.18. The sample contained about 1 million atoms.

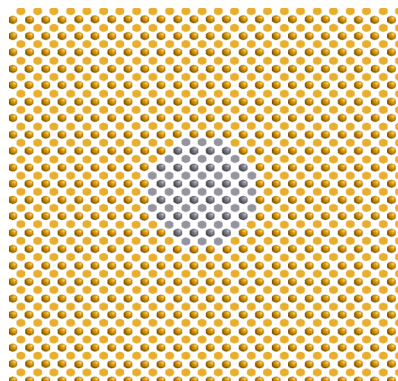


Figure 3.2.1.18: 1.0 nm-thick cut of a MD sample containing a spherical Cr precipitate, 2 nm in diameter, in its centre. ●: Fe atoms in the front, ●: Fe atoms in the back. ●: Cr atoms in the front, ●: Cr atoms in the back.

3.2.2 TEM image simulations

We present here the results of TEM image simulations of all the defects created by MD simulations in pure bcc Fe and Fe-He materials. TEM image simulations were performed using the method described under § 2.4.2.

Damage induced by atomic displacement cascades:

One would expect that the TEM image contrast arising from the damage produced by atomic displacement cascades is rather weak because it stems from tiny clusters of self-interstitial atoms (SIAs) and/or vacancies and/or He. Helium by itself won't induce any significant contrast in TEM images, as the scattering factor of He for the electrons is weak relatively to the one of Fe. However, there might be some TEM image contrast arising from the strain in the surrounding matrix, induced by the possible clustering of these He atoms.

Figures 3.2.2.1, 3.2.2.2 and 3.2.2.3 show the resulting simulated TEM dark field images of the damage produced by a 10 keV atomic displacement cascade in pure Fe and in Fe containing either 0.1 or 1 at.% He atoms in substitutional position, respectively, for two diffraction conditions, namely $g(2.1g)$ and $g(4.1g)$, and using the diffraction vector $g = (200)$. The sample thickness was 80 nm in all cases, and the cascade was produced approximately in the middle of the sample. The contrast, minimum, maximum and average intensities in the image as a function of the depth are also displayed in Figures 3.2.2.1, 3.2.2.2 and 3.2.2.3. In these Figures, the vertical left axis refers to the amplitude of minimum (Min), maximum (Max) and average intensities (Mean), while the vertical right axis refers to the contrast.

It appears that there is some contrast in the simulated TEM images arising from cascade damage, for the three materials and all the diffraction conditions investigated. However, the contrast features cannot be clearly resolved and identified, as e.g. Ashby-Brown contrasts [213]. They appear as background variations and at most as well identified bright dots. These bright dots relate to the largest clusters obtained in MD simulations of atomic displacement cascades. When comparing the intensities as a function of depth, it appears that the cascade damage in pure Fe induces a slightly stronger TEM image contrast than the cascade damage in both Fe-He(S) materials.

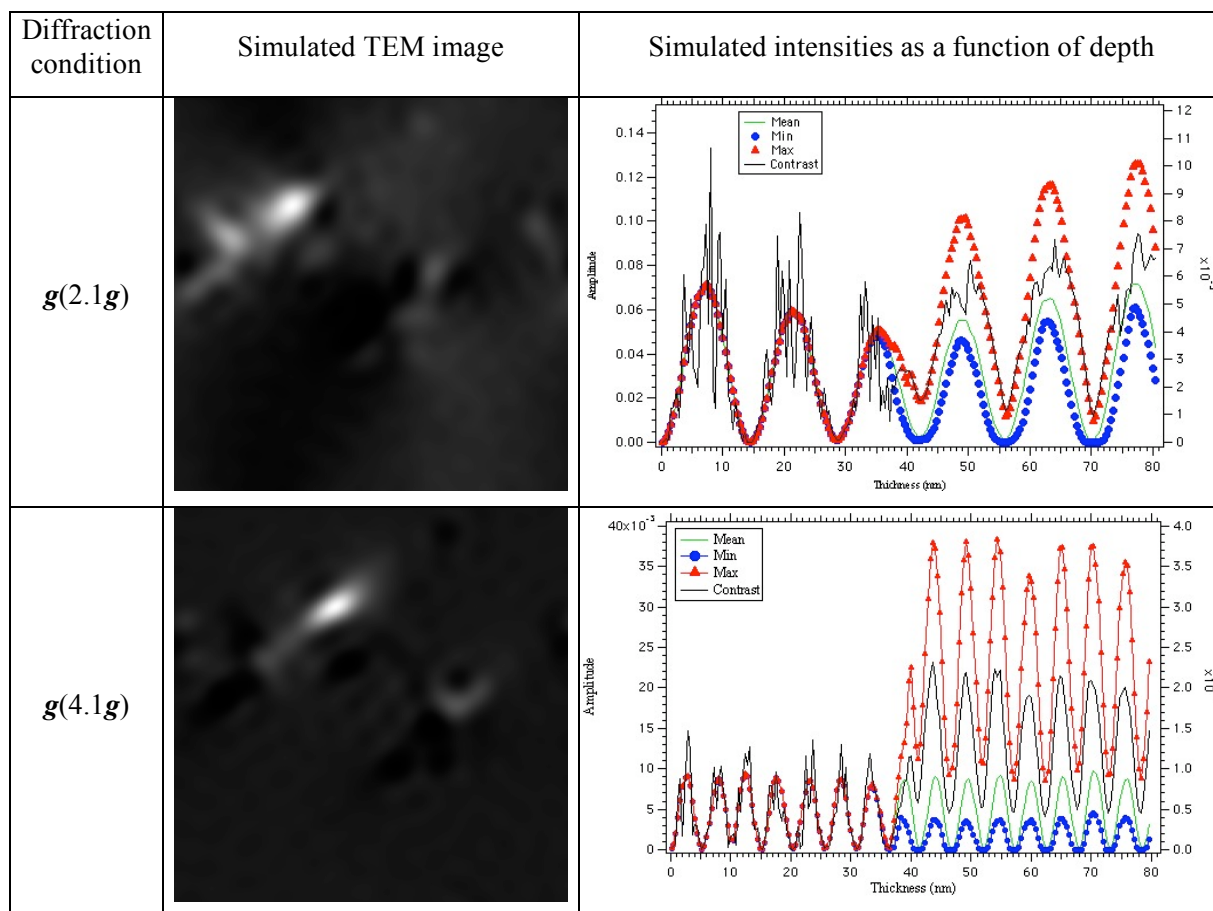


Figure 3.2.2.1: Simulated TEM dark field images, about $10 \times 10 \text{ nm}^2$ in size, of a 0.8 million atoms MD sample of pure Fe containing the damage produced by an atomic displacement cascade, and corresponding simulated intensity as a function of depth, for different diffraction conditions and using a diffraction vector $g = (200)$, $z = [015]$.

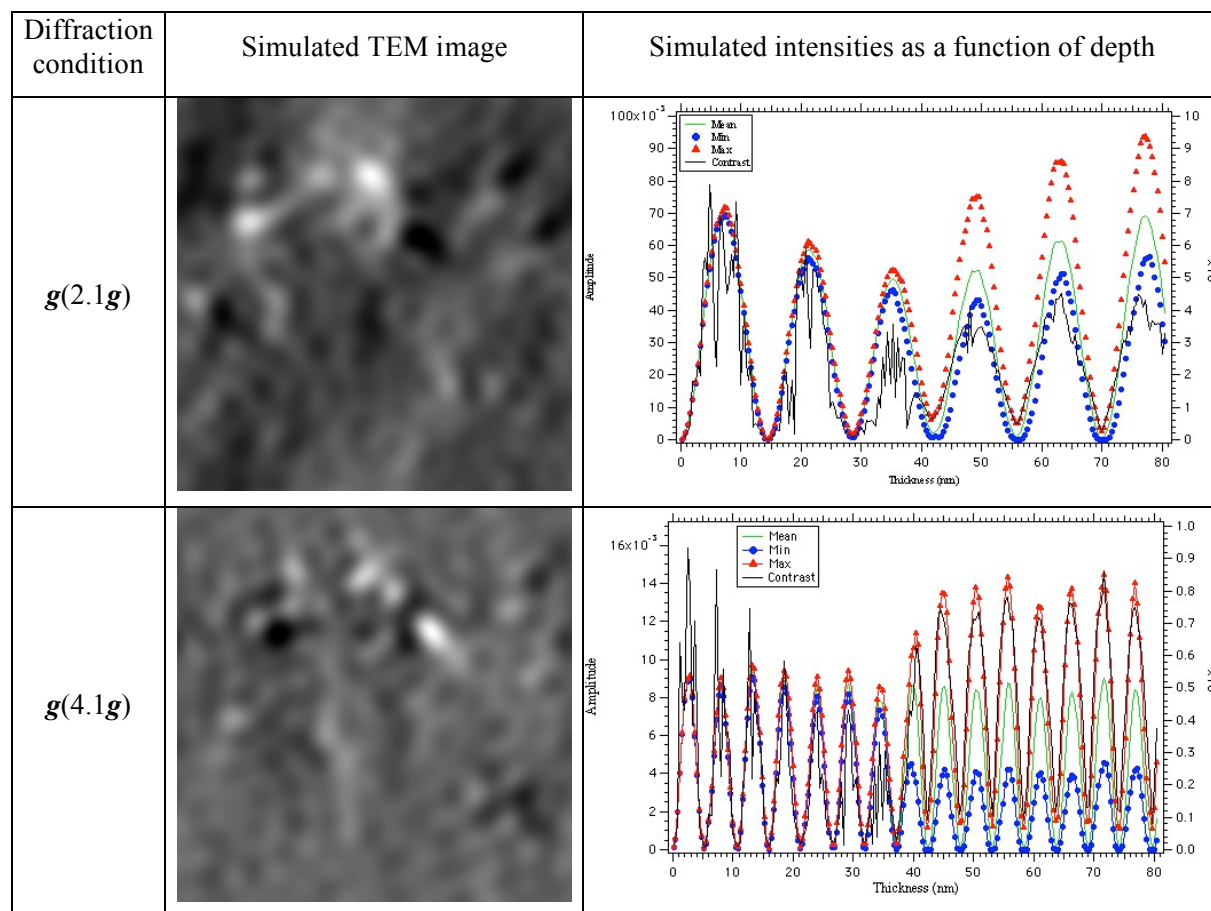


Figure 3.2.2.2: Simulated TEM dark field images, about $10 \times 10 \text{ nm}^2$ in size, of a 0.8 million atoms MD sample of Fe-0.1 at.% He(S) containing the damage produced by an atomic displacement cascade, and corresponding simulated intensity as a function of depth, for different diffraction conditions and using a diffraction vector $g = (200)$, $z = [015]$.

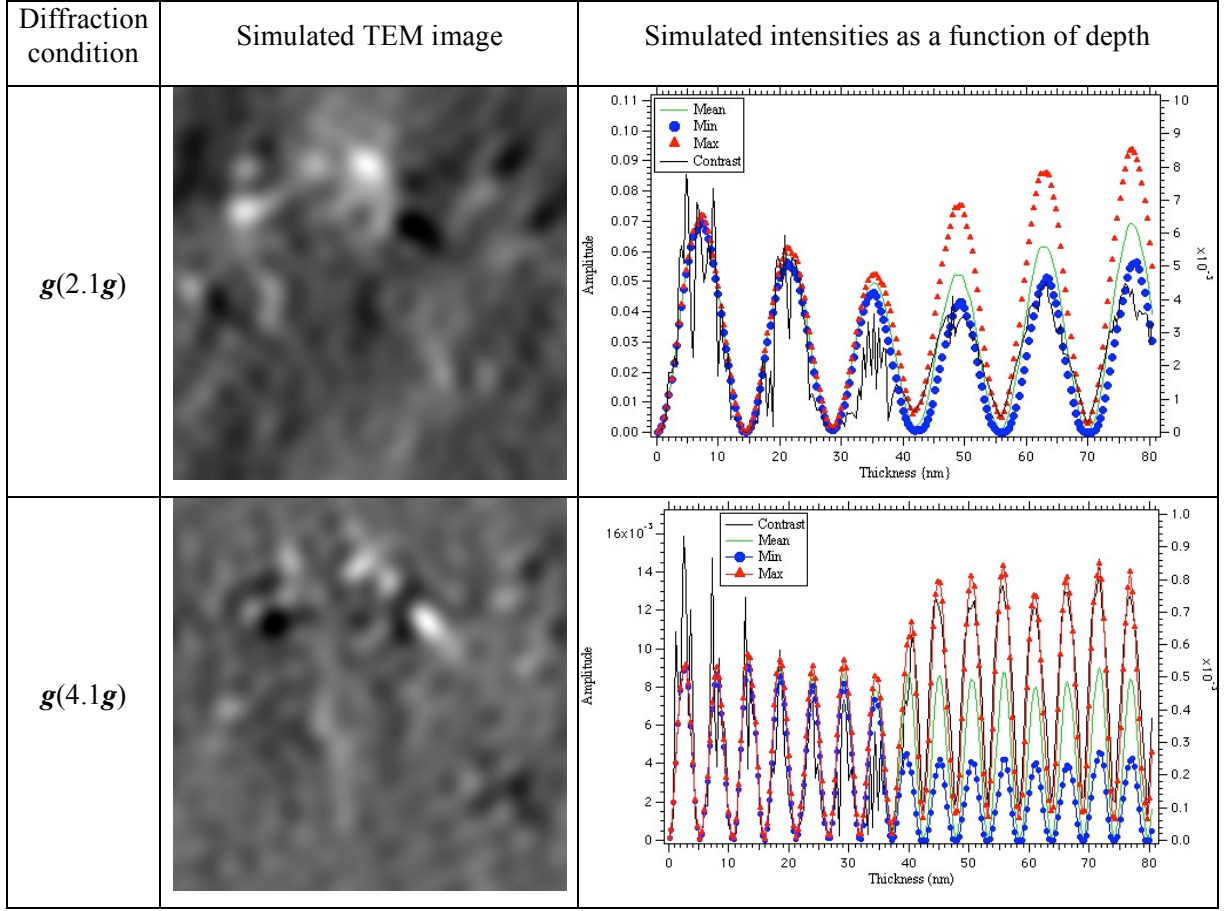


Figure 3.2.2.3: Simulated TEM dark field images, about $10 \times 10 \text{ nm}^2$ in size, of a 0.8 million atoms MD sample of Fe-1.0 at.% He(S) containing the damage produced by an atomic displacement cascade, and corresponding simulated intensity as a function of depth, for different diffraction conditions and using a diffraction vector $g = (200)$, $z = [015]$.

Interstitial dislocation loops (I-loops):

The contrast, σ , of a TEM image is defined by the following standard deviation:

$$\sigma = \sqrt{\frac{1}{N} \left(\sum_{i=1}^N I_i^2 \right) - I_m^2} \quad (3.2.2.1),$$

where I_i is the intensity of the pixel i and I_m is the average intensity. The contrast of a TEM image relates to the effective extinction distance, ξ_g^{eff} , as the following [201]:

$$\xi_g^{eff} = \frac{\xi_g}{\sqrt{1 + \omega^2}} = \frac{\xi_g}{\sqrt{1 + \xi_g^2 \cdot s_g^2}} \quad (3.2.2.2),$$

where ξ_g is the extinction distance, which depends on both the material and the selected operating diffraction beam, \mathbf{g} , and s_g is the deviation parameter to the Ewald's sphere, which characterizes the excitation of the imaging diffraction vector, and can be calculated as:

$$s_g = n(n - m)g^2 \frac{\lambda}{2} \quad (3.2.2.3),$$

where λ is the electron wavelength, and n characterizes the weak beam diffraction condition in $\mathbf{g}(n\mathbf{g})$. It indicates where the systematic row, defined by the operating diffraction beam, \mathbf{g} , is intersected by the Ewald's sphere. Therefore, in this work, the contrast variations may be explained by the different apparent thicknesses seen by the beam due to the different sample orientations. As an example, for a sample thickness of 80 nm, the $\mathbf{g}(4.1\mathbf{g})$ condition with $\mathbf{g} = \{200\}$ or $\mathbf{g} = \{110\}$ seems favorable for qualitative imaging of I-loops in steels, as it allows both the Burgers vectors and habit planes to be detected and differentiated.

$a_0 \langle 100 \rangle$ I-loops:

Figure 3.2.2.4 shows simulated dark field TEM images, about $10 \times 10 \text{ nm}^2$ in size, of a MD sample containing a $a_0 100$ I-loop, 2 nm in diameter, for three different diffraction conditions, namely $\mathbf{g}(2.1\mathbf{g})$, $\mathbf{g}(3.1\mathbf{g})$ and $\mathbf{g}(4.1\mathbf{g})$, and using the diffraction vector $\mathbf{g} = (200)$. The specimen was 80 nm thick. The simulation cell was created with the I-loop located at a depth of 10 nm, corresponding to a zone close to the surface of the foil. The contrast, minimum, maximum and average intensities in the image as a function of the depth are also displayed in Figure 3.2.2.4, together with the corresponding image.

Simulated TEM images show that the I-loop exhibits a bright double bean contrast over a dark background, typical of dislocation loops observed in dark field TEM imaging [213]. This contrast is described here for convenience as two half moons. Figure 3.2.2.4 shows that with increasing the diffraction condition, i.e., with increasing the deviation parameter to the Ewald's sphere, s_g , the width of the contrast decreases, as expected when going towards a weak beam TEM imaging condition, such as $\mathbf{g}(4.1\mathbf{g})$. This is clearly seen when comparing the $\mathbf{g}(2.1\mathbf{g})$ image to the $\mathbf{g}(4.1\mathbf{g})$ one.

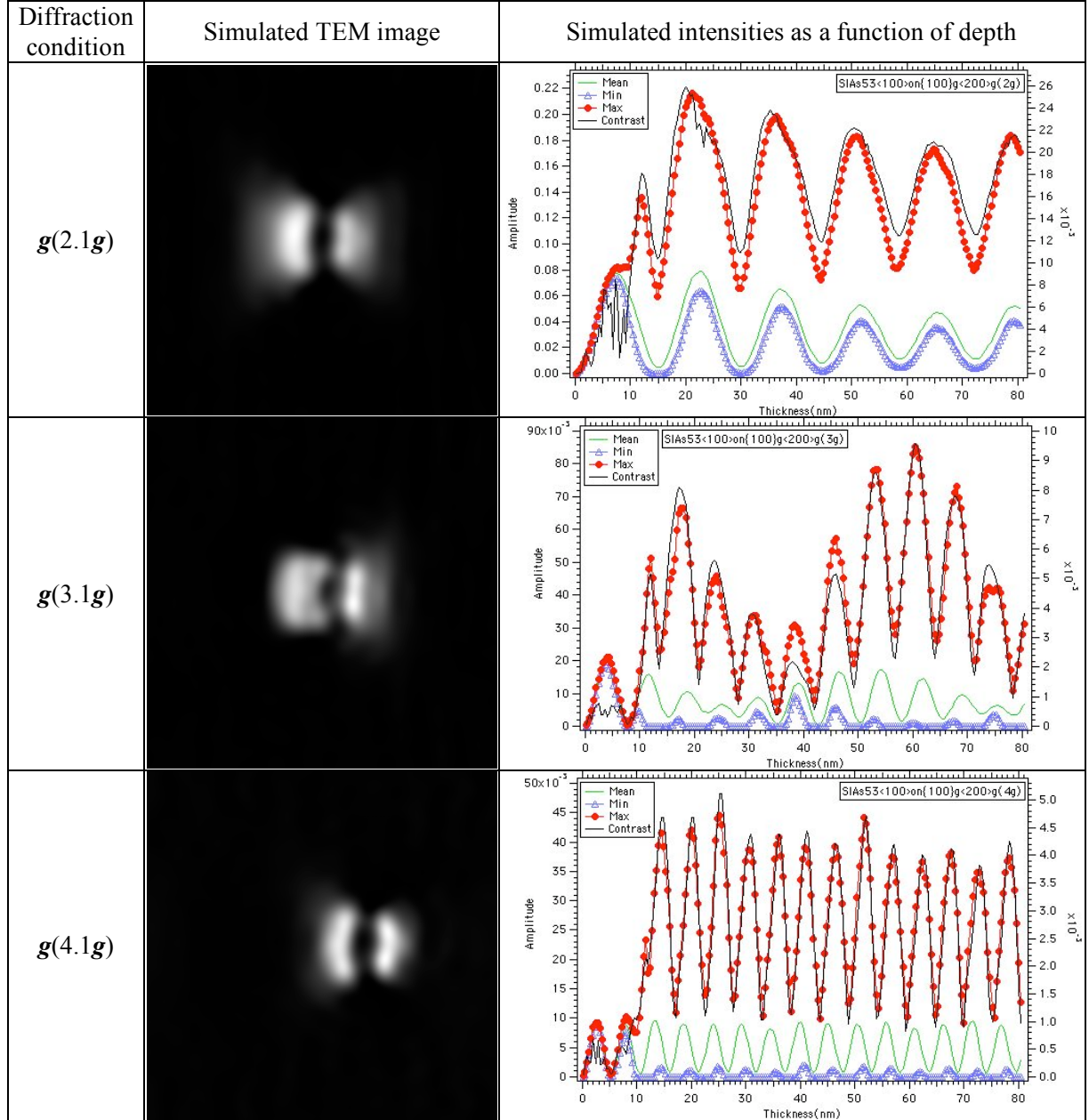


Figure 3.2.2.4: Simulated dark field TEM images, about $10 \times 10 \text{ nm}^2$ in size, of a 0.8 million atoms MD sample containing a a_0100 I-loop, 2 nm in diameter, and corresponding simulated intensities as a function of depth, for three different diffraction conditions and using the diffraction vector $\mathbf{g} = (200)$, $\mathbf{z} = [015]$.

The average intensity as a function of depth shows the classical thickness oscillations, whose periodicity should be equal to the effective extinction distance, ξ_g^{eff} . It appears that as the diffracted beam meets the defect in the foil, at a depth of 10 nm, the maximum intensity suddenly increases and the minimum intensity decreases. Both induce a corresponding rise in

contrast. This feature indicates that the observed contrast in the center of the simulated TEM images actually originates from the I-loop. More precisely, the contrast originates from the defect-induced displacement field in the surrounding atomic planes and not so much from the core of the dislocation delineating the interstitial platelet [201].

Another feature of the dislocation image contrast is its orientation relative to the operating diffraction beam. In the case of the a_0 100 I-loop imaged with $\mathbf{g} = (200)$, the two half moons are perpendicular to it. In other words, the line joining the two half moons is perpendicular to the diffraction beam. This contrast feature, characteristic of dislocation loops observed edge-on, i.e., with their habit plane perpendicular to the image, is commonly used to identify their habit plane in experimental weak beam TEM images.

Effect of depth on the I-loop image contrast: Figures 3.2.2.5 and 3.2.2.6 show a series of simulated TEM images of the faulted specimen as a function of depth in the foil for two different diffraction conditions, namely $\mathbf{g}(2\mathbf{g})$ and $\mathbf{g}(4\mathbf{g})$, respectively. Note that the intensities are normalized to the absolute minimum and maximum intensities found in the series. It allows a visual comparison of the images. In particular, a clear beating of the background intensity with depth can be seen, which relates to the thickness oscillations, as quantified by the graphs showing the intensities as a function of depth in e.g. Figure 3.2.2.4.

As mentioned earlier, there is a related oscillation in the TEM image contrast of the I-loop. It appears that only at specific thicknesses, over a short depth range, does the I-loop exhibit a strong contrast, with white features over a dark background. In between these the I-loop contrast is decreased. The I-loop either exhibits a very low or no contrast, and would be thus invisible experimentally, or in some cases presents an inverted contrast, i.e., a contrast darker than the background. In the case of the diffraction conditions $\mathbf{g}(2\mathbf{g})$ and $\mathbf{g}(4\mathbf{g})$, invisibility or very weak visibility starts occurring at 14.8 and 17.2 nm and repeats each 7.3 and 5.3 nm, which corresponds to minima in the thickness contrast oscillations, while contrast inversion starts occurring at 22.0 and 14.8 nm and repeats each 7.3 and 5.3 nm, respectively.

In addition, the contrast features in the simulated TEM images and the contrast at maximum amplitude, in other words at depths corresponding to peaks in intensities, do not vary with defect depth. Interestingly, it appears that the contrast propagates without any significant loss through the specimen, besides the thickness oscillations (Figure 3.2.2.4). Although there is no significant loss in contrast with depth, the peaks in contrast do vary a little bit with depth, but in a non-monotonous way. This shows the benefit of weak beam imaging technique, as in the latter cases a strong variation of contrast features and contrast maximum amplitude occurs with defect depth [213].

It should be noted that, experimentally, in this series of images as a function of depth, one would typically only consider the I-loop images that appear white and exhibit the highest contrast and brightest intensity, for obvious reasons of visibility. This implies that, experimentally, one would implicitly neglect a part of the population of I-loops. This should be taken into account when measuring the number density of I-loops.

In addition, the two half moons may exhibit contrast intensities that are inverted relatively to each other, that is to say that one may appear bright while the other appears dark. This is clearly seen in Figure 3.2.2.6, which presents the same defect and sample configuration than in Figure 3.2.2.5 but for the diffraction condition $\mathbf{g}(4\mathbf{g})$ instead of $\mathbf{g}(2\mathbf{g})$. This occurs at a

depth of 11.6, 18.8, ..., and 76.4 nm, for instance. Moreover, the neglect of a part of the population of I-loops due to poor visibility or invisibility, as mentioned in the previous paragraph, would be more pronounced in this diffraction condition.

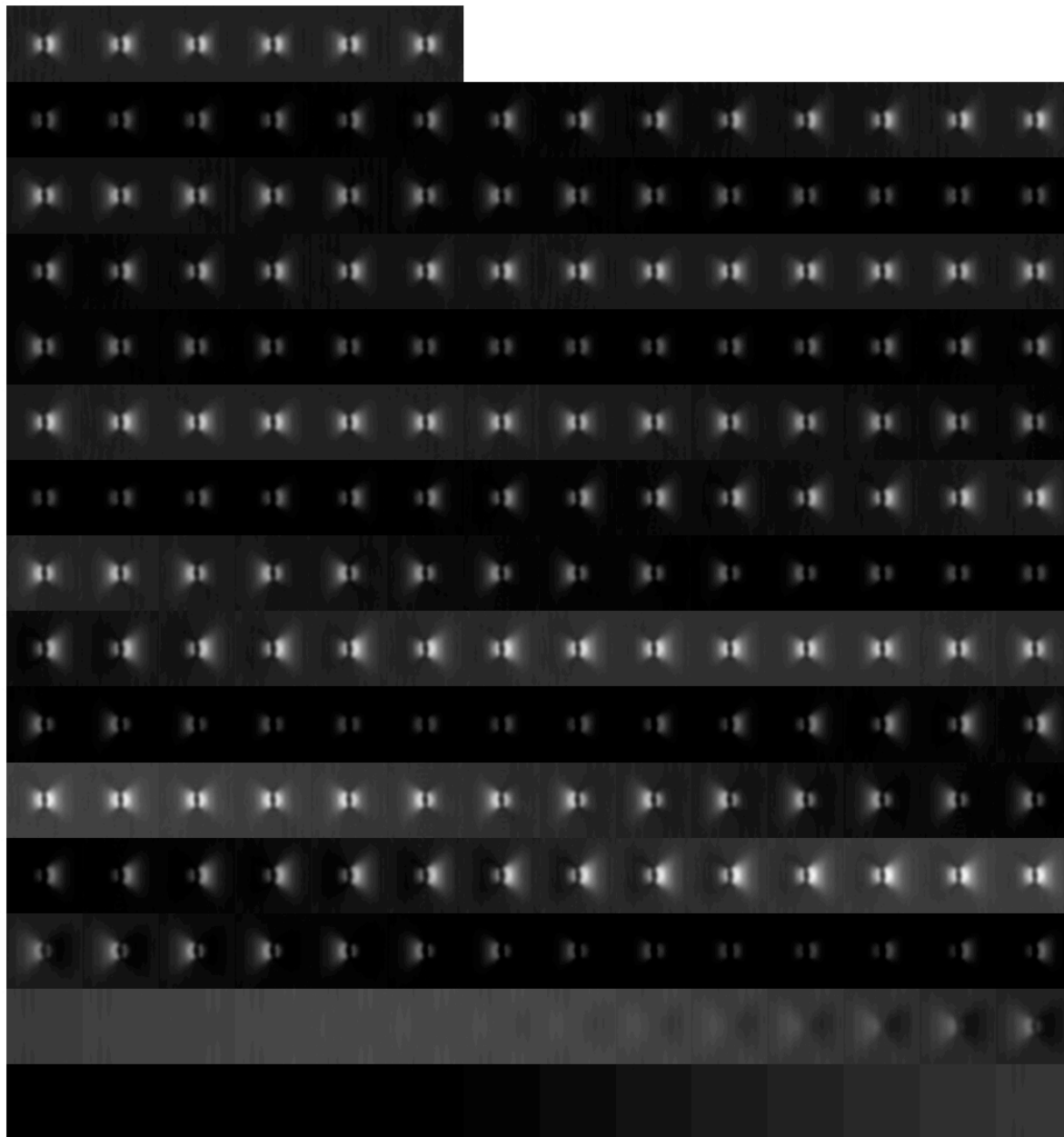


Figure 3.2.2.5: Series of simulated dark field TEM images, about $10 \times 10 \text{ nm}^2$ in size, of a 0.8 million atoms MD sample containing a a_0100 I-loop, 2 nm in diameter, and located at a depth of 10 nm, as a function of depth in the foil, starting at the bottom left and going towards the right and upwards and finishing at the top right, for the diffraction condition $\mathbf{g}(2\mathbf{g})$ and using the diffraction vector $\mathbf{g} = (200)$, $z = [015]$. Note that the intensities are normalized to the absolute minimum and maximum intensities to allow for visual comparison.

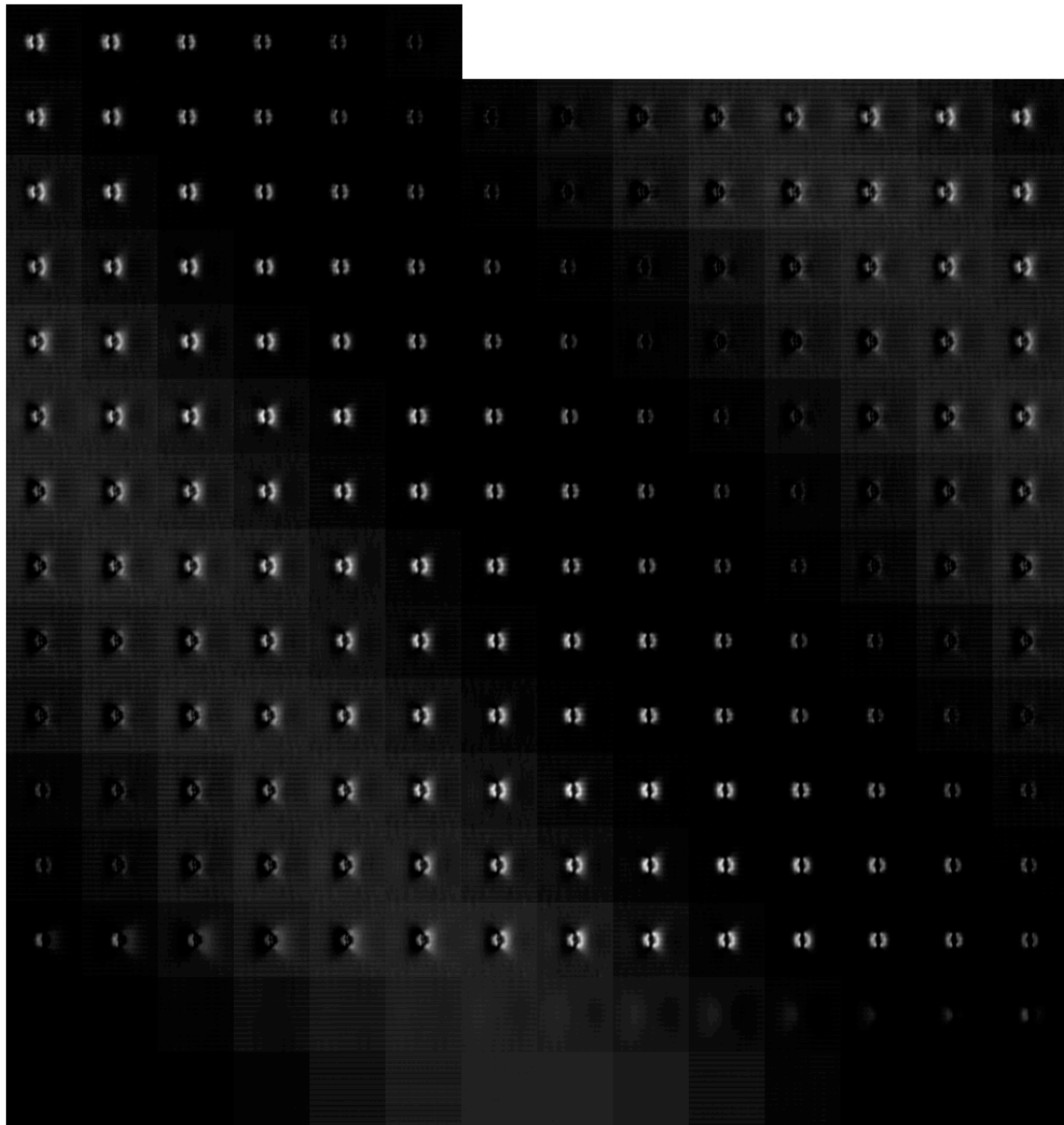


Figure 3.2.2.6: Series of simulated dark field TEM images, about $10 \times 10 \text{ nm}^2$ in size, of a 0.8 million atoms MD sample containing a $a_0 100$ I-loop, 2 nm in diameter, and located at a depth of 10 nm, as a function of depth in the foil, starting at the bottom left and going towards the right and upwards and finishing at the top right, for the diffraction condition $g(4g)$ and using the diffraction vector $g = (200)$, $z = [015]$. Note that the intensities are normalized to the absolute minimum and maximum intensities to allow for visual comparison.

Effect of operating diffraction beam: Figure 3.2.2.7 shows simulated dark field TEM images, about $10 \times 10 \text{ nm}^2$ in size, of a MD sample containing a $a_0 100$ I-loop, 2 nm in diameter, for three different diffraction conditions, namely $g(1.3g)$, $g(2.1g)$ and $g(4.1g)$, and using the diffraction vector $g = (110)$. The specimen was 80 nm thick. The simulation cell was created with the I-loop located at a depth of 20 nm, corresponding to the first quarter of the depth of the foil. The contrast, minimum, maximum and average intensities in the image as a function of the depth are also displayed in Figure 3.3.3.7, together with the corresponding image.

It appears that the I-loop exhibits a light and dark bean contrast over a dark background, similar to the so-called Ashby-Brown contrast defined for precipitates [213]. In that case, one can define one bright half moon and one dark half moon. This is different from the contrast obtained with $\mathbf{g} = (200)$, for which two bright half moons are usually observed. In addition, the orientation of the I-loop, defined by the line joining the two beans, is not perpendicular to the diffraction beam because with $\mathbf{g} = (110)$ the loop is not observed edge-on. However, the I-loop image contrast exhibits a similar behavior with depth as for $\mathbf{g} = (200)$, and the increase in diffraction condition or deviation parameter, s_g , also decreases the width of the I-loop image contrast.

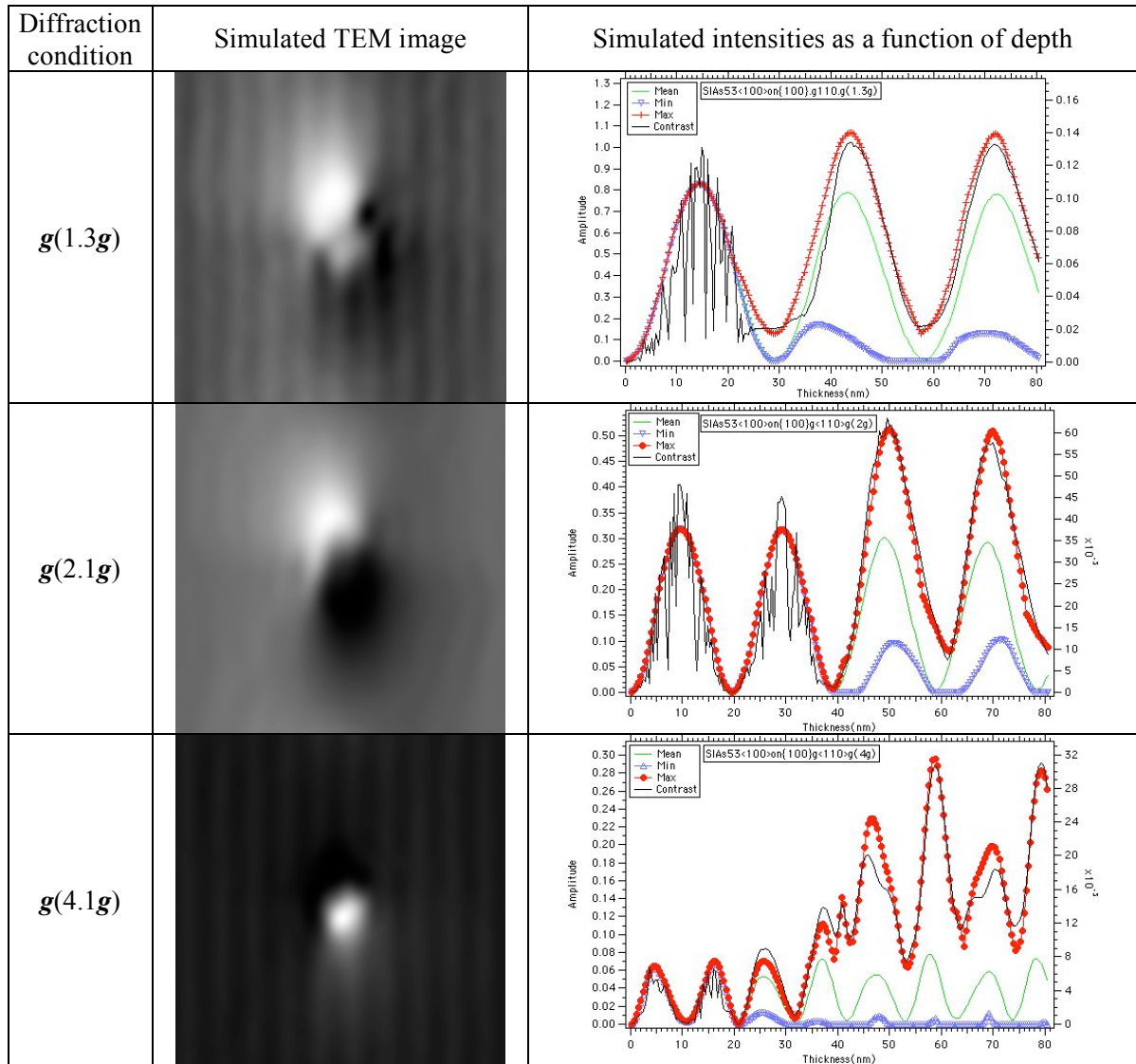


Figure 3.2.2.7: Simulated dark field TEM images, about $10 \times 10 \text{ nm}^2$ in size, of a 0.8 million atoms MD sample containing a $a_0 100$ I-loop, 2 nm in diameter, and corresponding simulated intensities as a function of depth, for three different diffraction conditions and using the diffraction vector $\mathbf{g} = (110)$, $\mathbf{z} = [-115]$.

$1/2 a_0 \langle 110 \rangle \{110\}$ I-loops:

Figure 3.2.2.8 shows simulated dark field TEM images, about $10 \times 10 \text{ nm}^2$ in size, of a MD sample containing a $1/2 a_0 110$ I-loop, 2 nm in diameter, for two different diffraction conditions, namely $g(1.3g)$ and $g(4.1g)$, and using the diffraction vector $g = (110)$. The specimen was 80 nm thick. The simulation cell was created with the I-loop located at a depth of 40 nm, corresponding to the middle of the foil. The contrast, minimum, maximum and average intensities in the image as a function of the depth are also displayed in Figure 3.2.2.8, together with the corresponding image.

The I-loop image contrast appears as two half moons. The features of the image contrast and intensities as a function of depth and diffraction conditions were found similar to those obtained for the $a_0 100$ I-loops. The change in the width of the image contrast with diffraction conditions was also found similar to the one obtained for the $a_0 100$ I-loops. As the $1/2 a_0 110$ I-loop simulated using the diffraction vector $g = (110)$ is seen edge-on, the line joining the half moons is perpendicular to the diffraction beam, as in the case of the $a_0 [100]\{100\}$ I-loop simulated using $g = (200)$. However, the image contrast of the $1/2 a_0 110$ I-loop appears less sharp than the one of the $a_0 100$ I-loop, as can be seen when comparing Figures 3.2.2.8 and 3.2.2.4 in the $g(4.1g)$ condition.

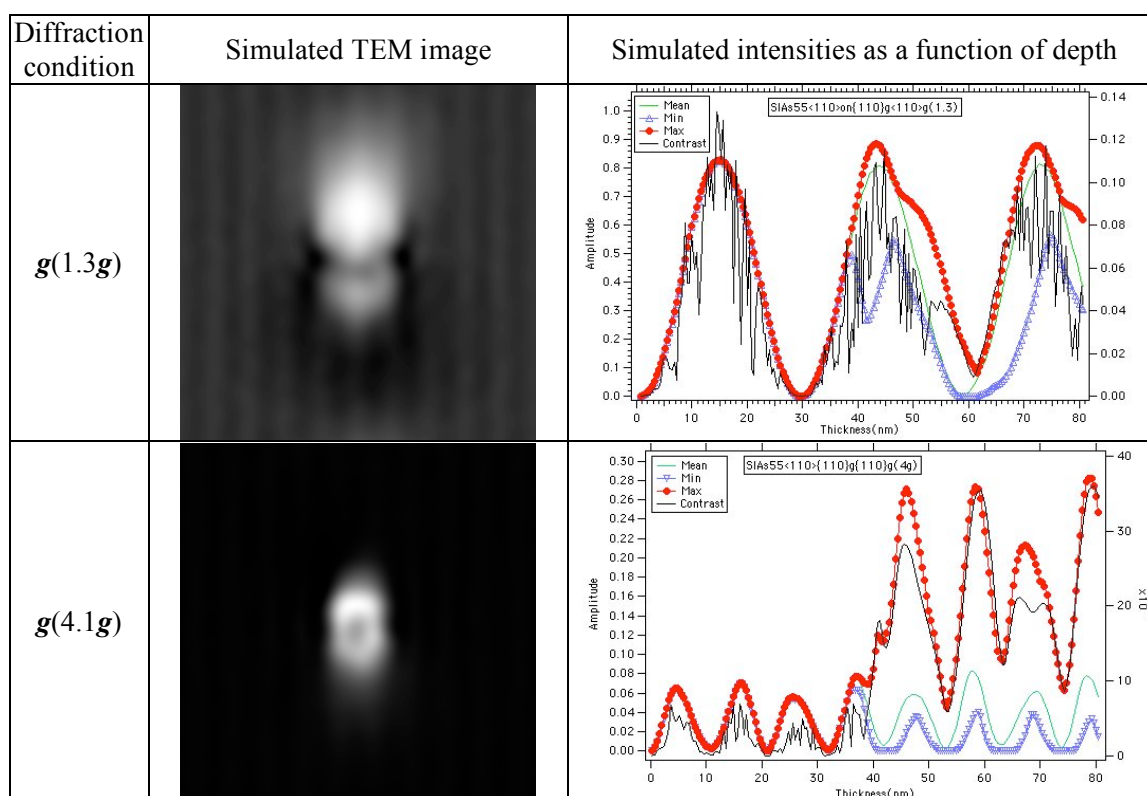


Figure 3.2.2.8: Simulated dark field TEM images, about $10 \times 10 \text{ nm}^2$ in size, of a 0.8 million atoms MD sample containing a $1/2 a_0 110$ I-loop, 2 nm in diameter, located at a depth of 40 nm, and corresponding simulated intensities as a function of depth, for two different diffraction conditions and using the diffraction vector $g = (110)$, $z = [-115]$.

Effect of I-loop depth: Figure 3.2.2.9 shows the evolution of the image intensities as a function of depth for the case of a $1/2 a_0 110$ I-loop located at two different depths of 10 and 40 nm, the specimen thickness being equal to 80 nm. One observes a strong image contrast for the loop located at 10 nm, as expected [213]. At the depth of 40 nm the contrast is still significant, contrary to what is said usually [213]. The I-loop depth in the foil was found to have no significant influence on the simulated TEM image contrasts. This observation has been made for all the defects simulated in this work and for all image simulation conditions.

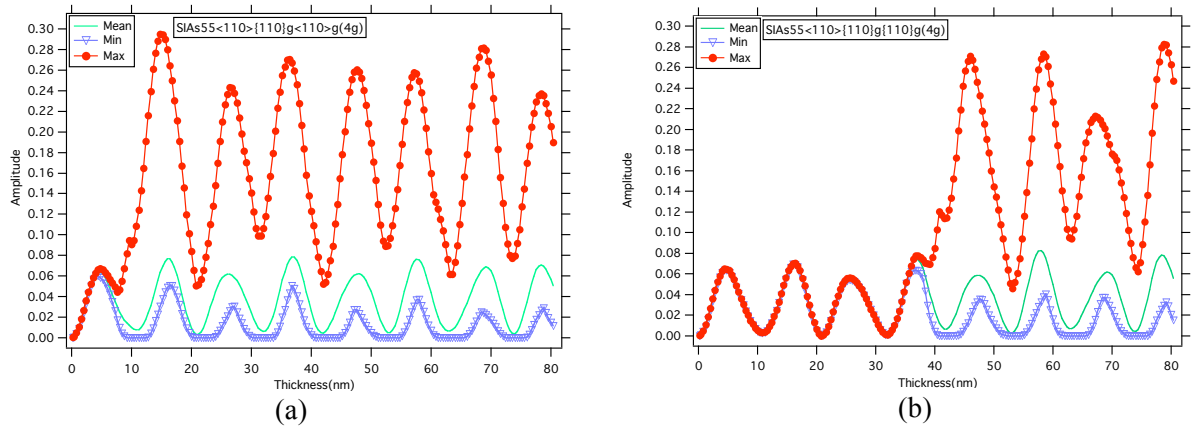


Figure 3.2.2.9: Simulated intensities as a function of depth for a 0.8 million atoms MD sample containing a $1/2 a_0 110$ I-loop, 2 nm in diameter, located at a depth of (a) 10 nm and (b) 40 nm, for the diffraction condition $g(4.1g)$ and using the diffraction vector $g = (110)$.

Effect of I-loop size: Figure 3.2.2.10 shows simulated dark field TEM images, about $10 \times 10 \text{ nm}^2$ in size, of a MD sample containing a $1/2 a_0 110$ I-loop, 1 nm in diameter, for two different diffraction conditions, namely $g(2.1g)$ and $g(4.1g)$, and using the diffraction vector $g = (110)$. The specimen was 40 or 80 nm thick with the I-loop located at a depth of 10 or 40 nm, respectively, corresponding to a zone close to the first quarter of the foil and to the middle of the foil. The contrast, minimum, maximum and average intensities in the image as a function of the depth are also displayed in Figure 3.3.3.10.

The I-loop image contrast appears as a light and dark bean contrast over a dark background in the $g(2.1g)$ condition, similar to the so-called Ashby-Brown contrast defined for precipitates [213], the operating diffraction beam being perpendicular to the line joining the two beans. However, the I-loop image contrast appears rather as a single moon in the $g(4.1g)$ condition. The features of the image contrast and intensities as a function of depth and diffraction conditions were found similar to those obtained for the $a_0 [100]\{100\}$ and $1/2 a_0 110$ I-loops with a diameter of 2 nm. The change in the width of the image contrast with diffraction conditions was also found similar to the one obtained for the $a_0 [100]\{100\}$ and $1/2 a_0 110$ I-loops with a diameter of 2 nm. However, the 1 nm I-loop exhibits a smaller TEM image contrast than the 2 nm I-loops, in direct relation to the smaller size of the I-loop.

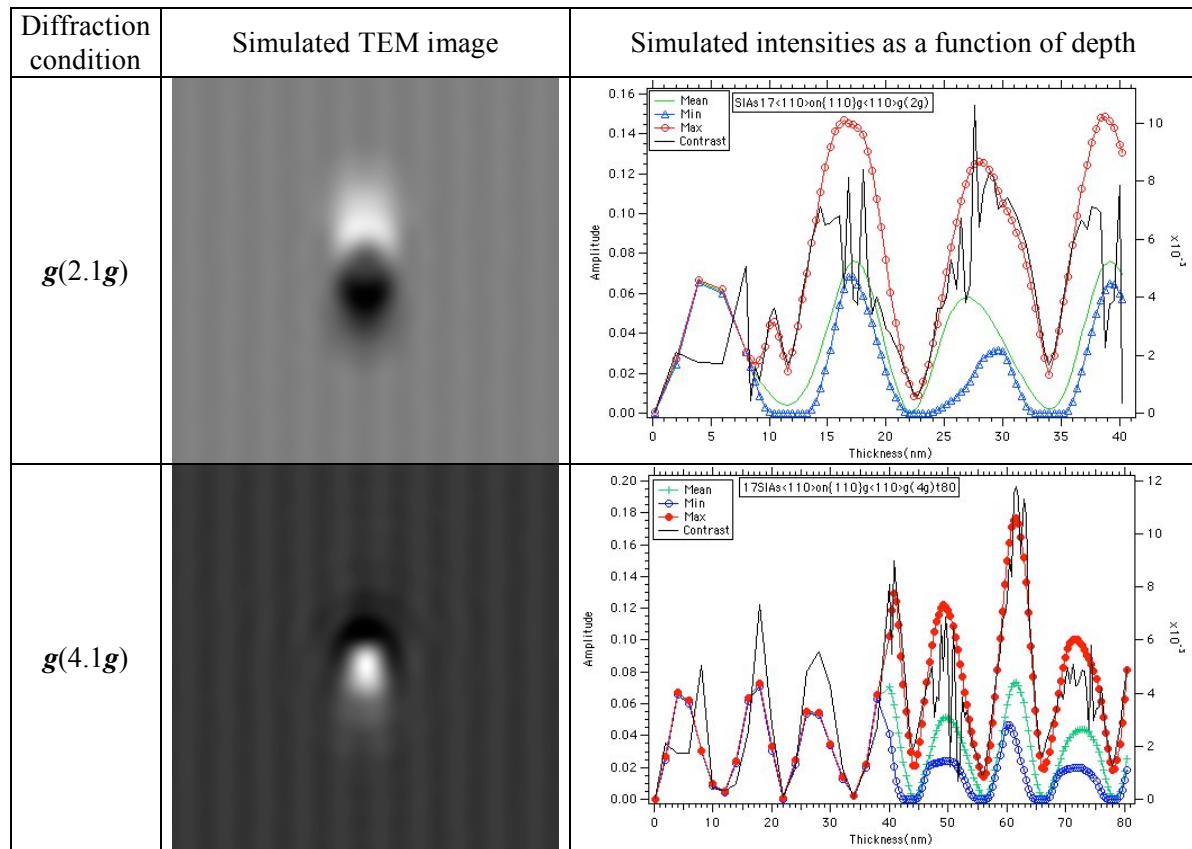


Figure 3.2.2.10: Simulated dark field TEM images, about $10 \times 10 \text{ nm}^2$ in size, of a 0.8 million atoms MD sample containing a $1/2 a_0 110$ I-loop, 1 nm in diameter, located at a depth of 10 or 40 nm in a specimen 40 or 80 nm thick, respectively, and corresponding simulated intensities as a function of depth, for two different diffraction conditions and using the diffraction vector $g = (110)$, $z = [-115]$.

Effect of operating diffraction beam: Figure 3.2.2.11 shows simulated dark field TEM images, about $10 \times 10 \text{ nm}^2$ in size, of a MD sample containing a $1/2 a_0 110$ I-loop, 2 nm in diameter, for four different diffraction conditions, namely $g(1.3g)$, $g(2.1g)$, $g(3.1g)$ and $g(4.1g)$, and using the diffraction vector $g = (200)$. The specimen was 80 nm thick. The contrast, minimum, maximum and average intensities in the image as a function of the depth are also displayed in Figure 3.2.2.11, together with the corresponding image. The I-loop image contrast appears as two overlapping half moons, not so well defined however, and the operating diffraction beam is not perpendicular to the line joining the two half moons. The features of the image contrast and intensities as a function of depth and diffraction conditions were found similar to those obtained in previous cases. The change in the width of the image contrast with diffraction conditions was also found similar to the one obtained in previous cases.

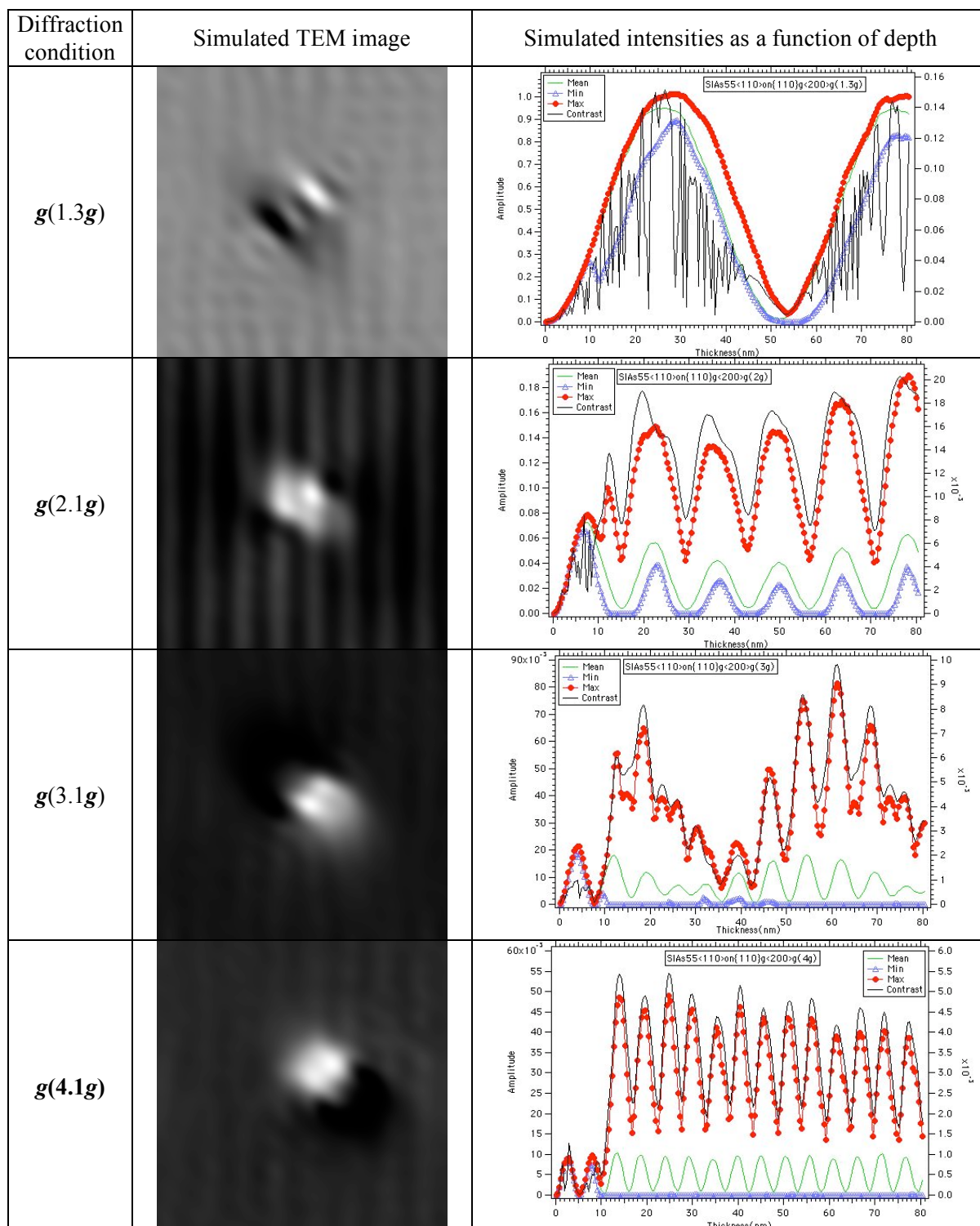


Figure 3.2.2.11: Simulated dark field TEM images, about $10 \times 10 \text{ nm}^2$ in size, of a 0.8 million atoms MD sample containing a $1/2 a_0 110$ I-loop, 2 nm in diameter, located at a depth of 10 nm, and corresponding simulated intensities as a function of depth, for four different diffraction conditions and using the diffraction vector $g = (200)$, $z = [015]$.

$1/2 a_0 \langle 111 \rangle \{110\}$ I-loops:

Figure 3.2.2.12 shows simulated dark field TEM images, about $10 \times 10 \text{ nm}^2$ in size, of a MD sample containing a $1/2 a_0 [111](110)$ I-loop, 2 nm in diameter, for two different diffraction conditions, namely $g(1.3g)$ and $g(4.1g)$, and using the diffraction vector $g = (110)$. The specimen was 80 nm thick. The contrast, minimum, maximum and average intensities in the image as a function of the depth are also displayed in Figure 3.2.2.12, together with the corresponding image.

It can be seen that the image contrast of the $1/2 a_0 [111](110)$ I-loop does not appear anymore clearly as two half moons but rather as a single big bright spot. This indicates that, experimentally, the habit plane and Burgers vector of the I-loop might be difficult to determine. The features of the image contrast and intensities as a function of depth and diffraction conditions were found similar to those obtained in previous cases. The change in the width of the image contrast with diffraction conditions was also found similar to the one obtained in previous cases.

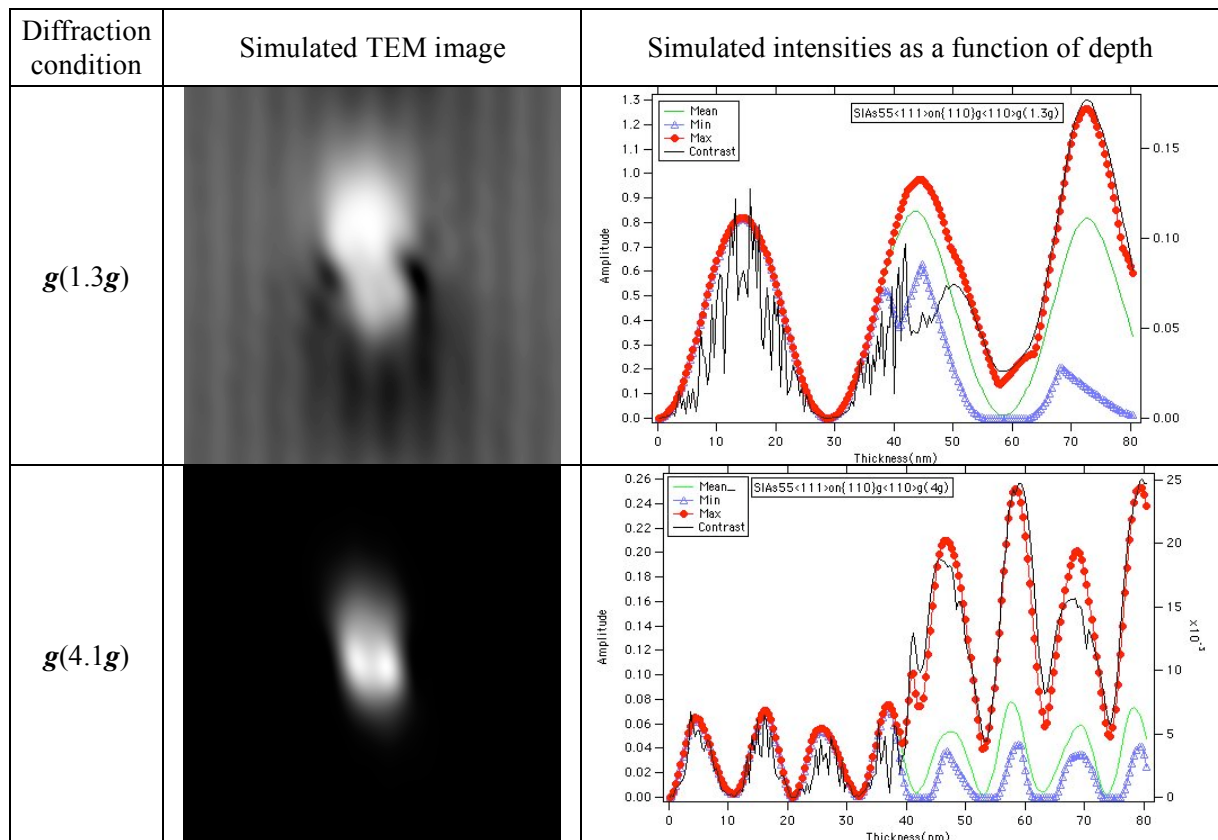


Figure 3.2.2.12: Simulated dark field TEM images, about $10 \times 10 \text{ nm}^2$ in size, of a 0.8 million atoms MD sample containing a $1/2 a_0 [111](110)$ I-loop, 2 nm in diameter, located at a depth of 40 nm, and corresponding simulated intensities as a function of depth, for two different diffraction conditions and using the diffraction vector $g = (110)$, $z = [-115]$.

Effect of the operating diffraction vector: Figure 3.2.2.13 shows simulated dark field TEM images, about $10 \times 10 \text{ nm}^2$ in size, of a MD sample containing a $1/2 a_0 [111](110)$ I-loop, 2 nm in diameter, for four different diffraction conditions, namely $\mathbf{g}(1.3\mathbf{g})$, $\mathbf{g}(2.1\mathbf{g})$, $\mathbf{g}(3.1\mathbf{g})$ and $\mathbf{g}(4.1\mathbf{g})$, and using the diffraction vector $\mathbf{g} = (200)$. The specimen was 80 nm thick. The contrast, minimum, maximum and average intensities in the image as a function of the depth are also displayed in Figure 3.2.2.13, together with the corresponding image.

The I-loop image contrast appears as two overlapping half moons, not so well defined however, and the operating diffraction beam is not perpendicular to the line joining the two half moons. The features of the image contrast and intensities as a function of depth and diffraction conditions were found similar to those obtained in previous cases. The change in the width of the image contrast with diffraction conditions was also found similar to the one obtained in previous cases. By comparing TEM image contrasts provided by the $1/2 a_0 110$ and $1/2 a_0 [111](110)$ I-loops, 2 nm in diameter, using the diffraction beam $\mathbf{g} = (200)$, it can be seen that they exhibit no significant difference, whatever the exact imaging condition being used. This indicates that, experimentally, these two kinds of I-loops cannot be distinguished from each other using a diffraction beam equal to $\mathbf{g} = (200)$.

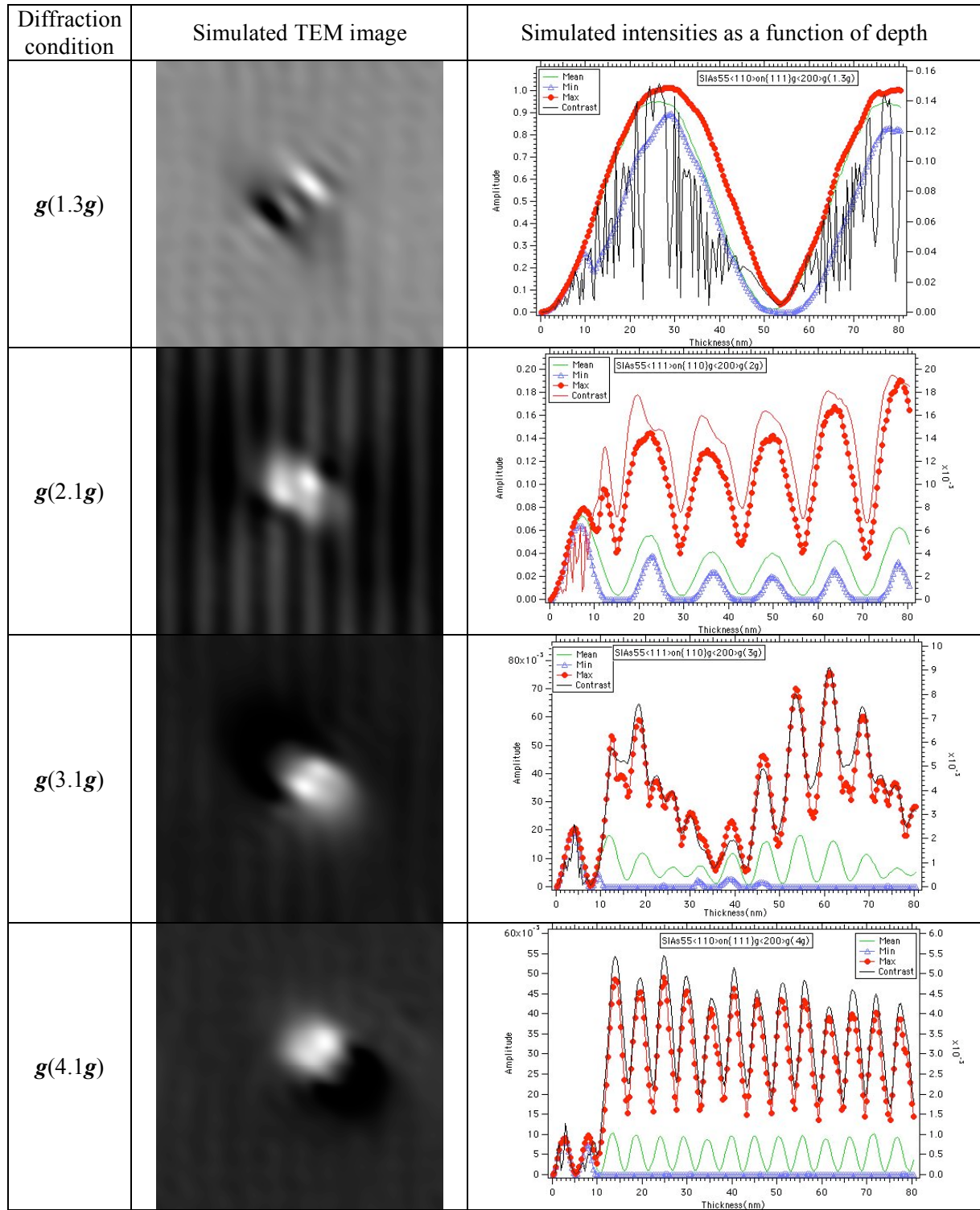


Figure 3.2.2.13: Simulated dark field TEM images, about $10 \times 10 \text{ nm}^2$ in size, of a 0.8 million atoms MD sample containing a $1/2 a_0 [111](110)$ I-loop, 2 nm in diameter, located at a depth of 10 nm, and corresponding simulated intensities as a function of depth, for four different diffraction conditions and using the diffraction vector $g = (200)$, $z = [015]$.

Voids:

Figure 3.2.2.14 shows simulated dark field TEM images, about $10 \times 10 \text{ nm}^2$ in size, of a MD sample containing a spherical void, 2 nm in diameter, for two different diffraction conditions, namely $g(2.1g)$ and $g(4.1g)$, and using the diffraction vector $g = (200)$. The specimen was 80 nm thick. The contrast, minimum, maximum and average intensities in the image as a function of the depth are also displayed in Figure 3.2.2.14, together with the corresponding image.

It can be seen in Figure 3.2.2.14 that the TEM image contrast of this small void appears as an intense bright spot. This contrast does not result so much from void-induced strain of the matrix, although some is expected, but rather from the lack of material in the cavity, which induces a strong contrast of the void with respect to the one of the matrix, due to a gap in thickness oscillations through the void.

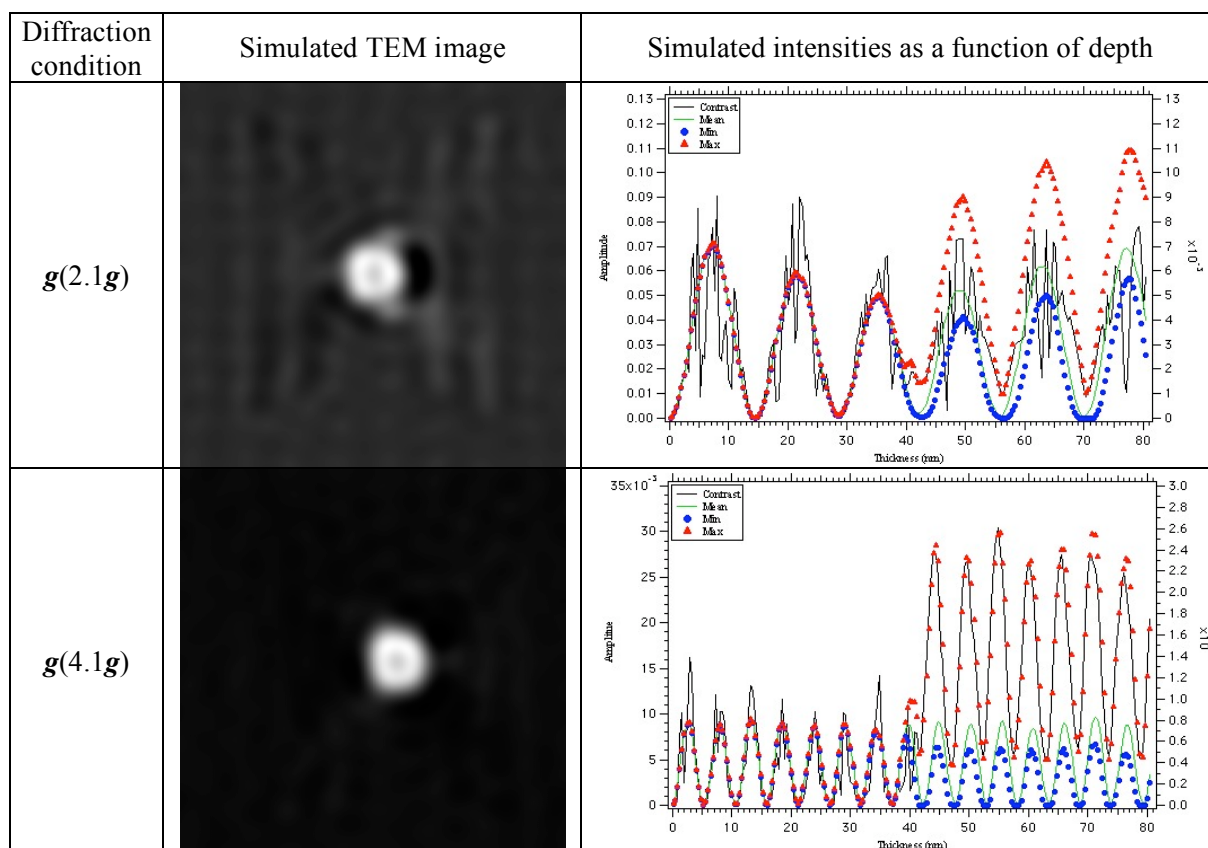


Figure 3.2.2.14: Simulated dark field TEM images, about $10 \times 10 \text{ nm}^2$ in size, of a 0.8 million atoms MD sample containing a spherical void, 2 nm in diameter, located at a depth of 40 nm, and corresponding simulated intensities as a function of depth, for two different diffraction conditions and using the diffraction vector $g = (200)$, $z = [015]$.

Helium bubbles:

Figure 3.2.2.15 shows simulated dark field TEM images, about $10 \times 10 \text{ nm}^2$ in size, of a MD sample containing a spherical He bubble, with a concentration of 100% (1:1) and 2 nm in diameter, for two different diffraction conditions, namely $g(2.1g)$ and $g(4.1g)$, and using the diffraction vector $g = (200)$. The specimen was 80 nm thick. The contrast, minimum, maximum and average intensities in the image as a function of the depth are also displayed in Figure 3.2.2.15, together with the corresponding image.

It can be seen in Figure 3.2.2.15 that the TEM image contrast of this small He bubble appears as an intense bright spot. This contrast does not result from the He contained in the cavity, as scattering of electrons by He is very weak. Like in the case of voids, the contrast does not result so much from void-induced strain of the matrix, although some is expected, but rather from the lack of material in the cavity, which induces a strong contrast with respect to the matrix due to a gap in thickness oscillations through the void. The width of the TEM image contrast of a He bubble was found to increase significantly with the He concentration.

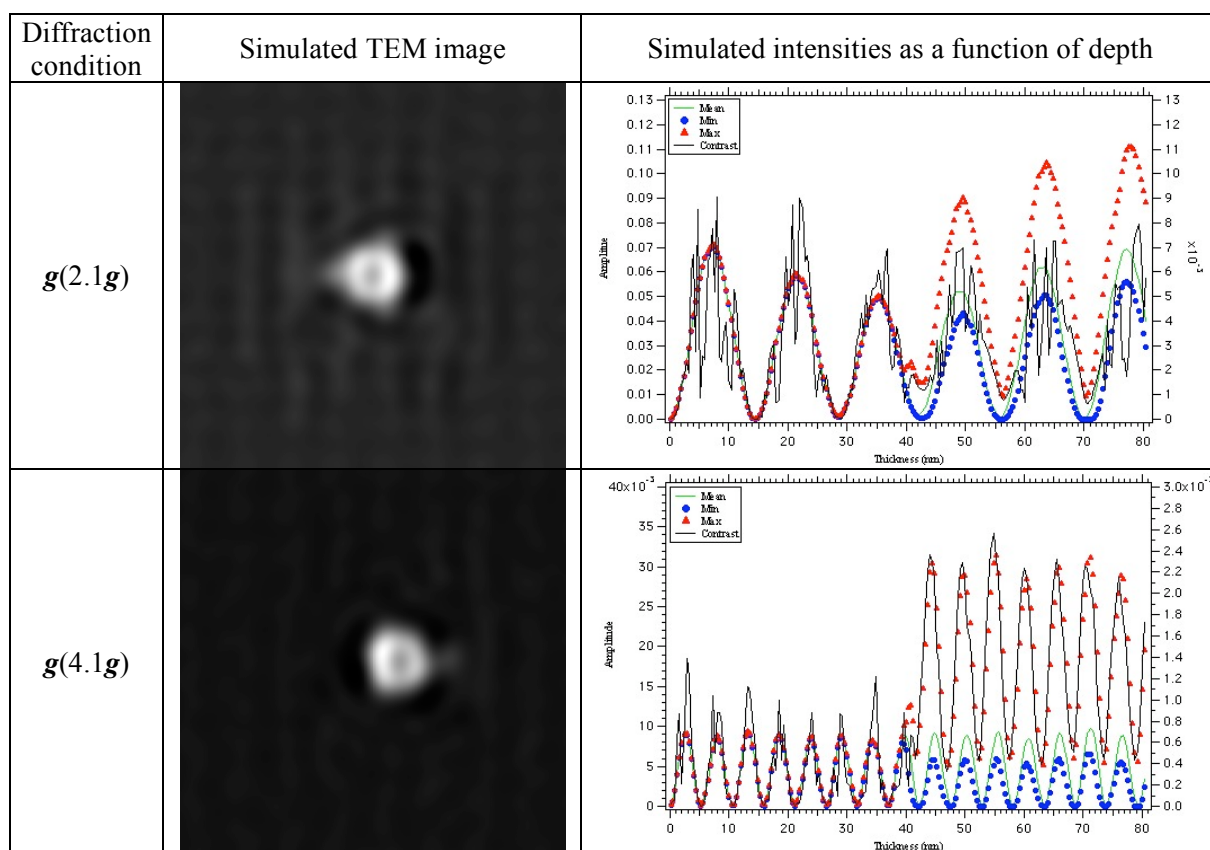


Figure 3.2.2.15: Simulated dark field TEM images, about $10 \times 10 \text{ nm}^2$ in size, of a 0.8 million atoms MD sample containing a spherical He bubble, with a concentration of 100% (1:1) and 2 nm in diameter, located at a depth of 40 nm, and corresponding simulated intensities as a function of depth, for two different diffraction conditions and using the diffraction vector $g = (200)$, $z = [015]$.

Cr precipitates:

Figure 3.2.2.16 shows simulated dark field TEM images, about $10 \times 10 \text{ nm}^2$ in size, of a MD sample containing a spherical Cr precipitate, 2 nm in diameter, for two different diffraction conditions, namely $g(2.1g)$ and $g(4.1g)$, and using the diffraction vector $g = (200)$. The specimen was 80 nm thick. The contrast, minimum, maximum and average intensities in the image as a function of the depth are also displayed in Figure 3.2.2.16, together with the corresponding image.

One would expect that the TEM image contrast of this small Cr precipitate exhibits the typical Ashby-Brown contrast arising from the strong precipitate-induced strain of the matrix, with its characteristic nearly symmetrical bright and dark lobes [214]. However, the Ashby-Brown contrast is partially hidden in Figure 3.2.2.16, due to a strong background noise made of periodic bright and dark fringes.

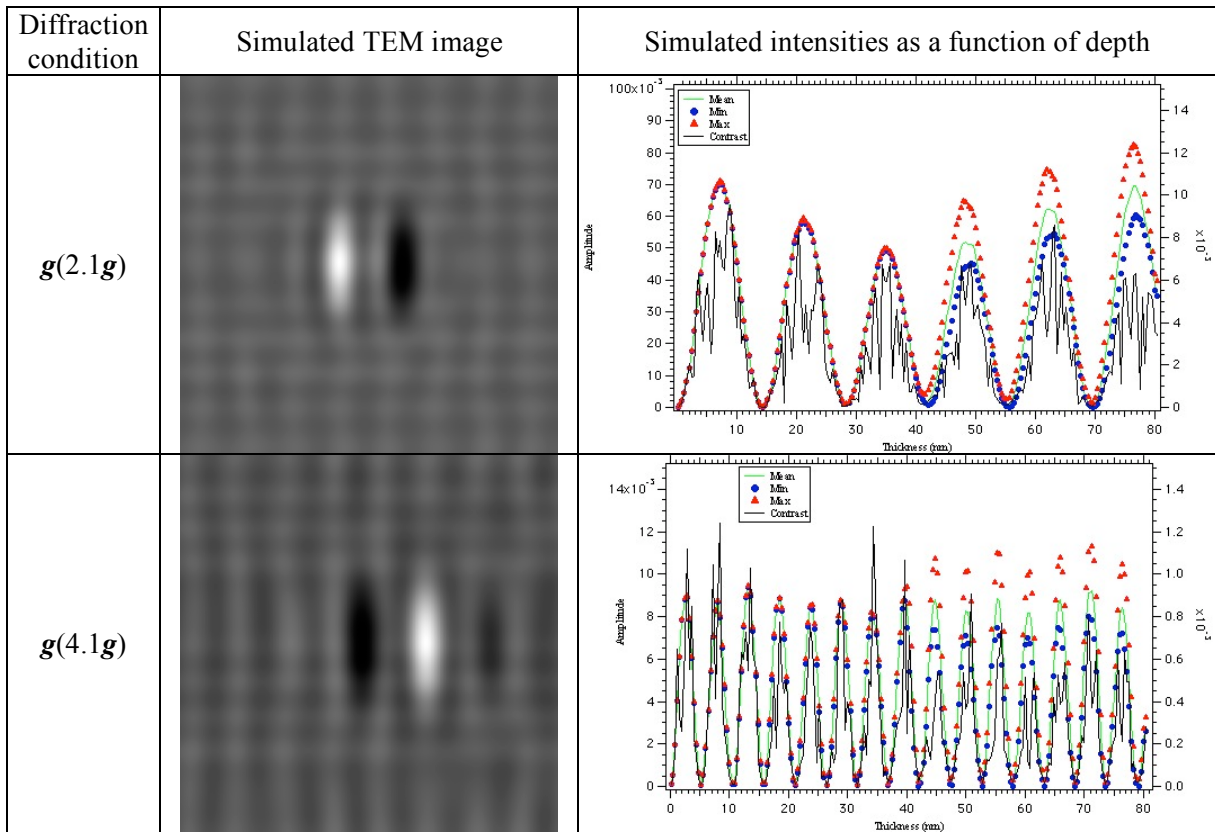


Figure 3.2.2.16: Simulated dark field TEM images, about $10 \times 10 \text{ nm}^2$ in size, of a 0.8 million atoms MD sample containing a spherical Cr precipitate, 2 nm in diameter, located at a depth of 40 nm, and corresponding simulated intensities as a function of depth, for two different diffraction conditions and using the diffraction vector $g = (200)$, $z = [015]$.

3.2.3 SANS signal simulations

We present here the results of simulations of the SANS signal provided by the defects created by MD simulations, for interpreting the results of SANS experiments. The simulations of the SANS signal were performed using the method described under § 2.4.3.

Figure 3.2.3.1 shows examples of simulated electron and neutron diffraction patterns for a perfect α -Fe sample containing 0.1 million atoms, which were obtained using a wavelength of electrons and neutrons of 0.00251 nm and 0.0350 nm, respectively, and a neutron scattering constant, b_c , equal to 9.452, 3.263 and 3.6357 fm for α -Fe, He and Cr, respectively (see Table 2.3.1.1). Note that the neutron wavelength that was used in the further SANS signal simulations is the one of the SANS facility at the PSI, namely $\lambda = 0.450$ nm.

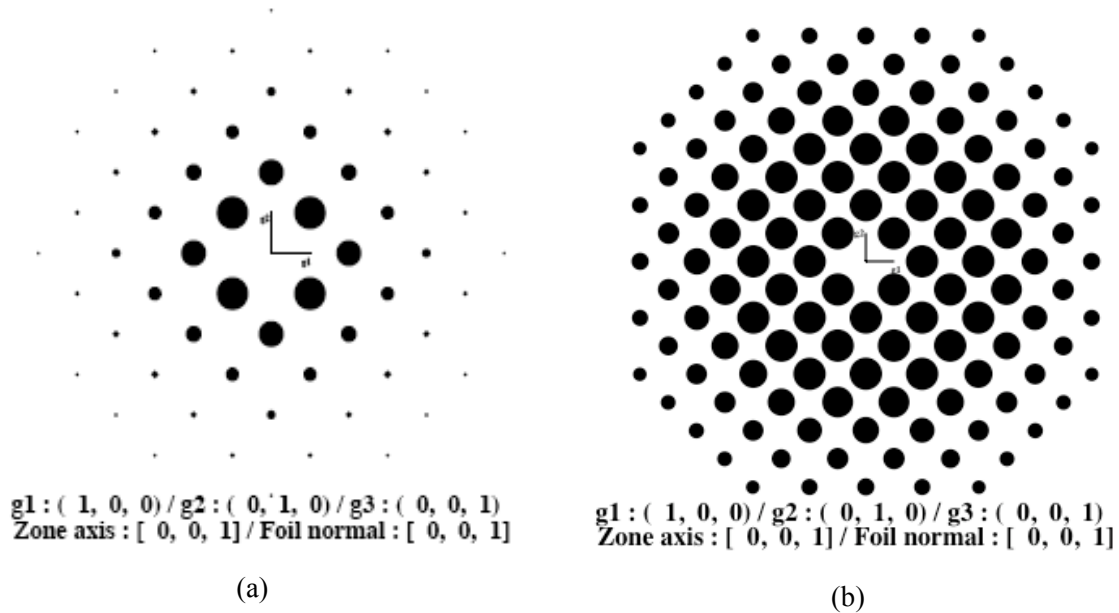


Figure 3.2.3.1: Simulated (a) electron and (b) neutron diffraction patterns of a perfect α -Fe sample.

Figure 3.2.3.2 shows simulated neutron diffraction intensity data versus Q values, which were obtained from the 2D neutron diffraction patterns of a perfect MD specimen of pure Fe and MD specimens containing the damage produced by atomic displacement cascades in pure Fe, Fe-0.1 at.% He(I) and Fe-0.1 at.% He(S), using a simulation cell of $18 \times 18 \times 18$ nm³, a temperature of 10 K and a PKA energy of 10 keV. It can be seen that the simulated SANS intensity decreases with increasing Q values. It can be also seen that the SANS intensity is the lowest for the perfect, i.e., unirradiated, specimen. Irradiated specimens exhibit a much larger SANS intensity. At very small Q values (< 0.4 nm⁻¹), pure Fe exhibits the highest SANS signal, while at larger Q values Fe-0.1 at.% He(S) exhibits a much larger SANS signal than pure Fe and Fe-0.1 at.% He(I). At very large Q values (≥ 5.4 nm⁻¹), no differences in the SANS intensity are detected any more.

These results indicate that the size of defect clusters produced by atomic displacement cascades is much larger in pure Fe than in He-containing specimens, revealing that small-sized defect clusters are actually stabilized by the presence of He, hindering subsequent diffusion, agglomeration and growing of defect clusters. In addition, it appears that the number density of small irradiation-induced effects is significantly larger in Fe-0.1 at.% He(S) than in pure Fe and in Fe-0.1 at.% He(I). Indeed, as already pointed out, during the first stage of an atomic displacement cascade, a substitutional He atom can be easily kicked out from its position to form a vacancy and an interstitial He atom.

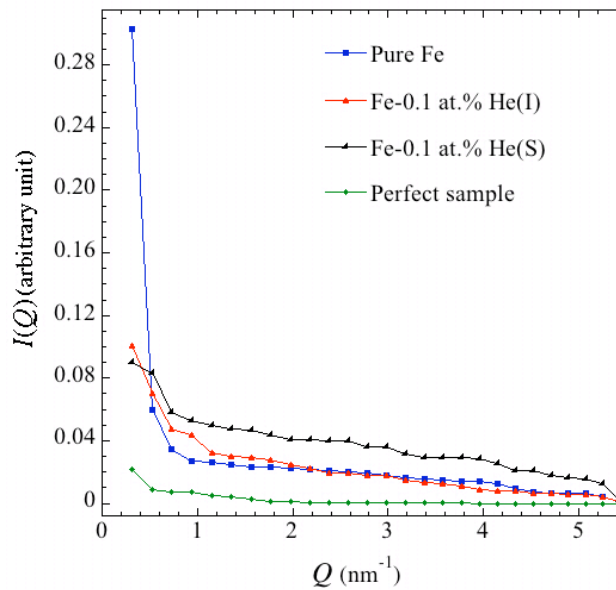


Figure 3.2.3.2: Simulated SANS intensity data versus Q values for a perfect MD specimen of pure Fe and MD specimens containing the damage produced by atomic displacement cascades in pure Fe, Fe-0.1 at.% He(I) and Fe-0.1 at.% He(S), using a simulation cell of $18 \times 18 \times 18 \text{ nm}^3$, a temperature of 10 K and a PKA energy of 10 keV.

Figure 3.2.3.3 shows simulated neutron diffraction intensity data versus Q values, which were obtained from the 2D neutron diffraction pattern of a MD specimen of pure Fe containing a spherical void, 2 nm in diameter, for four different incident beam directions. It can be seen that the SANS intensity decreases with increasing Q values, whatever the incident beam direction. The final SANS intensity data versus Q values were obtained by performing a rotational average of the 2D neutron diffraction pattern, i.e., by averaging the data obtained for the four incident beam directions. Results are shown in Figure 3.2.3.4.

The theoretical SANS intensity versus Q values, which was calculated analytically using the equation (3.1.4.1), is also reported in Figure 3.2.3.4 for comparison purposes. It appears that there is a good agreement between the two approaches. The scatter in the simulated SANS intensity, relative to the calculated one, stems from the limited sampling of the 2D neutron diffraction pattern.

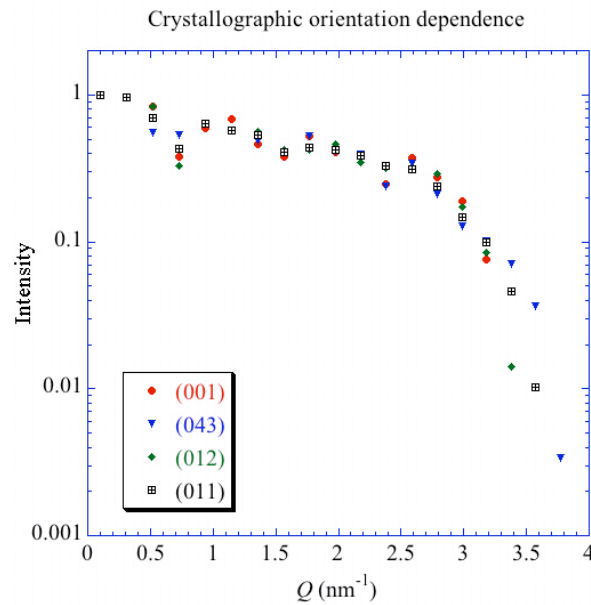


Figure 3.2.3.3: Simulated SANS intensity data versus Q values for a MD specimen of pure Fe containing a spherical void, 2 nm in diameter, using four different incident beam directions: (001), (012), (011), and (043).

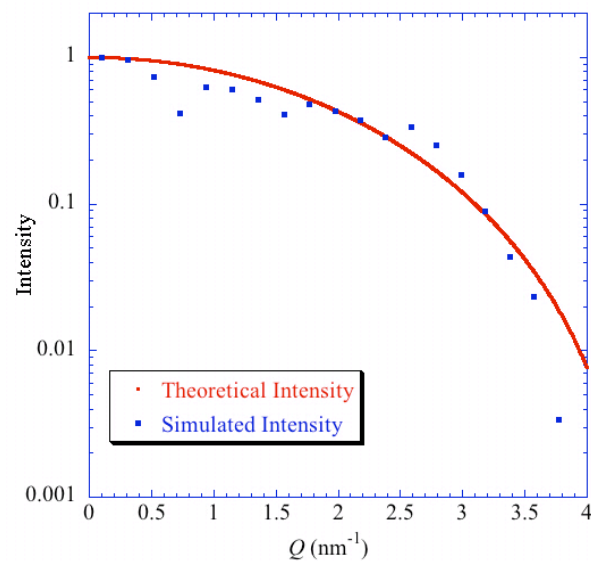


Figure 3.2.3.4: Comparison between the averaged simulated SANS intensity data versus Q values, for a MD specimen of pure Fe containing a spherical void, 2 nm in diameter, and the theoretical SANS intensity, calculated using the equation (3.1.4.1), versus Q values.

The neutron intensity scattered by a population of small dislocation loops with an isotropic distribution of orientations was calculated using a continuum approach by A. Seeger and M. Rühle [215]. More recently, it was shown that the neutron intensity scattered by dislocation loops is three orders of magnitude smaller than the neutron intensity scattered by an He-implanted sample containing mainly He bubbles [76].

Figure 3.2.3.5 shows simulated neutron diffraction intensity data versus Q values, which were obtained from 2D neutron diffraction patterns of a perfect MD specimen of pure Fe and MD specimens of pure Fe containing a spherical void, 2 nm in diameter, or a $a_0 \langle 100 \rangle \{100\}$ I-loop, 2 nm in diameter. It can be seen that the simulated SANS signal provided by a simple void is much higher than the one provided by a dislocation loop. In fact, there is almost no difference between the simulated SANS signal arising from a perfect crystal and the one arising from a dislocation loop. Therefore, in practice, the SANS signal provided by dislocation loops will be hidden by the experimental noise.

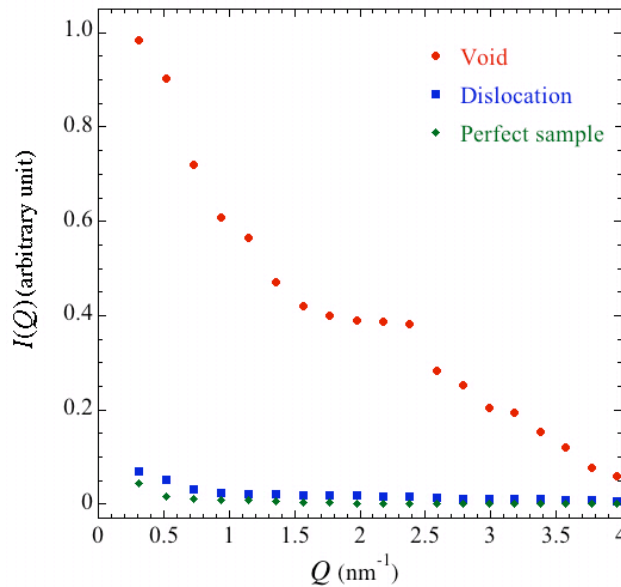


Figure 3.2.3.5: Simulated SANS intensity data versus Q values for a perfect MD specimen of pure Fe and MD specimens of pure Fe containing a void, 2 nm in diameter, or a $a_0 \langle 100 \rangle \{100\}$ I-loop, 2 nm in diameter.

Figure 3.2.3.6 shows simulated neutron diffraction intensity data versus Q values, which were obtained from 2D neutron diffraction patterns of a perfect MD specimen of pure Fe and MD specimens of pure Fe containing a spherical He bubble, 2 nm in diameter, with different He concentrations: 0% (void), 50% (1:2), 100% (1:1), 200% (2:1), 300% (3:1). It can be seen that the SANS signal provided by a He bubble is much higher than the one provided by a perfect crystal but significantly lower than the SANS signal provided by a void. In addition, the SANS signal of a He bubble decreases with increasing He concentration inside the cavity and tends to saturation for a He concentration of 200% (2:1).

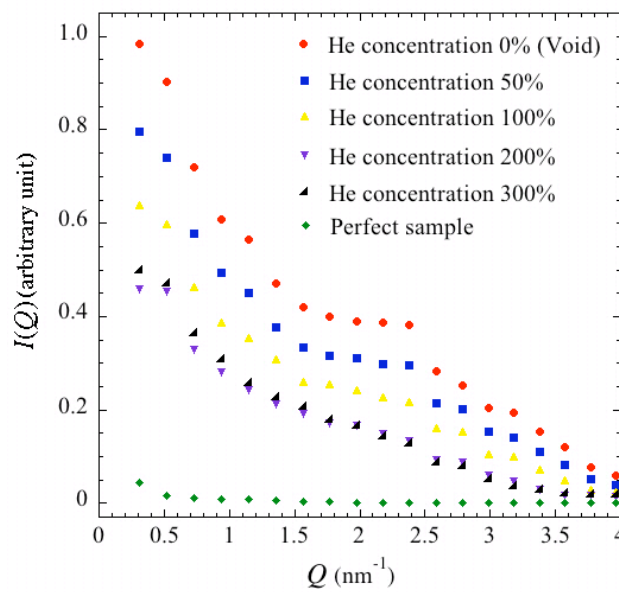


Figure 3.2.3.6: Simulated SANS intensity data versus Q values for a perfect MD specimen of pure Fe and MD specimens of pure Fe containing a He bubble, 2 nm in diameter, with different He concentrations: 0% (void), 50% (1:2), 100% (1:1), 200% (2:1), 300% (3:1).

Figure 3.2.3.7 shows simulated neutron diffraction intensity data versus Q values, which were obtained from 2D neutron diffraction patterns of a perfect MD specimen of pure Fe and MD specimens of pure Fe containing a spherical void, 2 nm in diameter, or a spherical Cr precipitate, 2 nm in diameter. It can be seen that the SANS signal provided by the Cr precipitate is much higher than the SANS signal provided by a perfect crystal. However, it appears significantly lower than the SANS signal provided by a void. It is actually more or less similar to the SANS signal provided by a He bubble with a He concentration of 100% (1:1), as expected, the neutron scattering constant, b_c , for chromium being very close to the one for helium.

Therefore, in practice, apart dislocation loops, all other possible types of irradiation-induced defects in pure Fe can be detected by means of the SANS technique. However, as there is only a very small difference between the SANS signal provided by a Cr precipitate and the one provided by a He bubble, these two kinds of defects appear difficult to distinguish from each other by using the SANS technique.

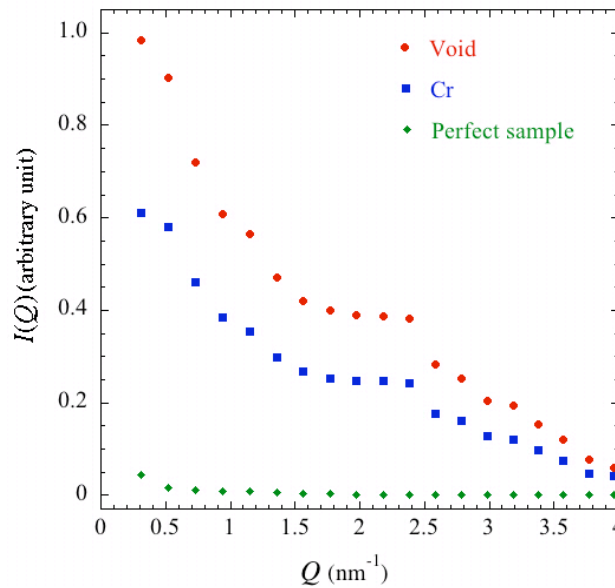


Figure 3.2.3.7: Simulated SANS intensity data versus Q values for a perfect MD specimen of pure Fe and MD specimens of pure Fe containing a void, 2 nm in diameter, or a Cr precipitate, 2 nm in diameter.

Note that in the cases of voids, He bubbles and Cr precipitates the sharp decrease of the scattering intensity occurring at a Q value about 2.50 nm^{-1} is due to statistical errors arising from the used spherical averaging method.

CHAPTER 4: DISCUSSION

4.1 SANS experiments

4.1.1 Size of irradiation-induced defects

The mean size (radius) of small and large irradiation-induced effects in the EUROFER 97 RAFM steel is summarized in Table 4.1.1.1 as a function of irradiation dose and temperature. It can be seen that the mean size decreases with increasing dose, whatever the irradiation temperature and the type of defects (small versus large). This indicates that defects mostly accumulate but not coarsen during the course of irradiation at a given temperature.

The mean size of small irradiation-induced defects evidenced in specimens irradiated to 0.3 or 1.0 dpa increases with temperature, while the mean size of small irradiation-induced effects evidenced in samples irradiated to 2.0 dpa shows no significant dependence on temperature between 50 and 250°C. This indicates that small defects irradiated to a given low dose tend to coarsen when the temperature is increased. It seems that small defects are quite unstable at low doses and reach some size stability at larger doses.

The mean size of large defects evidenced in specimens irradiated to 2.0 dpa appears to increase with temperature between 50 and 250°C. Like in the case of small defects, this indicates that large defects tend to coarsen when the temperature is increased.

It has to be noted that a large part of the small defects evidenced in SANS have a size well below the TEM resolution limit in weak beam imaging, i.e., about 1 nm.

Dose (dpa)	Mean size at 50°C (nm)		Mean size at 250°C (nm)		Mean size at 350°C (nm)	
	R_1	R_2	R_1	R_2	R_1	R_2
0.3	0.42673	-	0.88559	-	1.0230	-
1.0	0.40178	2.7262	0.80770	-	0.86787	-
2.0	0.29309	0.70306	0.28525	2.1798	-	-

Table 4.1.1.1: Mean size (radius) of small (R_1) and large (R_2) irradiation-induced defects in the EUROFER 97 RAFM steel as a function of irradiation dose and temperature.

4.1.2 Number density of irradiation-induced defects

The number density of small and large irradiation-induced effects in the EUROFER 97 RAFM steel is summarized in Table 4.1.1.2 as a function of irradiation dose and temperature. As the number density is expressed in arbitrary units the absolute values have no real sense. Only the tendencies with dose and temperature are actually meaningful.

It can be seen that the number density increases with dose, whatever the irradiation temperature and the type of defects (small versus large). This confirms the behavior of the mean size versus dose and the idea that defects mostly accumulate but not coarsen during the course of irradiation at a given temperature.

The number density of small irradiation-induced defects evidenced in specimens irradiated to a given dose tends to decrease with increasing temperature. This effect is much less important at 2.0 dpa than at 0.3 and 1.0 dpa, however. This confirms the idea that small defects tend to disappear with increasing temperature, probably by coarsening phenomenon, as shown by mean size measurements, and that small defects are quite unstable at low doses and reach some size and number density stability at larger doses.

The number density of large defects evidenced in specimens irradiated to 2.0 dpa appears to decrease with increasing temperature between 50 and 250°C. Like in the case of small defects, this indicates that large defects tend to disappear by coarsening phenomenon when the temperature is increased.

Dose (dpa)	Number density N 50°C		Number density N 250°C		Number density N 350°C	
	N_1	N_2	N_1	N_2	N_1	N_2
0.3	0.0121	-	0.9760×10^{-4}	-	1.99×10^{-5}	-
1.0	0.0202	1.5793×10^{-6}	2.6216×10^{-4}	-	2.88×10^{-5}	-
2.0	0.1337	2.4632×10^{-4}	0.1294	0.5553×10^{-5}	-	-

Table 4.1.2.1: Number density (in arbitrary units) of small (N_1) and large (N_2) irradiation-induced defects in the EUROFER 97 RAFM steel as a function of dose and temperature.

4.1.3 Geometry of irradiation-induced defects

In SANS the asymptotic behavior of the scattered intensity provides useful information about the geometry of scattering objects. Assuming a dilute and dispersed system of scattering objects, the scattered intensity is then proportional to $Q^{-\gamma}$ for large Q values (Q being the magnitude of the diffraction vector), according to the Porod law [84, 98, 99], as described in § 1.3.7 and § 1.3.8. $\gamma=4$ corresponds to three-dimensional scattering objects, $\gamma=2$ to two-dimensional scattering objects (surface scattering), $\gamma=1$ to elongated scattering objects and $\gamma<1$ to fractal objects. In the latter case, the number distribution of scattering objects of mass M is given by equation (1.3.8.12), where τ is the polydispersity exponent, M_z is the z -averaged mass, as given by equation (1.3.8.13) and $h(M/M_z)$ is a scaling function for the polydispersity, which decays rapidly for $M > M_z$. $\tau=2.2$ for three-dimensional percolation model and $\tau=2.5$ for Bethe lattice. The polydispersity averaged scattered intensity $I(q)$ is given by equation (1.3.8.14). The asymptotic behavior of $I(q)$ for polydispersed mass fractals is given by equation (1.3.8.15). When $\tau > 2.5$, $D(3-\tau) < 1$, where D is the fractal dimension [84].

Figure 4.1.3.1 shows a plot of $\ln I(Q)$ versus $\ln Q$ over the Q -range 1-4.7 nm⁻¹ for an unirradiated specimen of the EUROFER 97 RAFM steel. The obtained results can be divided into two regions: (1) for Q values above about 1.87 nm⁻¹ the $\ln I(Q)$ values appears more or less constant, typical of a uniform matrix with no nano-sized defects; (2) for Q values below about 1.87 nm⁻¹ the $\ln I(Q)$ values decrease with increasing $\ln Q$ values, which corresponds to a γ value of about 4.0772. This value is indicative of three-dimensional objects, such as precipitates, having a size larger than the nanometer.

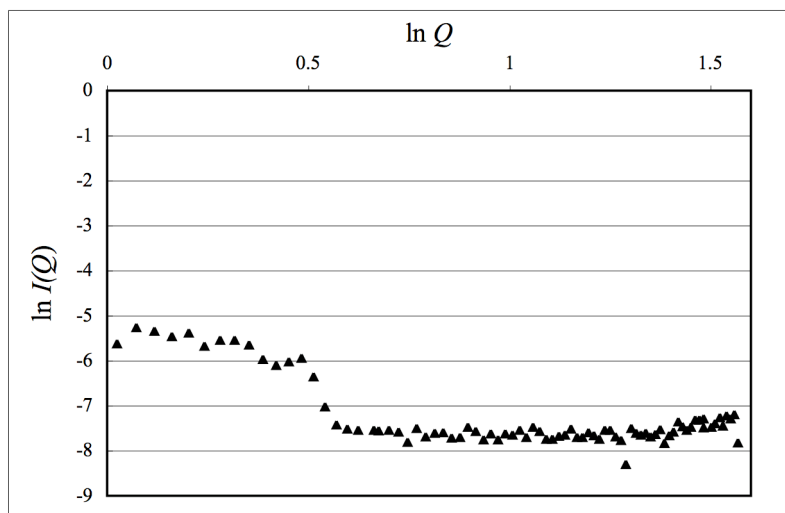


Figure 4.1.3.1: $\ln I(Q)$ versus $\ln Q$ for an unirradiated specimen of the EUROFER 97 RAFM steel.

Figure 4.1.3.2 shows plots of $\ln I(Q)$ versus $\ln Q$ over the Q -range $1\text{--}4.7\text{ nm}^{-1}$ for specimens of the EUROFER 97 RAFM steel irradiated either at 50°C to 0.3, 1.0 or 2.0 dpa or at 250°C to 2.0 dpa. It can be seen that the $\ln I(Q)$ values decrease with increasing $\ln Q$ values, over the whole Q -range investigated. Corresponding γ values are equal to 0.2652, 0.6377, 0.5254 and 0.3195. Therefore, at the given temperature of 50°C the γ value is maximal for the dose of 1.0 dpa. At the given dose of 2.0 dpa the γ value decreases with increasing temperature from 50 to 250°C . The obtained γ values are indicative of fractal irradiation-induced defects, such as helium bubbles, with a nanometer size or above.

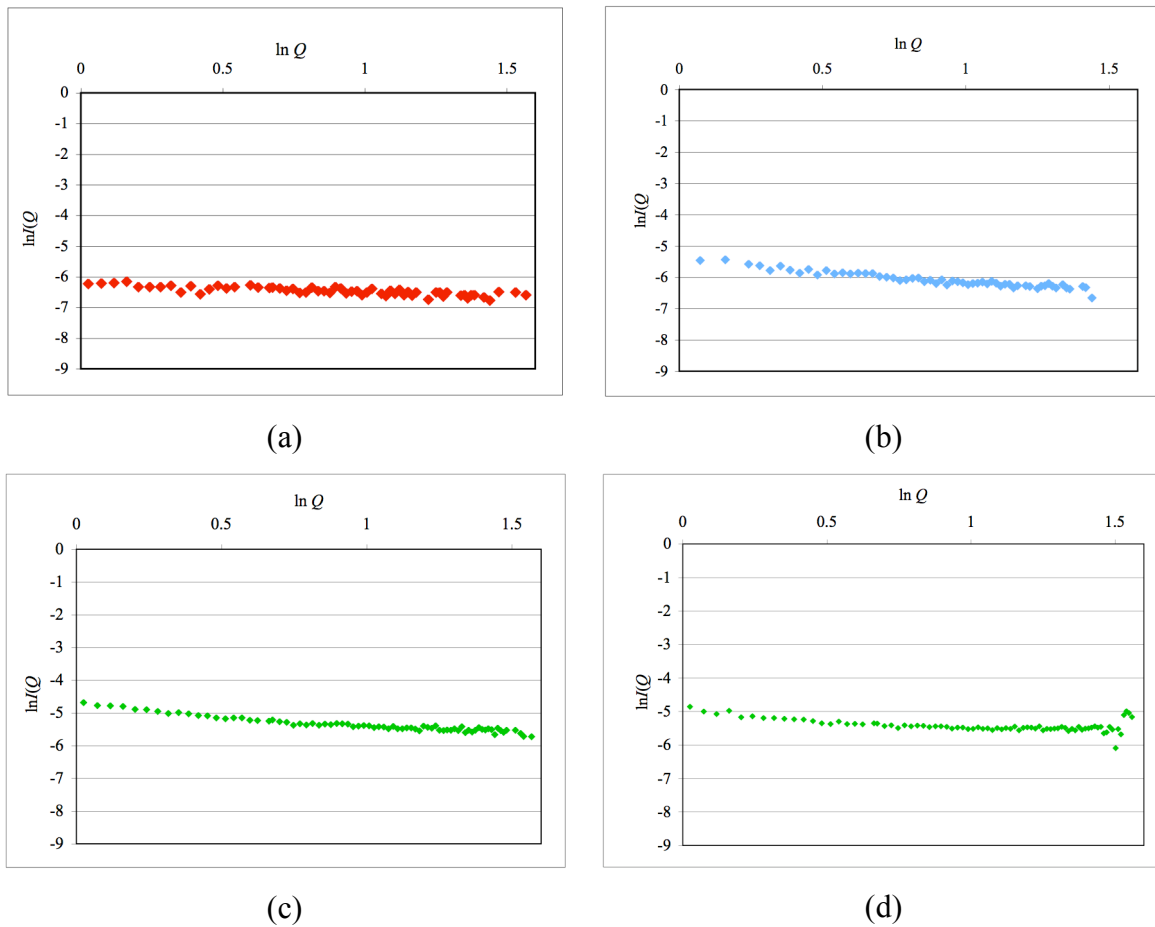


Figure 4.1.3.2: $\ln I(Q)$ versus $\ln Q$ for specimens of the EUROFER 97 RAFM steel irradiated at 50°C to (a) 0.3 dpa, (b) 1.0 dpa, and (c) 2.0 dpa, and at (d) 250°C to 2.0 dpa. Corresponding γ values are equal to 0.26523, 0.63774, 0.52536 and 0.31946.

4.1.4 Type of irradiation-induced defects

A variety of small irradiation-induced defects may contribute to the additional SANS intensity scattered by irradiated specimens of RAFM steels at large Q values. These include cascade damage (vacancies, interstitials, clusters of vacancies, clusters of interstitials) nanometer-sized cavities (voids and/or helium bubbles), precipitates and dislocation loops.

Although SANS experiments provided us important information about the mean size, relative number density and geometry (via the γ value) of the irradiation-induced defects, their actual type is more difficult to assess with certainty.

Our simulations of the SANS signal arising from either cascade damage or various types of dislocation loops, or a void, or a helium bubble, or a precipitate, revealed that the contribution of cascade damage and dislocation loops to the SANS signal can be considered as negligible.

Fe-rich (α) and Cr-rich (α') precipitates have not been observed in RAFM steels in the unirradiated state. On the contrary, such precipitates are frequently observed by means of TEM in RAFM steels having a Cr content above a critical threshold value (about 7.2 at% at 325°C). However, they usually exhibit a mean size well above 1 nm. The relatively low irradiation doses investigated in the present study are not expected to lead to phase separation in RAFM steels and then to the formation of α - α' precipitates. However, their production under the irradiation conditions investigated in the present work cannot be totally excluded.

Therefore, the small irradiation-induced evidenced in RAFM steels using the SANS technique could be either nano-sized cavities (voids and/or helium bubbles) and/or precipitates. In order to clarify this point, the A parameter has been calculated for a large number of possible, nano-sized, irradiation-induced defects in RAFM steels.

Indeed, when applying a saturating magnetic field to the sample during SANS experiments, it is possible to obtain information about the nature of the scattering objects by calculating the A parameter that is the ratio of the magnetic plus nuclear scattering to the nuclear scattering. In the case of a system composed of a matrix and one type of defects, the A parameter can be written as:

$$A = 1 + \left(\frac{b_m^{matrix} / \Omega^{matrix} - b_m^{defect} / \Omega^{defect}}{b_n^{matrix} / \Omega^{matrix} - b_n^{defect} / \Omega^{defect}} \right)^2 \quad (4.1.4.1),$$

where b_m^{matrix} and b_n^{matrix} are the coherent magnetic and nuclear scattering lengths of the matrix, respectively, b_m^{defect} and b_n^{defect} are the coherent magnetic and nuclear scattering lengths of the defects, respectively, and Ω^{matrix} and Ω^{defect} are the average atomic volumes of the matrix and the defects, respectively.

In the case of voids, equation (4.1.4.1) reduces to:

$$A = 1 + \left(\frac{b_m^{matrix} / \Omega^{matrix}}{b_n^{matrix} / \Omega^{matrix}} \right)^2 \quad (4.1.4.2).$$

In the case of helium bubbles, equation (4.1.4.1) reduces to:

$$A = 1 + \left(\frac{b_m^{matrix} / \Omega^{matrix}}{b_n^{matrix} / \Omega^{matrix} - b_n^{He} / \Omega^{He}(r)} \right)^2 \quad (4.1.4.3).$$

$\Omega^{He}(r)$ is directly related to the helium pressure inside a bubble, which is expected to depend on the bubble size (r). b_n^{matrix} was calculated from the coherent nuclear scattering lengths of the different elements in solid solution in the matrix of the EUROFER 97 RAFM steel:

$$b_n^{matrix} = \sum_i b_n^i f_i \quad (4.1.4.4),$$

where b_n^i is the coherent nuclear scattering length of the element i and f_i is the atomic percentage of the element i in the matrix. b_n^{matrix} was determined to be 8.7828 fm and $\Omega^{matrix} = 11.8170 \text{ \AA}^3$ for the matrix of the EUROFER 97 RAFM steel. b_n^{He} was determined to be 3.263 fm and $\Omega^{He} = 39.50 \text{ \AA}^3$ (Van der Waals atomic volume of He). Therefore:

$$\Delta\rho_n = \frac{b_n^{matrix}}{\Omega^{matrix}} = 7.4322 \times 10^{10} \text{ cm}^{-2} \quad \text{for voids} \quad (4.1.4.5),$$

$$\Delta\rho_n = \frac{b_n^{matrix}}{\Omega^{matrix}} - \frac{b_n^{He}}{\Omega^{He}} = 6.6063 \times 10^{10} \text{ cm}^{-2} \quad \text{for He bubbles} \quad (4.1.4.6).$$

b_m^{matrix} was determined using the following equation:

$$b_m^{matrix} = (\gamma_m e / 2m_0 c^2) f(q) \mu_m \quad (4.1.4.7),$$

where γ_m is the magnetic moment of neutrons, e and m_0 are the electron charge and mass, respectively, $f(q)$ is the atomic form factor, which is equal to 1 at small angle, and μ_m is the mean magnetic moment per matrix atom, which was calculated as follows [216]:

$$\mu_m = M_0 - M_1 C_{Cr} \quad (4.1.4.8),$$

where C_{Cr} is the chromium concentration in the matrix of the EUROFER 97 RAFM steel. M_0 and M_1 are equal to 2.20 and 2.39 μ_B per atom, respectively, where μ_B is the Bohr magneton. b_m^{matrix} was determined to be 5.2388 fm. Therefore, for all non-magnetic defects, like voids, pure helium clusters or bubbles, pure chromium carbides and so on:

$$\Delta\rho_m = \frac{b_m^{matrix}}{\Omega^{matrix}} = 4.4333 \times 10^{10} \text{ cm}^{-2} \quad (4.1.4.9).$$

The neutron and magnetic scattering length density, ρ_n and ρ_m , the neutron and magnetic scattering contrast, $\Delta\rho_n$ and $\Delta\rho_m$, and the A value for a large number of possible, nano-sized, irradiation-induced defects in the EUROFER 97 RAFM steel are listed in Table 4.1.4.1.

Type of nano-sized irradiation-induced defects	Neutron scattering length density ρ_n (10^{10} cm^{-2})	Neutron scattering contrast $\Delta\rho_n$ (10^{10} cm^{-2})	Magnetic scattering length density ρ_m (10^{10} cm^{-2})	Magnetic scattering contrast $\Delta\rho_m$ (10^{10} cm^{-2})	<i>A</i> ratio
Void	0	7.4322	0	4.4333	1.3558
He bubble	0.8261	6.6063	0	4.4333	1.4503
He clusters (substitutional)	2.7613	4.6709	0	4.4333	1.9008
He clusters (interstitial)	3.4516	3.9807	0	4.4333	2.2403
CrHe (Cr ₃ He ₃ , Cr ₄ He ₄ , etc.)	2.6525	4.7798	0	4.4333	1.8603
FeHe (Fe ₃ He ₃ , Fe ₄ He ₄ , etc.)	5.035	2.3973	2.2924	2.1409	1.7978
Cr ₉₅ Fe ₅ (α')	2.8712	4.5610	0.1608	4.2725	1.8775
Cr ₂ FeHe ₃	3.4334	3.9990	0.4580	3.9753	1.9882
CrHe ₂ C	3.5327	3.8995	0	4.4333	2.2924
Cr ₂ HeC	3.6947	3.7375	0	4.4333	2.40687
Cr ₃ C	3.8483	3.5839	0	4.4333	2.5301
(FeHeCrHe) ₇ C ₃	4.1169	3.3154	0.7976	3.6357	2.2026
(FeHeCr) ₇ C ₃	4.7021	2.7302	1.1566	3.2766	2.4407
(FeHe) ₄ C	5.2790	2.1532	1.9895	2.4438	2.2882
(FeHe) ₃ C	5.3537	2.0786	1.9030	2.5303	2.4818
(FeHe) ₂ C	5.4979	1.9344	1.7472	2.6861	2.9282
(FeCr) ₇ C ₃	5.7051	1.7272	1.8114	2.6219	3.3045
FeHeC	5.8821	1.5502	1.3838	3.0495	4.8697
Fe ₂ HeC	6.3686	1.06374	2.2924	2.1409	5.049
Fe ₃ C	7.8129	-0.38066	3.6553	0.7780	5.1776
Fe ₂ C	7.7736	-0.34126	3.2009	1.2324	14.04

Table 4.1.4.1: Neutron and magnetic scattering length density, ρ_n and ρ_m , neutron and magnetic scattering contrast, $\Delta\rho_n$ and $\Delta\rho_m$, and *A* value for a large number of possible, nano-sized, irradiation-induced defects in the EUROFER 97 RAFM steel.

It can be seen in Table 4.1.4.1 that the A values are the smallest, equal to about 1.36 and 1.45, in the case of voids and helium bubbles, respectively. The A values are ranging between 1.80 and 5.05 for helium-containing Fe-rich or Cr-rich precipitates. The A value is equal to about 2.53 for pure chromium carbides, 1.88 for Cr-rich precipitates (α') and are ranging between 5.18 and 14.04 for pure Fe carbides.

Unirradiated EUROFER 97 RAFM steel: By combining the A value (about 2) reported under § 3.1.6 with the γ value (about 4.08) reported under § 4.1.3, as deduced from results of SANS experiments, it appears that the defects evidenced by SANS in unirradiated specimens of the EUROFER 97 RAFM steel could be small carbides. Indeed, voids and/or helium bubbles are not expected in unirradiated specimens, as well as helium-containing precipitates. In addition, such carbides are three-dimensional objects, as suggested by the obtained γ value of about 4.08, and fit well the A value of about 2 which was obtained over the Q -range of 0.426-0.70 nm⁻¹, suggesting that these precipitates have a size larger than the nanometer. On the other hand, such carbides are in good agreement with results reported in the literature (see § 1.5.1).

Irradiated EUROFER 97 RAFM steel: By combining the A values reported under § 3.1.6 with the γ values reported under § 4.1.3, as deduced for results of SANS experiments, it appears that the defects evidenced by SANS in irradiated specimens of the EUROFER 97 RAFM steel could be nano-sized helium bubbles. Indeed, the obtained γ values, which are in all cases well below 1 in the Q -range of 1-4.7 nm⁻¹, suggest that the irradiation-induced effects are fractal objects with a nanometer size. In addition, the A values of about 2, which were obtained in the Q -range of 0.426-4.826 nm⁻¹, are relatively close to the A value of 1.4503 obtained for helium bubbles and to the A values obtained for helium-containing Cr-rich precipitates. However, such precipitates are three-dimensional objects and do not fit very well the small γ values obtained. On the other hand, nano-sized helium bubbles are in good agreement with results reported in the literature (see § 1.5.2).

As a result from atomic displacement cascades, a central depleted zone forms and He impurities are expected to remain in this area to produce interstitial He and vacancy clusters by He pinning effect and kick out mechanism. This area having an undefined 3D shape, the interstitial He and vacancy clusters may result in a fractal distribution of nano-sized He bubbles. Moreover, as a result from MD simulations, one may see that the shape of such nano-sized He bubbles is fractal [208].

The larger defects evidenced by means of SANS experiments have been analyzed less in detail. However, they could correspond to the interstitial defect clusters evidenced in TEM, commonly referred to as 'black dot' damage and usually identified as interstitial dislocation loops or to second-phase precipitates at larger doses.

4.2 Simulations

4.2.1 MD simulations

Atomic displacement cascades up to 10 keV were simulated by means of MD in Fe and Fe-He materials using fitted and validated EAM many-body potentials. A content of 0.1 at.% He in interstitial or substitutional position does not seem to affect the collisional stage of the cascade, but it does influence the distribution of dumbbell species during the post-collisional stage. Most of the interstitials belong to mixed Fe-He dumbbells in Fe-0.1 at.% He(I), mostly oriented along $\langle 100 \rangle$, and to Fe-Fe dumbbells in Fe-0.1 at.% He(S), mostly oriented along $\langle 110 \rangle$. The size and number density of interstitial clusters is much higher in Fe-0.1 at.% He(I) than in Fe-0.1 at.% He(S) and in pure Fe. The defect production efficiency is also slightly higher in Fe-0.1 at.% He(I) than in Fe-0.1 at.% He(S) and in pure Fe. The formation of Fe-He dumbbells seems to reduce recombination phenomena. The interstitial clusters of small and medium size contain a large percentage (50%) of He atoms, which stabilize them. This feature may drastically reduce the mobility of interstitial clusters in Fe-0.1 at.% He(I), as compared to pure Fe, with significant impact on the mechanical properties of the material. The size and number density of interstitial clusters increase with the PKA energy and temperature in the range 10-523K. There are no vacancies neither substitutional He nearby the interstitial clusters.

4.2.2 TEM image simulations

Cavities are usually observed using bright field TEM imaging in defocusing mode. However, in the present work we used dark field/weak beam TEM imaging for simulating all kinds of defects, for comparison purposes, as the dark field/weak beam TEM imaging mode provides the best image contrast and spatial resolution for most of the nano-sized defects of interest in this work, even if voids are sometimes easier highlighted using bright field TEM imaging in defocusing mode.

Figure 4.2.2.1 shows the contrast, as defined by the standard deviation of the image intensity, as a function of depth of the simulated TEM images of most defects created in Fe by MD. The specimen was 80 nm thick with the defect being located in the middle of the foil. The imaging conditions were $g(2g)$ and $g(4g)$ using $g = (200)$. It was shown in chapter 3 that all dislocation loops, whatever their Burgers vector and habit plane, actually exhibit nearly the same contrast for a given imaging condition. Therefore, there are represented by a single and common curve per imaging condition in Figure 4.2.2.1. It can be seen that, when using the $g(2g)$ imaging condition (Figure 4.2.2.1, left), the dislocation loops and He bubbles with a He concentration of 200% (2:1) exhibit a similar contrast. In addition, these two kinds of defects exhibit a much higher contrast, by a factor of about 4, than all the other ones. These observations still hold for the $g(4g)$ imaging condition (Figure 4.2.2.1, right). However, in that case, the contrast presented by the dislocation loops and He bubbles with a He concentration of 200% (2:1) is higher by a smaller factor of about 2 than the contrast provided by cascade damage in pure Fe, cascade damage in Fe-0.1 at.% He(S), voids, and He

bubbles with a He concentration of 100% (1:1), while it is still higher by a factor of about 4 than the contrast provided by cascade damage in Fe-1.0 at.% He(S) and Cr precipitates.

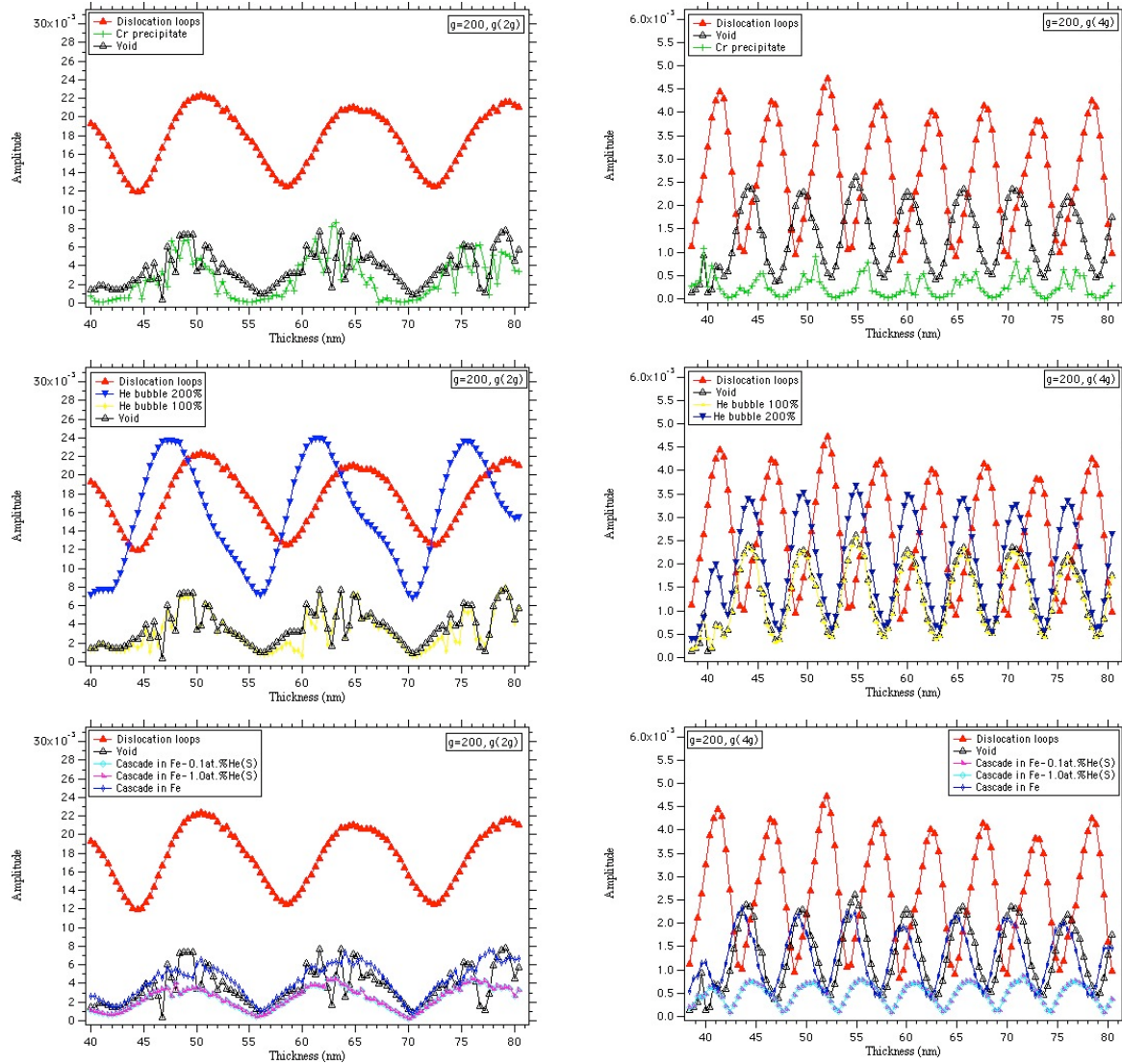


Figure 4.2.2.1: Contrast, as defined by the standard deviation of the image intensity, as a function of depth of the simulated TEM images of most defects created in Fe by MD. The specimen was 80 nm thick with the defect being located in the middle of the foil. The imaging conditions were (left) $g(2g)$ and (right) $g(4g)$, using $g = (200)$.

It can be concluded for these observations that the phase defects present much less image contrast than the structural defects in TEM. Structural defects are here defined as defects producing a lattice deformation of the surrounding Fe matrix. They include dislocation loops as well as He bubbles with a He concentration of 200% (2:1). Indeed, the inner pressure provided by the latter defects also engenders some lattice deformation of the surrounding

matrix, like dislocation loops. Corresponding simulated TEM images of He bubbles with a He concentration of 200% (2:1) clearly show that the image contrast of the He bubbles extends well beyond the region defined by the bubbles itself, so delineating the deformed region of the surrounding lattice. In the $g(4g)$ imaging condition, the image contrast provided by voids and He bubbles with a He concentration of 100% (1:1) are increased, leading to a smaller difference in image contrast with structural defects.

The Cr precipitates exhibit much less TEM image contrast than the structural defects because the scattering factor of Cr is close to the one of Fe, and because of the similarity of the structures, bcc, and of the lattice parameters, which inherently produce Cr precipitates that are fully coherent with the matrix and yield limited lattice deformation of the surrounding matrix. This results in a limited structural contrast, which actually appears as a weak Ashby-Brown contrast. The image contrast of the Cr precipitates is close to the one of the voids in the $g(2g)$ imaging condition, but it is much less than the ones of the voids in the $g(4g)$ imaging condition.

The cascade residues present a relatively weak TEM image contrast in all cases studied here, be it in pure Fe, or in Fe-0.1 at.% He(S) or Fe-1.0 at.% He(S). Among them it appears that the residues in pure Fe present the highest contrast, a contrast that is similar to the one of the voids in both $g(2g)$ and $g(4g)$ conditions. It is however slightly less in the $g(4g)$ condition. This could stem from the fact that the cascade residues include vacancy clusters that are smaller than the 2 nm voids considered here. In the case of the Fe-He materials, the increase in the imaging condition to $g(4g)$ does not allow distinguishing them. This suggests that He prevents the formation of vacancy clusters.

These simulations provide indications to the microscopist for the best TEM imaging conditions allowing the distinction between the different types of nano-sized defects. It appears that the use of a rather dynamical dark field condition, $g(2g)$, with $g = \{200\}$, allows separating the structural defects from the phase defects considered here. They will appear with a much brighter contrast than the other ones. This should be done in comparison with an image taken with a true weak beam dark field condition, here $g(4g)$, as this image will reveal all defects with a brighter contrast, even those that might be invisible in the $g(2g)$ condition. In addition, the $g(4g)$ condition may allow distinguishing voids from Cr precipitates, the latter presenting a very weak contrast in all imaging conditions.

4.2.3 SANS signal simulations

He bubbles

Figure 4.2.3.1 shows cut views of MD specimens of pure Fe, which contain a He bubble with various He concentration, before and after relaxation, as well as their corresponding SANS signal, in comparison to the ones provided by a perfect crystal and voids. It can be seen that the SANS signal of the He bubble with a He concentration of 100% (1:1) is unaffected by the relaxation process. However, the SANS signal of the He bubbles with a He concentration of 200% (2:1) or 300% (3:1) is strongly improved at low Q values (below about 3 nm^{-1}) by the relaxation process, the effect increasing with the He content in the cavity.

Closer examination of the atomic positions shows that in the relaxed MD specimens there is always a void gap around the He bubble, resulting from the strong He-Fe repulsion, and this

void gap is responsible for the observed increase in SANS intensity. Otherwise, i.e., without the gap, as the scattering factor of about three He atoms is equal to that of one Fe atom, one obtains almost the same SANS signal from a perfect crystal of pure Fe and a He bubble with a He concentration of 300% (3:1).

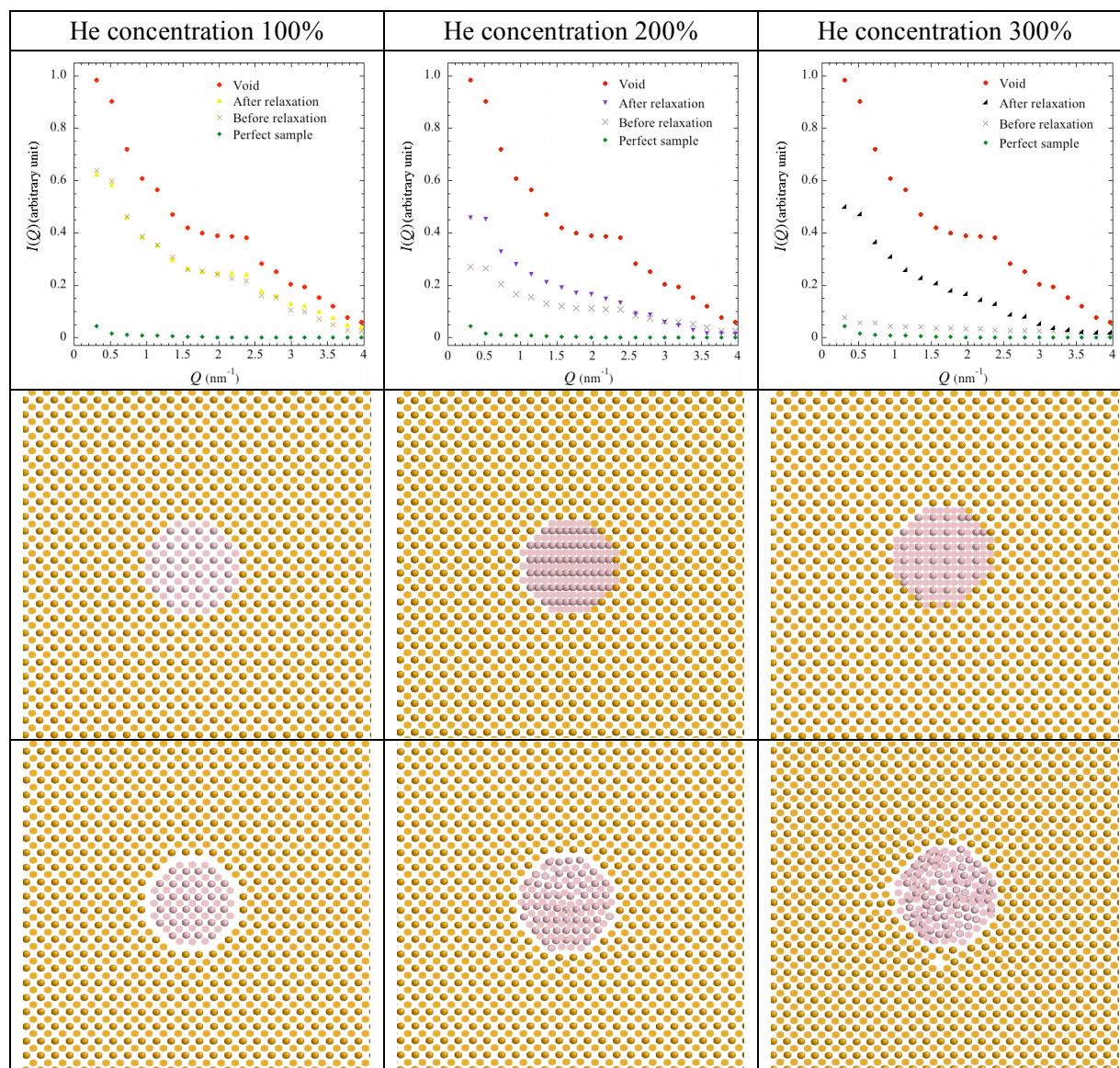


Figure 4.2.3.1: Cut views of MD specimens of pure Fe, containing a He bubble with various He concentration, before (middle part) and after (bottom part) relaxation, as well as their corresponding SANS signal (upper part), in comparison to the ones provided by a perfect crystal and voids.

Cr precipitates

Figure 4.2.3.2 shows a comparison of cut views of MD specimens of pure Fe, which contain either a He bubble with a He concentration of 100% (1:1) or a Cr precipitate, before and after relaxation, as well as their corresponding SANS signal, in comparison to the ones provided

by a perfect crystal and voids. It can be seen that, although the scattering length of Cr is almost equal to the one of He, relaxation does not yield any increase in the SANS signal of Cr precipitates. Indeed, relaxation does not lead the formation of any gap in between the Cr precipitate and the surrounding matrix, the Cr precipitate maintaining its full coherency with the surrounding lattice.

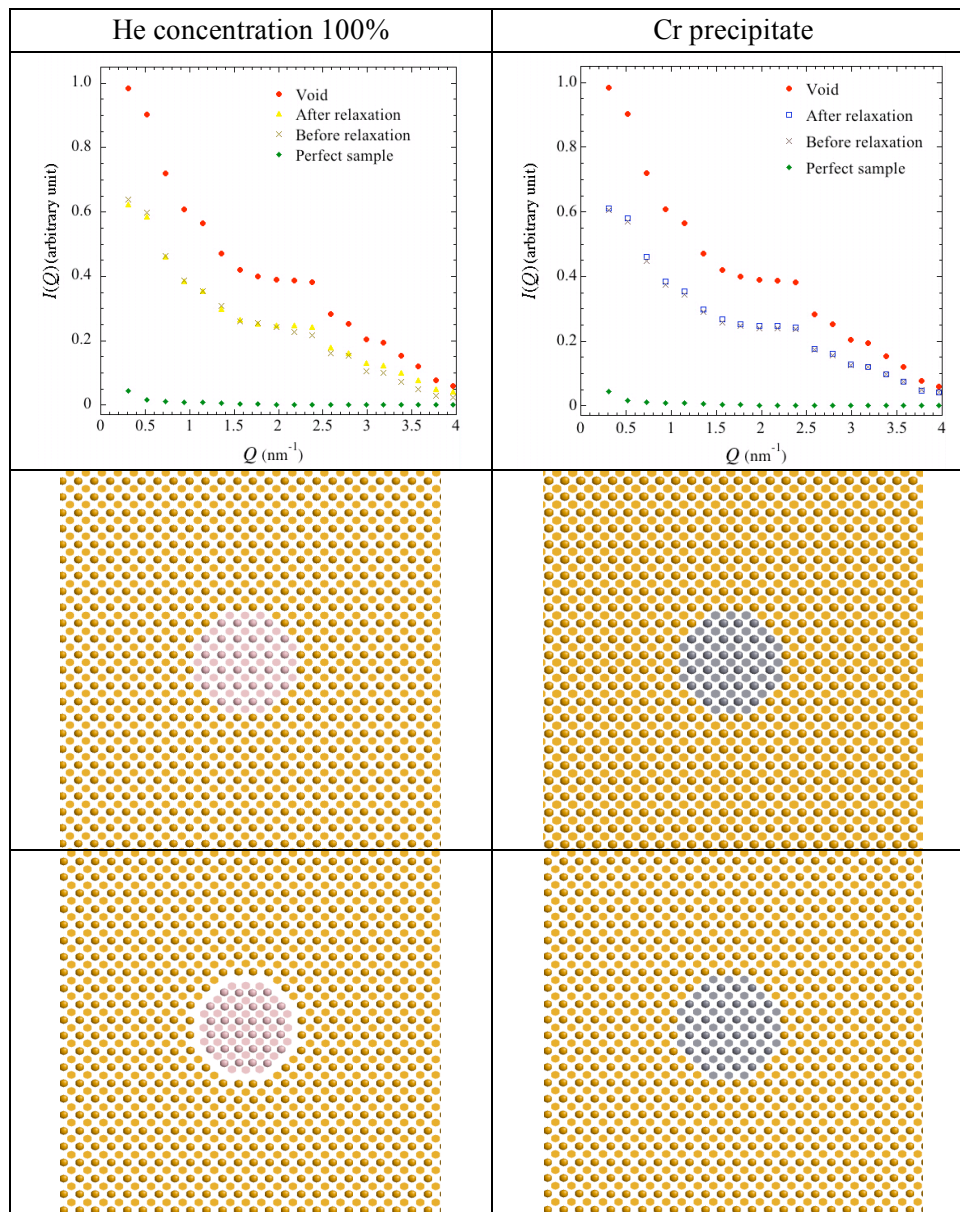


Figure 4.2.3.2: Comparison of cut views of MD specimens of pure Fe, containing either a He bubble with a He concentration of 100% (1:1) or a Cr precipitate, before (middle part) and after (bottom part) relaxation, as well as their corresponding SANS signal (upper part), in comparison to the ones provided by a perfect crystal and voids.

4.3 General discussion

4.3.1 TEM/SANS comparison

Generally speaking it appears from our simulations that TEM is most adapted to investigate structural defects, such as dislocation loops and He bubbles with high He concentration, while SANS is most adapted to investigate phase defects, such as voids, He bubbles with low He concentration and Cr precipitates. The latter ones provide a high contrast in SANS, contrary to the one obtained in TEM, because of the significant difference between scattering of neutrons by Fe and Cr, contrary to the case of electrons. SANS provides a poor signal from structural defects, because a distortion of the lattice does not induce a significant perturbation in the neutron wave, contrary to the electron wave. The two techniques are thus not competing in the investigation of the same types of defects, but are truly complementary investigation tools, as even in the same material they are sensitive to very different types of nano-size defects, which is a remarkable outcome of those simulations.

There are other differences worth mentioning here. TEM, on the one hand, remains the method of choice in the case of the investigation of the spatial configuration of an individual defect, of any type, as it allows a direct visualization of it. This of course is valid when one has access to the tools to interpret the observed contrast in the TEM image, an interpretation that relies mainly on simulation tools. TEM is however limited by the fact that all observations have to be performed in samples that are transparent to electrons, which energy at about 200 keV limits its thickness to about 100 nm. In addition, in order to have access to sufficient spatial resolution, the observed area is limited to a few square microns due to the significant magnification and the limited area of the image acquisition systems, be it a photographic negative or a CCD camera. This imposes serious limitations on the defect densities that are accessible by TEM. Indeed, below a density of about 10^{19} defects per cubic meters, the actual number of defects in the TEM image reduces to about 1 for the relevant image dimension and specimen thickness. This means that defect densities of this order of magnitude or below cannot be measured by TEM. The thickness of the TEM specimen introduces bias in the measurement by the proximity of free surfaces. These will act as strong sinks to point defects such as interstitials and vacancies and present strong image forces to dislocations, such as nano-sized dislocation loops. These surfaces may subsequently absorb defects or modify their configurations.

SANS, on the other hand, remains the method of choice in the investigation of phase defects. In addition, it allows probing cubic millimeters, if not centimeters, because of the deep penetration of the neutrons in any type of material, contrary to electrons. This makes SANS the method of choice for the measurement of defect densities, down to densities much lower than 10^{19} defects per cubic meters. SANS on the other suffers from a strong limitation, which is the fact that with SANS one cannot observe individual defects. The base of SANS is diffraction, which in essence provides an average signal of the defect population present in the specimen. In order to interpret the signal one has to provide blindly a model for the defect population. This model includes the nature or chemical composition and structure of the defect, its shape and its size distribution, be it bimodal for instance.

4.3.2 Summary of main results available for RAFM steels

Rate of damage accumulation

Irradiation-induced defects in RAFM steels are known to accumulate to a lesser rate than in other metals. When compared to fcc pure metals, for instance, the irradiation-induced defect density, for defects observable in TEM, is two to three orders of magnitude lower in RAFM steels for the same irradiation dose, as shown in Figure 4.3.2.1 [217]. In other terms, the irradiation dose needed to reach the same defect density as in fcc metals, such as Cu or Pd, is three to four orders of magnitude higher. This primarily relates to the bcc structure of RAFM steels, as also observed in irradiated pure Fe [218].

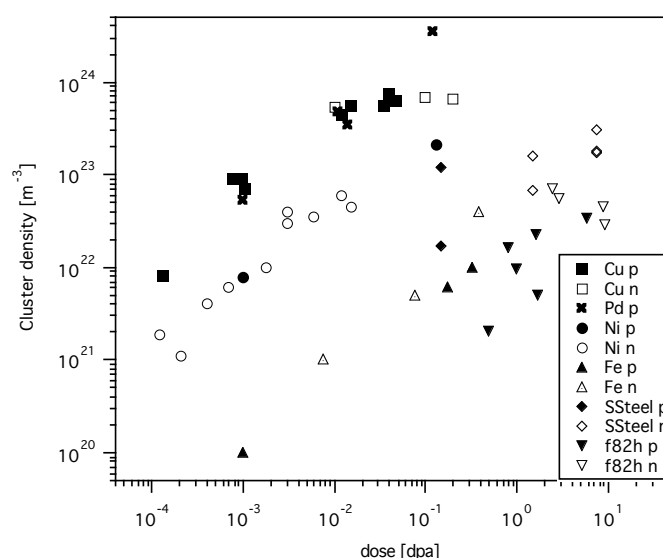


Figure 4.3.2.1: Defect cluster density as a function of irradiation dose in pure metals, an austenitic stainless steel (SSteel) and the F82H RAFM steel (p: irradiation with 590 MeV protons, n: irradiation with fission neutrons). Irradiations have been performed at various temperatures between 50°C and 250°C [217].

TEM observations

The first contrasts to appear in TEM in irradiated RAFM steels are black dots of about 1 nm, which correlate with irradiation-induced clusters of point defects with sizes of about 1 nm or slightly less [164]. These black spots are formed by diffraction contrast. High-energy proton and fission neutron irradiation give rise at low doses to similar black spots, which quantify to similar sizes and densities [219]. When the dose is increased the black dots grow in size and can generally be resolved above 2 dpa as dislocation loop contrasts [219] or second phase precipitate contrasts. In addition, when the irradiation dose is sufficiently high, the defocusing technique [220] reveals cavity contrasts.

Small angle neutron scattering measurements

As shown in the present work, a relatively large fraction of irradiation-induced defects in RAFM steels have a size below the TEM resolution limit in weak beam imaging, equal to about 1 nm, which are expected to contribute to radiation hardening and/or embrittlement effects of RAFM steels occurring at irradiation temperatures below about 400°C.

Positron annihilation spectroscopy measurements

In order to investigate possible sites for the location of irradiation-produced helium, the evolution of vacancy clusters has been studied by performing positron annihilation spectroscopy measurements on unirradiated and high-energy proton- or neutron-irradiated specimens (at 50-350°C to 0.2-0.3 dpa) of pure Fe and the F82H RAFM steel. It was found that in pure Fe and steels cavities with sizes around 1 nm (voids or helium bubbles) form in the whole temperature range investigated [221]. At both 250 and 350°C, the cavity density in the F82H RAFM steel is appreciably lower than in pure Fe. The results obtained for specimens of pure Fe irradiated in the PIREX facility (high helium production rate) do not differ significantly from those obtained for neutron-irradiated specimens (low helium production rate), which indicates that the irradiation-produced helium is being accumulated in the cavity microstructure.

Radiation hardening

The irradiation hardening following proton irradiation at 250°C was measured by means of tensile tests carried out on the F82H RAFM steel at a temperature identical to that of irradiation [217]. Specimens irradiated at different doses ranging from 0.26 dpa up to 2.5 dpa were tested. It is well established that the increase in the yield stress with dose strongly tracks the microstructural changes induced by irradiation. In order to relate this irradiation-induced hardening, measured from the tensile tests, to the irradiation-induced defects observed in TEM, the number density, N , and diameter, d , of the defect clusters evidenced in TEM were determined as a function of dose from the TEM micrographs. The spacing between these obstacles was expressed as $(Nd)^{-1/2}$, whose dose dependence is reported in Figure 4.3.2.2. Note that $(Nd)^{-1/2}$ was determined for 590 MeV proton- and neutron-irradiated specimens as well as for specimens irradiated in the SINQ facility with a mixed spectrum of 570 MeV protons and spallation neutrons. Interestingly, no effect of the irradiation mode was found on the dose dependence of $(Nd)^{-1/2}$ and all the data points fall along the same curve. It can be seen that the mean spacing between the loops decreases strongly for doses below 2 dpa and tends to a constant value of about 70 nm. Taking into account the uncertainty in the determination of $(Nd)^{-1/2}$ and the lack of data between 2.5 and 5 dpa, it was not possible to draw a firm conclusion on the dose at which the saturation level is actually reached.

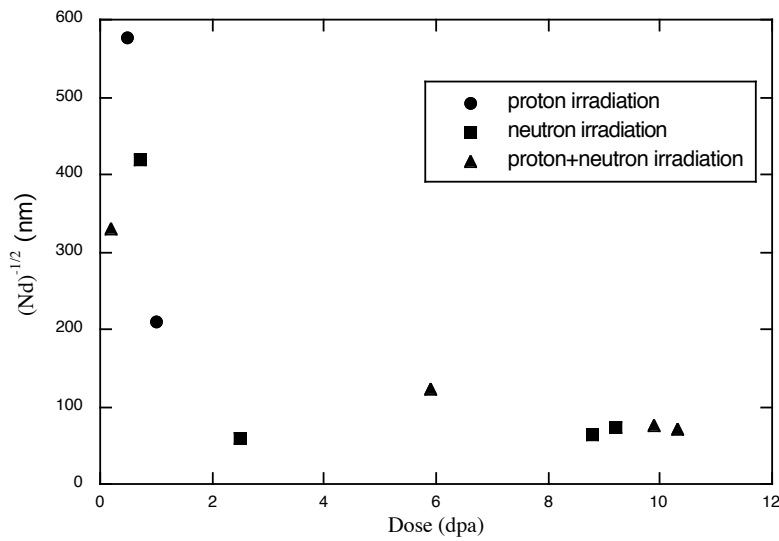


Figure 4.3.2.2: Mean obstacle spacing as a function of dose in the F82H RAFM steel irradiated at 250°C in various facilities [217].

Having determined the irradiation-induced dislocation defect cluster density, N , and the mean diameter, d , an attempt to correlate these data to the radiation hardening measured by tensile tests, $\Delta\sigma_y$, was done [217]. Assuming that these defect clusters act as dispersed obstacles for moving dislocations in their glide plane, they are then responsible for a short distance interaction with the moving dislocations and yield a radiation hardening $\Delta\sigma_y$. This local interaction constitutes the basis for the so-called dispersed-barrier hardening model [222] and the associated equation reads:

$$\Delta\sigma_y = \alpha M \mu b (Nd)^{1/2} \quad (4.3.2.1),$$

where M is the Taylor factor, α is a dimensionless constant, μ is the shear modulus, b is the Burgers vector of the moving dislocations and $(Nd)^{1/2}$ is the mean discrete obstacle spacing. The following values are commonly used for RAFM steels: $M = 3$ [223], $\mu = 80,000$ MPa [224] and $b = 0.268$ nm [225]. Considering the irradiation-induced defect clusters as weak obstacles, the α value was taken equal to 0.1 [222]. In Figure 4.3.2.3, the experimental data are reported along with the calculated contribution according to equation 4.3.2.1 above. A significant discrepancy can be seen between the experimental data and the calculated $\Delta\sigma_y$ with $\alpha = 0.1$. A good fit of the data could be obtained by increasing α to 0.3. However, such a high α value may not be relevant to characterize the strength of the irradiation-induced defects, since it has been observed in TEM that they can be readily destroyed by the moving dislocations, leading to localized deformation and then to channel formation [173], for instance. The measured radiation hardening is likely to stem not only from irradiation-induced defect clusters evidenced in TEM but from a variety of defects evidenced in TEM and/or SANS and/or PAS and whose relative strength and importance is not yet precisely determined.

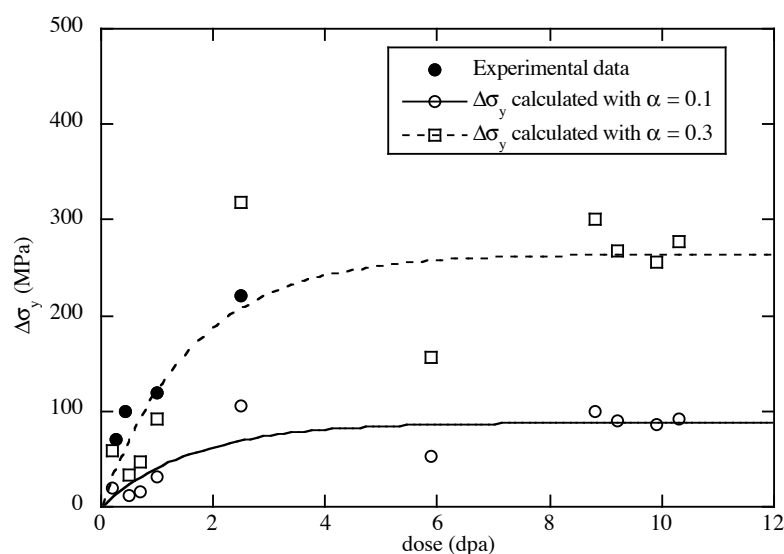


Figure 4.3.2.3: Radiation hardening, $\Delta\sigma_y$, versus dose for the F82H RAFM steel, as measured by means of tensile tests at $T = 250^\circ\text{C}$ [217].

4.3.3 Radiation hardening of the EUROFER 97 RAFM steel

Results of tensile tests

Typical tensile stress-strain curves obtained for the EUROFER 97 RAFM steel irradiated with 590 MeV protons in the PIREX facility at 50 and 350°C to various doses and tensile tested at the same temperature as the irradiation one are presented in Figure 4.3.3.1, along with the reference curves of unirradiated specimens [226]. One salient observation is the fact that at 350°C the uniform elongation increases in comparison to the unirradiated curve. This occurs typically for doses of about 0.3-0.4 dpa, beyond which the uniform elongation is strongly reduced. A careful look at the tensile curves at these low doses reveals that the initial strain hardening tends to be more linear than that of the unirradiated specimen, which presents a more pronounced curvature or equivalently a stronger strain-hardening reduction with strain. That strain-hardening behavior at small doses combined with a relative moderate increase of the overall flow stress results in an increase of the uniform elongation.

The tensile data obtained for specimens of the EUROFER 97 RAFM steel irradiated at 50, 250 or 350°C to various doses ranging between 0.16 and 1.36 dpa are summarized in Table 4.3.3.1 [227].

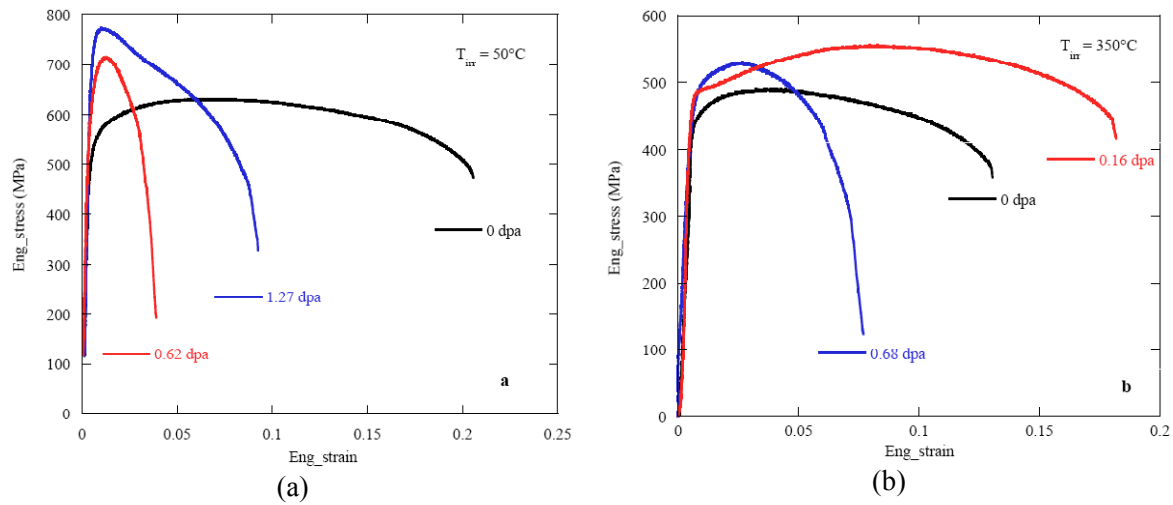


Figure 4.3.3.1: Typical tensile stress-strain curves obtained for unirradiated specimens and specimens of the EUROFER 97 RAFM steel irradiated at (a) 50°C and (b) 350°C to various doses [226]. $T_{test} = T_{irrad}$, the stain rate was $5 \times 10^{-4} \text{ s}^{-1}$.

$T_{irrad} (^\circ\text{C})$	Dose (dpa)	$\Delta\sigma_{0.2} \text{ (MPa)}$	UTS (MPa)	UE
50	0.22	191	766	0.014
50	0.62	97	714	0.0127
50	0.62	197	762	0.025
50	0.62	116	749	0.014
50	1.27	219	772	0.011
50	1.27	230	823	0.0175
250	0.28	39	592	0.043
250	0.28	76	588	0.039
250	0.63	138	661	0.018
250	1.36	94	638	0.010
350	0.16	20	557	0.0650
350	0.16	25	555	0.0820
350	0.68	25	529	0.0260
350	0.68	26	549	0.0350

Table 4.3.3.1: Tensile data obtained for specimens of the EUROFER 97 RAFM steel irradiated at 50, 250 or 350°C to various doses ranging between 0.16 and 1.36 dpa. $T_{test} = T_{irrad}$. $\Delta\sigma_{0.2}$ = radiation hardening, UTS = ultimate tensile strength, UE = uniform elongation.

The radiation hardening, $\Delta\sigma_{0.2}$ ($\Delta\sigma_y$ measured at 0.2% plastic strain), is presented in Figure 4.3.3.2 against the square root of the dose, where a significant large dispersion of the results was measured. At these small doses, the radiation hardening increases fast with dose so that

any uncertainty in the dose determination translates into a significant variation of the yield stress. It is reminded that the doses reported here carry an uncertainty of the order of $\pm 20\%$. Note also that the irradiation temperature fluctuations of $\pm 30^\circ\text{C}$, associated with the proton beam instability, add to the overall scatter in the data. Despite these uncertainties in irradiation dose and temperature, it was possible to extract a general trend in the variation of the radiation hardening with irradiation dose and temperature. The initial rate of radiation hardening is commonly modeled by $\Delta\sigma_{0.2} = k(T_{\text{irrad}}) \text{ dpa}^{1/2}$, see for instance [228, 229]. The coefficient k was calculated from the data and its temperature dependence is shown in Figure 4.3.3.3. The indicated error bars correspond to the fluctuations in the real irradiation temperatures and from the uncertainties in the calculated doses.

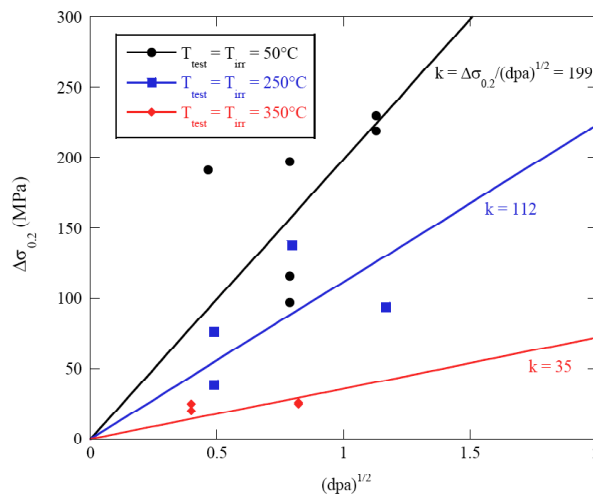


Figure 4.3.3.2: Radiation hardening versus $(\text{dose})^{1/2}$ for specimens of the EUROFER 97 RAFM steel irradiated at 50, 250 or 350°C to various doses and tensile tested [226]. $T_{\text{test}} = T_{\text{irrad}}$.

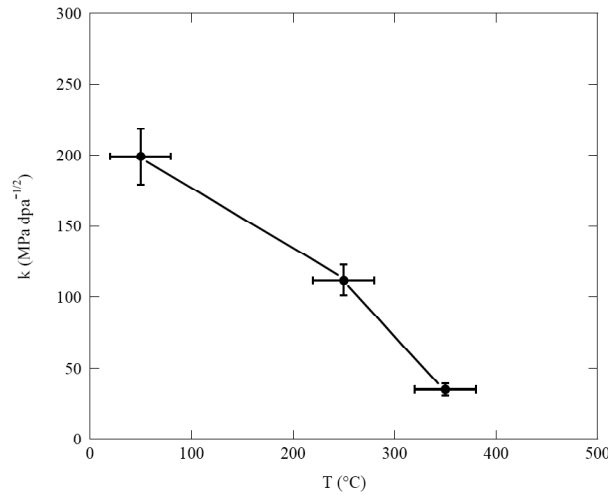


Figure 4.3.3.3: Temperature dependence of the coefficient k , determined for specimens of the EUROFER 97 RAFM steel irradiated at 50, 250 or 350°C to various doses and tensile tested [226]. $T_{test} = T_{irrad}$.

Mean obstacle spacing

As reported above, it was shown in [217] that the radiation hardening cannot be satisfactorily described by using the dispersed-barrier hardening model by taking into account only the density of defects visible in TEM. Thus, the nano-sized defects evidenced by SANS in the present study have to be taken into account for modeling the radiation hardening of RAFM steels. The key parameter to be used would be the inter-defect spacing, L , which can be calculated with the following equation [222]:

$$L = \left[\int dN(R) dR \right]^{-1/2} = \left[\int 2RN(R) dR \right]^{-1/2} \quad (4.3.3.1),$$

where d is the diameter of the scattering defects. Clearly, L is dependent on the distribution function $N(R)$. We recall that the shape parameter, s , of the presented size distributions was not fitted but that a fixed value of 0.2 was chosen. A number of parameter fits were actually performed and it was observed, on the one hand, that the fitted value of s falls in the range 0.1-0.3 and, on the other hand, that various sets of three parameters (N , R_0 , s) can actually yield good fitting. However, even if different distributions are possible, all of them peak below one nanometer. The inter-defect spacing, L , was calculated for three distribution functions $N(R)$ obtained respectively with $s = 0.1$, 0.2 and 0.3, and it was found that the uncertainty on s yields an error bar on L of maximum 30%. The inter-defect spacing remains comparable independently of the distribution used and the associated error bar is of the same order as the one that would be expected on the α constant characterizing the strength of the obstacle in the Orowan's equation [222]. Finally, it should be noted that using another distribution function like the normal distribution affects only little the mean inter-defect spacing.

Evaluation of the number density

TEM images of irradiation-induced defects in the EUROFER 97 RAFM steel irradiated in the conditions investigated in the present work are not yet available. However, one may assume that they should be similar to those observed in the F82H RAFM steel irradiated in the same conditions of dose and temperature.

Therefore, for the EUROFER 97 RAFM steel irradiated with 590 MeV protons in the PIREX facility at 250°C, the mean spacing of the defects visible in TEM, $(Nd)^{-1/2}$, has been estimated from the equation of the fit with $\alpha = 0.1$ in Figure 4.3.2.3 and by inverting equation 4.3.2.1. The corresponding contribution to the total radiation hardening was also deduced from Figure 4.3.2.3. The obtained values are reported in Table 4.3.3.2. As can be seen in Table 4.3.3.2, the radiation hardening arising from the defects visible in TEM is not sufficient to explain the measured one. The difference is believed to be due to the nano-sized irradiation-induced defects evidenced by using the SANS technique, which also contribute to the overall increase of the yield stress. Provided that the strength of the defects is similar for both types of defects and given by $\alpha = 0.1$ (weak defects), the superposition of the two short-range obstacle-dislocation interactions, namely from the defects visible in TEM and the defects detected with SANS, is given by:

$$\Delta\sigma_{tot}^2 = \Delta\sigma_{TEM}^2 + \Delta\sigma_{SANS}^2 \quad \text{and, therefore,} \quad \Delta\sigma_{SANS} = \sqrt{\Delta\sigma_{tot}^2 - \Delta\sigma_{TEM}^2} \quad (4.3.3.2).$$

T_{irrad} (°C)	Dose (dpa)	Measured $\Delta\sigma_{0.2}$ (MPa)	TEM contribution to $\Delta\sigma_{0.2}$ (MPa)	$(Nd)^{-1/2}$ for the TEM defects (nm)	SANS contribution to $\Delta\sigma_{0.2}$ (MPa)	N of the SANS defects (m ⁻³)	d of the SANS defects (nm)	$(Nd)^{-1/2}$ for the SANS defects (nm)
250	0.28	39	11	460	36	1.81E+22	1.77	176
250	0.28	76	27	460	74	7.62E+22	1.77	86
250	0.63	138	27	226	135	2.59E+23	1.7	47
250	1.36	94	27	128	79	9.57E+22	1.6	80

Table 4.3.3.2: Calculated contributions to radiation hardening measured at 0.2% plastic strain ($\Delta\sigma_{0.2}$) versus mean size and number density of irradiation-induced defects in the EUROFER 97 RAFM steel irradiated with 590 MeV protons in the PIREX facility at 250°C to various doses.

The number density, N , of the nano-sized irradiation-induced defects evidenced by SANS was finally calculated by using equation 4.3.2.1 with $\Delta\sigma = \Delta\sigma_{SANS}$. The number density of the SANS defects and corresponding mean spacing are reported in Table 4.3.3.2. One may see that the number density and mean spacing of the SANS defects, assumed to be small helium bubbles, are quite comparable to the number density and mean spacing of the TEM defects, usually assumed to be small interstitial clusters at low doses, which transform into interstitial dislocation loops at larger doses.

CHAPTER 5: CONCLUSIONS AND PERSPECTIVES

The Small Angle Neutron Scattering (SANS) technique has been proven to be a very powerful tool for detecting nano-sized irradiation-induced defects and a tool well complementary to Transmission Electron Microscopy (TEM) for characterizing such very small irradiation-induced defects. It was found in particular that:

- A large part of the defects produced in RAFM steels by high-energy proton irradiation, at temperatures in the range 50-350°C to doses in the range 0.3-2.0 dpa, have a size below 1 nm, i.e., below the resolution limit of the weak beam TEM imaging technique.
- The mean radius of these small irradiation-induced defects is ranging between 0.25 and 0.9 nm, depending on the irradiation dose and temperature. It tends to decrease with increasing the irradiation dose and to increase with the irradiation temperature, at least for the two lowest investigated doses of 0.3 and 1.0 dpa.
- The number density of these small irradiation-induced defects increases with the irradiation dose and decreases with increasing the irradiation temperature, at least for the two lowest investigated doses of 0.3 and 1.0 dpa. No absolute number density values could be determined by using the SANS technique.
- It was possible to get information about the nature of the small irradiation-induced defect by applying a strong magnetic field to the specimens during SANS experiments. The so-called A ratio, which represents the ratio of the total scattered intensity to the nuclear scattered intensity, was determined from the SANS spectra to be equal to about 2.05 ± 0.15 and compared to the A ratio values calculated for a large number of possible irradiation-induced defects in RAFM steels.
- It was possible to get information about the geometry of the small irradiation-induced defect by analyzing the SANS spectra using the Porod law. The obtained value for the exponent $\gamma < 1$ indicates that these small defects could exhibit a fractal geometry.
- The SANS signal provided by a large number of possible irradiation-induced defects in pure Fe and Fe-He alloys, as model materials for RAFM steels, has been simulated *for the first time*.
- TEM is most adapted to investigate structural defects, defined here as defects producing lattice deformation of the surrounding matrix, such as dislocation loops and He bubbles with high He concentration, while SANS is most adapted to investigate phase defects, such as voids, He bubbles with low He concentration and Cr precipitates.
- By combining the results of SANS experiments with those of MD simulations, TEM image simulations and SANS signal simulations, the nano-sized irradiation-induced defects were tentatively identified as small helium bubbles.
- While the radiation hardening measured for RAFM steels cannot be explained by accounting only for the defects observed in TEM, it could be successfully modeled by accounting also for a reasonable number density of the nano-sized defects evidenced using the SANS technique.

In order to assess definitively the nature of the nano-sized irradiation-induced defects evidenced using the SANS technique, three types of additional experiments could be envisaged:

- (1) Small Angle X-ray Scattering (SAXS) experiments, as precipitates can be clearly distinguished experimentally from cavities by using the SAXS technique, although it is not sure that helium bubbles could be distinguished from voids if the He concentration in the cavities is too low;
- (2) SANS experiments on unirradiated and irradiated specimens of pure Fe, as the irradiation-induced formation of Cr precipitates in this material can be excluded;
- (3) SANS experiments on specimens of pure Fe and RAFM steels irradiated with fission neutrons instead of high energy protons, for instance, in order to vary the amount of helium produced by nuclear transmutation reactions in the specimens.

APPENDIX

```

c      calculate intensity versus scattering vector q (linear)
program intq
parameter (pi=3.1415927)
      parameter (det=7.50000000)
      parameter (nbinmax=81)
character*80 infile,outfile,header
      double precision nbin(nbinmax),scaint(nbinmax)
      integer i,j,h,k,l,m,n
      double precision x,y,wlnm,cam,screen,scaint1,q,rq
c      open the files containing the datas and read.
print*, 'input file (e.g. posint)'
      read*, infile
      open(unit=4,file=infile,status='unknown')
print*, 'name of output file:'
      read*, outfile
      open(unit=5,file=outfile,status='unknown')
      write(5,*) 'Q,I'
read(4,*) header
      read(4,*) wlnm,cam,screen
c      calculate intensity with the radial distance of the spot
from the center
do 80 m=1,nbinmax
      scaint(m)=0
      nbin(m)=det*(m-1)
80    continue
      do 70 while(k.eq.0)
        read (4,*,err=1000,iostat=k) h,n,l,x,y,rq,scaint1
        m=0
        do 60 while (rq.ge.nbin(m+1))
          m=m+1
60      continue
        scaint(m)=scaint(m)+scaint1
70      continue
        do 90 m=1,nbinmax-1
          scaint(m)=scaint(m)/(4*pi*(nbin(m+1)*nbin(m+1)-
nbin(m)*nbin(m)))
          q=(4*pi/wlnm)*sin(atan((nbin(m)+nbin(m+1))/2/cam)/2)
          write(5,*) q,scaint(m)
90      continue
        close (4)
        close (5)
1000 end

```


REFERENCES

- [1] C. P. C. Wong, R. E. Nygren, C. B. Baxi, P. Fogarty, N. Ghoniem, H. Khater, K. McCarthy, B. Merrill, B. Nelson, E. E. Reis, S. Sharafat, R. Schleicher, D. K. Sze, M. Ulrickson, S. Willms, M. Youssef, S. Zinkle, *Fusion Engineering and Design* 49-50 (2000/11) p. 709.
- [2] M. Rieth, M. Schirra, A. Falkenstein, P. Graf, S. Heger, H. Kempe, R. Lindau, H. Zimmermann, *EUROFER 97 - tensile, Charpy, creep and structural tests*, 2003, 0947-8620.
- [3] R. Lindau, A. Möslang, M. Rieth, M. Klimiankou, E. Materna-Morris, A. Alamo, A. A. F. Tavassoli, C. Cayron, A. M. Lancha, P. Fernandez, N. Baluc, R. Schöublin, E. Diegele, G. Filacchioni, J. W. Rensman, B. v. d. Schaaf, E. Lucon, W. Dietz, *Fusion Engineering and Design* 75-79 (2005) p. 989.
- [4] A. Kimura, R. Kasada, A. Kohyama, S. Konishi, M. Enoeda, M. Akiba, S. Jitsukawa, S. Ukai, T. Terai, A. Sagara, *Fusion Engineering and Design* 81 (2006) p. 909.
- [5] E. Materna-Morris, B. Dafferner, M. Klimiankou, P. Graf, A. Falkenstein, U. Jäntsch, R. Lindau, C. Petersen, D. Preininger, H. Zimmermann, *Nuclear fusion programme: Mechanical and structural characterization of EUROFER 97-2*, 2005, 0947-8620, FZK.
- [6] A. Möslang, E. Diegele, M. Klimiankou, R. Lässer, R. Lindau, E. Lucon, E. Materna-Morris, C. Petersen, R. Pippa, J. W. Rensman, M. Rieth, B. v. d. Schaaf, H. C. Schneider, F. Tavassoli, *Nuclear Fusion* 45 (2005) p. 649.
- [7] A. G. Ioltukhovskiy, V. M. Chernov, M. V. Leonteva-Smirnova, V. V. Novikov, L. I. Reviznikov, M. I. Solonin, V. V. Tsvelev, A. V. Vatulin, T. M. Bulanova, V. N. Golovanov, V. E. Shamardin, in *Contribution 08-45 to the 12th International Conference on Fusion Reactor Materials*, Santa Barbara, 2005
- [8] V. M. Chernov, M. V. Leonteva-Smirnova, M. M. Potapenko, N. I. Budylkin, Y. N. Devyatko, A. G. Ioltoukhovskiy, E. G. Mironova, A. K. Shikov, A. B. Sivak, G. N. Yermolaev, A. N. Kalashnikov, B. V. Kuteev, A. I. Blokhin, N. I. Loginov, V. A. Romanov, V. A. Belyakov, I. R. Kirillov, T. M. Bulanova, V. N. Golovanov, V. K. Shamardin, Y. S. Strebkov, A. N. Tyumentsev, B. K. Kardashev, O. V. Mishin, B. A. Vasiliev, *Nuclear Fusion* 47 (2007) p. 839.
- [9] K. Ehrlich, S. W. Cierjacks, S. Kelzenberg, A. Möslang, in *17th International Symposium on Effects of radiation on materials* edited by D. S. Gelles, R. K. Nanstad, A. S. Kumar and E. A. Little, American Society for Testing and Materials, West Conshohocken, PA (United States), United States, 1996, Vol. 1270, pp. 1109-1122.
- [10] M. Zucchetti, L. A. El-Guebaly, R. A. Forrest, T. D. Marshall, N. P. Taylor, K. Tobita, *J. Nucl. Mater.* 367-370 (2007) p. 1355.
- [11] B. van der Schaaf, E. Diegele, R. Laesser, A. Moeslang, *Fusion Engineering and Design* 81 (2006) p. 893.
- [12] C. Petersen, A. Povstyanko, V. Prokhorov, A. Fedoseev, O. Makarov, M. Waltera, *J. Nucl. Mater.* to appear (2008) p.

- [13] A. Alamo, J. L. Bertin, Irradiation performance - neutron irradiation to 70 dpa at 325°C and PIE, Annual Report of the Association EURATOM-CEA: fusion technology 2004, 2004.
- [14] C. Petersen, E. Materna-Morris, B. Dafferner, M. Klimiankou, P. Graf, A. Falkenstein, U. Jäntschi, R. Lindau, D. Preininger, H. Zimmermann, Fast reactor irradiations, 2005, 0947-8620, FZK.
- [15] E. Lucon, P. Benoit, P. Jacquet, E. Diegele, R. Lasser, A. Alamo, R. Coppola, F. Gillemot, P. Jung, A. Lind, S. Messoloras, P. Novosad, R. Lindau, D. Preininger, M. Klimiankou, C. Petersen, M. Rieth, E. Materna-Morris, H. C. Schneider, J. W. Rensman, B. van der Schaaf, B. K. Singh, P. Spaetig, Fusion Engineering and Design 81 (2006) p. 917.
- [16] A. Alamo, J. L. Bertin, V. K. Shamardin, P. Wident, J. Nucl. Mater. 367 (2007) p. 54.
- [17] C. Petersen, A. Povstyanko, V. Prokhorov, A. Fedoseev, O. Makarov, B. Dafferner, J. Nucl. Mater. 367 (2007) p. 544.
- [18] A. Alamo, P. Wident, V. K. Shamardin, Post-irradiation examinations of materials irradiated in BOR 60 reactor at 325°C up to 42 dpa, Final report on the EFDA Task TW2-TTMS-001 Deliverable 2, 2006.
- [19] W. Schilling, H. Ullmaier, Book Nuclear Materials, Chemie, Weinheim, 1994.
- [20] J. O. Stiegler, L. K. Mansur, Ann. Rev. Mater. Sci. 9 (1979) p. 405.
- [21] M. T. Robinson, J. Nucl. Mater. 216 (1994) p. 1.
- [22] M. Kiritani, N. M. Ghoniem, S. Ishino, T. D. de la Rubia, M. Kiritani, B. N. Singh, E. Kuramoto, H. L. Heinisch, S. J. Zinkle, C. H. Woo, P. Vajda, S. I. Golubov, R. E. Stoller, H. Wollenberger, Y. Kato, N. Yoshida, H. Matsui, M. Victoria, J. N. Yu, J. Nucl. Mater. 272 (1999) p. 540.
- [23] C. Hardtke, W. Schilling, H. Ullmaier, Nuclear Instruments & Methods in Physics Research Section B-Beam Interactions with Materials and Atoms 59 (1991) p. 377.
- [24] S. N. Rosenwasser, P. Miller, J. A. Dalessandro, J. M. Rawls, W. E. Toffolo, W. Chen, J. Nucl. Mater. 85-86 (1979) p. 177.
- [25] A. D. G. Stewart, M. W. Thompson, J. Mater. Sci. 4 (1969) p. 56.
- [26] J. F. Ziegler, Nuclear Instruments & Methods in Physics Research Section B-Beam Interactions with Materials and Atoms 6 (1985) p. 270.
- [27] Alsmille.Rg, Armstron.Tw, W. A. Coleman, Nuclear Science and Engineering 42 (1970) p. 367.
- [28] M. S. Wechsler, D. R. Davidson, L. R. Greenwood, W. F. Sommer, in proceeding: Effects of Radiation on Materials: 12th conference, F.A. Garner and J.S. Perrin, 1985, pp. 1189.
- [29] G. H. Kinchin, R. S. Pease, Reports on Progress in Physics 18 (1955) p. 1.
- [30] P. G. Lucasson, R. M. Walker, Discussions of the Faraday Society (1961) p. 57.
- [31] G. Youngblood, S. Myhra, J. W. Deford, Physical Review 188 (1969) p. 1101.
- [32] J. Lindhard, V. Nielsen, M. Scharff, Matematisk-Fysiske Meddelelser Udgivet Af Det Kongelige Danske Videnskabernes Selskab 36 (1968) p. 3.
- [33] M. J. Norgett, M. T. Robinson, I. M. Torrens, Nucl Eng Des 33 (1975) p. 50.
- [34] U. Theis, H. Wollenberger, J. Nucl. Mater. 88 (1980) p. 121.
- [35] S. J. Zinkle, R. L. Sindelar, J. Nucl. Mater. 155 (1988) p. 1196.
- [36] A. J. E. Foreman, C. A. English, W. J. Phythian, Philosophical Magazine a-Physics of Condensed Matter Structure Defects and Mechanical Properties 66 (1992) p. 655.

- [37] H. Hsieh, T. D. Delarubia, R. S. Averback, R. Benedek, *Physical Review B* 40 (1989) p. 9986.
- [38] D. J. Bacon, A. F. Calder, F. Gao, V. G. Kapinos, S. J. Wooding, *Nuclear Instruments & Methods in Physics Research Section B-Beam Interactions with Materials and Atoms* 102 (1995) p. 37.
- [39] A. Almazouzi, M. J. Caturla, M. Alurralde, T. D. de la Rubia, M. Victoria, *Nuclear Instruments & Methods in Physics Research Section B-Beam Interactions with Materials and Atoms* 153 (1999) p. 105.
- [40] D. S. Gelles, in: M.F. Ashby, R. Bullough, C.S. Hartley and J.P. Hirth (Eds.) *Dislocation Modelling of Physical Systems*, Pergamon Press, New York, 1980, pp. 158.
- [41] D. S. Gelles, *J. Nucl. Mater.* 104 (1982) p. 975.
- [42] G. M. Pressouyre, *Acta metall.* 28 (1980) p. 895.
- [43] I. M. Bernstein, A. W. Thompson, *Journal of Metals* 33 (1981) p. A17.
- [44] N. Yoshida, *J. Nucl. Mater.* 174 (1990) p. 220.
- [45] R. Schäublin, Z. Yao, N. Baluc, M. Victoria, *Phil. Mag.* 85 (2005) p. 769.
- [46] P. J. Maziasz, *Effect of He Content on Microstructural Development in Type 316 Stainless Steel under Neutron Irradiation*, 1985, Oak Ridge National Laboratory, Oak Ridge, TN 37831.
- [47] A. C. Nicol, M. L. Jenkins, M. A. Kirk, *Matrix damage in iron*, in proceeding: *Materials Research Society Symposium - Proceedings*, G.E. Lucas, L.L. Snead, M.A. Kirk and R.G. Elliman, 2001, pp. R1.3.1-R1.3.6.
- [48] M. L. Jenkins, C. A. English, B. L. Eyre, *Phil. Mag. A* 38 (1978) p. 97
- [49] R. Schaeublin, M. Victoria, *Identification of Defects In Ferritic/Martensitic Steels Induced by Low Dose Irradiation*, in proceeding: *Microstructural Processes in Irradiated Materials*, G.E. Lucas, L. Snead, M.A. Kirk and R.G. Elliman, Boston, 2001, pp. 81-86.
- [50] R. Schaeublin, D. Gelles, M. Victoria, *J. Nucl. Mater.* 307 (2002) p. 197.
- [51] E. A. Little, *J. Nucl. Mater.* 87 (1979) p. 11.
- [52] D. S. Gelles, *J. Nucl. Mater.* 108 (1982) p. 515.
- [53] D. S. Gelles, R. E. Schaublin, *Materials Science and Engineering a-Structural Materials Properties Microstructure and Processing* 309 (2001) p. 82.
- [54] R. Bullough, R. C. Perrin, *Proceedings of the Royal Society A* 305 (1967) p. 541.
- [55] X. Jia, Y. Dai, *J. Nucl. Mater.* 356 (2006) p. 105.
- [56] X. Jia, Y. Dai, *J. Nucl. Mater.* 318 (2003) p. 207.
- [57] X. Jia, Y. Dai, M. Victoria, *J. Nucl. Mater.* 305 (2002) p. 1.
- [58] R. L. Klueh, D. R. Harries, *Book High-Chromium Ferritic and Martensitic Steels for Nuclear Applications*, ASTM, West Conshohocken, PA, 2001.
- [59] P. Olsson, I. A. Abrikosov, L. Vitos, J. Wallenius, *J. Nucl. Mater.* 321 (2003) p. 84.
- [60] R. M. Fisher, E. J. Dulis, K. G. Carroll, *Transactions of the American Institute of Mining and Metallurgical Engineers* 197 (1953) p. 690.
- [61] R. O. Williams, H. W. Paxton, *Transactions of the American Institute of Mining and Metallurgical Engineers* 212 (1958) p. 422.
- [62] J. L. Boutard, *J. Nucl. Mater.* 179 (1991) p. 1179.
- [63] P. J. Maziasz, *J. Nucl. Mater.* 205 (1993) p. 118.

- [64] D. S. Gelles, L. E. Thomas, in: M.F. Ashby, R. Bullough, C.S. Hartley and J.P. Hirth (Eds.) *Dislocation Modelling of Physical Systems*, Pergamon Press, New York, 1980, pp. 559-568.
- [65] Y. Dai, G. S. Bauer, F. Carsughi, H. Ullmaier, S. A. Maloy, W. F. Sommer, *J. Nucl. Mater.* 265 (1999) p. 203.
- [66] Y. Dai, F. Carsughi, W. F. Sommer, G. S. Bauer, H. Ullmaier, *J. Nucl. Mater.* 276 (2000) p. 289.
- [67] S. J. Zinkle, W. G. Wolfer, G. L. Kulcinski, L. E. Seitzman, *Philosophical Magazine a-Physics of Condensed Matter Structure Defects and Mechanical Properties* 55 (1987) p. 127.
- [68] S. J. Zinkle, E. H. LEE, *Metallurgical Transactions a-Physical Metallurgy and Materials Science* 21 (1990) p. 1037.
- [69] L. D. Glowinski, J. M. Lanore, C. Fiche, Y. Adda, *J. Nucl. Mater.* 61 (1976) p. 41.
- [70] S. J. Zinkle, L. E. Seitzman, W. G. Wolfer, *Philosophical Magazine a-Physics of Condensed Matter Structure Defects and Mechanical Properties* 55 (1987) p. 111.
- [71] A. Moslang, D. Preininger, *J. Nucl. Mater.* 155 (1988) p. 1064.
- [72] N. Wanderka, E. Camus, H. Wollenberger, *Microstructure evolution of selected ferritic-martensitic steels under dual-beam irradiation*, in proceeding: *Microstructure Evolution During Irradiation*, 1996, pp. 451.
- [73] K. Farrell, E. Lee, *Ion bombardment damage in a modified Fe-9Cr-1Mo steel*, in proceeding: *Effects of Radiations on Materials: 12th International conference*, F. Garner and J. Perrin, 1985, pp. 383.
- [74] D. Gilbon, C. Rivera, *J. Nucl. Mater.* 155 (1988) p. 1268.
- [75] P. Jung, J. Henry, J. Chen, J. C. Brachet, *J. Nucl. Mater.* 318 (2003) p. 241.
- [76] J. Henry, M. H. Mathon, P. Jung, *J. Nucl. Mater.* 318 (2003) p. 249.
- [77] H. Schroeder, H. Ullmaier, *J. Nucl. Mater.* 179 (1991) p. 118.
- [78] E. Snoeck, J. Majimel, M. O. Ruault, M. J. Hytch, *J. Appl. Phys.* 100 (2006) p.
- [79] Q. Li, W. Kesternich, H. Schroeder, D. Schwahn, H. Ullmaier, *Acta metall. mater* 38 (1990) p. 2383.
- [80] W. Jäger, R. Manzke, H. Trinkaus, R. Zeller, J. Fink, G. Crecelius, *Radiation Effects and Defects in Solids* 78 (1983) p. 315.
- [81] L. K. Mansur, E. H. Lee, *J. Nucl. Mater.* 179-181 (1991) p. 162.
- [82] R. Pynn, *Neutron Scattering: A Primer*, 1990, Los Alamos National Laboratory, LA-UR-90-3000.
- [83] L. S. Lerner, *Book Physics for Scientists and Engineers*, Jones & Bartlett Publishers, 1997.
- [84] M. Shibayama, H. Jinnai, T. Hashimoto, *Neutron Scattering*, in: T. Tanaka (Eds.) *Experimental Methods in Polymer Science: Modern Methods in Polymer Research and Technology*, Academic Press, 1999, pp. 604.
- [85] P. Lindner, T. Zemb, *Book Neutrons, X-rays, and light : scattering methods applied to soft condensed matter*, Elsevier, Amsterdam; Boston, 2002.
- [86] S. Kline, in *Neutron Small Angle Scattering and Reflectometry from Submicron Structures NCNR Summer School*, 2000, pp. 1-21.
- [87] M. Born, E. Wolf, *Book Principles of opotics*, Pergamon Press, New York, 1980.
- [88] E. Bakshi, *Physics Letters A* 283 (2001) p. 243.

-
- [89] H. E. Fischer, J. Neuefeind, J. M. Simonson, R. Loidl, H. Rauch, *Journal of Physics-Condensed Matter* 20 (2008) p.
- [90] Y. ITO, C. G. Shull, *Physical Review* 1 (1969) p. 961.
- [91] J. Fitter, T. Gutberlet, J. Katsaras, *Book Neutron Scattering in Biology: Techniques and Applications*, Springer, 2006.
- [92] M. Shibayama, S. Nomura, T. Hashimoto, E. L. Thomas, *J. Appl. Phys.* 66 (1989) p. 4188.
- [93] A. Guinier, G. Fournet, *Nature* 160 (1947) p. 501.
- [94] A. Guinier, G. Fournet, *Book Small-angle Scattering of X-rays*, John Wiley & Sons, New York, 1955.
- [95] A. Guinier, *Ann. Phys. (Paris)* 12 (1939) p. 161.
- [96] G. Fournet, *Bulletin de la Société Française de Minéralogie et de Cristallographie* 74 (1951) p. 39.
- [97] O. Kratky, G. Porod, *Journal of Colloid Science* 4 (1949) p. 35.
- [98] G. Porod, *Colloid & Polymer Science* 124 (1951) p. 83.
- [99] G. Porod, *Colloid & Polymer Science* 125 (1952) p. 51.
- [100] W. Ruland, *J. Appl. Cryst.* 4 (1971) p. 70.
- [101] C. G. Vonk, *J. Appl. Cryst.* 6 (1973) p. 81.
- [102] H. Tomita, *Progress of Theoretical Physics* 72 (1984) p. 656.
- [103] H. Tomita, *Progress of Theoretical Physics* 75 (1986) p. 482.
- [104] T. Hashimoto, M. Takenaka, H. Jinnai, *J. Appl. Cryst.* 24 (1991) p. 457.
- [105] M. Takenaka, T. Hashimoto, *Journal of Chemical Physics* 96 (1992) p. 6177.
- [106] J. E. Martin, *J. Appl. Cryst.* 19 (1986) p. 25.
- [107] B. B. Mandelbrot, *Book The fractal geometry of nature*, Freeman, W.H., San Francisco, 1982.
- [108] D. Stauffer, *Physics Reports* 54 (1979) p. 1.
- [109] R. Coppola, R. Kampmann, M. Magnani, P. Staron, *Acta mater.* 46 (1998) p. 5447.
- [110] C. Bailat, *SANS measurement*, 1999, PSI, CH5232 Villigen.
- [111] M. H. Mathon, Y. de Carlan, G. Geoffroy, X. Averty, A. Alamo, C. H. de Novion, *J. Nucl. Mater.* 312 (2003) p. 236.
- [112] F. Bley, *Acta metall. mater* 40 (1992) p. 1505.
- [113] E. A. Little, D. A. Stow, *J. Nucl. Mater.* 87 (1979) p. 25.
- [114] M. H. Mathon, G. Geoffroy, Y. de Carlan, A. Alamo, C. H. de Novion, *Physica B* 276 (2000) p. 939.
- [115] G. R. Odette, C. L. Liu, B. D. Wirth, *Microstructure evolution during irradiation*, in proceeding: MRS Symposium, I.M. Robertson, G. S. Was, L.W. Hobbs and T. D. Rubia, 1997, pp. 457-462.
- [116] R. S. Averback, D. N. Seidman, *Mater. Sci.* 15-18 (1987) p.
- [117] D. J. Bacon, T. D. Delarubia, *J. Nucl. Mater.* 216 (1994) p. 275.
- [118] P. Sigmund, *Physical Review* 184 (1969) p. 383.
- [119] V. I. Arnold, *Book Mathematical Methods of Classical Mechanics*, Springer, 2000.
- [120] D. Raabe, *Book Computational Materials Science: The Simulation of Materials Microstructures and Properties*, Wiley-VCH, 1998.
- [121] J. E. Lennard-Jones, *Proceedings of the Physical Society* 43 (1931) p. 461.
- [122] F. London, *Zeitschrift Fur Physikalische Chemie-Abteilung B-Chemie Der Elementarprozesse Aufbau Der Materie* 11 (1930) p. 222.

- [123] F. London, *Zeitschrift für Physik A Hadrons and Nuclei* 63 (1930) p. 245.
- [124] R. Eisenschitz, F. London, *Zeitschrift für Physik* 60 (1930) p. 491.
- [125] J. E. Lennard-Jones, *Proceedings of the Physical Society A* 106 (1924) p. 463.
- [126] M. Shibahara, K. Inoue, K. Kobayashi, A Molecular Dynamics Study on Effects of Nanostructural Clearances at an Interface on Thermal Resistance (Technical), in proceeding: *Proceedings of MNHT2008, Micro/Nanoscale Heat Transfer International Conference*, Tainan, Taiwan, 2008, pp. MNHT2008-52276.
- [127] D. Frenkel, B. Smit, *Book Understanding Molecular Simulation: From Algorithms to Applications*, 2nd, Academic Press, 2002.
- [128] M. S. Daw, M. I. Baskes, *Physical Review B* 29 (1984) p. 6443.
- [129] J. Tersoff, *Physical Review B* 37 (1988) p. 6991.
- [130] J. Tersoff, *Physical Review B* 38 (1988) p. 9902.
- [131] D. W. Brenner, *Physical Review B* 42 (1990) p. 9458.
- [132] J. Tersoff, *Phys. Rev. Lett.* 61 (1988) p. 2879.
- [133] Y. Mishin, A. Y. Lozovoi, *Acta mater.* 54 (2006) p. 5013.
- [134] J. Marian, B. D. Wirth, R. Schäublin, G. R. Odette, J. M. Perlado, *J. Nucl. Mater.* 323 (2003) p. 181.
- [135] A. E. Ward, S. B. Fisher, *J. Nucl. Mater.* 166 (1989) p. 227.
- [136] B. C. Masters, *Phil. Mag.* 11 (1965) p. 881.
- [137] E. A. Little, R. Bullough, M. H. Wood, *Proceedings of the Royal Society of London Series a-Mathematical Physical and Engineering Sciences* 372 (1980) p. 565.
- [138] Y. N. Osetsky, A. Serra, B. N. Singh, S. I. Golubov, *Philosophical Magazine a-Physics of Condensed Matter Structure Defects and Mechanical Properties* 80 (2000) p. 2131.
- [139] N. Soneda, T. D. de la Rubia, *Philosophical Magazine a-Physics of Condensed Matter Structure Defects and Mechanical Properties* 78 (1998) p. 995.
- [140] J. Marian, B. D. Wirth, J. M. Perlado, *Phys. Rev. Lett.* 88 (2002) p.
- [141] P. Olsson, J. Wallenius, C. Domain, K. Nordlund, L. Malerba, *Physical Review B* 72 (2005) p. 214119.
- [142] A. Caro, D. A. Crowson, M. Caro, *Phys. Rev. Lett.* 95 (2005) p. 075702.
- [143] D. A. Terentyev, L. Malerba, R. Chakarova, K. Nordlund, P. Olsson, M. Rieth, J. Wallenius, *J. Nucl. Mater.* 349 (2006) p. 119.
- [144] J. Yu, Z. Yao, G. Yu, R. Schaeublin, *J. Nucl. Mater.* (2007) p. in press.
- [145] L. Yang, X. T. Zu, H. Y. Xiao, F. Gao, H. L. Heinisch, R. J. Kurtz, K. Z. Liu, *Applied Physics Letters* 88 (2006) p. 91915.
- [146] T. Harry, D. J. Bacon, *Acta mater.* 50 (2002) p. 195.
- [147] T. Harry, D. J. Bacon, *Acta mater.* 50 (2002) p. 209.
- [148] D. J. Bacon, Y. N. Osetsky, *Materials Science and Engineering A* 400-401 (2005) p. 353.
- [149] D. J. Bacon, Y. N. Osetsky, Z. Rong, *Phil. Mag.* 86 (2006) p. 3921.
- [150] Y. N. Osetsky, D. J. Bacon, *Modelling and Simulation in Materials Science Engineering* 11 (2003) p. 427.
- [151] Y. N. Osetsky, D. J. Bacon, *J. Nucl. Mater.* 323 (2003) p. 268.
- [152] Y. N. Osetsky, D. J. Bacon, *Nuclear Instruments and Methods in Physics Research Section B: Beam Interactions with Materials and Atoms* 202 (2003) p. 31.

-
- [153] Y. N. Osetsky, D. J. Bacon, *Materials Science and Engineering A* 400-401 (2005) p. 374.
 - [154] S. M. Hafez Haghighat, J. Fikar, R. Schaeublin, submitted to *Journal of Nuclear Materials* (2007) p.
 - [155] R. Schaeublin, N. Baluc, *Nuclear Fusion* 47 (2007) p. 1690.
 - [156] V. Vitek, *Phil. Mag.* 84 (2004) p. 415.
 - [157] R. Schaeublin, Y. L. Chiu, *J. Nucl. Mater.* 362 (2007) p. 152.
 - [158] S. M. Hafez Haghighat, R. Schaeublin, Submitted to *Computer-Aided Materials Design* (2007) p.
 - [159] S. M. Hafez Haghighat, R. Schaeublin, Molecular dynamics modeling of cavity strengthening in irradiated iron, in proceeding: *Multiscale Materials Modeling*, Freiburg, 2006
 - [160] W. R. Wampler, T. Schober, B. Lengeler, *Phil. Mag.* 34 (1976) p. 129.
 - [161] K. Shiraishi, A. Hishinuma, Y. Katano, *Radiation Effects and Defects in Solids* 21 (1974) p. 161.
 - [162] C. C. Fu, F. Willaime, *Physical Review B* 72 (2005) p. 064117.
 - [163] W. D. Wilson, C. L. Bisson, M. I. Baskes, *Physical Review B* 24 (1981) p. 5616.
 - [164] R. Schaeublin, A. Almazouzi, Y. Dai, Y. N. Osetsky, M. Victoria, *J. Nucl. Mater.* 276 (2000) p. 251.
 - [165] D. J. H. Cockayne, I. L. F. Ray, M. J. Whelan, *Phil. Mag.* 20 (1969) p. 1265.
 - [166] R. Schaeublin, P. de Almeida, A. Almazouzi, M. Victoria, *J. Nucl. Mater.* 283-287 (2000) p. 205.
 - [167] R. Schaeublin, Y. Dai, Y. N. Osetsky, M. Victoria, CTEM quantification of stacking fault tetrahedra in irradiated Cu, in proceeding: *International conference on electron microscopy*, H.A. Calderon Benavides and M.J. Yacaman, Cancun, 1998, pp. 173-174.
 - [168] R. Schaeublin, M. J. Caturla, M. Wall, T. Felter, M. Fluss, B. D. Wirth, T. D. de la Rubia, M. Victoria, *J. Nucl. Mater.* 307 (2002) p. 988.
 - [169] M. Rühle, *Book Radiation Damage in Reactor Materials*, International Atomic Energy Agency, 1969.
 - [170] B. L. Eyre, *Journal of Physics F-Metal Physics* 3 (1973) p. 422.
 - [171] M. Kiritani, *J. Nucl. Mater.* 133 (1985) p. 85.
 - [172] M. L. Jenkins, *J. Nucl. Mater.* 216 (1994) p. 124.
 - [173] T. D. de la Rubia, H. M. Zbib, T. A. Khraishi, B. D. Wirth, M. Victoria, M. J. Caturla, *Nature* 406 (2000) p. 871.
 - [174] M. Victoria, N. Baluc, C. Bailat, Y. Dai, M. I. Luppo, R. Schaeublin, B. N. Singh, *J. Nucl. Mater.* 276 (2000) p. 114.
 - [175] A. Ulbricht, J. Bohmert, M. Uhlemann, G. Muller, *J. Nucl. Mater.* 336 (2005) p. 90.
 - [176] G. Kostroz, *Treatise on Materials Science and Technology*, in: G. Kostroz and H. Herman (Eds.) *Neutron Scattering*, Academic Press, London, 1979, pp. 227-289.
 - [177] R. Coppola, F. Fiori, E. A. Little, M. Magnani, *J. Nucl. Mater.* 245 (1997) p. 131.
 - [178] J. Marian, B. D. Wirth, R. Schaeublin, J. M. Perlado, T. Diaz de la Rubia, *J. Nucl. Mater.* 307-311 (2002) p. 871.
 - [179] A. Moslang, E. Diegele, M. Klimiankou, R. Lasser, R. Lindau, E. Lucon, E. Materna-Morris, C. Petersen, R. Pippan, J. W. Rensman, M. Rieth, B. van der Schaaf, H. C. Schneider, F. Tavassoli, *Nuclear Fusion* 45 (2005) p. 649.

- [180] R. Schaeublin, N. Baluc, P. Spaetig, Microstructural stability under irradiation, Final Report on the EFDA Task SM 6.2, 2002.
- [181] N. Baluc, K. Abe, J. L. Boutard, V. M. Chernov, E. Diegele, S. Jitsukawa, A. Kimura, R. L. Klueh, A. Kohyama, R. J. Kurtz, R. Lasser, H. Matsui, A. Moslang, T. Muroga, G. R. Odette, M. Q. Tran, B. Van der Schaaf, Y. Wu, I. Yu, S. J. Zinkle, *Nuclear Fusion* 47 (2007) p. S696.
- [182] D. Gavillet, 1991, Paul Scherrer Institute.
- [183] J. Kohlbrecher, W. Wagner, *J. Appl. Cryst.* 33 (2000) p. 804.
- [184] V. Wagner, H. Friedrich, P. Wille, *Physica B* 180 (1992) p. 938.
- [185] H. Heer, M. Konnecke, D. Maden, *Physica B* 241 (1997) p. 124.
- [186] S.-M. Choi, in *Neutron Small Angle Scattering and Reflectometry from Submicron Structures NCNR Summer School, 2000*, pp. 1-25.
- [187] T. D. Delarubia, M. W. Guinan, *J. Nucl. Mater.* 174 (1990) p. 151.
- [188] G. J. Ackland, D. J. Bacon, A. F. Calder, T. Harry, *Phil. Mag. A* 75 (1997) p. 713.
- [189] G. J. Ackland, M. I. Mendelev, D. J. Srolovitz, S. Han, A. V. Barashev, *Journal of Physics-Condensed Matter* 16 (2004) p. S2629.
- [190] W. D. Wilson, D. R. Johnson, *Book Rare gases in metal*, Plenum, 1972.
- [191] D. E. Beck, *Molecular Physics* 14 (1968) p. 311.
- [192] M. W. Finnis, J. E. Sinclair, *Philosophical Magazine a-Physics of Condensed Matter Structure Defects and Mechanical Properties* 50 (1984) p. 45.
- [193] P. T. Wedepohl, *Proceedings of the Physical Society of London* 92 (1967) p. 79.
- [194] J. P. Biersack, J. F. Ziegler, *Nuclear Instruments & Methods in Physics Research* 194 (1982) p. 93.
- [195] L. Malerba, D. Terentyev, P. Olsson, R. Chakarova, J. Wallenius, *J. Nucl. Mater.* 329-333 (2004) p. 1156.
- [196] C. W. Gear, *Book Numerical Initial Value Problems in Ordinary Differential Equations*, Prentice-Hall, 1971.
- [197] J. D. Honeycutt, H. C. Andersen, *Journal of Physical Chemistry* 91 (1987) p. 4950.
- [198] P. A. Stadelmann, *Ultramicroscopy* 21 (1987) p. 131.
- [199] J. M. Cowley, A. F. Moodie, *Acta cryst.* 10 (1957) p. 609.
- [200] R. Schäublin, P. Stadelmann, *Materials Science and Engineering A* 164 (1993) p. 373.
- [201] P. B. Hirsch, A. Howie, R. B. Nicholson, D. W. Pashley, M. J. Whelan, *Book Electron microscopy of thin crystals*, Butterworth, London, 1965.
- [202] G. Kostorz, *Neutron Scattering*, in: G. Kostorz (Eds.) *Treatise on Materials Science and Technology* 15, Academic Press, New York, 1982, pp.
- [203] K. Morishita, B. D. Wirth, T. Diaz de la Rubia, A. Kimura, *Effects of Helium on Radiation Damage Processes in Iron*, in *proceeding: The Fourth Pacific Rim International Conference on Advanced Materials and Processing (PRICM4)*, S. Hanada, Z. Zhong, S.W. Nam and R.N. Wright, Hawaii, USA, 2001, pp. 1383.
- [204] R. E. Stoller, *J. Nucl. Mater.* 276 (2000) p. 22.
- [205] U. Gosele, W. Frank, A. Seeger, *Applied Physics* 23 (1980) p. 361.
- [206] C. S. Becquart, C. Domain, A. Legris, J. C. Van Duysen, *J. Nucl. Mater.* 280 (2000) p. 73.
- [207] C. Domain, C. S. Becquart, L. Malerba, *J. Nucl. Mater.* 335 (2004) p. 121.
- [208] G. Lucas, R. Schäublin, *Journal of Physics: Condensed Matter* 20 (2008) p. 415206.
- [209] L. Ventelon, B. Wirth, C. Domain, *J. Nucl. Mater.* 351 (2006) p. 119.

-
- [210] K. Shiba, A. Hishinuma, J. Nucl. Mater. 283 (2000) p. 474.
- [211] K. Morishita, R. Sugano, H. Iwakiri, N. Yoshida, A. Kimura, Thermal helium desorption from arufa iron, in proceeding: The Fourth Pacific Rim International Conference on Advanced Materials and Processing (PRICM4), S. Hanada, Z. Zhong, S.W. Nam and R.N. Wright, Hawaii, USA, 2001, pp. 1395.
- [212] D. J. Bacon, A. F. Calder, F. Gao, J. Nucl. Mater. 251 (1997) p. 1.
- [213] J. W. Edington, Book Interpretation of transmission electron micrographs, MacMillan, London, 1974.
- [214] M. F. Ashby, The deformation of plastically non-homogeneous alloys, in: A. Kelly and R.B. Nicholson (Eds.) Strengthening methods in crystals, Applied Science Publishers Ltd., 1971, pp. 137-192.
- [215] A. Seeger, M. Rühle, Annalen der Physik 466 (1963) p. 216.
- [216] A. J. Ardell, Metallurgical Transactions a-Physical Metallurgy and Materials Science 16 (1985) p. 2131.
- [217] N. Baluc, R. Schaeublin, P. Spaetig, M. Victoria, Hardening mechanisms in ferritic/martensitic steels, in: M. L. Grossbeck, T. R. Allen, R.G. Lott and A. S. Kumar (Eds.) Effects of Radiation on Materials: 21st International Symposium, ASTM STP 1447, ASTM International, West Conshohocken, PA, 2003, pp. 341-351.
- [218] M. I. Luppó, C. Bailat, R. Schaublin, M. Victoria, J. Nucl. Mater. 283 (2000) p. 483.
- [219] R. Schaublin, M. Victoria, Comparison Between 590 MeV Proton Irradiation and Neutron Irradiation on the F82H Ferritic/Martensitic Steel, in proceeding: Microstructural Processes in Irradiated Materials, S. J. Zinkle, G.E. Lucas, R. Ewing and J. Williams, 1999, pp. 597-602.
- [220] M. Rühle, M. Wilkens, Defocusing Contrast of Cavities. I. Theory, in: (Eds.) Crystal Lattice Defects, 1975, pp. 129-140.
- [221] M. Eldrup, B. N. Singh, S. J. Zinkle, T. S. Byun, K. Farrell, J. Nucl. Mater. 307 (2002) p. 912.
- [222] A. L. Bement, Fundamental Materials Problems in Nuclear Reactors, in proceeding: the Second International Conference on the Strength of Metals and Alloys, Asilomar Pacific Grove CA USA, 1970, pp. 693-728.
- [223] R. E. Stoller, S. J. Zinkle, J. Nucl. Mater. 283 (2000) p. 349.
- [224] K. Edsinger, University California Santa Barbara, 1995, Vol. PhD Thesis
- [225] R. Schaublin, P. Spatig, M. Victoria, J. Nucl. Mater. 263 (1998) p. 1178.
- [226] P. Spaetig, R. Stoenescu, P. Mueller, G. R. Odette, D. Gragg, J. Nucl. Mater. to appear p.
- [227] P. Spaetig, Proton irradiation of EUROFER 97 steel plate up to 1 dpa of plate, for He effect testing, Final report of the EFDA Task TW1-TTMS-001 deliverable 3, 2007.
- [228] T. Yamamoto, G. R. Odette, H. Kishimoto, J. W. Rensman, J. Nucl. Mater. 356 (2006) p. 27.
- [229] M. J. Makin, F. J. Minter, Acta metall. 8 (1960) p. 691.

ACKNOWLEDGMENTS

I am grateful to my thesis supervisor, Prof. Nadine Baluc, the leader of the Fusion Technology – Materials Group of the CRPP, for her great guidance and helpful discussions during my thesis. Also, I would like to thank her for her encouragement and help in the completion of the present manuscript and for her patience during this period.

I am grateful to Drs. R. Schäublin and P. Spätig of the Fusion Technology – Materials Group of the CRPP for their kind and excellent guidance and discussions along these years of my thesis.

I also wish to heart fully thank Dr. M. Victoria for his kind and excellent discussions during my thesis.

I also thank very much Drs. J. Chen, G. Lucas and J. Fikar, and M.S.H. Haghighat for their helpful discussions in MD simulations during my thesis.

For their great and indispensable help during my PhD work, I would like to give my thanks to Dr. R. Bonade, Dr. A. Ramar, Dr. Z. Yao, Dr. Y. Chiu, C. Gavillet, A. Kramer, S. Thoma, Dr. N. Nita, Dr. D. Hamaguchi, Dr. P. Marmy, Dr. Y. Dai, B. Long, N. Gao, Z. Tong, Dr. Z. Oksiuta and Dr. X. Jia, which are past, present or close members of the CRPP materials group in PSI.

CURRICULUM VITAE

Mr. Gang Yu

Né le 06 March 1970 à Beijing, République Populaire de Chine

- | | |
|-------------|---|
| 1989 – 1993 | Etudes de physique
Fudan Université, République Populaire de Chine
Diplome obtenu: Bachelor of Science |
| 1994 – 2003 | Chercheur, Laboratoire de Génie Atomique
China Institute of Atomic Energy, République Populaire de Chine |
| 2004 – 2008 | Doctorant au Centre de Recherches en Physique des Plasmas,
Ecole Polytechnique Fédérale de Lausanne
5232 Villigen PSI, Suisse |